Ref : BFR 05/115 2006-2009

École Doctorale Mathématiques, Sciences de l'Information et de l'Ingénieur

Mémoire de

THÈSE

Présentée en vu de l'obtention du grade de

Docteur de l'Université de Strasbourg

Par **Muhammad Ali SIDDIQUI**

Numerical Modelling and Simulation of Electromagnetic Forming Process

Discipline : *Sciences pour l'Ingénieur*
Spécialité : *Mécanique des Matériaux*

Thèse soutenue publiquement *le 26 juin 2009* à *14h30* à l'Institut de Mécanique des Fluides et des Solides de Strasbourg devant le jury composé de :

Membres du jury :

Directeur de thèse :	S. Ahzi	Professeur, Université de Strasbourg
Rapporteur externe :	L. Daridon	Professeur, Université de Montpellier
Rapporteur externe :	M. Martiny	Maître de Conférences (HDR), Université de Metz
Examinateur	Y. Rémond	Professeur, Université de Strasbourg
Examinateur	S. Belouettar	Chercheur, CRP-Henri Tudor, Luxembourg
Examinateur	J.P de Magalhaes Correia	Maître de Conférences, Université de Strasbourg

Institut de Mécanique des Fluides et des Solides, IMFS, UdS / CNRS ; Strasbourg

Acknowledgements

Acknowledgements

The work presented in this thesis was carried out at the "*Institut de Mécanique des Fluides et des Solides de Strasbourg*" and was financed by the "*Ministère de l'Education, de la Culture et de la Recherche du Grand Duché du Luxembourg*" in collaboration with "*Centre de Recherche Public Henri Tudor*". I would like to render my utmost gratitude to these institutions which helped me accomplish this Ph.D. research. I would like to thank all, who assisted, supported and counselled me during the three years from March 2006 till the end of my thesis in mid 2009. I would like to add few lines here to acknowledge to all who contributed in the progress of this Ph.D. research work.

First and foremost, I would like to express my sincere appreciation to the director of the *IMFS-Strasbourg*, Prof. Yves REMOND, who accepted me at this institute and has participated in various aspects of my research work.

I am also thankful to the ministry of "*Education, de la Culture et de la Recherche du Grand Duché du Luxembourg* » and to "*Centre de Recherche Public Henri Tudor*" who, not only generously provided me the financial support through out the Ph.D. research but also assisted in my active participations for international conferences. I acknowledge profoundly their support and willingness to finance all new intriguing projects in the domain of science and technology.

My sincere gratitude to Prof. Saïd AHZI, my thesis director, who introduced to me this research subject and provided me the opportunity to integrate into his research team. He always encouraged my research work and guided me in all scientific as well as administrative aspects. With his generous and kind supervision, this work has been completed in the best of the environment. I wish to record the relentless, timely and untiring guidance, I received from him.

I would like to thank extremely, Dr. de Magalheas Correia from *IMFS*, who was always there to support my research work. His scientific background, ideas and way of approaching the problems made a valuable learning experience for me. His suggestions, advices and supervision allowed the advancement of my work. His tireless efforts for the completion of this Ph.D. project are worth mentioning. I would like to thank him, for all guidance and management of my work. He always provided me new ideas and interesting fields to precede my work. He always corrected the errors and contributed for the betterment of the thesis. He was always willing to provide help and flexibility to my work with great deal of inspiration

and patience. His guidance, creativity and enthusiasm made it possible for me to complete this dissertation.

I would like to thank Dr. Salim Belouettar, from "*Centre de Recherche Public Henri Tudor*, *Luxembourg*", who always granted me his generous support, both financially and scientifically. His collaboration in this research work was vital, and it helped me to complete this project in time.

I would like to address my gratitude to Prof. Loïc DARIDON from "*Université de Montpellier II*" and Dr. Marion MARTINY from "*Université de Metz*", who accepted to be the members of the jury for my Ph.D. defence as external reporters. I would like to thank the members of jury of the defence.

I would also like to thank all the team of *IMFS-Strasbourg*, particularly the researchers and my lab-mates: Dr. N. Bahlouli, Dr. S. M'Guil, Dr. K. Hizoum, Dr. N. Joulaee, Dr. O. Geuguen, Dr. L. Dong and the rest of our team.

I would like to thank all my friends, I have during my stay in Strasbourg; their undeniable support was always with me. I owe a great deal of thanks and appreciation to all. My friends helped me solve problems related to the French language. Many thanks to all who directly or indirectly contributed to the completion of this thesis, and who brought something into my life.

In the end, I would to thank from the depth of my heart my parents and my family for their support, understanding, encouragement and confidence. They were always supportive and helpful even they were not near to me during the past years of research, but their moral presence was always there to provide me the zeal to complete this project. I dedicate my Ph.D. research work to my parents, to my family and to my friends.

Résumé

MODELISATION ET SIMULATION NUMERIQUE DE PROCEDES DE FORMAGE ELECTROMAGNETIQUE

Le réchauffement global de la planète est un des problèmes majeur auquel nous devons faire face aujourd'hui en termes d'écologie. Afin de réduire la consommation de carburant et les émissions de gaz à effet de serre, la réduction du poids des véhicules est l'une des solutions envisagées. Les alliages d'aluminium sont alors identifiés par l'industrie automobile comme les matériaux les plus intéressants pour réduire de manière significative le poids des véhicules. Néanmoins, la formabilité (ou la capacité de déformation) de l'aluminium pose un réel problème en emboutissage classique. En effet, l'aluminium a une formabilité beaucoup plus faible que l'acier. Ceci limite donc son utilisation pour faire des pièces de géométrie compliquées comparables à celles en acier. Pour étendre les limites de formabilité de matériaux tels que l'aluminium, de nouvelles techniques de mise en forme ont donc été développées : l'hydroformage, le formage superplastique par explosion et le formage électromagnétique. Depuis la fin des années 60, la mise en forme à l'aide de champs magnétiques pulsés intenses, appelée formage électromagnétique ou encore magnétoformage, a été employée sur les matériaux à haute conductivité électrique. Le magnétoformage est un procédé de mise en forme des métaux à grande vitesse de déformation. Ce procédé permet de déformer des pièces métalliques en déchargeant un courant pulsé intense à travers une bobine se situant à proximité de la pièce à déformer [1]. En fonction de la forme et de la position des bobines, des pièces métalliques peuvent être réalisées par compression, expansion ou bien encore assemblées ou également soudées. Ce procédé s'applique principalement aux métaux très bons conducteurs d'électricité (aluminium, cuivre, etc.) puisque la résistivité du matériau doit être la plus faible possible (la puissance transmise étant fonction de cette résistivité [2]). Par rapport à un procédé de mise en forme classique, le magnétoformage possède un certain nombre d'avantages : un procédé simple à mettre en œuvre, peu onéreux, qui grâce aux grandes vitesse augmente la formabilité des matériaux, un très fort gain de productivité, une réduction des risques de plissement, une meilleure maîtrise des phénomènes liés au retour élastique, et une réduction des effets dus au frottement (aucun contact entre les outils pendant la déformation). Les applications industrielles du magnétoformage sont nombreuses. Des secteurs industriels comme l'industrie automobile ou aérospatiale ainsi que la fabrication des emballages alimentaires peuvent être intéressés par ce procédé. Diverses applications de ce procédé sont présentées sur la Fig. 1.

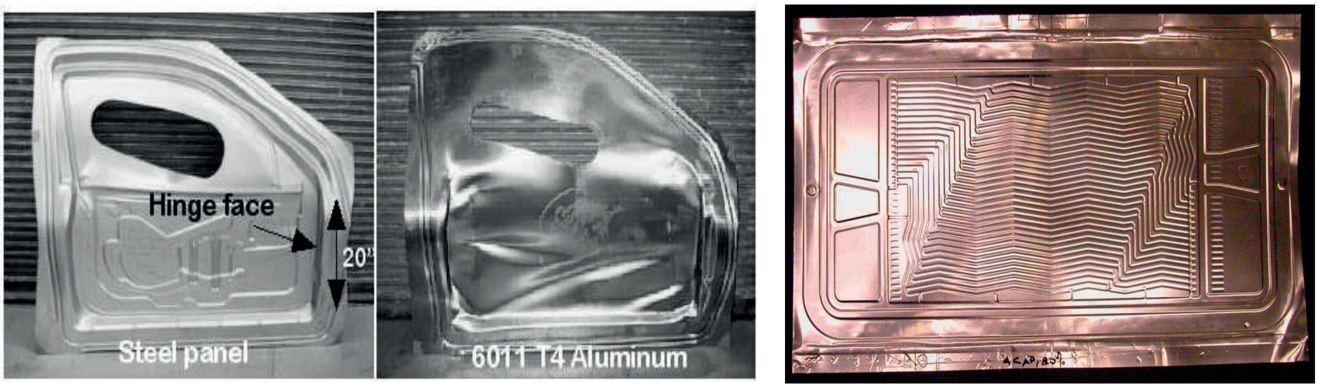

Industrie automobile [3] *Panneau pour les piles à combustible [4]*

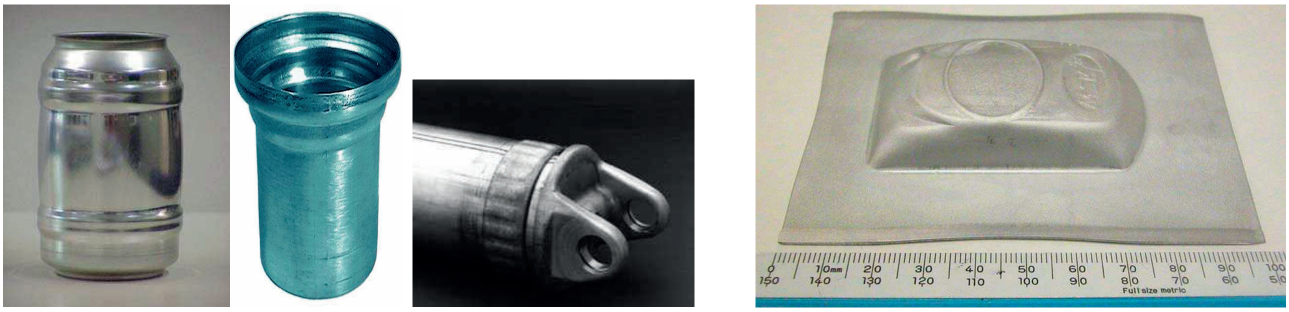

Emballages [5, 6,7] *Téléphonie mobile [4]*

Figure 1: Exemples du magnétoformage : (a) expansion, (b) compression.

Pour réaliser une opération de magnétoformage, il est nécessaire d'avoir un générateur de courant (composé de plusieurs capacités), une bobine, une pièce à déformer (soit sous la forme d'une tôle ou d'un tube) et une matrice sur laquelle viendra se plaquer la pièce à déformer [8]. Un exemple de montage du procédé du formage électromagnétique est présenté sur la Fig. 2. Afin de modéliser le magnétoformage, nous allons décrire brièvement les différents phénomènes physiques qui se déroulent lors de ce procédé. Dans un premier temps, un courant de forte intensité produit par le générateur traverse la bobine. Celle-ci génère alors un champ électromagnétique dans la région de l'espace située entre la bobine et la pièce. Un courant induit se propage ensuite dans la pièce à déformer. Ce courant induit génère à son tour un champ magnétique qui s'oppose à celui généré par la bobine. En conséquence il se développe de grandes forces de répulsion entre la bobine et la pièce. Ces forces de répulsions encore appelées forces de Lorentz projettent la pièce à une grande vitesse (aux environs d'une centaine de mètres par seconde). Lorsqu'une matrice est utilisée, la pièce vient se plaquer contre celle-ci, et prend ainsi la forme désirée. En l'absence de matrice la pièce se déforme librement. Dans tous les cas, la forme finale de la pièce dépend de plusieurs paramètres tels que la conductivité magnétique de la pièce, le courant de décharge, la distance entre la bobine et la tôle.

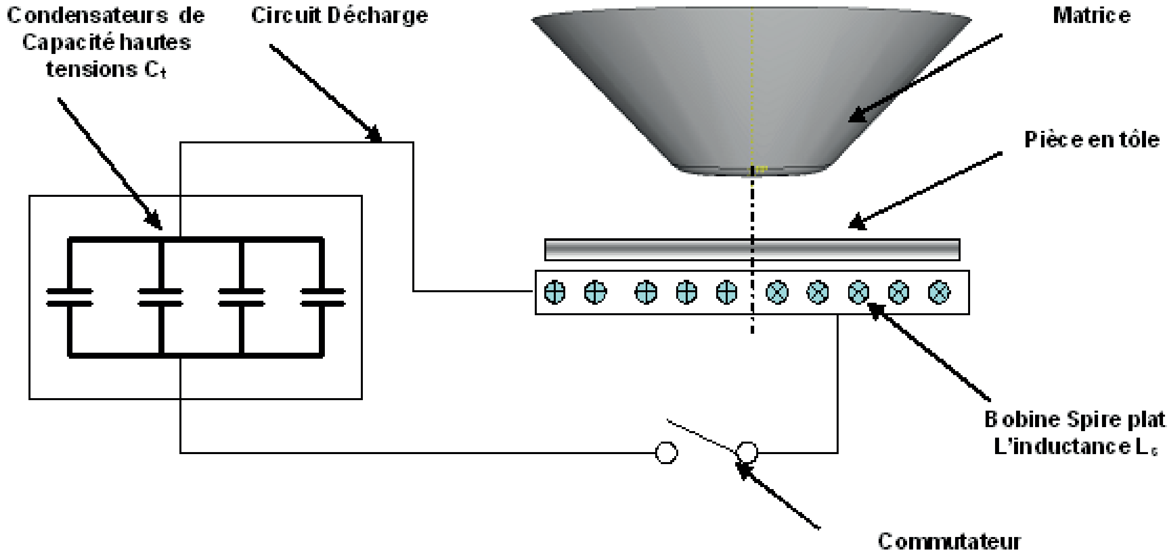

Figure 2: Schéma du montage du procédé de formage électromagnétique.

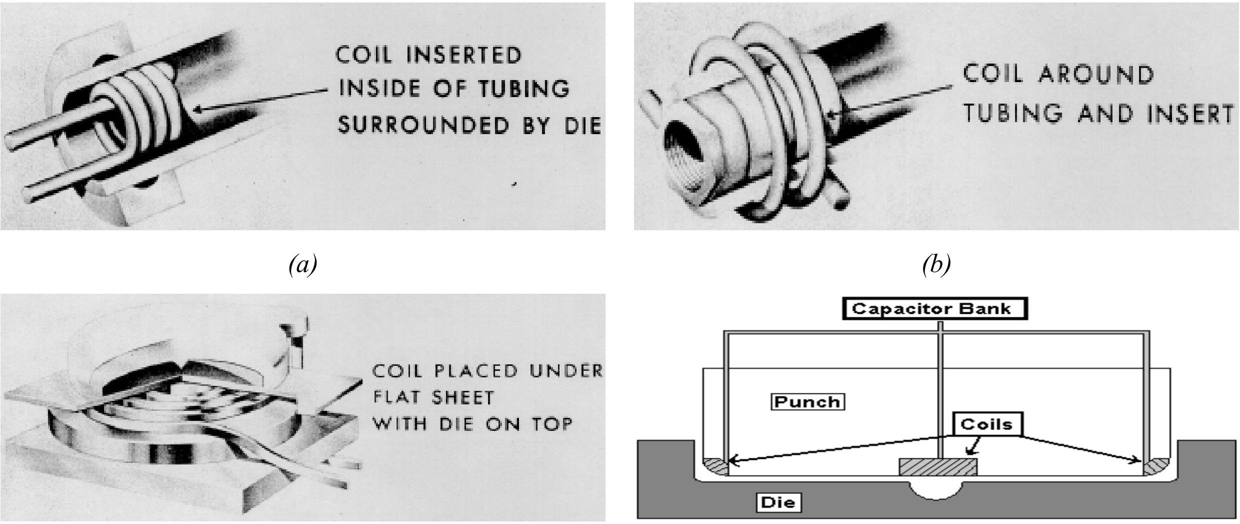

(a) *(b)*

(c) *(d)*

Figure 3: Exemples d'opérations de magnétoformage :
(a) expansion d'un tube [9], (b) compression d'un tube [9], (c) mise en forme par emboutissage électromagnétique [9] et (d) système hybride de magnétoformage [10].

Le procédé du formage électromagnétique peut être appliqué à différents types de géométrie : la mise en forme des tôles et le mise en forme des tubes. Pour l'opération de magnétoformage des tôles, une bobine plate est généralement placée sous la pièce à déformer.

Quant aux opérations d'expansion ou de compression de tubes, elles sont réalisées à l'aide de bobines radiales placées à l'intérieur (cas de l'expansion) ou l'extérieur de tubes (cas de la compression). Plus récemment des systèmes hybrides sont apparus ; des bobines sont placées dans un outil conventionnel (comme le poinçon dans une opération d'emboutissage). Ces bobines interviennent alors en complément à un procédé de mise en forme classique. Des exemples de différents types de procédé de formage électromagnétique sont présentés sur la Fig. 3.

En général, le développement d'un outillage ou d'un nouveau procédé de mise en forme est une opération onéreuse et longue. Comme une entreprise se doit de maîtriser ses coûts, d'augmenter sa productivité, d'améliorer la qualité des produits et de réduire ses délais de développement, celle-ci se tourne alors vers la modélisation numérique. La modélisation numérique des procédés de mise en forme est une approche couramment utilisée pour créer, développer et améliorer (par la réalisation d'études paramétriques) de nouveaux procédés. Ces études numériques offrent la possibilité de mieux comprendre les phénomènes physiques qui se produisent au cours du procédé étudiés. Elles permettent de prévoir et ainsi d'améliorer l'efficacité et la productivité du nouveau procédé. La modélisation numérique offre la possibilité de mieux comprendre les phénomènes multi physiques qui se produisent au cours des procédés étudiés. Le but de ce travail est de développer un simulateur numérique afin de décrire le procédé de formage électromagnétique et de mieux comprendre les phénomènes physiques intervenant pendant la déformation de la pièce. Dans les cas des études numériques trois approches ont été développées :

- Couplage fort entre le problème magnétique et le problème mécanique [11],
- Couplage faible entre le problème magnétique et le problème mécanique [12, 13],
- Aucun couplage entre les deux problèmes [14].

Dans ce travail nous avons décidé d'adopter l'approche avec couplage faible. Dans cette approche le problème magnétique et le problème mécanique sont traités indépendamment. Nous avons arbitrairement choisi d'étudier que des procédés à géométrie axisymétrique. Les phénomènes magnétiques sont décrits par les équations de Maxwell. En accord avec [15], nous avons décidé d'utiliser les équations de la magnétostatique, c'est-à-dire que la vitesse de déplacement de la pièce à déformer est négligeable. Le problème électromagnétique est résolu par la méthode des différences finies afin d'obtenir la pression agissant sur la face de la pièce métallique la plus proche de la bobine. La méthode des différences finies utilisée pour résoudre les équations de Maxwell a été programmée en langage FORTRAN. Ce programme a été, dans un premier temps, validé sur un cas test et comparé aux résultats expérimentaux disponibles dans la littérature [16] et aux prévisions obtenues avec un code libre de calcul par élément finis pour les problèmes de magnétisme (FEMM [17]). La géométrie utilisée pour le cas test a été proposé par [16] et est présentée sur la Fig. 4.

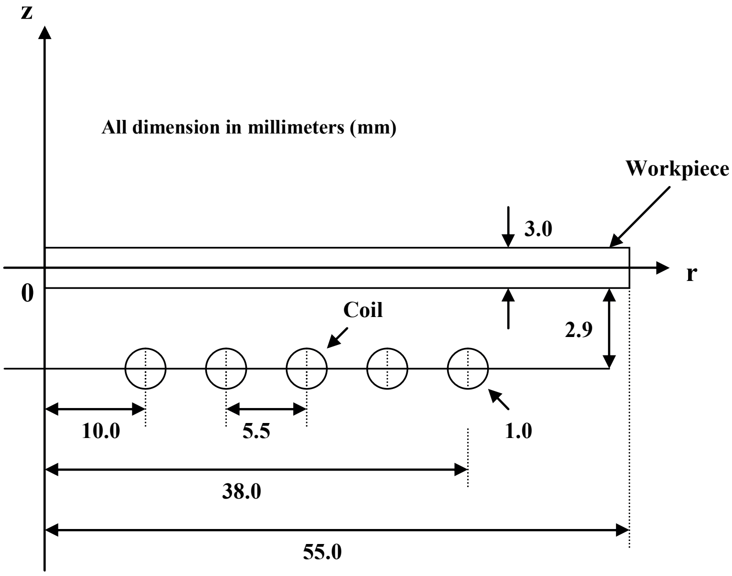

Figure 4: Géométrie de l'essai proposé par [12].

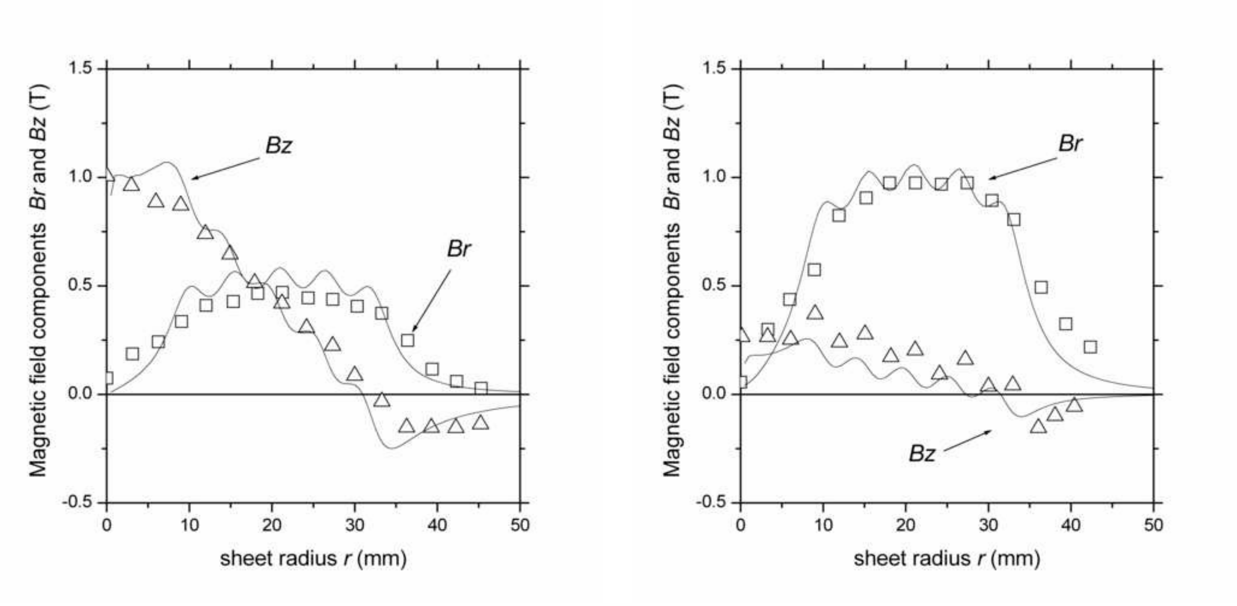

(a) (b)

Figure 5: Distribution du champs magnétique B: (a) sans la pièce (b) avec la pièce en aluminium.

Dans la configuration géométrique présentée sur la Fig. 4, les distributions de la composante radiale et axiale du champ magnétique ont été tracées sur la Fig. 5. Les lignes représentent les prévisions numériques tandis que les points représentent les résultats expérimentaux. Nous observons un bon accord entre les prévisions numériques et les résultats expérimentaux [16].

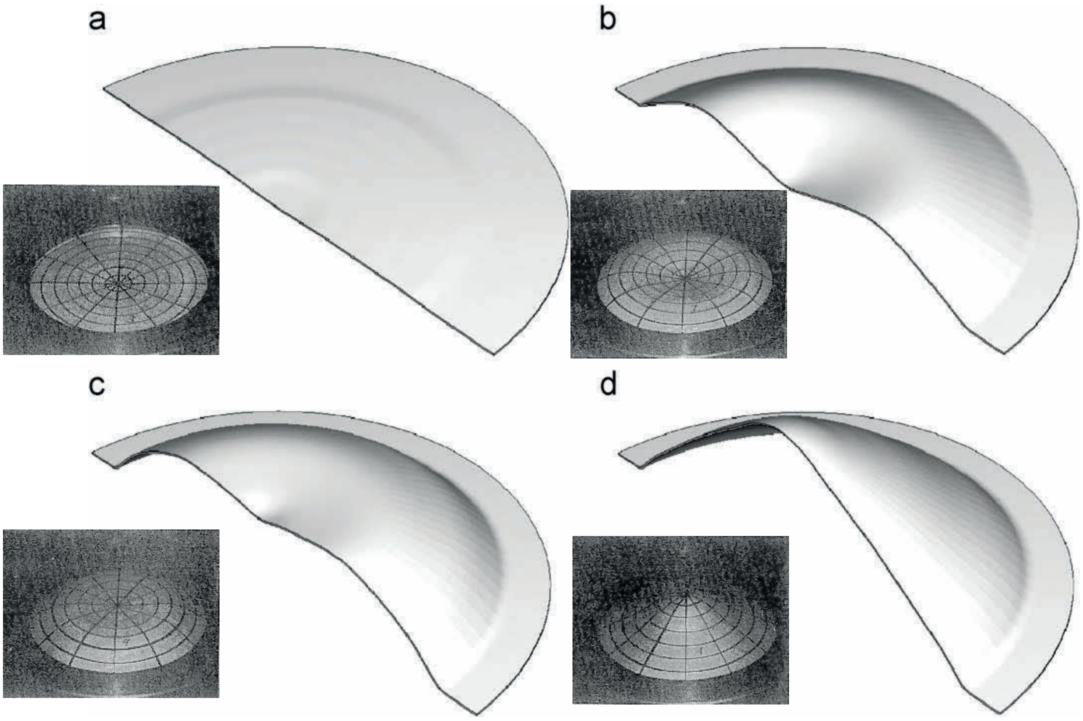

Figure 6: Les prévisions et résultats expérimentaux de la géométrie déformée de la pièce à différent pas de temps: (a) à t = 19 µs, (b) à t = 95 µs, (c) à t = 135 µs et (d) à t = 240 µs.

Le code de calcul par différences finies permettant de simuler le problème magnétique étant validé, nous pouvons résoudre le problème mécanique. Le problème mécanique est quant à lui traiter par un code commercial de calcul de structures par éléments finis (ABAQUS) en utilisant un algorithme de résolution de type dynamique avec une intégration du temps de type explicit (ABAQUS/Explicit [18]). Le code de calcul par différences finies a été ensuite introduit dans le logiciel ABAQUS via un sous-programme utilisateur VDLOAD. Des simulations d'essais d'expansion (libre ou avec matrice) de tôles métalliques ainsi que des essais d'expansion et de compression de tubes métalliques ont été réalisées. Dans un premier temps l'essai de formage électromagnétique proposé dans [16] a été modélisé en axisymétrique. Les outils (la matrice et les serre-flans) ont été supposés comme des corps rigides. La pièce a été modélisée en utilisant des éléments de type CAX4R. Les prévisions obtenues sont en accord avec les résultats expérimentaux disponibles dans la littérature [16].

La Fig. 6 présente la comparaison entre les prévisions obtenues avec ABAQUS et les résultats expérimentaux issus de [16]. Les simulations de l'expansion et de la compression des tubes ont été réalisées par la suite. Les prévisions numériques obtenues ont été comparées avec les résultats expérimentaux disponibles dans la littérature. Sur la Fig. 7, nous montrons la comparaison de l'évolution de la déformation du centre du tube pendant le procédé de compression du tube. La prévision du code de calcul a été comparée avec les résultats numériques et expérimentaux de [19]. Nous constatons, sur la Fig. 7, que les résultats obtenus par nos simulations sont en assez bon accord avec les résultats de [19].

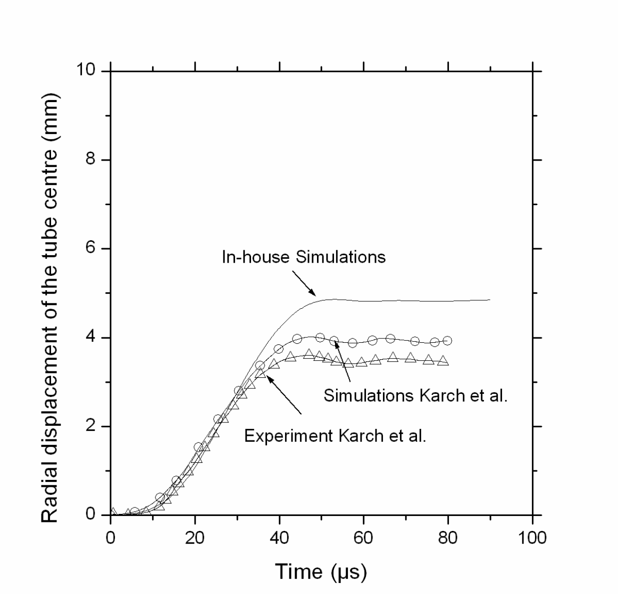

Figure 7: Evolution de la déformation du centre du tube en fonction du temps.

Ensuite, une étude paramétrique a été menée afin de déterminer les paramètres prépondérants du procédé de magnétoformage par expansion libre de tôles métalliques. Le but de cette partie est de mieux comprendre le comportement et les effets des différents paramètres du circuit sur la déformation de la pièce. De cette étude paramétrique, il apparaît que les paramètres les plus importants sont l'épaisseur de la tôle, la distance entre la tôle et la bobine et enfin l'intensité du courant de décharge. Nous avons aussi comparé différents types de procédés de mise en forme de tôles afin de déterminer l'influence des grandes vitesses de déformation sur le retour élastique de la pièce. Les résultats obtenues montrent que le retour élastique obtenu par le procédé de formage électromagnétique est inférieur à ce qui à été obtenu par un essai d'emboutissage. Nous avons conclu que cela est dû aux importantes valeurs de déformation plastique équivalente atteintes dans le procédé de magnétoformage.

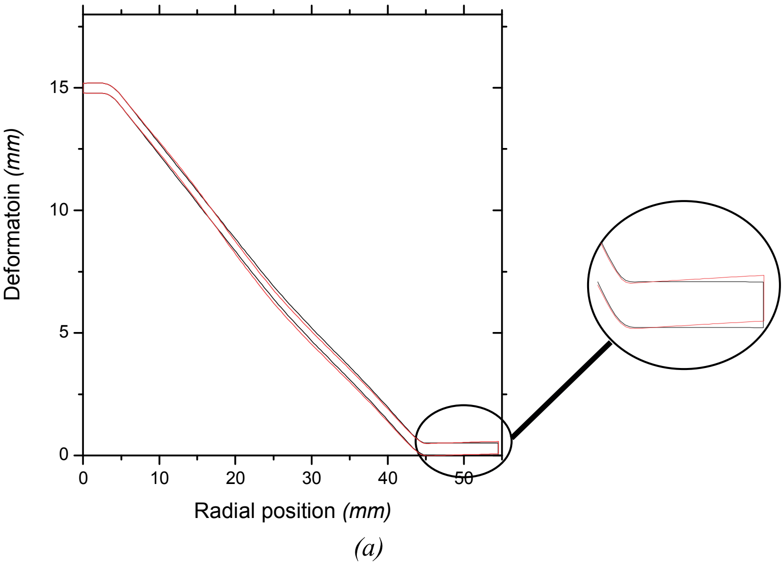

(a)

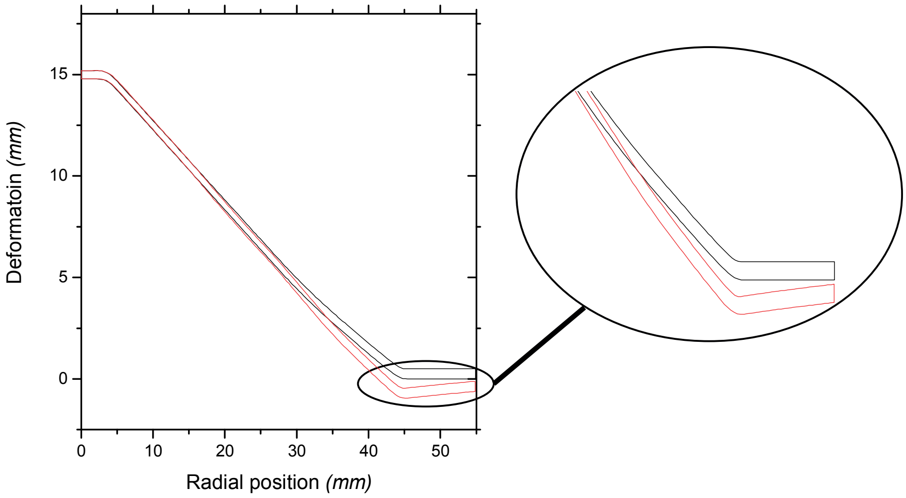

(b)

Figure 8: Comparaison de la géométrie déformée et la géométrie obtenue après l'enlèvement des outils (a) formage électromagnétique avec une matrice (b) emboutissage classique.

La Fig. 8 présente la comparaison de la géométrie déformée et la géométrie obtenue après retour élastique dans le cas du magnétoformage avec une matrice (a) et dans le cas d'un essai d'emboutissage conventionnelle (b). Les comparaisons entre les résultats expérimentaux de formage électromagnétique et les simulations réalisées avec ABAQUS sont bonnes. Ces résultats montrent que les simulations des procédés sont en bon accord avec les résultats expérimentaux. Concernant la modelisation et la simulation de procédés de formage électromagnétique, on peut considérer que notre modèle est capable de simuler avec un bon accord la déformation des pièces métalliques.

Référence:

[1] Belyy I.V., Fertik S.M., and Khimenko L.T., *Electromagnetic Metal forming Handbook,* translated by Altynova M.M., Material Science and engineering department, The Ohio State University.

[2] Mamalis A.G., Manolakos, D.E., Kladas, A.G., Koumoutsos, A.K., Electromagnetic forming and powder processing: Trends and developments, *Applied Mechanics Review* (2004), 57; pp. 299-324.

[3] Mallein V., Magnétoformage de pièces en aluminium pour automobile, Étude expérimentale et développement numérique associe. Thèse de Génie des Procèdes. Grenoble : INPG 2003.

[4] Manish Kamal, A uniform pressure electromagnetic actuator for forming flat sheets, Doctorate thesis, The Ohio State University, 2005

[5] Teodora-Emilia MOTOASCA, Electrodynamics in deformable solids for electromagnetic forming, Universitatea “Transilvania”, Brasov, Roumania, 2003.

[6] Jozef Bednarczyk, Distribution of forces in the inductors used in metal processing in the pulse magnetic field, *Journal of Materials Processing Technology (2003)*, vol. 133,pp. 340-247.

[7] Yu Hai-ping and Li Chun-feng, Effects of coil length on tube compression in electromagnetic forming, *Transactions of Nonferrous Metals Society of China 17(2007),* pp. 1270–1275.

[8] Gourdin W.H., Analysis and assessment of electromagnetic ring expansion as a high – strain rate test; *Journal of applied physics* (1989), 65(2); pp. 411-422.

[9] Padmanabhan M., Wrinkling and Spring Back in electromagnetic sheetmetal forming and Electromagnetic ring compression. Master of Science Thesis: The Ohio State University, 1997.

[10] Vincent J. Vohnout, A hybrid quasi-static/dynamic process for forming large sheet metal parts from aluminum alloys, Doctorate thesis, The Ohio State University, 1998.

[11] Unger J.A, Modeling and simulation of coupled electromagnetic field problems with application to model identification and metal forming, Doctor Engineer Thesis, University of Dortmund, Deutschland (2007).

[12] Correia J.P.M., Siddiqui M.A., Ahzi S., Belouettar S. and Davies R., A simple model to simulate electromagnetic sheet free bulging process, *International Journal of Mechanical Sciences* (2008), 50, pp.1466–1475.

[13] Sung Ho Lee and Dong Nyung Lee, A finite element analysis of electromagnetic forming for tube expansion, *Journal of Engineering Materials and Technology* (1994), 116; pp. 250-254.

[14] Jablonski J. and Wrinkler R., Analysis of the electromagnetic forming process, *International Journal of mechanical sciences* (1978), 20; pp.315-325.

[15] Manea T.E., Verweij, M.D., Blok, H., The importance of velocity term in the electromagnetic forming process, *Proceedings of 27th General Assembly of the International Union of Radio Science, URSI 2002,* Maastricht; pp. 112-115.

[16] Takatsu N., Kato M., Sato K., Tobe T., High speed forming of metal sheets by electromagnetic forces, *International Journal of Japanese Society for Mechanical Engineering* (1980), 60; pp. 142-148.

[17] FEMM4.0, http://femm.foster-miller.net/wiki/HomePage (visité en Mai 2009).

[18] ABAQUS/Explicit, Version 6.5 Manuals, Hibbitt, Karlsson and Sorensen Inc., Pawtucket, USA (2005) (visité en Mai 2009).

[19] Karch C. and Roll K., Transient simulation of electromagnetic forming of aluminium tubes, *Advanced Materials Research,* vol. 6-8 (May 2005), pp. 639-646

Table of contents

Table of contents

Chapter I: Literature review

Chapter II: Finite difference model for resolution of the electromagnetic problem of EMF process

Chapter III: Finite element implementation and application of the EMF Numerical model

Chapter IV: Parametric study of EMF process and FE predictions of springback

CONCLUSION AND PERSPECTIVES

List of Figures

List of Figures

Notations Used

Notations Used

Symbol	Definitions	units
$I_0(t)$	Maximum intensity of discharge current	A
$I_1(t)$	Discharge current	A
$I_2(t)$	Induced current	A
L_1	Inductance of circuit	H
L_2	Inductance of workpiece	H
L_C	Inductance of coil	H
L	Total Inductance of the circuit	H
R_1	Resistance of circuit	Ω
R_2	Resistance of workpiece	Ω
R_C	Resistance of coil	Ω
R	Total Resistance of the circuit	Ω
M	Mutual inductance between coil and workpiece	H
t	Time, step time	s
t_f	Total simulation time	s
τ	Damping coefficient	s
E	Charging energy	J
V_0	Charging voltage	V
B	Magnetic field density	T
B_r	Magnetic field density radial component	T
B_z	Magnetic field density axial component	T
B_0	Coil Magnetic field density	T
B_1	Workpiece Magnetic field density	T
J_f	Current density	A/m^2
H	Magnetic flux	T/m^2
μ	Electrical Permeability of medium	H/m
μ_0	Electrical Permeability of free space	H/m
v	Workpiece velocity	m/s
σ_w	Electrical conductivity	S/m
ω	Angular frequency of discharge current	Rad/s
$\mathbf{E}$	Electric field intensity	N/C
F	Electromagnetic force density	N
f_r	Radial component of Electromagnetic force density	N
f_z	Axial component of Electromagnetic force density	N
P	Electromagnetic pressure	N/m^2
P_r	Radial component of Electromagnetic pressure	N/m^2
P_z	Axial component of Electromagnetic pressure	N/m^2
d_g	Gap distance between coil and workpiece	m

Symbol.	**Definitions**	**units**
e	Workpiece thickness	m
r	Workpiece radius	m
$u(t)$	Actual position of workpiece with respect to time	m
A_θ	Azimuthal electromagnetic vector potential	
g	Geometric factor	
$K(g)$	Elliptic integral of 1st kind	
$E(g)$	Elliptic integral of 2nd kind	
dV	Differential volume	m^3
dS	Differential surface	m^2
i	Increment in z-direction	
j	Increment in r-direction	
k	Step time increment	
Δ	Delta operator(incremental operator)	
∇	Nabla operator	
$\sum$	Summation operator	
∇^2	Laplace operator	
N	Number of turns of the coil	
ρ_n	Electrical resistivity of the material	Ω-m
δ	Skin depth	m
S_0	Unit surface with in the workpiece	m^2
σ	Effective stress	Pa
ε^p	Effective plastic strain	
A	Material constant for Johnson-Cook model	MPa
B	Material constant for Johnson-Cook model	MPa
T	Temperature	K
α	Material constant for Johnson-Cook model	
β	Material constant for Johnson-Cook model	
m	Material constant for Johnson-Cook model	
n	Material constant for Johnson-Cook model	

Introduction

Introduction

The term "*High Velocity Forming (or high energy forming)*" covers a large group of processes including methods such as explosive forming, electric discharge forming, electromagnetic forming. During these processes, the workpiece is submitted to a high kinetic energy early in the process, and the deformation is largely followed due to inertial effects of the high velocity. Finally, this kinetic energy dissipates as plastic deformation. Among a lot of advantages, these processes allow an increase of formability of materials like aluminium alloys. These processes have been applied in industries to some extent, and are capable to address the problems faced in conventional forming techniques. Light-weight manufacturing industry can benefit instrumentally from the high-speed processes. In recent year, a significant interest using these techniques in the automobile and aerospace industry has developed. Keeping in view the main advantages of weight saving and eventually fuel efficiency, more and more industries are thriving to use lighter metals such as aluminium or high strength steel sheets. The automotive industry has been determined to replace steel components with light metals such as aluminium alloys. As a consequence, there is a renewed interest in high velocity forming applications, which have been proven to tackle many issues of conventional metal forming processes through dramatic improvements. The implementation of these processes in the industry, including electromagnetic forming process in particular, represents an extremely promising approach.

In electromagnetic forming (call EMF in the following) process, strong transient electromagnetic field is developed in the gap between the forming coil and the metallic workpiece. A high-current pulse is discharged through the circuit using a capacitor bank. This current runs through the forming coil in order to generate the electromagnetic field in gap. The transient nature of the electromagnetic field creates an induced Eddy current inside the workpiece, flowing opposite to the initial discharge current. The interaction between the two running currents, opposite to each other, consequently produces intense repulsive body forces between the forming coil and the workpiece, causing the workpiece to move and deform rapidly. Normally, two types of geometries can be conceived through EMF process: radial tubes and flat sheet metals. Theoretically, the same forming system can be used to obtain radial deformation of the workpieces, i.e. operations of compression and expansion with a spiral coil. For sheetmetal forming process, a pancake flat spiral coil is frequently used. EMF process has many advantages that make it a striking alternative to conventional forming systems and even to other high velocity forming processes. Using EMF process, the workpiece can be accelerated to velocities on the order of *200-300 m/s* in a few microseconds. High formability, reduced wrinkling, high productivity and elimination of elastic springback are prominent advantages.

Between 1960 and 1970, a great interest in the scientific study of EMF process was developed. Early literature provides considerable information on the principles of this forming process. The subject was not studied extensively as applications at an industrial level were not feasible due to the lack of high-performance components and materials. With the development of promising efficient tools, a new scope for studying the EMF has emerged. Both experimental and numerical aspects of the EMF system are cited in the literature. However, the early literature on the EMF process seems to report little emphasis on the numerical modelling, which is mainly attributed to the limited availability of analytical modelling tools. Particularly, due to the multiphysics nature of interacting phenomena taking place during the deformation in EMF, the existing machines were rather slow or even incapable to achieve the convergence for the related problems. The details of the physical phenomena were known but could not be accurately computed. Moreover, the lack of fast computers to perform the required complicated numerical simulations also contributed to slow development of numerical tools. With the progress in the domain of computation, more and more studies have been carried out EMF. The most frequently used method for numerically predicting the process is the finite element analysis. Several studies had been put forward during the last few years. Early work by Al-Hassani *et al.* [1] described the basic equations of the physics. This work provided the state of the art in the mid 1960s and 1970s. The forming circuit was designed as a combination of coil and workpiece as a single equivalent circuit. The distribution of the magnetic pressure was presented using different configurations of forming coils. This work is considered as the pioneer in the field of both experimental and numerical aspects of the EMF process. The work that followed by Jablonski *et al.* [2] and Gourdin [3] provided the solution of the forming system analytically using a simpler set of electromagnetic equations. During the same time, Takatsu *et al.* [4] provided a detailed approach to model the electromagnetic forming of thin metal parts, and compared their numerical results with experiments. This work resulted in simplified expressions for the calculation of magnetic fields in the forming coil and the workpiece. The electromagnetic Maxwell's equations were used. The electromagnetic pressure was calculated from simplifying the forming coil into elementary circular loops each carrying individually the discharge current. Takatsu *et al.* [4] took into account the evolution of the electromagnetic field with the deforming workpiece. The effects of the changing geometry provided even more precise modelling of the EMF process. Apart from the studies that explicitly dealt with experimental and numerical aspects of the electromagnetic forming process, many papers investigated other subjects related to the influence of process and geometrical parameters [5,6], effect of tool-sheet interactions [7,8], coil design [9,10], hyperplasticity [11] etc.

A large number of existing codes mentioned in the literature solved Maxwell's equations and incorporate the evolution of magnetic field with the deforming workpiece. The main difficulty these codes share is their complicated approach towards solving the equations. The approaches, hereby mentioned are either too slow to obtain convergence, or very intricate to implement. The numerical predictions obtained from these codes still needed more improvement. Research found in the publication has formulated the tools to model the electromagnetic process, but needed to quantitatively provide the outlet to investigate the dynamics of deformation, interaction between the different phenomena and to influence of process parameters. The main objective of our research study was to develop a simple but efficient computational tool to simulate the EMF process. The models developed are intended to provide insight into the various aspects and their interactions during the process. These numerical tools are desired to address both aspects of electromagnetic and mechanical phenomena occurring during deformation. Our aim was to develop a numerical tool which is capable of calculating the basic parameters, and can predict the final shape of the workpiece. Our research work presents a new simpler approach. This numerical model offers a computationally cost effective method for analyses. The present work aims at a systematic study to develop a simpler model for the numerical simulation of EMF, both in sheetmetal and in tube forming processes. We aimed to provide a mathematical model for EMF process, and validate it with some existing numerical tool and experiments.

This dissertation begins with the basic introduction of the EMF process. The forming system and details of various components of EMF system are provided. General aspects are developed in order to understand the properties of the system. The reported components are described from the point of view of diverse applications. The potential advantages and disadvantages of the process are then briefly discussed. An extensive investigation of the existing literature is presented. This section of the **CHAPTER-I** is focussed on a nonexhaustive review of the experimental and numerical techniques developed during the past few years. The eloquent details of the experimental studies comprising both flat sheetmetal as well as tubular forming processes are reported. In addition, existing numerical method for the modelling of the process of EMF are also explored in the last section of this chapter. Various different approaches on the aspects of the modelling the multiphysics phenomena are then presented. A number of numerical studies are discussed, with the main goal of exploring fundamentals about the designing of a simpler but accurate approach towards EMF process. Comparison of these approaches is presented Comments on the advantages and limitations of the various numerical methods developed during the course of past few years are then discussed in the end of this chapter.

The electromagnetic problem and its details are developed in the **CHAPTER II.** The chapter commences with the introduction to the electromagnetic system. The methodology applied for the resolution of the Maxwell's equations is then presented. In order to model the electromagnetic problem, and still keeping in the framework of a simpler numerical model, certain primary assumptions were made. A section entails the details on the simplifying assumption and hypothesis applied for the resolution of the electromagnetic equations related to the EMF process. After the presentation of the basic suppositions, the description of the electromagnetic problem is then reported. The calculation of the basic circuit parameters is performed. Firstly, we started with the presentation of the geometry used for the calculations. Then, the discretization of the basic equations for the geometry concerned is carried out. The initial and boundary conditions are necessary to resolve the equations under consideration. These are discussed in the next section of this chapter. Once, the whole electromagnetic problem is correctly developed; the determination of the magnetic field density and the electromagnetic pressure is carried out. The results obtained from the in-house code are compared with a preliminary experimental case test taken from the work of Takatsu *et al.* [4]. Subsequently, the results obtained from the in-house code are verified and validated using open source finite element software FEMM [13]. This software treats the problems evoked in most electromagnetic systems. In the next section of this chapter, a study of the numerical parameters is presented. This parametric study deals with the parameters of the domain discretization applied in the in-house code for the calculations. Influence of the time step and meshing are studied in this section. To conclude, the comparison of the results obtained from the in-house, the experimental results found in literature and the ones from FEMM [13] are presented.

CHAPTER III deals with the implementation of the in-house code into the finite element code ABAQUS/ Explicit [14] by means of a user-defined subroutine VDLOAD. The proposed model is an axisymmetric planar model. The coupling scheme between the electromagnetic problem and the mechanical problem is detailed. The in-house code is adapted to the requirements of the finite element analyses. The requirements and necessities for the numerical modelling method are discussed. The material properties, the geometrical aspects of the EMF forming systems are then presented. Three different applications of the EMF process are modelled for the simulations. At first, the flat sheetmetal free bulging simulations are carried out. Numerical predictions are compared with the experiments of Takatsu *et al.* [4]. Then the in-house code is further adapted for its implementation to the tubular radial forming operations such as tube expansion and compression processes. Basic experimental and numerical parameters for the simulations are detailed in this section. The results obtained from the numerical analyses are compared with the experimental ones reported in the literature [15,16].

In order to identify the effects of process parameters and geometrical factors of the EMF system, a parametric study based on the sheetmetal free forming process is presented in **CHAPTER IV.** EMF process depends on several different variables of the system. We studied a number of important features. Influence of these variables on the distribution of the magnetic field, electromagnetic force and deformation is presented. Our in-house code provides the possibility to simulate the process; we can modify the process and geometrical parameters in both the electromagnetic problem as well as in the mechanical problem. An attempt is made to determine the effect of several materials and process parameters on the deformation during process. In the later section of the **CHAPTER IV,** comparison between the EMF process and conventional deep drawing process is presented. EMF process is known to have several advantages over conventional processes for sheetmetal forming. This part investigates the issues of higher formability and the time required for the process to be completed. Furthermore, investigation of the phenomenon of elastic springback in the EMF process is also included. The comparison of the final shapes obtained from EMF die forming and conventional deep drawing simulation is carried out. Through this study, we were able to investigate the level of springback achieved using the two processes. Numerical predictions from the point of view of deformation, total calculation time, equivalent plastic strain, and final geometry after the deformation and after the tool removal are reported in the end of the section.

Finally general conclusions for this research work are reported which are followed by the perspective and certain suggestions for the continuity for future work. General trends have been noted and possible explanations are suggested in the conclusion. The perspectives provide new possibilities for the improvements of the model, different new fields to be investigated through our numerical model. These viewpoints would lead to develop a better connection for the validation of our model, and also provide a connection for application into industry. The author hopes that the results of this study would indicate the path to more detailed studies on one or more of the perspectives. The results of this research work may provide a platform for a better control and understanding the process.

Reference

[1] Al-Hassani S.T.S, Magnetic pressure distribution in the sheet metal forming, Electrical Methods of Machining, Forming and Coating, *Institute of Electrical Engineering Conference*, publication no 1975, pp. 1-10.

[2] Jablonski J. and Wrinkler R., Analysis of the electromagnetic forming process, *International Journal of Mechanical Sciences* 20 (1978); pp.315-325.

[3] William H. Gourdin, Analysis and assessment of electromagnetic ring expansion as a high strain-rate test, *Journal of Applied Physics;65 (1989)*, pp. 411–422.

[4] Takatsu N., Kato M., Sato K., Tobe T., High speed forming of metal sheets by electromagnetic forces, *International Journal of Japanese Society for Mechanical Engineering 1980*; 60; pp. 142-148.

[5] Zhang H., and Murata M., Suzuki H., Effects of various working conditions on tube bulging by Electromagnetic forming, *Journal of Materials Processing Technology (1995)*; 48, pp. 113–121.

[6] Song F.M., Zhang X., WANG Z.R., Yu L.Z., A study of tube electromagnetic forming, *Journal of Materials Processing Technology(2004)*, vol.151; pp. 372-375.

[7] Imbert Boyd J.M.S. Increased Formability and the Effects of the Tool/Sheet Interaction in Electromagnetic Forming of Aluminium Alloy Sheet Thesis. Master of Science. Waterloo : University of Waterloo. 2005.

[8] Mamalis A.G., Manolakos, D.E., Kladas, A.G., Koumoutsos, A.K., Electromagnetic forming and powder processing: Trends and developments, *Applied Mechanics Review 2004*, 57; pp. 299-324.

[9] Yu Hai-ping and Li Chun-feng, Effects of coil length on tube compression in electromagnetic forming, *Transactions of Nonferrous Metals Society of China 17,(2007)*, pp. 1270–1275.

[10] Oliviera D.A., Worswick M.J., Finn M., Newman D., Electromagnetic forming of aluminum alloy sheet: Free-form and cavity fill experiments and model, *Journal of Materials Processing Technology* (2005), vol.170; pp. 350-362.

[11] Mala Seth, Vincent J. Vohnout, Glenn S. Daehn, Formability of steel sheet in high velocity impact, *Journal of Materials Processing Technology* (2005), vol. 168, pp. 390-400.

[12] J.P.M. Correia, M.A. Siddiqui, S. Ahzi, S. Belouettar and R. Davies, A simple model to simulate electromagnetic sheet free bulging process, *International Journal of Mechanical Sciences 50 (2008)*, pp.1466–1475.

[13] Foster-Miller Inc., FEMM, Open source FEA software Ver. 3.3 by Meeker D. (2003), http:// femm.foster-miller.net (April 2009).

[14] ABAQUS/Explicit, Version 6.5 Manuals, Hibbitt, Karlsson and Sorensen Inc., Pawtucket, USA, 2005.

[15] Karch C. and Roll K., Transient simulation of electromagnetic forming of aluminium tubes, *Advanced Materials Research,* vol. 6-8 (May 2005), pp. 639-646.

Chapter I
Literature review

Chapter I: Literature review

I.1. Introduction

Electromagnetic forming process (called EMF in the following) is a typical high velocity, non-contact forming technique, in which large forces can be imparted to a conductive metallic workpiece by pure electromagnetic interactions. EMF is a relatively new technology for material forming. This forming process can be very advantageous as compared to conventional forming process. Improved formability, reduction in wrinkling, elimination and control of the springback and better distribution of strain are major advantages achieved using EMF [1, 2, 3]. In this chapter the principles of EMF are briefly reviewed. The electrical properties of the circuit are next reported. Afterwards the different types of EMF process are reported. And finally a literature review of experimental and numerical studies on EMF is presented.

I.2. Presentation of EMF

I.2.1. Principles of EMF

EMF process is one of the most attractive high velocity forming methods that achieved significant industrial applications in metal forming. This process is based on the repulsive forces generated by opposing magnetic fields in adjacent conductors. A fundamental requirement for this process is that the workpiece must be a very good conductor of electricity. Deformation is driven by the interaction of an induced current in the workpiece with the magnetic field generated by a coil adjacent to it. A charged capacitor bank is discharged, causing a time varying current to flow through a coil which is closed to the workpiece. Lorentz forces are generated by the discharge current, causing a transient magnetic field that induces the Eddy current in the workpiece. These currents flowing opposite to one another, develops the necessary body forces that govern the deformation of the workpiece. It is a dynamic, high velocity forming method in which large strain rates of the order of 10^3 to $10^4\ s^{-1}$ are achieved [4]. As opposed to many conventional forming processes, during the EMF, there is almost no mechanical contact between the workpiece and tools.

Therefore, this process is roughly without any frictional and contact effects of tooling. Since the duration of the impulse is very short, the inertia forces play an important role in the plastic deformation of the workpiece. The principle features of EMF assembly are shown in Fig. I-1.

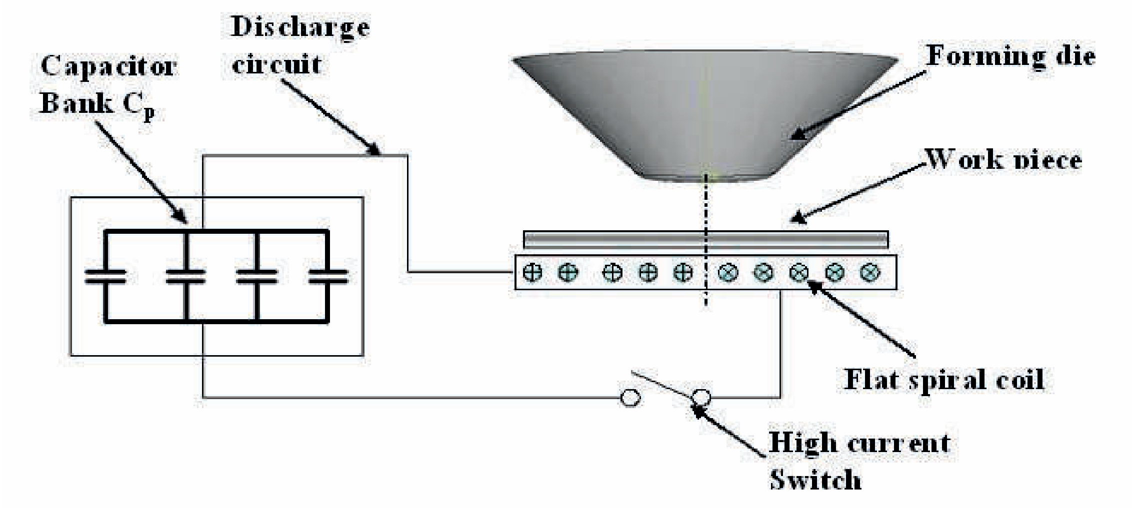

Figure I-1: Schematic view of an EMF process.

The main components of the assembly for an EMF process are:

- A generator consisting of several capacitors (Capacitor Bank) that stores electrical energy. The capacitor bank supplies electric energy to the coil.
- A coil whose geometry depends upon the forming operation.
- A workpiece (sheet or tube) made of non-magnetic conducting material as aluminium, brass, silver, etc. In the case of poor conductors it is necessary to add a conducting material (actuators) between workpiece and the coil for achieving the deformation.
- A die that forms the material in the desired shape.
- A vacuum producing system is usually necessary to accomplish an EMF process. The vacuum avoids entrapment of air between the workpiece and the die and then eliminates the surface defects.

The fundamental steps of the electromagnetic forming process are described below:

1. Energy is stored in the capacitor bank (total capacitance C_0) with an initial charging voltage V_0.
2. Discharge of energy as current I_1 *(t)* flows through a coil (flat spiral, helical, etc.) using high speed switches ignitrons.
3. A transient magnetic field $\mathbf{B_0}$ is produced in the coil due to the discharging current.

4. This magnetic field penetrates into the workpiece placed in the vicinity of the coil.
5. Eddy current $I_2(t)$ develops in the workpiece due the transient magnetic field $\mathbf{B_0}$ of the coil.
6. This Eddy current limits the penetration of the magnetic field $\mathbf{B_0}$ of the coil and creates its own induced magnetic field $\mathbf{B_1}$ in the opposite direction to that of $\mathbf{B_0}$ in the coil. Induced magnetic field $\mathbf{B_1}$ should not diffuse through the thickness of the workpiece. The depth through which the effects of the interaction of the two magnetic fields are limited within the workpiece is called the skin-depth δ.
7. Within the skin-depth, repulsive magnetic fields $\mathbf{B_0}$ and $\mathbf{B_1}$ in the workpiece result as the Lorentz body forces **F**.
8. These forces produce a magnetic pressure exerted on the workpiece.
9. If the magnetic pressure is higher than the yield strength of the workpiece, the dynamic deformation of the workpiece takes place.

To develop a better understanding of the process, a detailed description of the characteristics of components of the EMF system is presented below:

I.2.2. Components of an EMF process

a) Forming Coil

Coil design is selected to transfer a maximum of stored energy into the workpiece placed in its vicinity. Even the coil design may appear simple, there are several complicating factors. The key issues involve material selection and design. Typically, the forming coil is subjected to the same magnetic pressure as the workpiece. The coil must withstand high magnetic forces without mechanical failure. The coil must also resist the high operating voltage, magnetic flux and heating. Thereby, a material mix is usually applied using copper wire for the coil winding in order to guarantee a high electrical conductivity and epoxy (e.g. Kevlar fibres) for the armouring in order to provide a high mechanical strength [5]. Depending upon the forming operations, different configurations and geometries of working coil are adopted. For radial components, a solenoid spiral coil is used. This coil can be placed inside or outside the workpiece for compression or expansion respectively. For forming flat sheets, flat pancake spiral coils are mostly used. The various geometries of the working coil employed in the EMF process are presented in Fig. I-2.

Radial spiral coils [6]

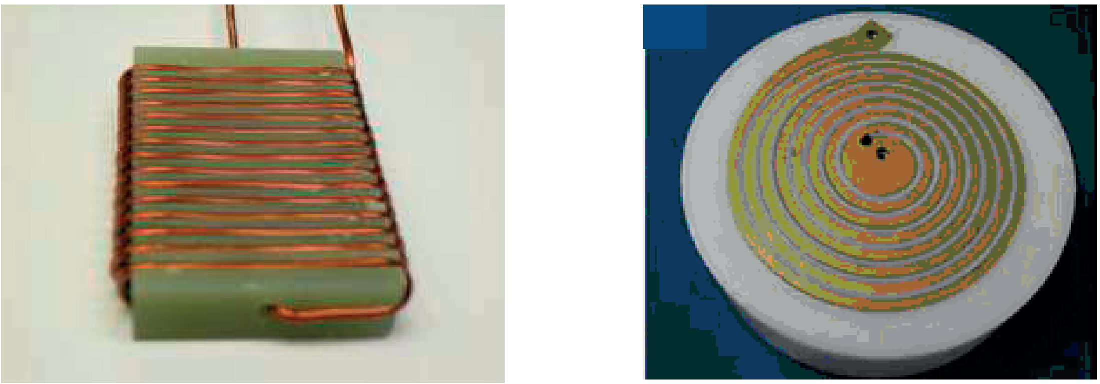

Uniform pressure flat coil [5]

Flat pan-cake coil [7]

Figure I-2: Examples of coils used in EMF process.

Failure of the coils may occur due to excessive heating and/or due to the magnetic pressure exerted on the workpiece (due to Lorentz forces). An example of coil failure occurred due to excessive heating and electrical arcing between coil and the workpiece is shown in Fig. I-3.

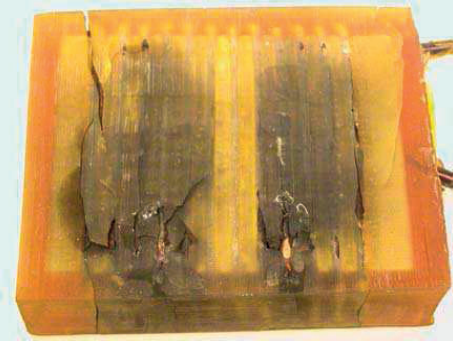

Figure I-3: Typical coil failure during EMF process [5].

The coil should have to be low-cost, with high durability and compatible to the forming process. In conventional EMF operations, it is important that the electromagnetic pressure distribution from the discharge coils is appropriate for the part that one would wish to form. In the designing of an efficient coil, a very common problem that designers encounter is the non-uniform distribution of pressure, specifically a significant drop in pressure in the area close to the centre of the coil for flat pancake coils. Uniform pressures is developed if the current in the coil and sheet are both uniform and the gap between them is constant. Many recent advances in work coil technology have been made. Mainly uniform pressure coils developed at the Ohio State University [5] can be used to overcome this dead spot condition for flat coils.

b) Pulse capacitors bank

In an EMF process, capacitor bank is used for storing and discharging the electrical energy. The pulse capacitor bank is the most important and expensive part of the EMF machine. Generally, the capacitor bank is subjected to high voltage and currents during the forming process. The function is to store electrical energy from the power supply, and then discharge it very quickly through the forming coil. The capacitors are normally connected in parallel to provide the increased total capacitance of the discharge circuit. Fig. I-4 shows a capacitor bank used in the experimental work of Balenatheram [8] on electromagnetic sheet forming.

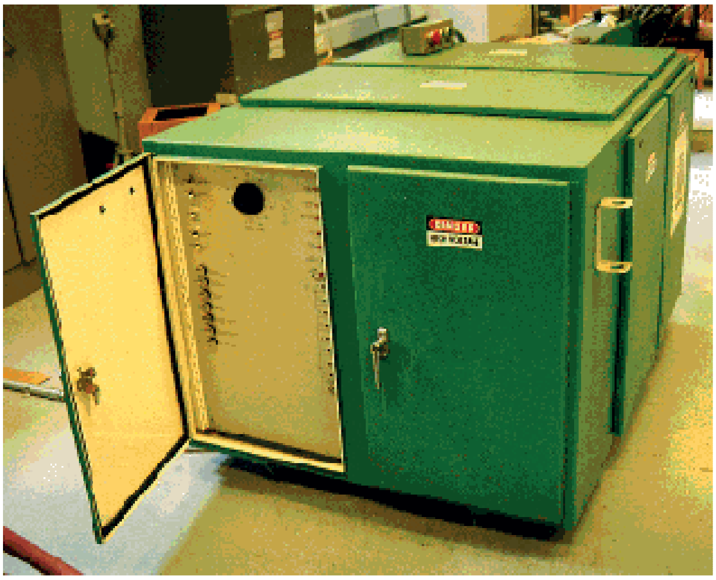

Figure I-4: Capacitor bank for energy storage [8].

The energy E stored in a capacitor bank for an EMF process is given by:

$$E = \frac{1}{2} C V^2 \tag{I-1}$$

where C is the total capacitance of the capacitor bank and V is the charging voltage. Fig. I-5 shows the evolution of capacitor bank voltage versus energy stored.

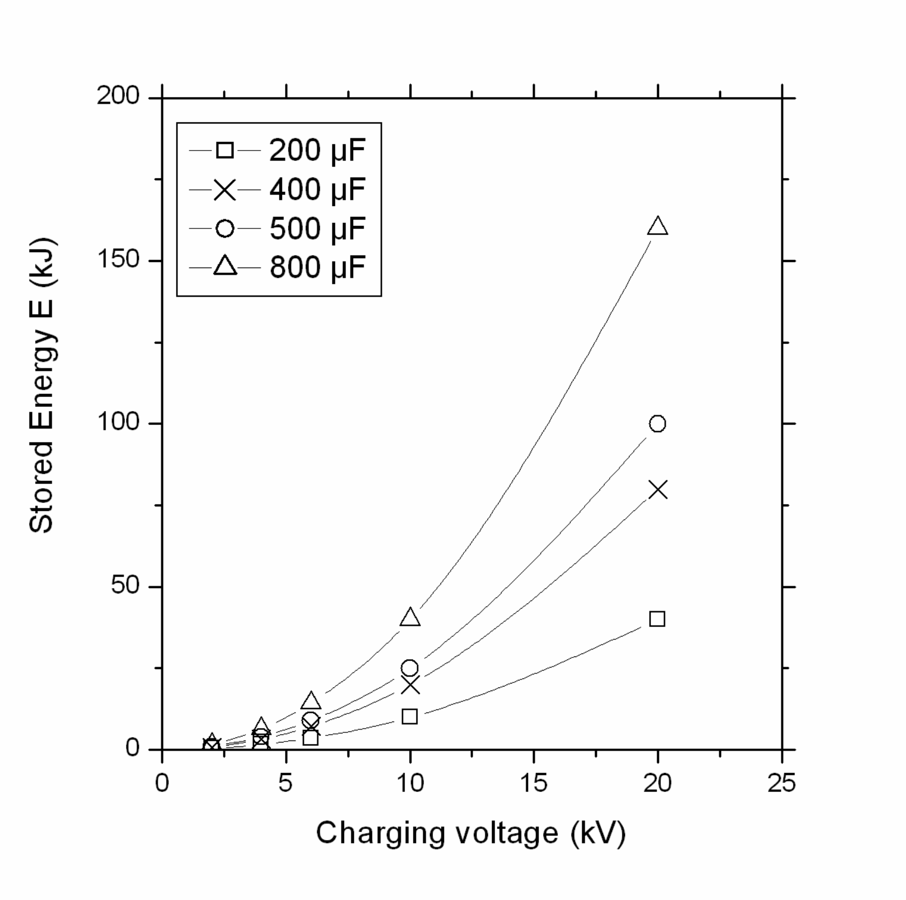

Figure I-5: Evolution of stored energy as function of charging voltage.

The discharge energy increases with the increase of the charging voltage, Fig. I-5. However, with higher voltage, the level of the personnel security raises and thus the process becomes rather dangerous for handling. Usually the stored energy used for the electromagnetic forming system lies between *1 kJ* to *20 kJ* for units used for small components [8]. Besides the components mentioned above, of the EMF systems, there are several other smaller elements such as: working die, vacuum producing devices, connecting wires, high speed switches, field shapers etc. A complete review of the electromagnetic system for flat sheet forming experiments is presented in [8].

I.2.3. Electrical properties of the EMF circuit

The EMF system can be represented as an equivalent *RLC* circuit [9]. Electrical properties of the assembled circuit can be estimated from the characteristics of an *RLC* circuit. The discharge of the current through the capacitor bank to the coil can be obtained using the classical oscillating equivalent *RLC* circuit equations as follows:

$$(L_1+L_C)\frac{d\,I_1(t)}{dt}+M\frac{dI_2(t)}{dt}+(R_1+R_C)I_1(t)+\frac{1}{C}\int I_1(t)dt = 0 \qquad \text{(I-2)}$$

$$\frac{d\left(L_2I_2\right)}{dt}+\frac{d\left(MI_1\right)}{dt}+R_2I_2= 0 \qquad \text{(I-3)}$$

where $I_1\ (t)$ and $I_2\ (t)$ are the coil current and the Eddy current in the workpiece respectively, L_1 and R_1 the coil inductance and resistance, L_2 and R_2 the workpiece inductance and resistance, L_c and R_c connecting wire inductance and resistance, M the total mutual inductance between the coil and the workpiece. Solving the set of equations (Eq. I-2, Eq. I-3), the discharging coil current $I_1\ (t)$ and the Eddy current $I_2\ (t)$ flowing through the workpiece can be obtained. The value of the capacitance of the capacitor bank is an initial data which is known. However the inductance and the resistance of the coil are unknown and must be determined.

Given the design geometry and material of the coil, the formulae for calculating the inductance can be found in basic electrical engineering handbooks [10]. The coil makes the major part of the total inductance of the discharge circuit in EMF process. The inductance of a spiral coil may be calculated by an approximate formula taken from the work of Groover *et al.* [11]. The inductance L of a flat spiral coil can be calculated by the following formula:

$$L = N^2 r \mu_0 \mu_r \left[\ln\left(\frac{8l}{a} \right) - 2 \right] \qquad \text{(I-4)}$$

where N is the number of turns, μ_0 the absolute permeability of the material (equal to 4π x 10^{-7} H/m), μ_r the relative permeability (equal to 1), r the average radius of the coil, l the active length of the coil and a the radius of the electric wire of the coil. For a simple N-turn solenoid coil, and in agreement with [7], the coil inductance can be estimated as:

$$L = \frac{\mu_0 N^2}{l}\left[\frac{A_0}{\left(1+\frac{A_i}{A_0}\right)}\right] \tag{I-5}$$

where A_0 an internal area and A_i a cross section area of wire, and l the active length of the coil. The section of the coil may be calculated using the following relation:

$$A_0 = \frac{\pi(d_{C_0}^2 - d_{C_i}^2)}{4} \tag{I-6}$$

where dc_o and dc_i are the internal and external diameters of the coil respectively. We can notice that the inductance of a coil strongly depends upon its length and the number of turns. As the number of turns in a coil increases, its inductance increases.

Resistance qualifies the tendency to of a material that opposes the current flow through it. The resistance of the any component of the discharging circuit may be calculated with the help of the following relation:

$$R = \rho\frac{l}{A} \tag{I-7}$$

where ρ the resistivity of the material, l is the length of the coil and A is the active surface area of the section. The general form of combining resistance (or inductance) of elements of a circuit can be found in elementary text books on electrical circuits [10], and is provided here for completeness (replace R with L for calculating the equivalent inductance of the circuit):

$$R_t = \sum_{1}^{n} R_i(\mathit{for\ circuit\ elements\ connected\ in\ series}) \tag{I-8}$$

$$\frac{1}{R_t} = \sum_{1}^{n} \frac{1}{R_i} (\textit{for circuit elements connected in parallel}) \tag{I-9}$$

Using the effective characteristics of the EMF system, the total circuit effective inductance is the sum of the effective coil inductance and the system inductance. Likewise the total circuit resistance is the sum of the coil and system resistance. However in the forming process, the coil inductance far exceeds the bank and workpiece inductance, due to the larger number of turns. Hence the system total inductance is given as a close approximation by the coil inductance. The discharge current depends upon different electrical characteristics of the system.

In agreement with [12], the intensity of the discharge current is calculated as follows:

$$I = I_0 \, e^{\frac{-t}{\tau}} \sin \omega t \tag{I-10}$$

where I_0 is the maximum current intensity, τ the damping factor and ω the current frequency. The maximum current is typically between about 10^4 to 10^6 amperes and the time to peak current is of the orders of tens of microseconds. This creates an extremely strong transient magnetic field in the vicinity of the coil. The peak current of a discharge coil at a particular energy level is related to its inductance. The maximum intensity of the current I_0, is defined as:

$$I_0 = V \sqrt{C_T / L} \tag{I-11}$$

where V is the voltage applied to the circuit, C_T the capacitance of the capacitor bank and L the inductance of the circuit (mainly the inductance of the coil). The damping coefficient τ that characterise the exponential decrease of the discharge current is given by the following equation:

$$\tau = 2 \frac{L}{R_T} \tag{I-12}$$

where R_T is the total resistance of the circuit. The frequency of the current ω given by:

$$\omega=\frac{1}{\sqrt{LC_T}} \tag{I-13}$$

The skin-depth δ of the current through the workpiece thickness can be estimated from:

$$\delta=\sqrt{\frac{2\rho}{\mu_0\omega}} \tag{I-14}$$

where ρ is the resistivity of the workpiece.

I.2.4. Different types of EMF process

Normally, EMF process can be divided into two major categories: forming of tubular components and flat sheetmetal forming. Recently new applications of the electromagnetic forming process have also emerged such as electromagnetic welding [13], piercing [14], joining [15], powder compaction [16] etc. The new applications also include hybrid systems [17] where the conventional forming tools are equipped with coils at specific locations to achieve complex geometries using electromagnetic forces. Consequently preformed components are reshaped into complex forms using hybrid systems. The different EMF processes are discussed below.

a) Tube forming (axisymmetric workpiece)

EMF of radial axisymmetric component has been extensively used in various industrial applications. The workpiece is a cylindrical tube. The magnetic pressure is produced by a solenoid or helical coil, Fig. I-6. The magnetic field thus produces is almost uniform. This uniform magnetic field, combined with an axisymmetric workpiece, renders the process extremely appropriate for application in industry. The tubular forms can be obtained by expansion or compression (Fig. I-6a and Fig. I-6b, respectively). Recently, another application of EMF of tubes has developed for dissimilar material welding [13] and joining [15].

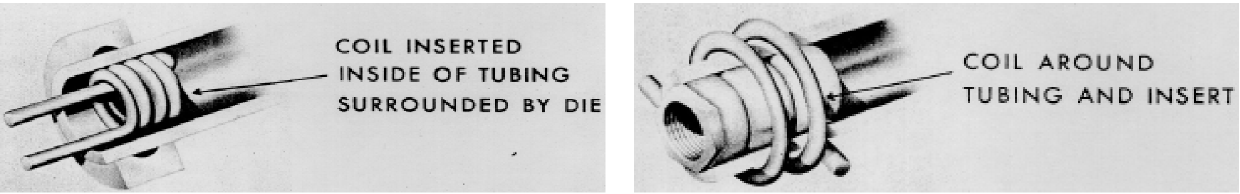

(a) *(b)*

Figure I-6: Examples of tube forming using EMF [18].

b) Sheetmetal forming

The workpiece is a flat sheet. In the simplest case, the pressure is produced by a coil rolled into a flat spiral pancake. This coil is placed under the metal sheet. The shape of the sheet is generally given by a die. But in the case of free-bulging process, a die is not necessary for forming the sheet. An example of electromagnetic sheetmetal forming process is depicted in Fig. I-7.

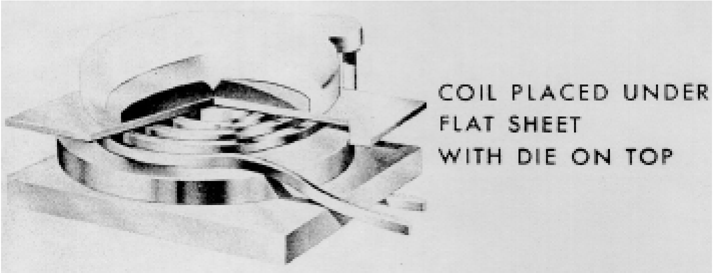

FigureI-7: Example of electromagnetic sheetmetal forming operation [18].

c) Hybrid Systems

In hybrid systems [17], the conventional forming operation is complemented with electromagnetic effects. In stamping, for example, one or more coils are installed inside the punch at localised regions like at the nose radius, Fig. I-8. While the punch pre-deforms the sheet, the magnetic field from the discharging coil permits to form the radius and sharp features into the die to obtain complex geometries. EMF can be used to form parts from flat sheet, or to sharpen features of pre-formed workpieces.

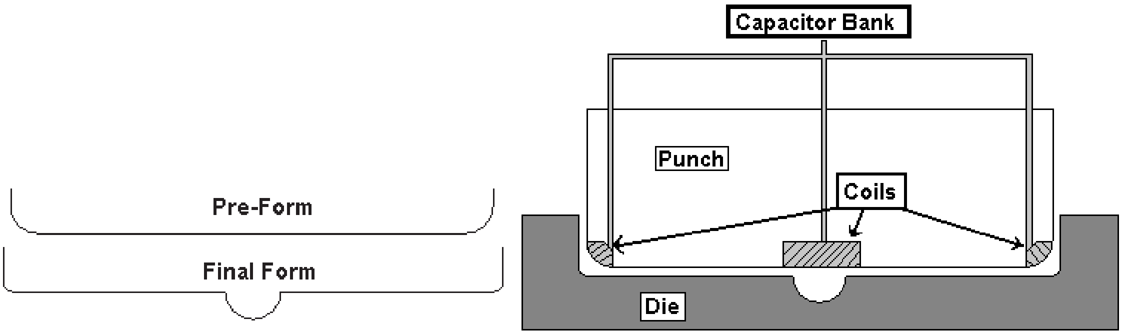

Figure I-8: Example of a hybrid electromagnetic forming system [17].

d) Typical industrial applications

EMF has vast application in the industry. Since the earlier developments of the process, EMF has been frequently used for diverse operations. Principal industries interested in advancement for its application are aerospace and automobile, where reduction of weight is the major concern. For example, in automotive industry, potentially major applications of this high velocity forming technology exist in the fabrication of aluminium alloy automotive body panels. Besides the industrial application of this novel forming process, significant interest is also developed in the scientific community for the research and development. Few of the recent industrial applications of EMF process are shown in Fig. I-9.

Automobile industry[17] *Thin walled structures (Fuel cell panel) [5]*

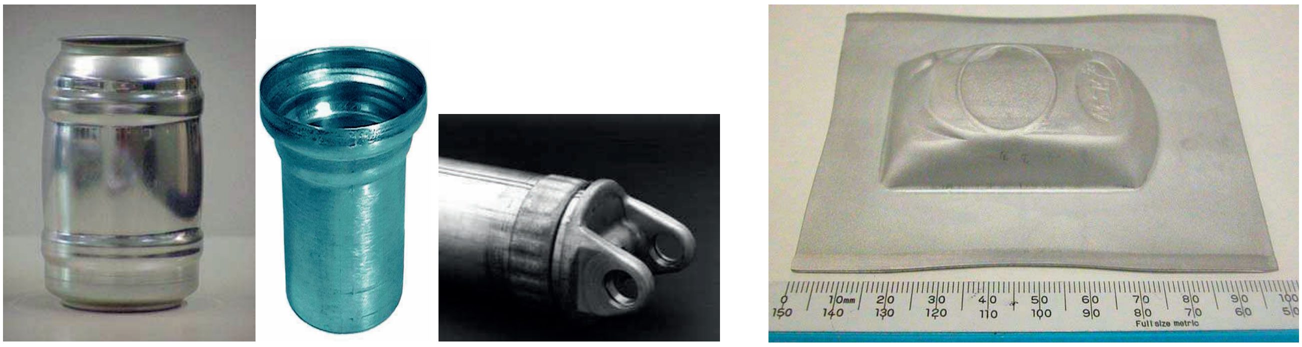

Packaging industry [19,20,14] *Cell phone casings [5]*

Figure I-9: Industrial examples of EMF

I.4.5. Advantages and limitations

a) Advantages

EMF has several advantages that make it an appropriate alternative of conventional forming processes. It is one of the most suitable techniques of plastic deformation amongst the high speed forming processes. The principal advantage of EMF is its controllability and repeatability, while the process equipment required is relatively simple. The principal advantages of EMF are listed below:

- High productivity (since average operation time is about *100-300* μs) [1].
- Low processing cost, focusing on low volume production through minimizing investment cost and more manufacturing flexibility.
- A significant increase in formability (working with a high deformation speeds permit the sheetmetal to be stretched without rupturing, a phenomenon termed as hyperplasticity [17]).
- Very close dimensional tolerances are achievable, because EMF process can renders minimum, or even eliminate any elastic springback.
- Wrinkling is suppressed. As the forming process takes place at high velocity, the change in direction of the compressive stress causing wrinkling is inhibited.
- A very flexible processing technology. Same circuit can be utilised for forming workpieces of different configurations.
- Since there is almost no mechanical contact (as compared to a punch in the conventional forming process), the surface finish can be achieved even before the operation of electromagnetic forming. Less surface damage owing to non contact forming process.
- Cost of die is reduced, as only one sided moulds are needed.
- The deformation of the workpiece takes place at room temperature and the expected temperature rise in a very short processing time within the system is comparatively small. Heat distortions of the workpiece, frequently experienced in

conventional forming processes associated with welding and piercing are eliminated. Consequently, handling of the final workpiece is simplified.

- EMF can be used to combine forming and joining operations for axisymmetic assemblies. Utilisation of inertia forces of the components of semi-finished products that are accelerated to a significant speed during the forming processes, which allows several forming operations to be carried out simultaneously.

a) Limitations and inconveniences

Besides having numerous advantages, there equally exist some limitations and inconveniences of the EMF process. The limitations of EMF are reported below:

- Materials with low resistivity can be easily formed, like copper, aluminium, low carbon steels etc. If materials of high resistivity are to be employed, the cost of the process may be comparatively higher.
- The deformation speed may be considered as a limitation of the process due to higher safety precautions and requirements.
- Because of the high intensity of current and voltage, the security level has to be kept high. Special safety precautions needed to be implemented before industrialisation of the EMF process.
- In practice, its applications are rather restricted to simpler shapes (tubes and flat sheets). For example, the process is convenient for metals sheet with small thicknesses [19].
- The technology at its actual state does not permit it to be applied to sheets of large dimensions, particularly because of the designing of the induction coils and requirement of more energy, which translate into larger capacitor banks and higher initial expenditure.
- Required equipment is still expensive and physically large, before implementation in automation.
- Only good electricity conducting materials can be deformed directly. For non conducting materials, an intermediate conducting piece must be required.

I.3. Literature review

The main purpose of this part is to review the studies in the literature concerning the EMF process. We investigated both experimental and numerical aspects during this literature review. The latest trends and developments of the forming techniques are presented in the work of Mamalis and Manolakos [21]. This study includes a very broad evaluation of the EMF process. Discussion on the process parameters and calculations of the magnetic pressure using numerical and experimental methods is presented. Basic characteristic parameters of the EMF process are provided; which can be used as benchmark data. Fundamental equations for calculating these parameters are also given. An equivalent circuit method is employed for this calculation. It is suggested in [21] that the workpiece motion plays an important role in the calculation of the magnetic pressure since the plastic deformation of the workpiece tends to change the mutual inductance between the induction and the coil. Temperature rises during the process is also investigated. Two heating sources are suggested to be responsible for the temperature rise during the process. At first, it is the plastic deformation of the workpiece that accounts for the temperature rise. The other factor is the electrical current passing through the workpiece, the phenomenon commonly termed as joule heating. This work is regarded as one of the most important compilation for the technical aspects related to the EMF process. The literature found on the EMF process provided a large number of experimental and numerical investigations carried out to evaluate its capacity as an alternative novel technology for forming metals. While the electromagnetic forming of tubular components by radial coils is relatively well investigated, the problem of the forming sheets metal by flat spiral coils is less analyzed.

I.3.1. Experimental studies

I.3.1.1 Tube forming

The experimental work carried out by Song *et al.* [22] focuses on the influence of varying the relative axial position of the coil and the workpiece on the distribution of the transient magnetic force. Experiments performed by Song *et al.* [22] are carried out with aluminium tubes and with a *14 kJ* EMF system. The deformed geometry of the tube is analyzed. It is observed that a variety of deformed shapes of the tube can be obtained by adjusting the relative position of the coil and the workpiece. This is attributed to the varying distribution of the electromagnetic force developed. Effects of coil parameter such as height to diameter ratio, the number of turns of the coil, and the cross section geometry are studied. The configuration used and the different deformed geometries obtained in [22] are shown in Fig. I-10. The experimental results provide [22], the insight on the influence of the parameters on the deformed shape of the tubes. It is found that the magnetic field intensity in the space between the workpiece and coil is proportional to magnetic inductance developed between the coil and the workpiece. The distribution of the transient magnetic force can be adjusted by changing the relative distance and the axial position of the workpiece. Various different shapes can be manufactured by altering the axial position of the workpiece due to the effects of the distribution of the magnetic force.

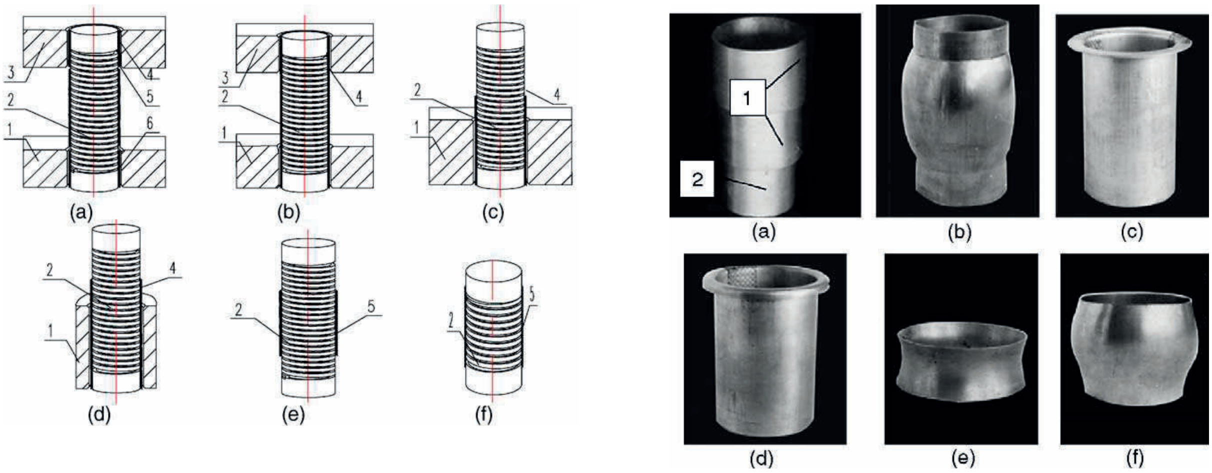

(a) Configurations used for the experiments

(b) Deformed workpieces for different coil configurations

Figure I-10: Experimental apparatus and deformed shapes presented in [22].

In a similar work carried out by Zhang *et al.* [23], the effect of working condition on tube expansion (also called tube bulging) is presented. Zhang *et al.* [23] performed an experimental and a numerical study. They particularly concentrated their work on the effects of the capacitor banks, coil length and charging energy for aluminium tubes. For the different working conditions, the profiles of the deformed tubes were recorded using a contour measuring instrument. The optimal working conditions are hence derived from experimental and numerical results. An example of experimental results obtained by [23] is presented in Fig. I-11.

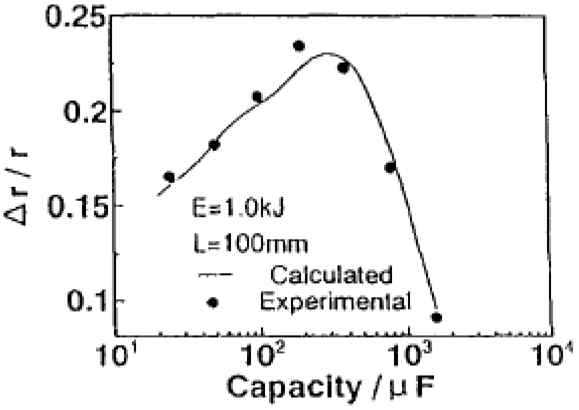

Figure I-11: Relationship between bulge height and capacity presented in [23].

Zhang *et al.* [23] demonstrates in Fig. [I-11] that when the capacity of the capacitor bank was too small or too large the deformation of the tube bulge decreased. Thus there exists a working window for capacitance, for which the deformation of the workpiece is deemed to be appropriate. In their work, Zhang *et al.* [23] concluded that the forming efficiency of the process, at a constant charged energy, becomes higher when the coil length decreases. For a constant coil length, the maximum of the forming efficiency occurs at a lower value of capacity. But also the forming efficiency depends on skin-depth. In the same manner, Yu and Li [24] studied the influence of coil length on tube compression. The effects of coil length on the waveform of the discharge current, on the peak value of magnetic pressure and on the deformation characteristics of the tube are investigated. Both numerical and experimental procedures are used to study the effects of the coil length on the forming process. Three coils of different geometry were used for experiments of compression of aluminium tubes (C1 of *100 mm*, C2 of *80 mm* and C3 of *50 mm* length respectively). As we know that the inductance of the coil depends upon its length, thus the circuit parameters strongly depend on the coil geometry. This, results in a change in the discharge current waveform as the length of the coil is altered (Eq. I-10). Fig. I-12 presents the final tube profiles obtained for different values of coil length.

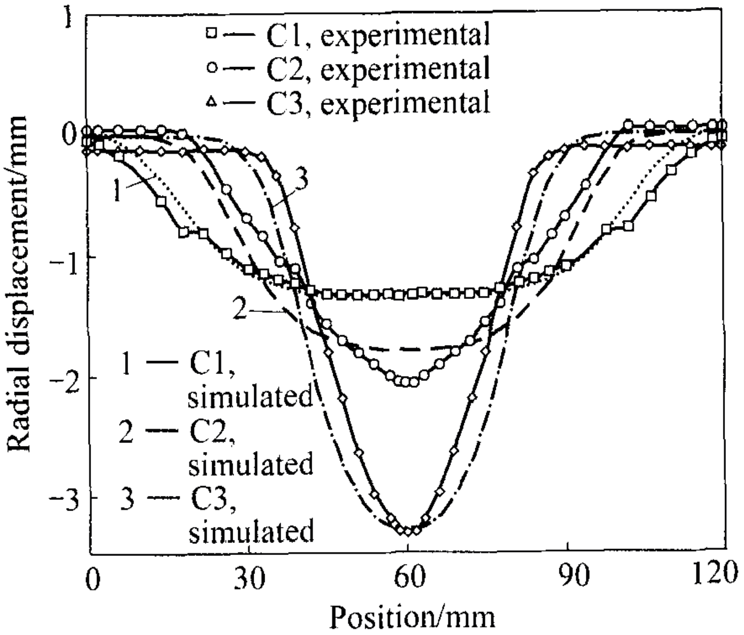

Figure I-12: Radial deformation of the tube for different coil lengths [24].

As shown in Fig. I-12, the tube radius increased rapidly as the coil length decreased. This effect is attributed to the increase in the electromagnetic force for a coil with shorter length. The peak value of the pressure is inversely proportional to the coil length due to the increase in the circuit inductance for longer coils. The conclusions of Yu and Li [24] for tube compression are in agreement with those of Zhang *et al.* [23] in tube expansion. Zhang *et al.* [23] and Yu and Li [24] have contributed to define the working window in EMF tube expansion and compression process. However defects like bursting or wrinkling occurring in conventional forming can arise in EMF tube process. These major defects, bursting and wrinkling, have also been investigated by means of electromagnetic tube forming tests. To prevent bursting or fracture, Forming Limit Diagram (called in the following FLD) can be used. These diagrams are valid for a material and show the critical combinations of major and minor strains that lead to failure by local necking and possibly local fracture. The formability of a material can be defined with a FLD.

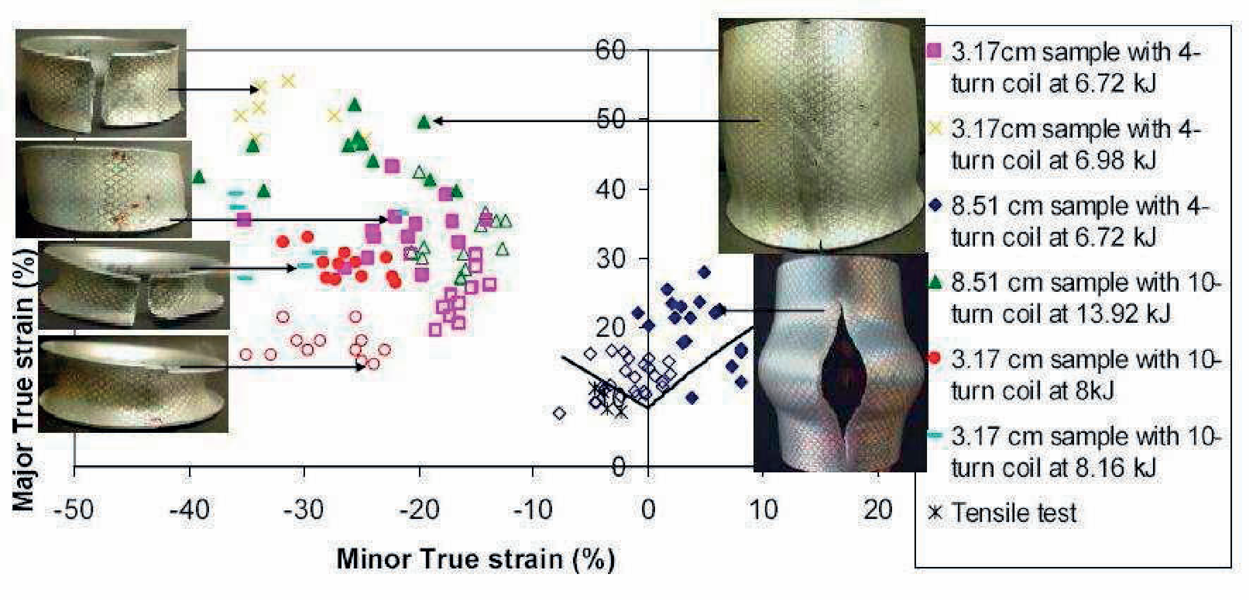

Figure I-13: True strain FLD at different coil - workpiece configurations [6].

The formability during high velocity forming of tubes has been studied by Seth [6] with EMF ring expansion tests. The material studied by Seth [6] is an AA6063 T6 aluminium alloy. In the study conducted by Seth [6], the primary and induced current plots, the high velocity strain distribution and the deformed geometry data were recorded during the experiments. Three configurations of discharge spiral coil (*2, 4* and *10* turns) made of copper were applied to study the effects of coil geometry on the final shape on the workpiece. Two Rogowski coils were applied to measure the primary and induced current through the coil and workpiece respectively. To measure the strain at various locations on the tube after deformation, the surface of the workpiece was electronically etched with non-touching circles. The samples were formed at incremental launch velocities. This was obtained by varying the energy discharged from the capacitor bank. Electromagnetic ring free-expansion experiments with rings of different aspect ratios were carried out. Thus a complete data set was created for plotting a FLD under high velocity conditions. The true strain FLD obtained by Seth [6] is plotted in Fig. I-13. Pictures of samples from which the strain data has been taken, are also shown in Fig. I-13. For each test case, a different symbol has been used. For each case, a solid symbol represents an unsafe strain while the corresponding open symbol represents safe strain in the sample. In Fig. I-13, true strains in the range of 10-55% have been achieved from AA6063 T6 which has a quasi-static ductility of 8-11%. This increase in formability through high velocity free expansion has been demonstrated by Seth [6].

The experimental study of wrinkling was carried out by Padmanabhan [18]. The ring compression electromagnetic test is used for the purpose of identifying the wrinkling. The experiments were performed using a single turn spiral coil made of copper. The effects of energy, ring thickness, ring height, and material were investigated. Many of the trends observed in the ring compression experiments were analogous to the ones obtained in the sheetmetal study. Two materials have been considered by Padmanabhan [18] an aluminium alloy and a copper alloy. Both materials exhibited a decrease in wrinkling as the energy is increased. For a particular value of energy to mass, wrinkling decreases as ring thickness increases. It was found that the wrinkling decreases as ring height increases. However, it was noted that, for a particular sample velocity, wrinkling would be independent of ring height. The samples obtained by Padmanabhan [18] after the ring compression experiments are presented in Fig. I-14. As one can notice, at lower energy levels, wrinkles are observed in both copper and aluminium samples. However these are eliminated by increasing the discharge energy for both the materials. It is concluded that, for a particular material, thickness and height, there exists an optimal energy level for which the wrinkling effects are minimal for tube compression EMF process.

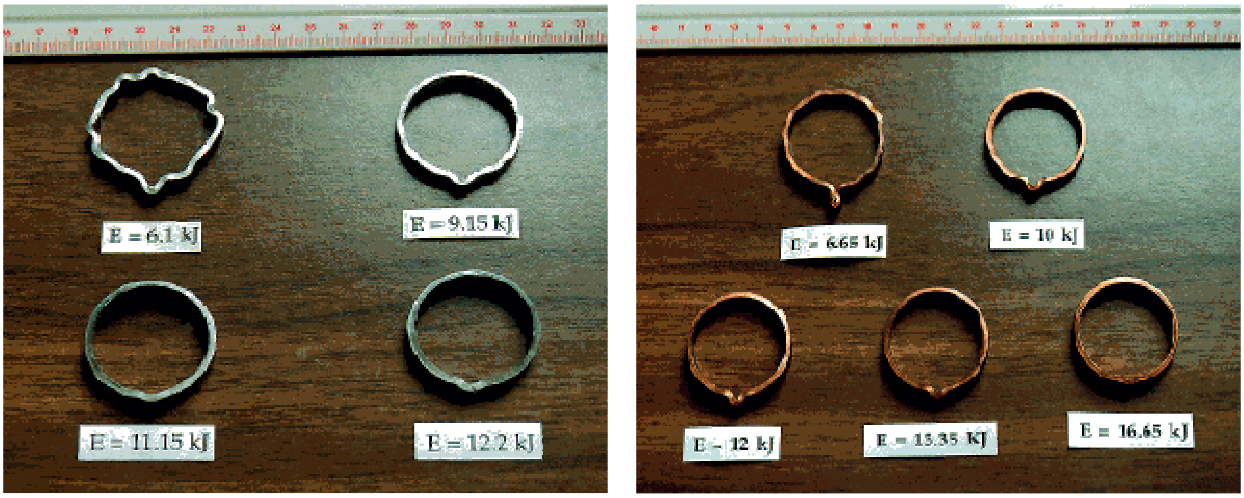

(a) Aluminium samples *(b) Copper samples*

Figure I-14: Photograph of Aluminium and copper ring samples formed at different energy levels [18].

I.3.1.2 Flat sheetmetal forming

The pioneer work on the electromagnetic forming process was presented in Al-Hassani [25]. Four types of spirally wound pancake coil were employed to form aluminium sheet of thickness *0.92 mm*. A die with dimpling holes was used for experimental purpose. The distribution of the magnetic pressure was obtained by measuring the height of each of the resulting dimples on the workpiece. The deformed shape of the workpiece is shown in Fig. I-15. Results obtained from the work of Al-Hassani [25] offer considerable scope in predicting the magnetic pressure distribution on a wide range of discharge coil configurations.

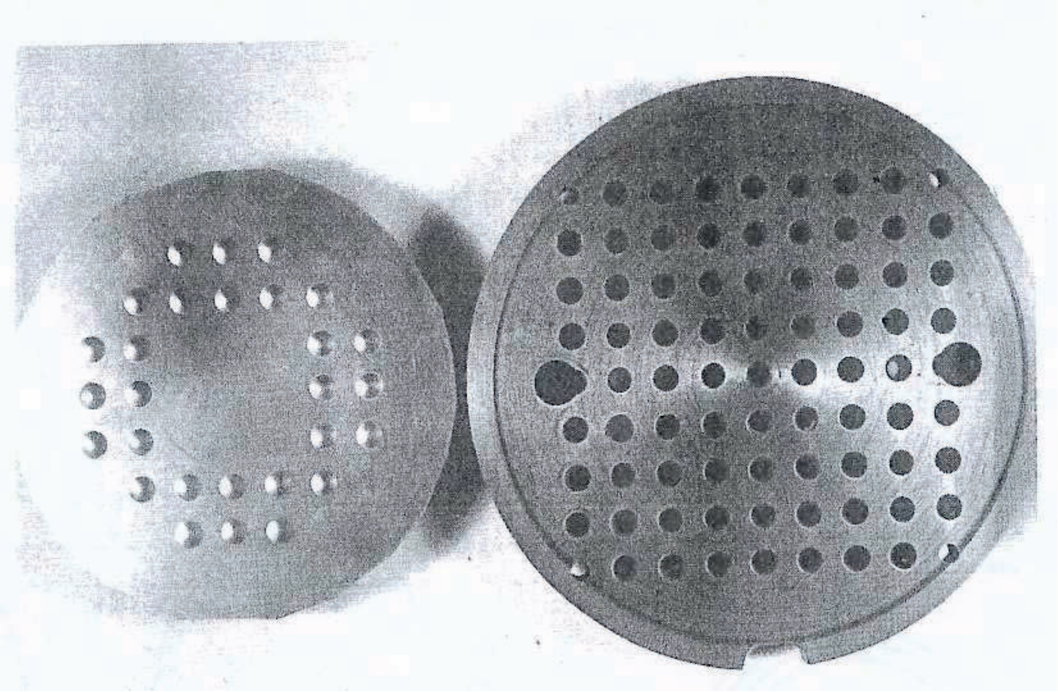

Figure I-15: Deformed workpiece with dimples and forming die [25].

Takatsu *et al.* [26] next investigated the electromagnetic free bulging of flat aluminium disks. The coil used by Takatsu *et al.* [26] is a pancake single layered *5* turn spiral coil made of copper. The affective diameter of the coil is *80 mm*. The workpiece used for the experiments is composed of annealed aluminium alloy *JIS A1050* of *110 mm* diameter with *0.5 mm* thickness. A capacitor bank of *40 μF* charged with *6.0 kV* power supply is used for the experiments. High-speed photographic imaging was used for the measurement of the deformation of the workpiece. The deformation is observed to start at approximately *19 μs* after the first discharge, which corresponded to the first positive peak of the discharge current. The deformation began at the distance of about *20 mm* from the centre of the disk at the annular part. The total forming process took place in about *250 μs* to accomplish the complete deformation. The dynamic profiles of the workpiece deformation evolution at different time steps as obtained through experiments are presented in Fig. I-16.

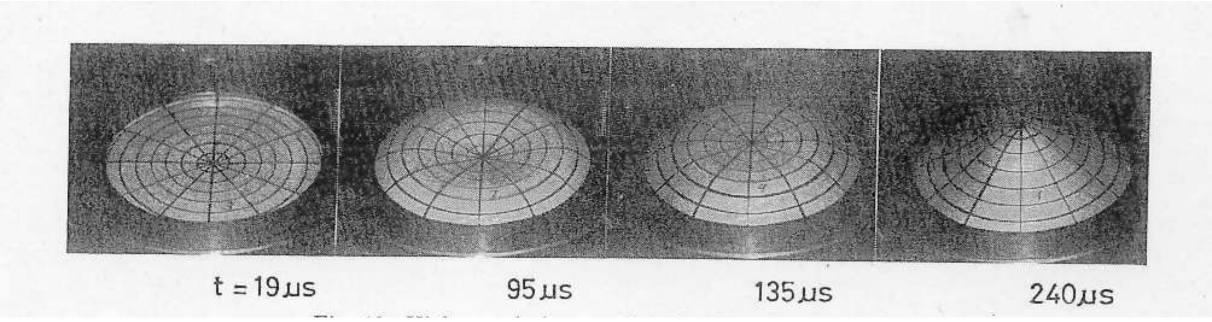

Figure I-16: Evolution of deformation as function of time [26].

It is noted in Fig I-16, that the deformation of the centre of the workpiece starts slightly later than of the periphery. The observed profile indicated the non-uniformity of the pressure distribution obtained using the pancake flat spiral coil. The deformation of the workpiece starts at the point where the magnetic pressure has a maximum value. This point lies a few millimetres (approximately *22mm*) away from the centre of the workpiece. Imbert [27] as well studied EMF of aluminium sheets. Imbert [27] concentrated his effort in the understanding of the benefit of tool/sheet interaction in the increase of formability. Two approaches were adopted for this investigation. At first, the sheet is free formed, while in the second tests a conical die was applied. A flat spiral coil is used for the forming process. Two commercial alloys were used for the experiments, *AA5754* and *AA6611*, in the form of *1 mm* thick sheets. Strain measurement was carried out using circular grid on the workpiece, while the metallographic and fractographic analyses were performed to show the evidence of increased formability. An example of the deformed workpieces achieved by Imbert [27] is presented in Fig. I-17.

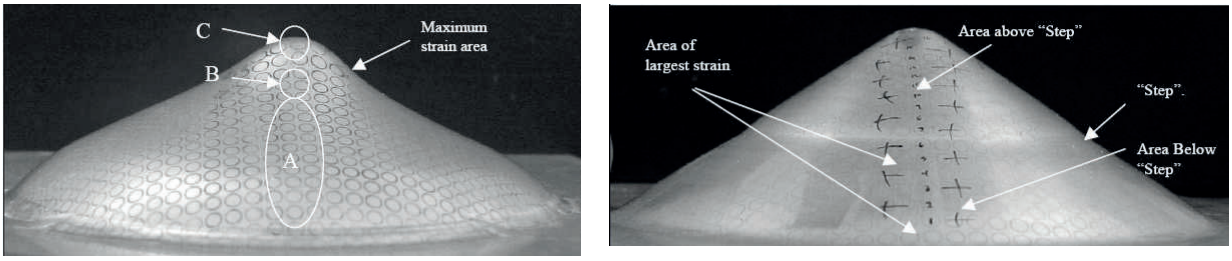

Figure I-17: Comparison of free formed and electromagnetic forming using a conical die [27].

The experiments carried out by Imbert [27] demonstrated a significant increase in formability when the conical die is used. The increase of formability is significant in areas where the contact with the die occurred. On the other hand, very little increase was recorded in the free-formed samples. Thus, it is suggested that the tool/sheet interaction played a vital role in the increase in the forming limit of the workpiece during the EMF process. In addition, during the experiments, Imbert [27] observed that, at certain charging voltages, the workpieces failed at central region. When no die is used, an increase in the discharge energy resulted in the development of a neck and a fracture at the top of the workpiece as shown in Fig. I-18.

Figure I-18: Failure of workpiece at high energy levels [27].

Padmanabhan [18] has carried out an experimental study on the EMF of sheetmetal and tubes. Padmanabhan [18] focuses his work on two phenomena which must be controlled or suppressed: wrinkling and springback. An attempt has been made to determine the effect of several materials and process parameters on wrinkling and springback. A schematic view of the apparatus used by Padmanabhan [18] is depicted in Fig. I-19. For the EMF of sheet metals, the flat sheet is intially placed on a flat spiral coil. The whole assembly is placed in a box in which vacuum is maintained, while the coil is connected to the generator composing of eight capacitors each of *120 µF*. The generator has maximum charging capacity of *50 kJ*. The experiments are carried out with four capacitors which are charged with an alternative current of *460 V*. Two different dies were used for the EMF test. The geometry of the two dies is presented in Fig. I-20. For each die geometry, the die is placed at *3.175 mm* above the sheet. All the sheets used by Padmanabhan [18] have an external diameter of *9.525 cm*. However different materials with different thicknesses have been used: a commercial aluminium alloy *1100-O* with a thickness of *1.6 mm* and of *1.0 mm*, a commercial aluminium alloy *6061-T6* with a thickness of *1.28 mm* and a copper alloy (Oxygen Free High Conductivity copper also called OHFC) with a thickness equal to *0.8 mm*.

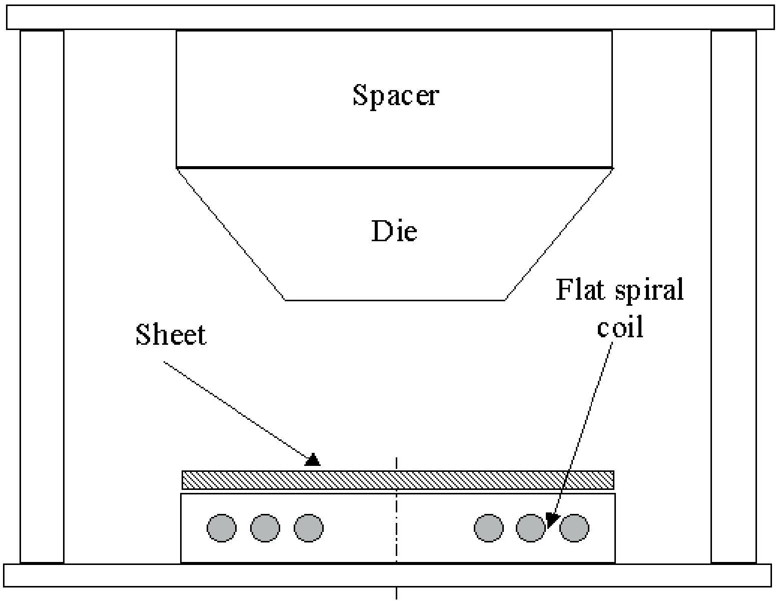

Figure I-19: A schematic view of the electromagnetic forming test proposed in [18].

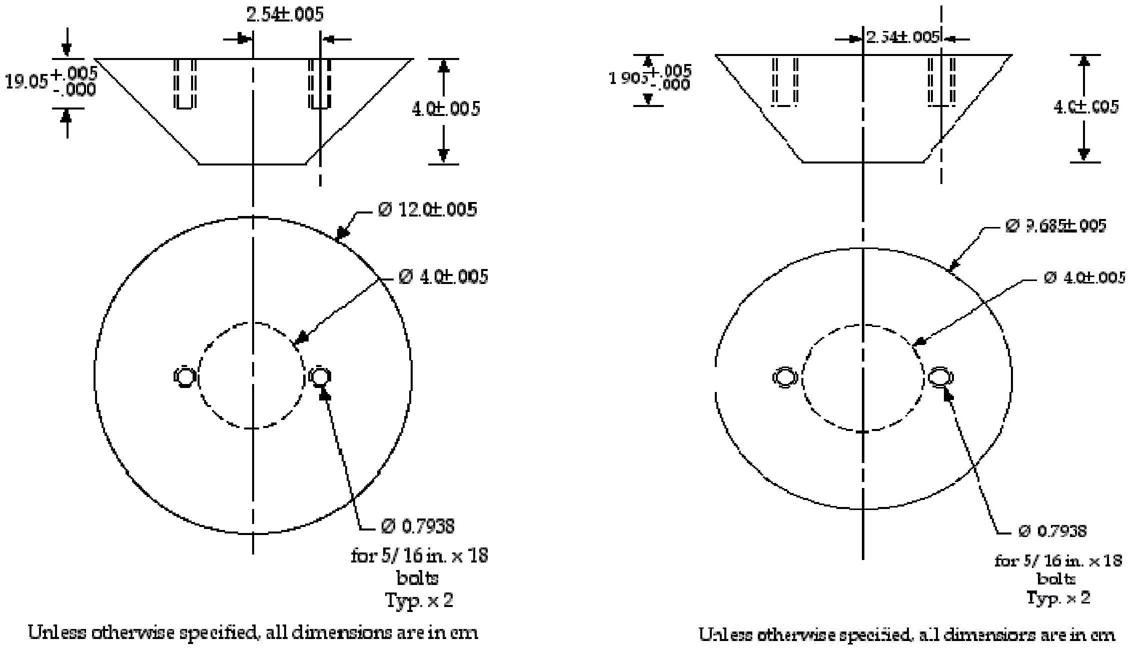

(a) die with 45 degree internal angle *(b) die with 30 degree internal angle*

Figure I-20: Dies used during the experiments by [18].

Padmanabhan [18] analyzed the effects of the energy of forming, thickness of the sheetmetal, material heat treatment, die geometry and stand-off distance (gap between coil and workpiece). Experimental trends have been obtained and possible explanations for the different phenomena are suggested. Images of the deformed workpieces at different energy levels are presented in Fig. I-21.

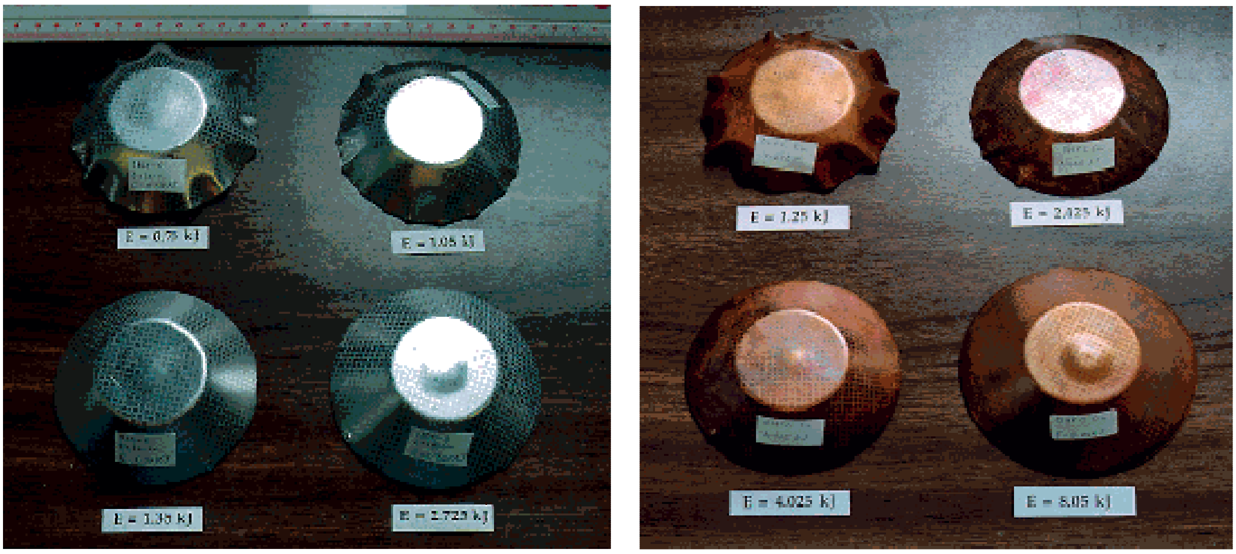

Aluminium samples *Copper OFHC samples*

Figure I-21: Photograph of 0.8 mm thick Aluminium and copper samples formed at different energy levels [18].

Padmanabhan [18] found that the number of wrinkles decreases as the intensity of magnetic field increases. But for very high intensities of magnetic field, Padmanabhan [18] observed the appearance of a dome over the plain part of the deformed sheet for both materials as shown in Fig. I-21. Wrinkling is found to decrease monotonically with energy for all the materials. Wrinkling is eliminated at a particular value of energy to mass. This seems to indicate that wrinkling increases as the distance between the blank and the die increases. Padmanabhan [18] has concluded that the number of wrinkles monotonically decreases as the discharge energy increases. For a fixed value of discharge energy, the number of wrinkles decreases as the sheet thickness increases. For a given displacement speed of the sheet, the number of wrinkles are more important for a die inclined at *30*° than for a die inclined at *45*°. At very low energies, the sheetmetal wrinkles and does not conform to the shape of the die. At very high energies, waviness is observed at the periphery of the sheet but the springback increases. Over a range of intermediate energies, the springback is consistently low and lies in the range of -*0.2mm* to *0.3 mm*. With a similar experimental setup, Seth *et al.* [28] have studied the high velocity formability of cold rolled sheet steel formed with a curved punch. Seth *et al.* [28] have plotted FLD in the case of steel sheets formed by EMF. Different steel sheet samples were electromagnetically launched, with a wide range of velocities (*50 – 220 m/s*), onto a fixed massive punch. A flat spiral coil and an aluminium driver sheet have been used. The details of the experimental setup are shown in Fig. I-22.

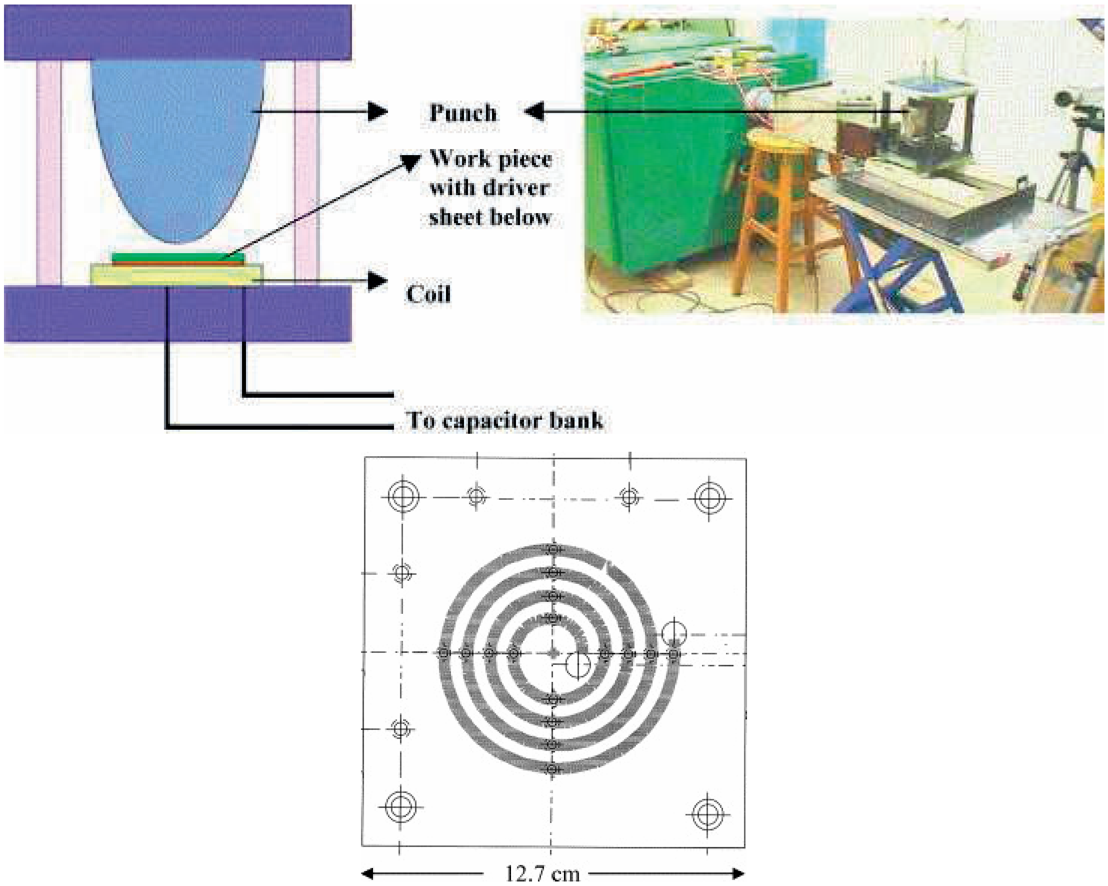

Figure I-22: Schematic view of the experimental setup and of the flat spiral wound coil [28].

A commercial Maxwell-Magneform capacitor bank composed of eight capacitors, *120 μF* each, connected in parallel. The total energy of the bank was *48 kJ* at the *10 kV* maximum charge voltage. In the experiments of Seth *et al.* [28] only four out of the eight capacitors were connected. Hence the maximum available discharge energy of the bank was *24 kJ*. The charging voltage was varied to control the discharge energy. A four-turn flat spiral coil has been used. This coil was made from square cross-section copper wire (*5.3 mm*), embedded in epoxy with a kevlar face sheet. The coil had an outer diameter of *12.7 cm* and was *2.4 cm* in height. The outer diameter of the spiral portion (*8.3 cm*) was approximately the same as the specimen (*8 cm*) to provide a uniform launch. The specimen, when placed on the top of the potted coil, was approximately *6 mm* above the top of the copper windings. Two different geometries of punch (made with casehardened steel) were used in [28].The geometries were all based on a simple parabolic equation ($y = a x^2$). All of the sheets studied by Seth *et al.* [28] are made in low cost, low carbon, low alloy steels that derive their strength from cold rolling rather than alloying. The workpieces have an initial diameter of *80 mm*. The blank surfaces were electrolytically etched with circles of *2.54 mm* diameter. Examples of deformed sheets obtained by Seth et al. [28] are presented in Fig. I-23.

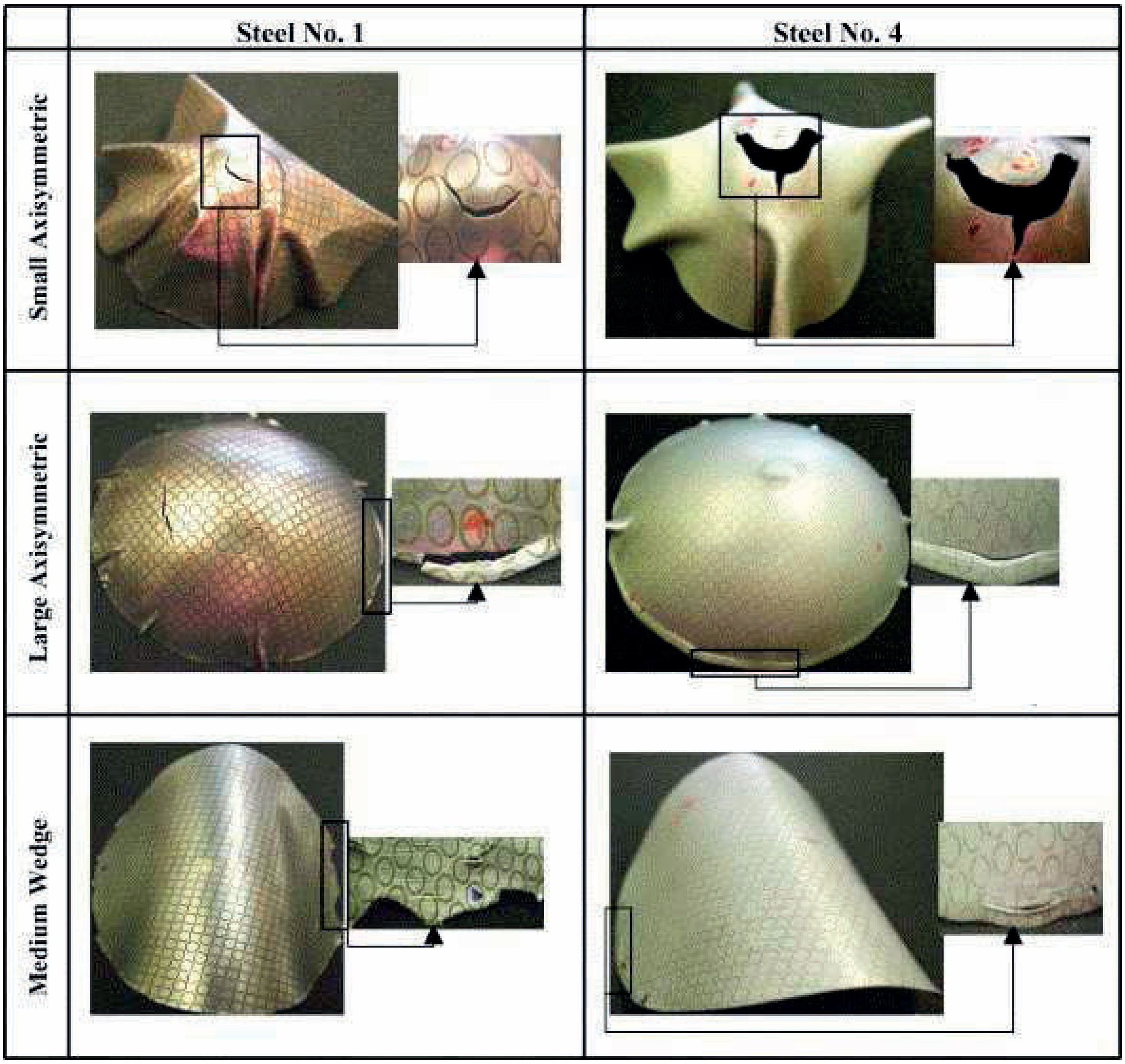

Figure I-23: Examples of failure modes observed in [28].

After high velocity deformation, the electro-chemically etched circles on the surface of the sheet steels distorted into ellipses. Measurement of the major and minor axes of the ellipse and the changes from the original diameter of the circle indicates the major and minor strains on the specimen. The local maximum strains were measured from areas of high strains, generally near the failure zone. Strain pairs from various parts of a sample of a given material were plotted on the traditional FLD. The different punch geometries were essentially used to obtain different strain states on the FLD. Seth *et al.* [28] have then plotted FLD for the five steels in high velocity conditions and compared them with the failure strains in quasi-static loading, Fig. I-24. The failure strains plotted in Fig. I-24 clearly shows that the useful formability of the low-ductility steels can be dramatically improved by EMF.

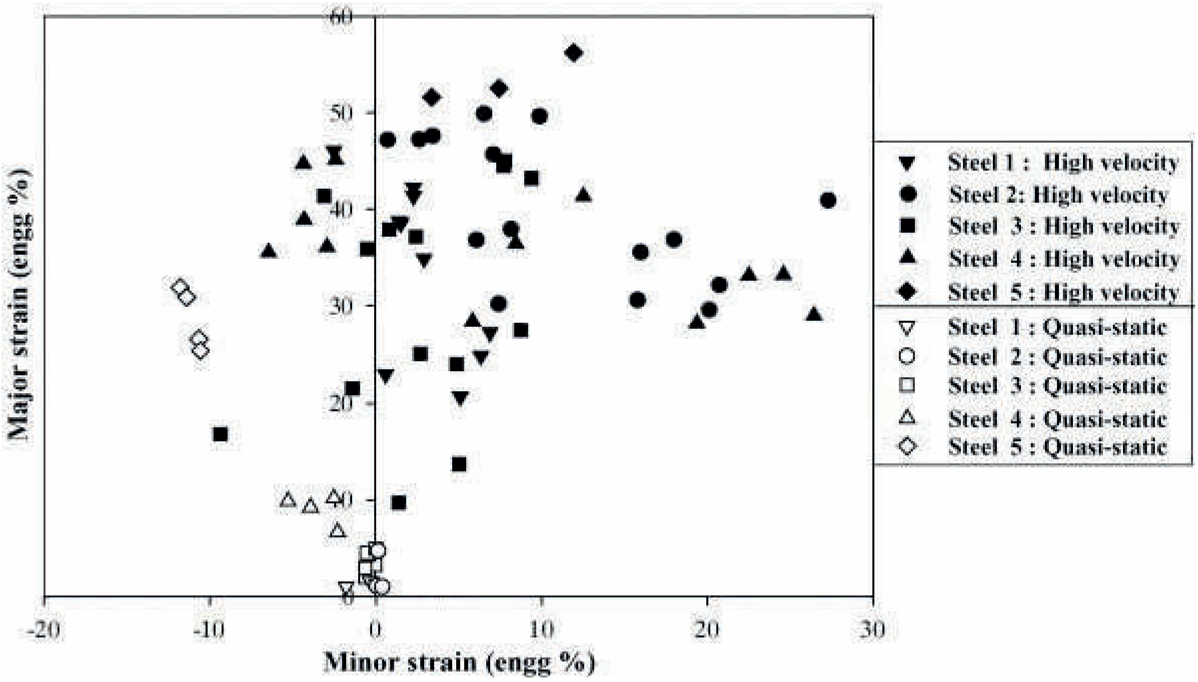

Figure I-24: Failure strains observed in [28].

More recently, a series of high-speed EMF experiments have been presented by Oliveira *et al.* [29]. Comparison between free forming and cavity fill die configuration is carried out for two different aluminium alloys *AA5754* and *AA5182* sheets. The effect of die geometry on formability, strain state and location of failure are examined through experiments. A flat double spiral coil was adopted that relocates the "dead spot" (region of low magnetic pressure) which usually occurs at the centre of the single pancake spiral coil windings. The coil is wound from copper wire with square cross-section of *5mm*. The geometry of the coil used is presented in Fig. I-25. The experiments were performed using a power supply provided by IAP research, the discharge energy raged from *4.8* to *16.9 kJ*, with the discharge frequency of *5-6 kHz*. Experimental test samples have an initial thickness equal to *1* and *1.6 mm*, and a diameter equal to *254 mm*. Repetitive tests were carried out at increasing energy levels until the energy level associated with the failure was established. The deformed profiles obtained for the free forming experiments are presented in Fig. I-26.

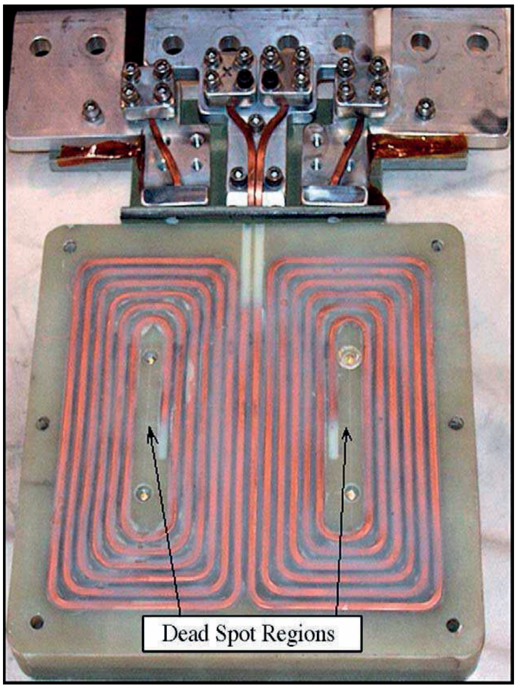

Figure I-25: Double spiral coil embedded in G10-garolite insulator [29].

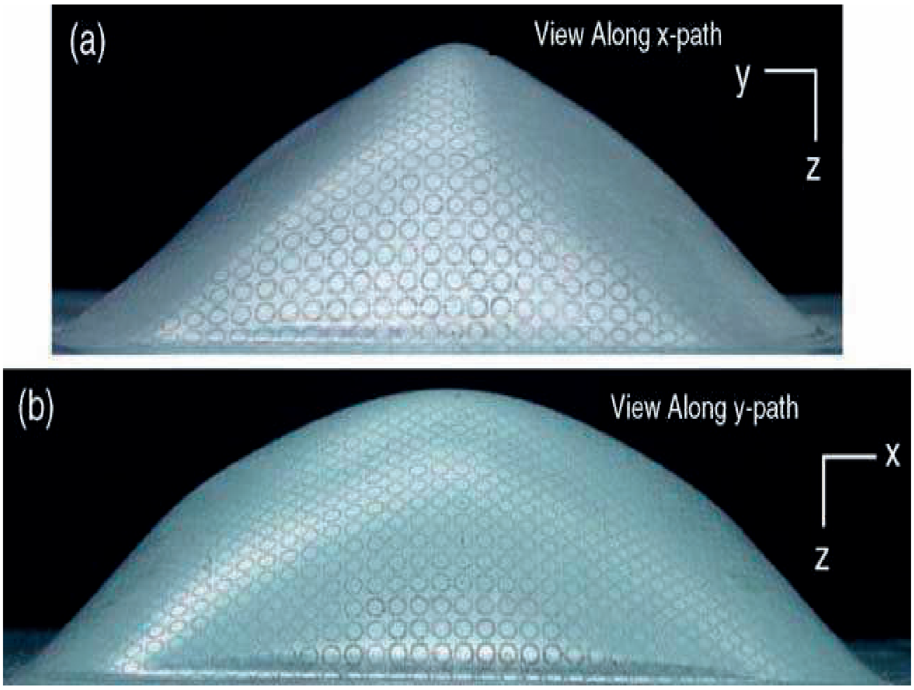

Figure I-26: Final profile of the actual workpiece:
(a) view along x-path, and (b) view along y-path [29].

Experimental investigation [29] illustrated the role of discharge voltage, sheet thickness and effects of die geometry on the EMF process of aluminium alloys. The limit strains from the experiments of free forming at three voltages (*5.5 kV, 6.0 kV* and *7.7 kV)* along with quasi-static forming limit diagram are reported in Fig. I-27. No improvements in formability are observed in Fig. I-27 for *5.5 kV* and *6.0 kV* energy levels. Only in the sample that had failed at *7 kV*, formability is noticed to be improved to levels higher than conventional FLD limits, Fig. I-26. On the contrary of Seth *et al.* [28], Oliveira *et al.* [29] observed that the formability of the workpiece remained below the conventional forming limits, and no “hyperplasticity” (behaviour defined by Daehn and co-workers [30] which corresponds to a large increase of material formability) was noted in the experiments. Despite the absence of hyperplasticity, the advantage of EMF was marked as a punchless non-contact process.

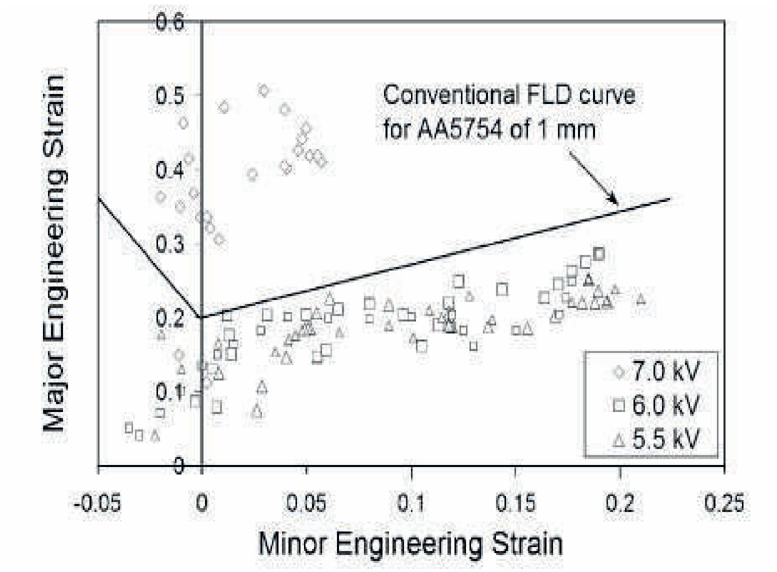

Figure I-27: Forming limit diagram using strain data at three charging voltages [29].

I.3.2. Numerical modelling and simulations

The EMF is a challenging task to numerically simulate, due to the requirement of simultaneous modelling of interacting electromagnetic, mechanical and thermal phenomena. A few decades ago, although the physics of these complex thermomechanical and electromagnetic phenomena were in principle well understood, scientists and researchers were unable to accurately simulate these complex highly dynamic processes. Along with the progress in the domain of computation, more and more studies have been carried out for simulating the EMF process. The EMF process is often considered as a combination of two main physical phenomena, namely electromagnetic problem and the mechanical deformation problem. As presented earlier, due to strong dependence of circuit parameters on the deformation of the workpiece, these two problems are generally inter-related. A detailed review of electromagnetic theory and the modelling of coupled electromagnetic and mechanical problems is presented in El-Azab *et al.* [31]. To simulate the EMF, three approaches are developed: *No coupling between electromagnetic and mechanical problems, Loose coupling between electromagnetic and mechanical problems* and *Strong coupling between electromagnetic and mechanical problems*. These approaches are further discussed in detail in this section.

I.3.2.1 Non-coupled approach

The simplest method is the uncoupled approach. Based on the properties of equipments and of system components, the circuit parameters are calculated. The Maxwell's equations are written without considering the deformation and the velocity of the workpiece during the process. The solution of the Maxwell's equations is performed using an analytical or a numerical approach. The Lorentz forces acting on the workpiece are next estimated. These forces are then transferred as input data to the mechanical problem, in order to simulate the deformation of the workpiece.

Very early work carried out by Al-Hassani [25] provides the state of the art in the mid to late 1960 and early 1970 on electromagnetic numerical analysis. Al-Hassani [25] determined analytically the magnetic pressure distributions caused by different coils on flat conductive plates. Several simple geometries were analyzed which led to the expression for the magnetic field intensity and the pressure distribution caused by a spiral coil. For a flat spiral coil, the magnetic pressure from the work of Al-Hassani [25] is given by:

$$P_r = \frac{\mu_0 I^2 N^2}{2\pi^2}\left\{\tan^{-1}\left[\frac{-2gr}{g^2 + a_2^{\,2} - r^2}\right] + \tan^{-1}\left[\frac{-2gr}{g^2 + a_1^{\,2} - r^2}\right]\right\}^2 \tag{I-15}$$

where I is the discharge current, N number of turns in the coil, g the distance from the coil to the workpiece, a_1 the distance from the centre of the coil to the first wind of the coil, a_2 the distance from the centre of the coil to the last wind of the coil and r the radius. Al-Hassani [25] compared the theoretical predictions (Eq. I-15) with experimental results. An example of comparison between the analytical predictions and experimental results for a spiral coil is shown in Fig. I-28. The distribution of the magnetic pressure obtained numerically was found to be in good agreement with the experimental measurements.

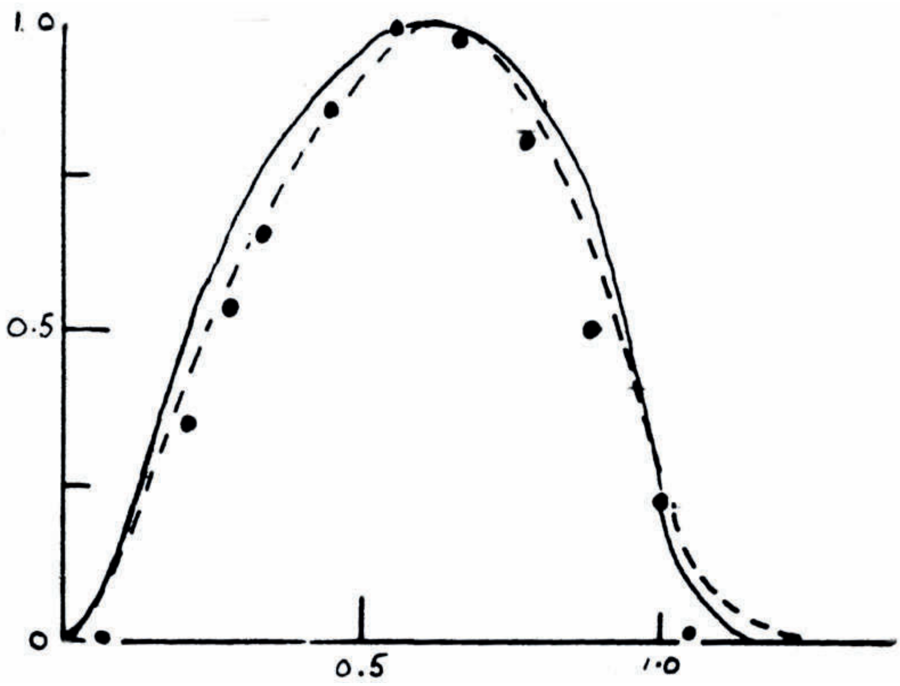

Figure I-28: Analytical and numerical distribution of magnetic pressure [25].

Analytical studies of EMF process have been conducted by Jablonski and Wrinkler [32] and by Gourdin [33]. These analytical studies are focused on simple axisymmetric geometries: tube compression (Jablonski and Wrinkler [32]) and ring expansion (Gourdin [33]). In the work of Jablonski and Wrinkler [32], the EMF equipment is modelled as an equivalent electrical circuit (*RLC* circuit) as presented in Fig. I-29. In order to obtain the current in the capacitor bank (primary circuit) and the current induced in the workpiece (secondary circuit), a set of two first order partial differential equations with respect to time must be solved. Knowing the current, the pressure acting on the tube is then derived from the energy balance. Jablonski and Wrinkler [32] solved the problem first with an approximate method (analytical method) and next with a numerical method (a fourth order Runge-Kutta method). However Jablonski and Wrinkler [32] have not taken into account the deformed shape of the tube in their calculations. Conditions for the optimal design of an EMF machine are obtained from the approximate solution. These conditions describe the optimum frequency for which the maximum deformation of the workpiece is achieved. Results from the numerical solutions are compared with the experimental ones, and were found to be consistent.

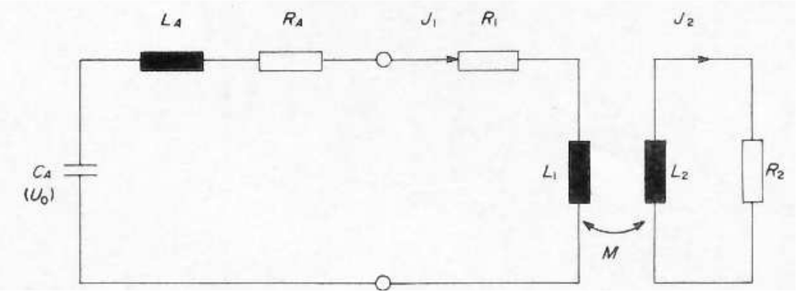

Figure I-29: Equivalent electrical circuit proposed in [32].

In a samilar manner, Gourdin [33] has led an analysis of the electromagnetic expansion of rings. Gourdin [33] formulated a non-coupled electromagnetic thermo-mechanical problem. A set of partial differential equations has been written and solved with a numerical method (a fourth order Runge-Kutta method). Gourdin [33] determined the currents flowing into the coil and induced in the workpiece, the temperature rise in the coil and in the workpiece, the expansion velocity and the plastic strain in the workpiece. But, as Jablonski and Wrinkler [32], the effects of the deformed shape of the ring have not been considered in the electromagnetic problem.

Nowadays, with the increase of calculus capacity of the computers, FE analyses become a major tool to predict the mechanical behaviour of the structures. In the framework of the non-coupled approach, Imbert *et al.* [34] and Imbert [27] performed a numerical analysis of EMF sheet tests. The aim of the work of Imbert *et al.* [34] and of Imbert [27] is to determine if EMF increases the formability of aluminium alloy sheets and, if so, to determine the mechanisms that play a role in the increased formability. The work presented by Imbert *et al.* [34] derived from the work carried out in the Master's research of Imbert [27]. The numerical analysis was carried out using the commercial explicit dynamic finite element code LS-DYNA [35]. The meshing of the tooling and of the workpiece used by Imbert [34] are depicted in Fig. I-30.

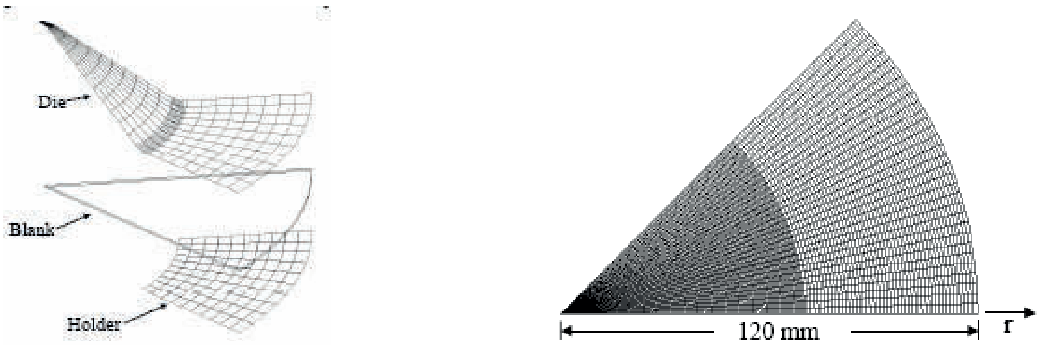

Figure I-30: Meshes of tooling and of flat metal sheet proposed in [34].

Imbert [27] have chosen to model one-eighth of the geometry in order to facilitate future coupling with an electromagnetic code. The flat sheet was meshed with constant stress eight-node brick solid elements. Seven through thickness elements were used to capture the shear stresses and to increase accuracy in future coupled simulations. Imbert [27] have also employed models with five elements through thickness and approximately half the number of elements but the FE results were unacceptable. The tooling is meshed with four nodes quadrilateral rigid elements. In order to reduce computational time, the analytical pressure distribution defined by Al-Hassani [25] has been applied to the workpiece in the FE analyses. Imbert [27] have proposed the radial and the temporal distribution of the pressure presented in Fig. I-31.

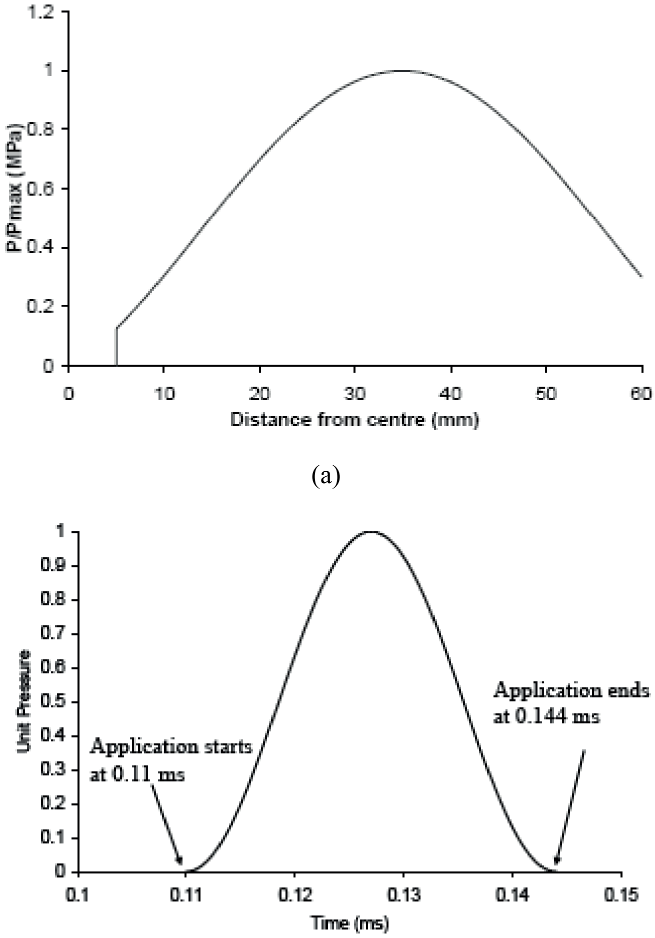

(a)

(b)

Figure I-31: Pressure generated by the coil and proposed in [34]: (a) radial distribution and (b) temporal distribution.

Two aluminium alloy sheets have been studied. The material damage behaviour is defined with the so-called Gurson-Tvergaard-Needleman constitutive model, which consists of the Gurson yield function [36] with the modifications proposed by Tvergaard [37] and Tvergaard and Needleman [38]. This type of model was chosen for its ability to predict damage evolution and ductile failure. The plastic behaviour of the material is described with isotropic rate-independent hardening law since the aluminium alloys studied present small rate sensitivity. In order to detect and understand the increased formability, simulations were performed for free-formed and for in-die forming operations.

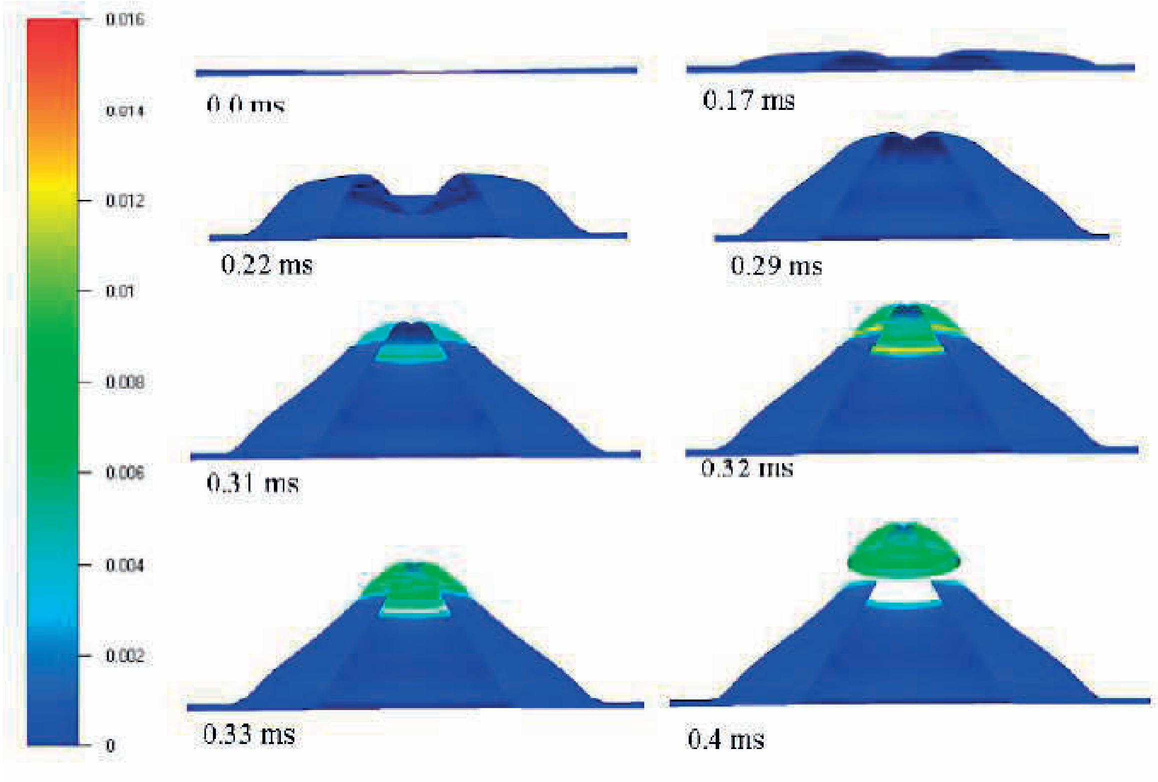

Figure I-32: Example of a free formed sheet in [27]: Contours are of void volume fraction.

An example of FE predictions for free forming achieved by Imbert [27] is presented in Fig. I-32. As described by Imbert *et al.* [34], the workpiece in EMF does not deform in a manner similar to a traditional manufacturing process such as punch forming. During the first ten milliseconds, the centre of the workpiece remains immobile; which is caused by the dead spot in the pressure distribution associated with a spiral coil. If the pressure is sufficient the centre part of the sheet bends upwards producing the final shape. However if the pressure achieved a critical value necking and failure eventually occur, Fig. I-32. An example of FE predictions for in-die conical forming achieved by Imbert [27] is presented in Fig. I-33.

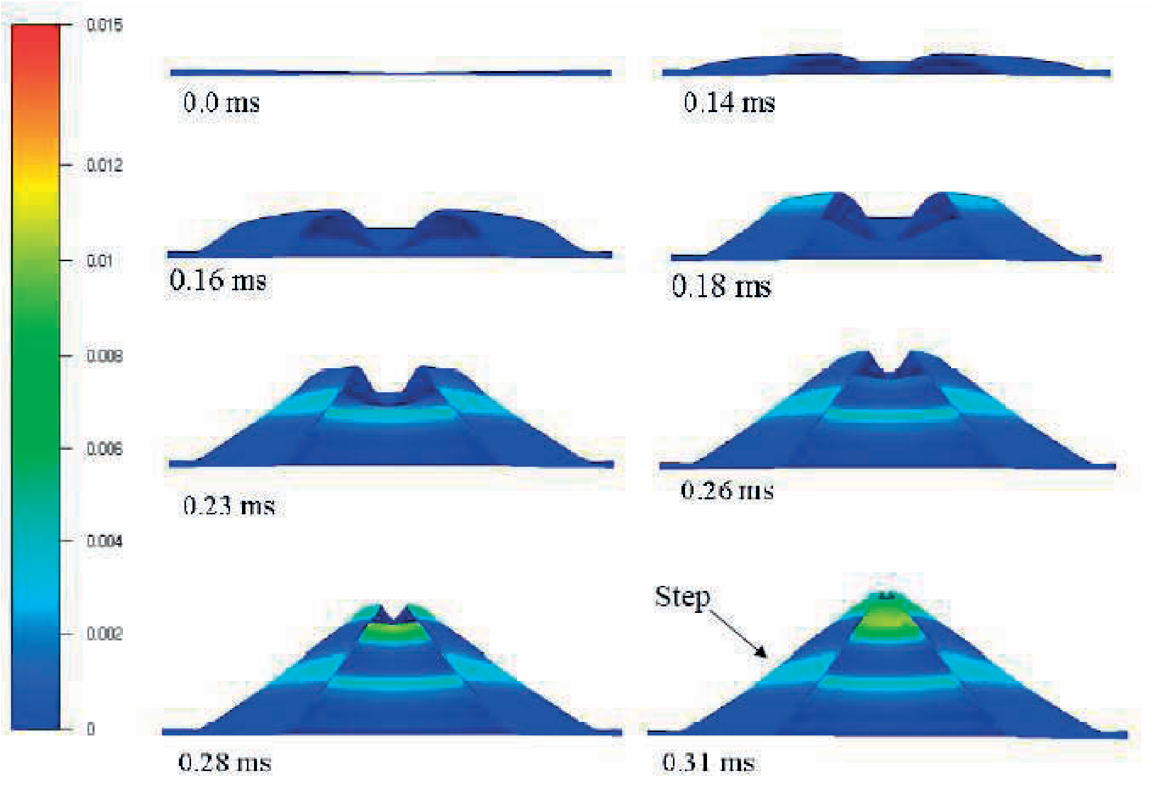

Figure I-33: Example of an in-die conical formed sheet in [34]: Contours are of void volume fraction.

As in the case of free forming, the sheet centre remains stationary during the first ten milliseconds of the EMF process with a conical die. On the contrary of free forming, failure is not predicted in case of in-die forming, Fig. I-33. To explain this increase of the formability, Imbert *et al.* [34] analyzed the damage evolution in both cases. For the free-form process, the predicted hydrostatic stress and then void volume fraction increase steadily with deformation. For the in-die conical process, the predicted hydrostatic stress and void volume fraction present a complex history (with positive and negative values for the predicted hydrostatic stress) with significant differences between the top and bottom elements in the workpiece. But the predicted void volume fraction never exceeds the critical value to initiate void coalescence. Thus failure was not predicted in the in-die conical EMF simulations. Even with this simple model, the FE simulations performed by Imbert *et al.* [34] are in agreement with their experimental results. Imbert *et al.* [34] concluded that damage suppression due to tool-sheet interaction is likely the main factor contributing to the increased formability reported in EMF.

I.3.2.2 Loosely-coupled approach

In the loosely-coupled method, at each step of time increment, the induced Lorentz forces are calculated by means of the electromagnetic model. The forces are then transferred automatically as an input load into the mechanical model. In the mechanical analysis, the deformation undergone by the workpiece is calculated and the geometry of the workpiece is updated. The new updated geometry from the mechanical model is used to calculate the electromagnetic forces for the next time increments. This process is repeated iteratively until the end of the process time. This strategy comes into use because it gives accurate results with a weak computational time. However, in the loosely coupled approach, thermal-conduction effects are neglected, since the process was assumed to be adiabatic. The coupling between the electromagnetic and the mechanical problem is presented in Fig. I-34.

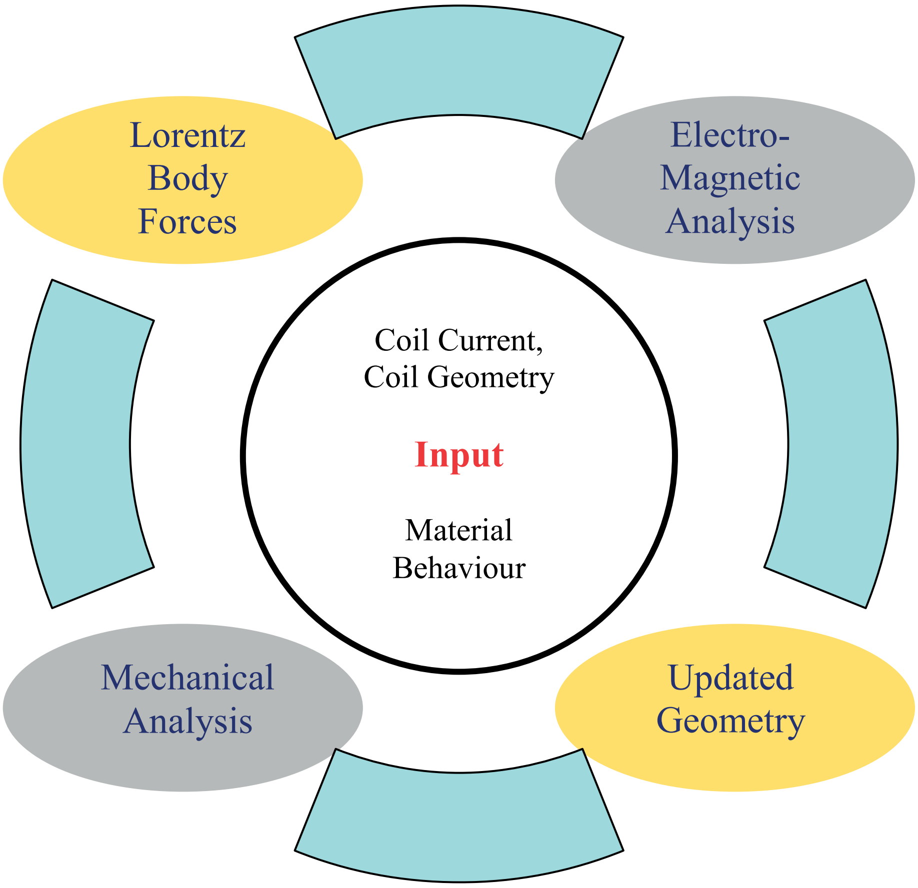

Figure I-34: Coupling in the loosely coupled approach.

Early work of Takatsu *et al.* [26] described the basic equations to simulate the electromagnetic free bulging of a flat sheet. Circuit analysis, electromagnetic field and dynamic plastic deformation equations of the workpiece were presented in [26]. An axisymmetric configuration for the numerical solution has been used for both workpiece and coil. Takatsu *et al.* [26] used an equivalent electrical circuit to compute the current flowing through the coil. The equation of the electrical problem is defined by:

$$(L_1 + L_C)\frac{dI_{1(t)}}{dt} + \frac{d}{dt}(MI_2(t)) + (R_1 + R_C)I_1(t) + \frac{1}{C_0}\int I_1(t)dt = 0 \qquad \text{(I-16)}$$

where I_1 *(t)* and I_2 *(t)* are the coil current and the Eddy current in the workpiece respectively, L_1 and R_1 the coil inductance and resistance, L_2 and R_2 the workpiece inductance and resistance, L_c and R_c connecting wire inductance and resistance, M the total mutual inductance between the coil and the workpiece. The quasi-stationary Maxwell's equations are written in cylindrical coordinate system as follows:

$$\begin{cases} -\dfrac{1}{\mu_0\sigma_w}\left(\dfrac{\partial^2}{\partial r^2} + \dfrac{1}{r}\dfrac{\partial}{\partial r} + \dfrac{\partial^2}{\partial z^2} - \dfrac{1}{r^2}\right)B_r + \dfrac{\partial B_r}{\partial t} = -\dfrac{\partial}{\partial z}(v_z B_r - v_r B_z) \\ -\dfrac{1}{\mu_0\sigma_w}\left(\dfrac{\partial^2}{\partial r^2} + \dfrac{1}{r}\dfrac{\partial}{\partial r} + \dfrac{\partial^2}{\partial z^2}\right)B_z + \dfrac{\partial B_z}{\partial t} = \dfrac{1}{r}\dfrac{\partial}{\partial r}(r(v_z B_r - v_r B_z)) \end{cases} \qquad \text{(I-17)}$$

where μ_0 is the permeability of free space, σ_w the metal sheet conductivity, B_r and B_z the radial and the axial component of the magnetic flux, v_r and v_z the radial and the axial component of the workpiece velocity. Furthermore, in their numerical approach, Takatsu *et al.* [26] considered the interaction between the magnetic field and the evolution of the workpiece shape. The equations of motion of the metal sheet are:

$$\begin{cases} \rho_0 h_0 r_0 \dfrac{\partial^2 u}{\partial t^2} = h\dfrac{\partial s}{\partial r_0}p_r + \dfrac{\partial}{\partial r_0}\left(\sigma_s hr\dfrac{\partial r}{\partial s}\right) - \sigma_\theta h\dfrac{\partial s}{\partial r_0} \\ \rho_0 h_0 r_0 \dfrac{\partial^2 w}{\partial t^2} = h\dfrac{\partial s}{\partial r_0}p_z + \dfrac{\partial}{\partial r_0}\left(\sigma_s hr\dfrac{\partial w}{\partial s}\right) \end{cases} \qquad \text{(I-18)}$$

where s is meridian distance measured from the centre of the disk, u and w are the displacements in the r and w directions, h the thickness, σ true stress and ρ_0 the density. The subscripts *s* and θ denote the meridian and the circumferential directions and a subscript *0* denotes the initial state. The pressures p_r and p_z are defined by integrating the Lorentz force through the workpiece thickness. The method used is more accurate than others that have been referenced early in this document. This method tracks the interactions between the magnetic force and the deformation of the workpiece more accurately. A change in geometry of the workpiece will change the inductance of the entire system. The numerical analysis developed by Takatsu *et al.* [26] is applied to the high-speed free forming of a circular disk in an EMF system with a flat pancake coil. Experimental and numerical studies have been carried out using a five turn flat spiral coil. In this work, the spiral coil is assumed to be as coaxial individual circular loops. Each loop is considered to be carrying the discharge current from the capacitor bank. The penetration of the magnetic field into the disk is calculated. A primary test is performed by Takatsu *et al.* [26] for the validation of the numerical method, in which at first the workpiece is not considered. The distribution of the magnetic field components are computed without the workpiece. Afterwards, the workpiece is considered to be fixed and placed on top of the coil. The numerical predictions and experimental results of Takatsu *et al.* [26] obtained for the preliminary validation are presented in Fig. I-35.

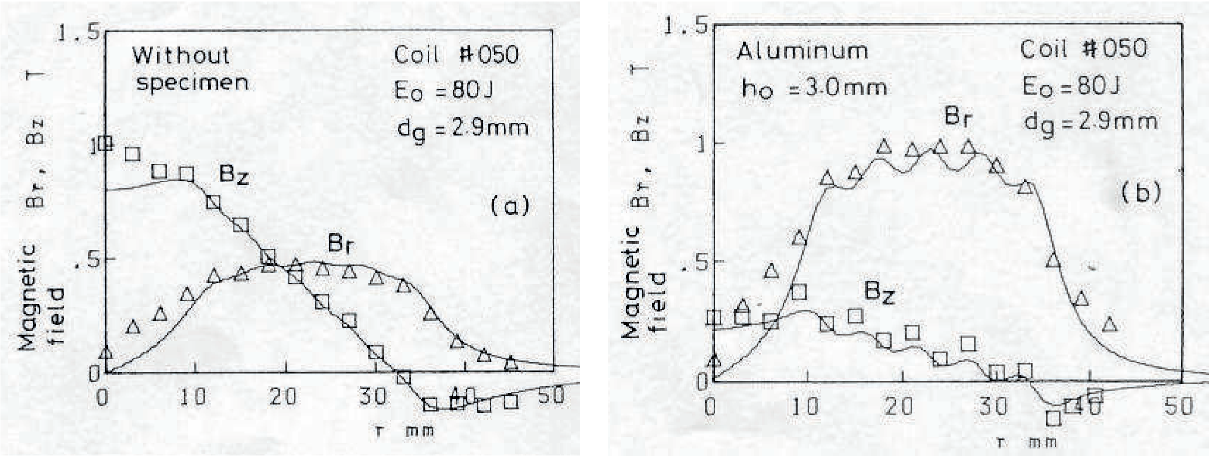

(a) without workpiece *(b) with a fixed aluminium workpiece*

Figure I-35: Radial distribution of magnetic field without and with a fixed workpiece [26].

In Fig. I-35, solid lines are the numerical predictions while the scattered points are experimental results. When the disk is mounted on the coil, Fig. I-35(b), the radial component of the magnetic field is increased significantly. They took into account the rate sensitivity and the geometry change of the workpiece on the induced currents but ignored temperature and bending effects. Their interest was in predicting the plate's deformed shape. In their simulations, Takatsu *et al.* [26] used a rate-independent hardening law (classical Hollomon law) and a hardening law including a logarithmic strain-rate dependency. The numerical results of Takatsu *et al.* [26] are presented in Fig. I-36. The numerical results of Takatsu *et al.* [26] are in good agreement with their experimental ones.

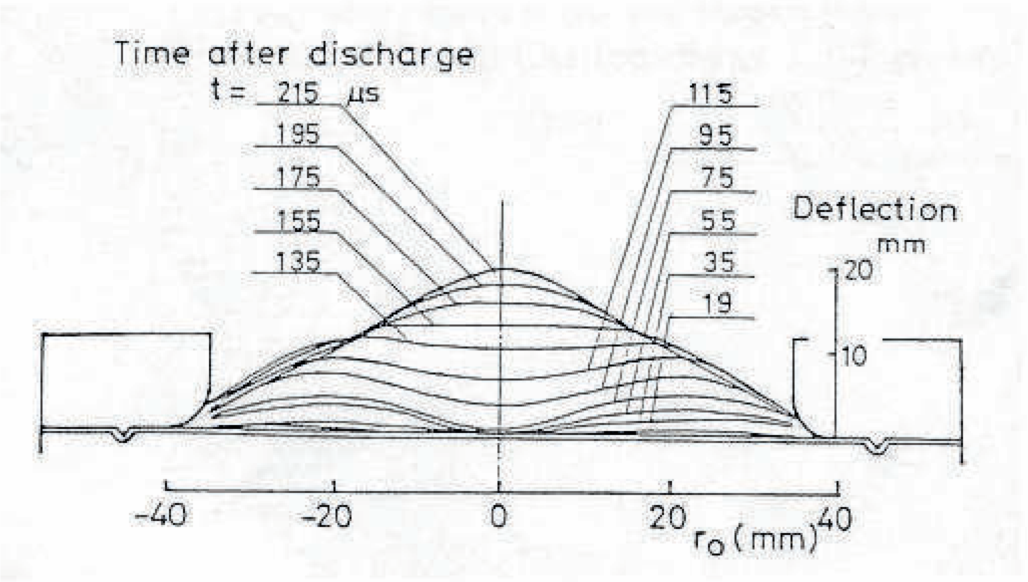

Figure I-36: Evolution of deformation as function of time [26].

The experimental values and the predicted values of the displacement of the workpiece at the centre and at *20 mm* from the centre with respect to time are presented in Fig. I-37.

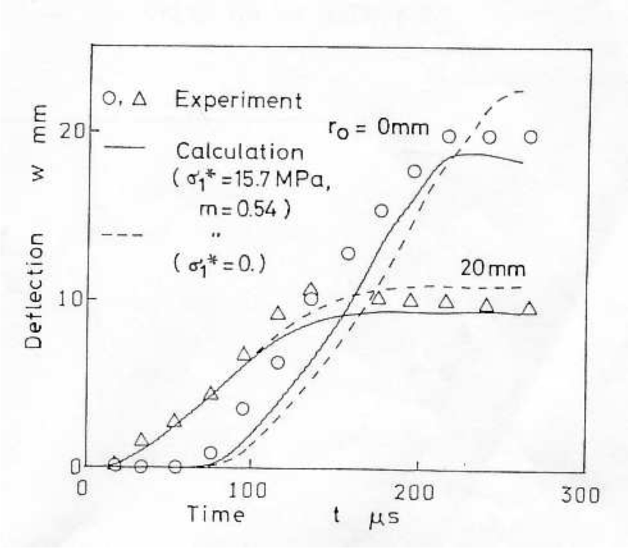

Figure I-37: Displacement of the workpiece at specified radial locations as function of time [26].

In Fig. I-37, circular and triangular marks are the experimental values. Solid lines are the calculated results with the viscoplastic hardening law and dashed lines those calculated ignoring the strain-rate effect. As attempted, for both predictions, the deformation of the centre of the workpiece is delayed with respect of the rest of the annular part. It is attributed to the existence of a dead spot at the centre of the flat spiral coil, where the magnetic pressure has almost a zero magnitude. The centre of the workpiece deforms mostly due to the high-velocity inertial effect of the deformation of the annular part. An interesting result of Takatsu *et al.* [26] is the slight difference between the predicted values of deflection achieved with the rate-independent and the viscoplastic hardening laws.

With the development of commercial FE codes, Kleiner and Brosius [39] proposed to combine two FE codes to simulate electromagnetic tube forming processes (expansion and compression). In [39], the commercial FE code MARC [40] is employed to simulate the mechanical dynamic simulation and a self developed FE code for the electromagnetic field simulation. The in-house FE code is implemented in MARC [40] via a user subroutine. The in-house FE code calculates the Lorentz forces and then the pressure applied on the tube (mechanical input into MARC [40]). The commercial FE code MARC [40] calculates the deformation of the tube and then updates the tube geometry in the self developed FE code.

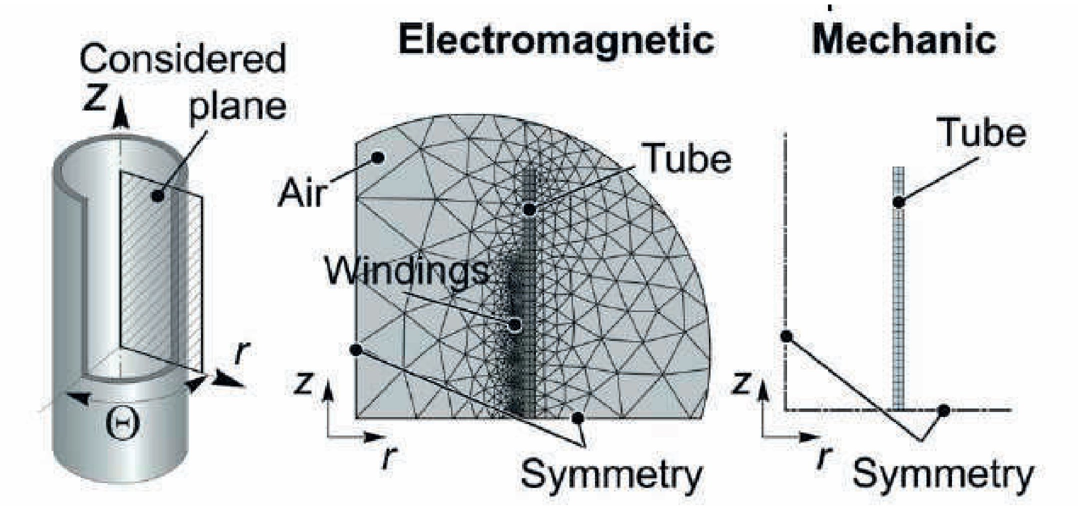

Figure I-38: FE Model developed in [39].

In the work of Kleiner and Brosius [39], an axisymmetric model has been developed due to the symmetry of the EMF tube process. As presented in Fig. I-38, two different meshes are used: the first one is the mechanical mesh and the second one is the electromagnetic mesh. Due to the deformation of the tube, the mesh in the electromagnetic FE analysis has to be updated. Kleiner and Brosius [39] proposed to use a re-meshing technique in order to update the tube geometry in electromagnetic FE analysis. To reduce time cost in the re-meshing algorithm, the FE mesh is divided into two parts. On one hand, a fixed mesh is created including coil windings and regions far away from the deformation zone. On the other hand the region nearby the deformation area has to be re-meshed with respect to the updated tube geometry. Kleiner and Brosius [39] propose to do this automatically with a Delauney triangulation. At the same time, Risch *et al.* [41] combined two FE codes in order to simulate the EMF of a flat circular sheet. The FE models developed by [41] are still axisymmetric models. In [41], the mechanical analysis is performed with the commercial FE code MARC [40] while the electromagnetic analysis is carried out with the open source software FEMM [42]. The pressure acting on the sheet and derived from the magnetic fields computed with FEMM [42] are used as input data in the mechanical analysis. The two FE codes exchange data regularly. At the beginning a FEMM [42] analysis is carried out followed by a mechanical analysis. The mechanical simulation stops when the deformation exceeds a defined value. After which a new magnetic field distribution is calculated with FEMM [42] from the deformed metal sheet. This exchange is repeated until the magnetic field does not act any longer. An example of the FE results of Risch *et al.* [41] is presented in Fig. I-39.

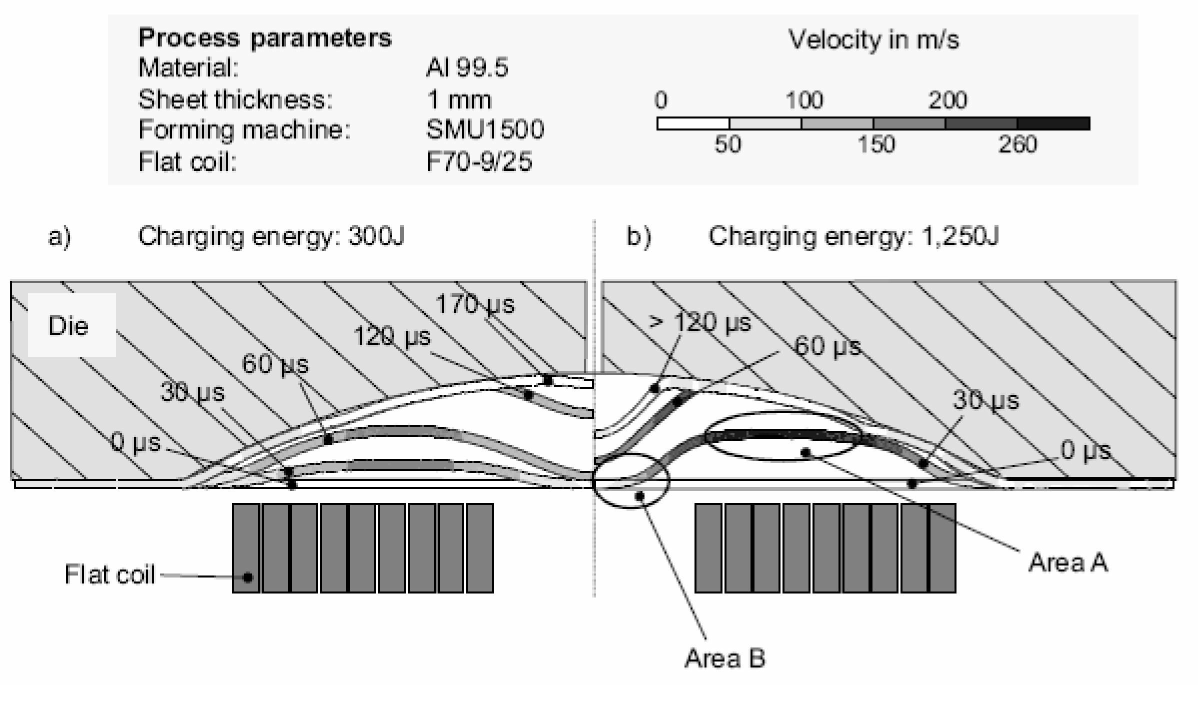

Figure I-39: Rebound effect reported by Risch et al. [41].

With their FE model, Risch *et al.* [41] studied the undesirable effects of the kinetic energy locally stored by metal sheet during an EMF process with a die. The undesirable effects studies by Risch *et al.* [41] are: inhomogeneous distribution of the velocity in the metal sheet and the rebound, Fig. I-39b. When the metal sheet contacts the die, the rebound effect occurs, if the kinetic energy is not completely dissipated (i.e. transferred from the metal sheet to the die).

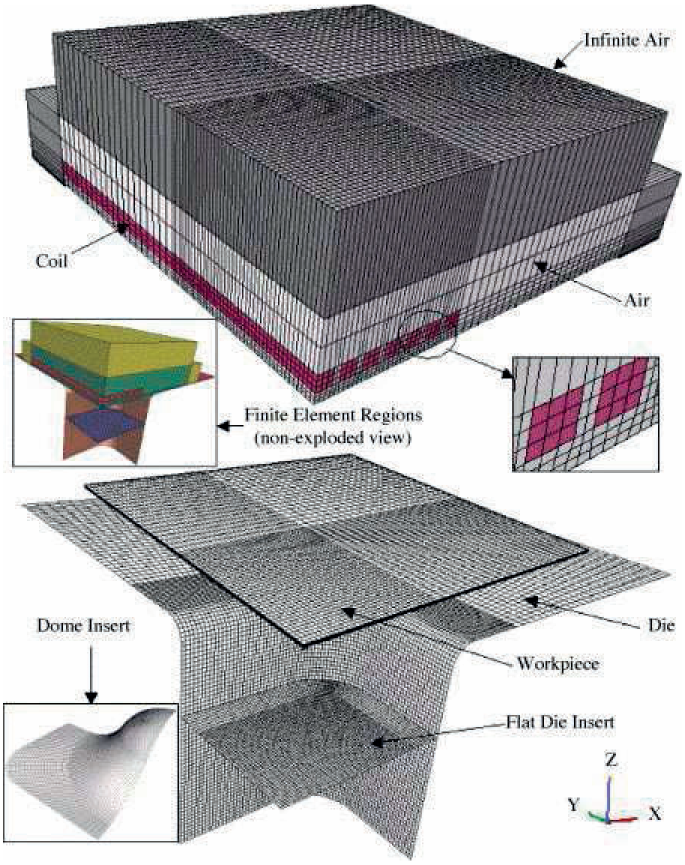

Figure I-40: 3D FE Model developed by Oliveira et al. [29].

Another approach has been proposed by Oliveira *et al.* [29]. They developed another 'loosely coupled' model to simulate sheet EMF process. In [29], a *3D* electromagnetic FE analysis is combined with a structural FE code to simulate the thermo-mechanical behaviour of the metal sheet. The commercial multi-physics FE code ANSYS [43] is employed to solve the transient electromagnetic phenomena occurring in the EMF process. The commercial explicit dynamic FE code LS-DYNA [35] is used to model the *3D*-mechanical behaviour of the sheet. An interface has been developed by Oliveira *et al.* [29] to allow the introduction, at small intervals (at each $6\ \mu s$), of electromagnetic force data from ANSYS [43] in the structural code LS-DYNA [35]. The predicted deformed shape of the sheet calculated with LS-DYNA [35] is then used to update the geometry of the metal sheet in the electromagnetic model in ANSYS [43].

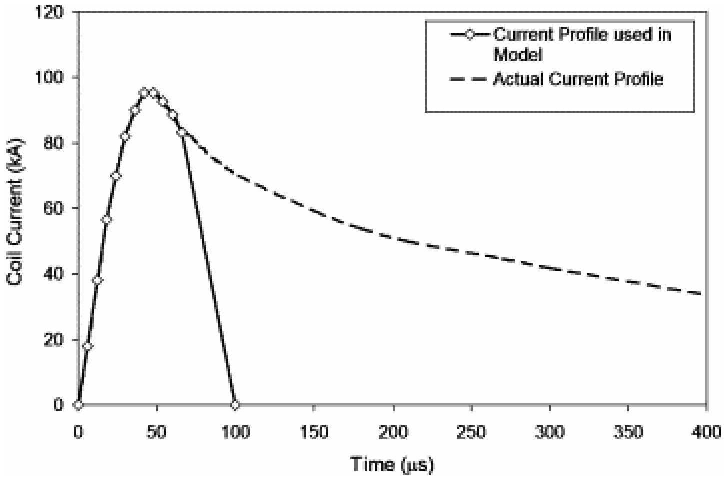

Figure I-41: Idealized current used by Oliveira et al. [29].

The FE model developed by Oliveira *et al.* [29] is presented in Fig. I-40. The mesh of the air, coil and workpiece is used for both the electromagnetic and mechanical analysis. The rigid tooling surfaces (die and holder) are only considered in the mechanical analysis. In their FE simulations, Oliveira *et al.* [29] use an idealized current profile (Fig. I-41) in order to increase the efficiency of their model.

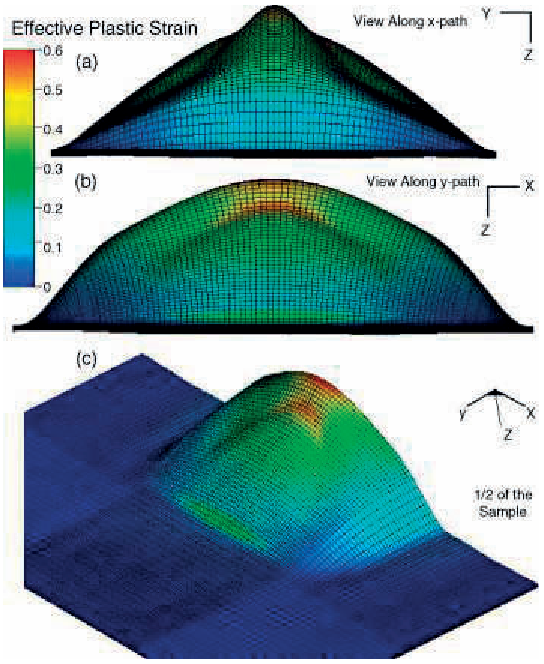

Figure I-42: Contours of effective plastic strain on the final profile of the workpiece [29].

An example of FE results obtained by Oliveira *et al.* [26] is presented in Fig. I-42. Oliveira *et al.* [26] demonstrated that a loosely coupled numerical model provides reasonable predictions of workpiece deformation and strain distribution. The models were able to predict the areas in the workpiece that would experience thinning and necking, but require damage-based constitutive models or other failure criteria before they can be used for formability prediction.

To conclude, a loosely coupled model can be used to simulate the EMF process with sufficient accuracy. The principal advantage of using the loosely coupled method is its computing cost efficiency. The numerical predictions obtained from this method are vastly in good agreement with the experimental ones. The capacity of modelling the process presented by this model is largely investigated and is found to be coherent and capable of simulating the dynamic deformation of workpiece.

I.3.2.3 Fully-coupled approach

In a fully coupled procedure, the effects of the coupled electromagnetic, mechanical and thermal fields are calculated in each element of the forming system. The mathematical description of the complete electromagnetic-mechanical equations is very complicated to solve in a compact environment. The main disadvantage of this procedure is the difficulty found in obtaining a converging solution, due to the very high computational cost for solving the inter-related equations.

A first attempt has been made by Bendjima and Féliachi [44]. Their efforts concentrated on bi-dimensional FE modelling of tube expansion by EMF. Bendjima and Féliachi [44] have carried out multi-physics FE simulations; nevertheless the simulation takes account only on the magnetic field interaction with the displacement of the tube. The tube movement is simulated through the displacement of a rectangular band; the deformation of the tube is not taken into account. Thus, at each new time step a new mesh is needed to be generated. In order to avoid this problem during the simulations, a suitable technique based on only one finite element meshing during the entire step by step simulation is carried out. A geometric band, divided into sub-region is generated to designate the moving workpiece as well as the part of air. At each time step, the physical properties assigned to sub-regions are up-dated according to their new positions. The numerical modelling employed by Bendjima and Féliachi [44] is presented in the Fig. I-43.

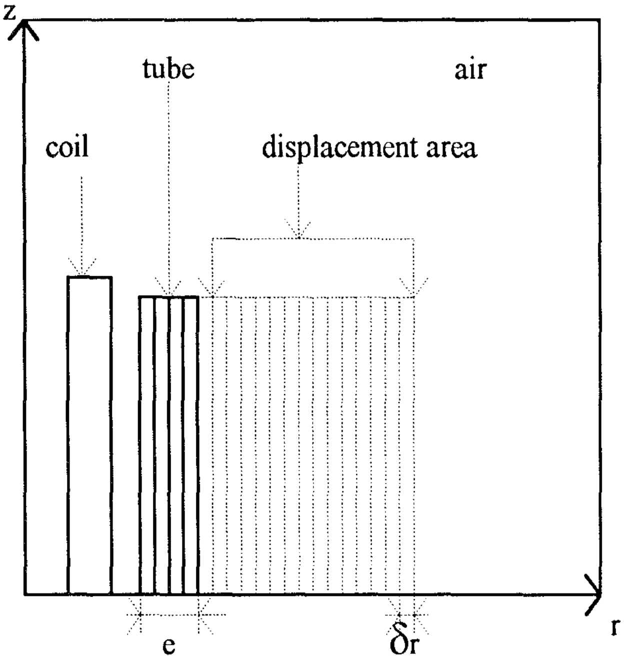

Figure I-43: FE model used by Bendjima and Féliachi [44].

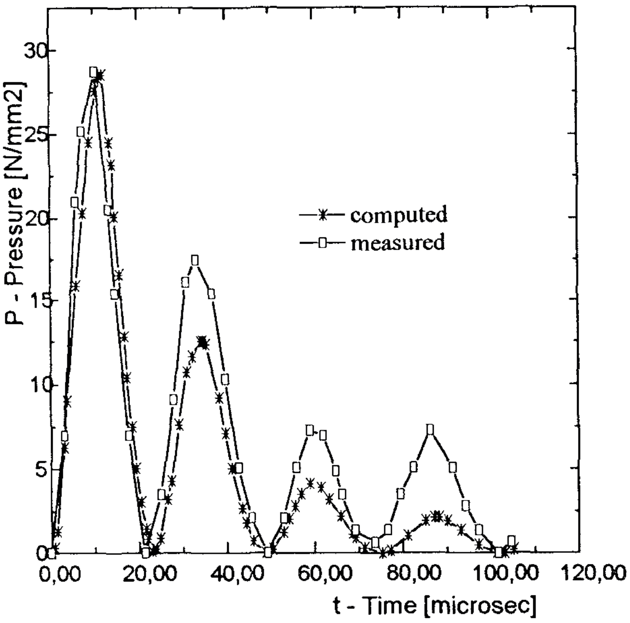

Figure I-44: Comparison of measured and calculated magnetic pressure [44].

Bendjima and Féliachi [44] compared the transient magnetic pressure obtained from the numerical simulations with their experimental results, Fig. I-44. We observe in Fig. I-44 that the applied magnetic pressure is a damped sinusoidal function. The pressure is supposed to be uniformly distributed along the wall thickness of the tube. The numerical results of Bendjima and Féliachi [44] are consistent with the experimental ones.

So as to construct a fully electromagnetic-mechanical coupling, Fenton and Daehn [45] developed a bi-dimensional FE model with the help of “CALE” code. The “CALE” code is an “Arbitrary Langragian-Eulerian” hydrodynamics computer code. But the CALE code is also magneto hydrodynamic. CALE has also the capability to handle the drawing and stamping operations (limited to two dimensional axially symmetric and plain strain configurations). This code was developed at Lawrence Livermore National Laboratory. In the study of Fenton and Daehn [45], a comparison between experimental data of an electromagnetically free formed clamped sheet (Takatsu *et al.* [26] experiments) and a 2D CALE model is presented. Althouth the strain rate has significant effect on the material behaviour, Fenton and Daehn [45] employed a hardening law independent of strain rate sensitivity. The initial undeformed geometry and mesh developed with CALE are presented in Fig. I-45.

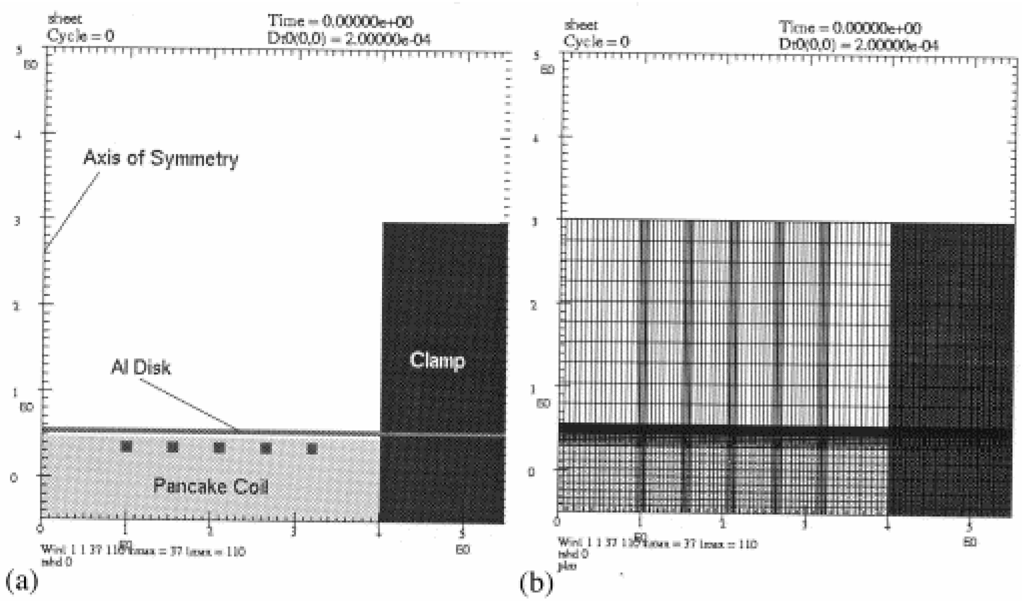

Figure I-45: (a)The undeformed geometry, (b) the undeformed mesh geometry with CALE [45].

In Fig. I-45, the five small squares indicate the windings in the pancake coil. The region which holds or surrounds the five small squares is a non-conductive nylon material which maintains the pancake coil shape. The thin line above the five squares is the aluminium flat sheet. The two large blocks on the right side of the figure are the clamping blocks which hold the aluminium sheet over the coil.

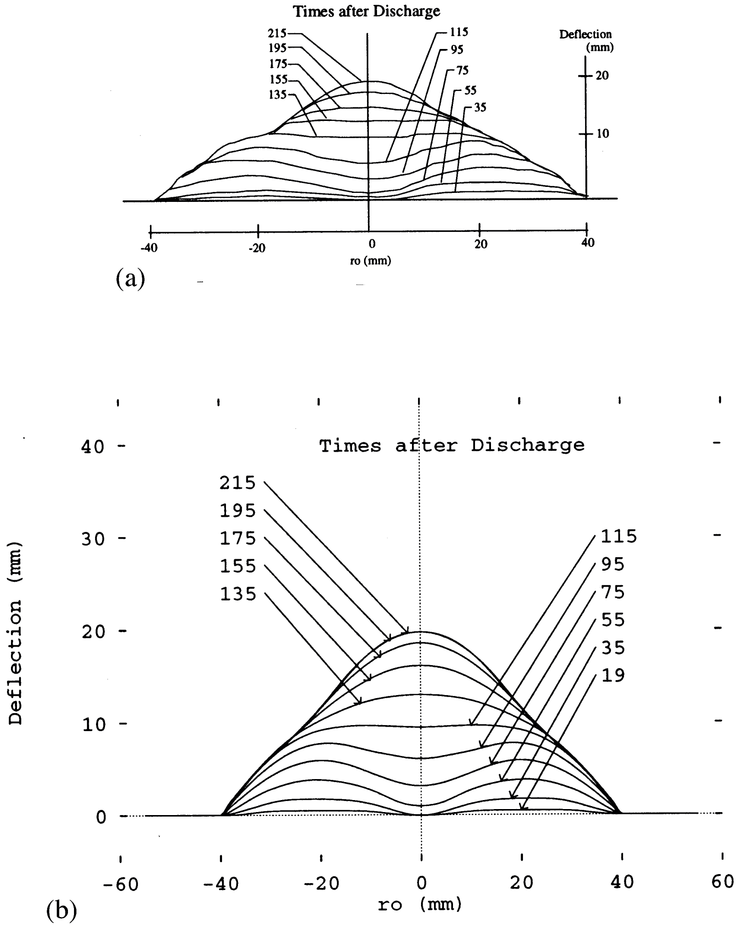

Figure I-46: Experimental profile data from Takatsu et al. [26] (a) and CALE predictions (b) time values are in μs [45].

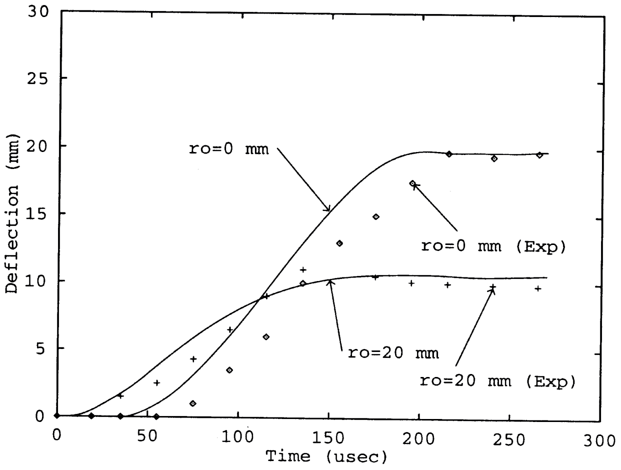

Figure I-47: CALE-calculated and experimental (Takatsu et al. [26]) deflections of the disk at specified locations on the disk [45].

The comparison between CALE calculated profiles of the disk and the experimental profiles from Takatsu *et al.* [26] are presented in Fig. I-46. The comparison between CALE calculated deflection of the disk and the results from Takatsu *et al.* [26] are shown in Fig. I-47. The predictions of Fenton and Daehn [45] are in agreement with the experimental results reported by Takatsu *et al.* [26], Fig. I-46 and Fig. I-47.

In this last five years, 3D fully coupled analyses have arisen in commercial codes and self developed codes. Based on a commercial FE code devoted to stamping (PAMSTAMP [46]), Conraux *et al*. [47] carried out 3D FE simulations of EMF of sheet process. The commercial FE software SYSMAGNA [48] is used for the numerical simulations of the electromagnetic part of the process. The coupling between the electromagnetic, thermal and mechanical problem is presented in Fig. I-48.

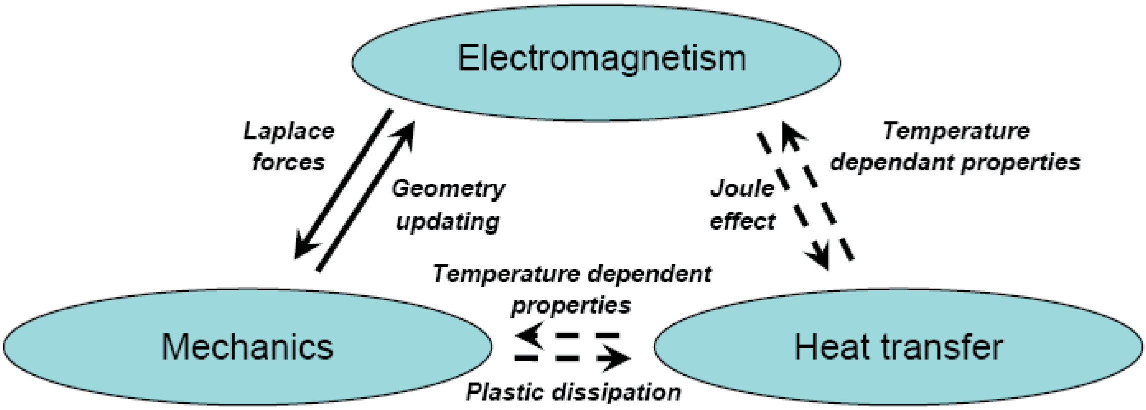

Figure I-48: Coupling of multi-physical phenomena proposed in [47].

As mentioned in the case of PAMSTAMP [46], an electromagnetism module has been developed for LS-DYNA [35] by L'Eplattenier *et al.* [49]. The coupling of multi-physical phenomena is same as proposed by Conraux *et al.* [47], Fig. I-48. In both cases [47, 49], the numerical predictions are then compared with experimental results and the efficiency of coupled *3D* numerical modelling is demonstrated. A particular effort has been made by the "Institut für Umformtechnik und Leichtbau" [50] of the Dortmund Technology University under the project "For 443". The first work completed in the project "For 443" is the work of Svendsen and Chanda [51]. The main purpose of the work of Svendsen and Chanda [51] is the continuum thermodynamic formulation of coupled-field models for the dynamic deformation of rate-dependent inelastic metals induced by strong magnetic fields. Based on the work of Svendsen and Chanda [51], Stiemer *et al.* [52] proposed a "fully coupled" model to simulate isothermal EMF process.

However, in all the FE approaches presented in this section, the different physical phenomena are treated separately. In most of the preliminary models, the electromagnetic problem and mechanical problem are treated individually without any linkage. These models are simpler but do not provide the true description of the process. Mostly, the Maxwell's equations are resolved analytically, and the electromagnetic pressure is obtained which is then introduced into the mechanical problem. The deformation of the workpiece is not taken into account for the calculation of the electromagnetic pressure.

Then, more recently the loosely-coupled techniques are presented, which are very accurate and rather uncomplicated. The electromagnetic problem calculates the basic electromagnetic parameters, which are then introduced in to the mechanical problem. The coupling between the two problems is carried out; the parameters are then recalculated at each time step taking into account the new deformed geometry of the workpiece.

Furthermore, the fully coupled models are moreover an extension of the loosely-coupled approach. However, in these FE models the related electromagnetic, mechanical and thermal problems are resolved separately, and their outputs are coupled together at each new time step, for new deformed geometry of the workpiece. Nevertheless, there are still similar to loosely coupled models.

Conclusion

EMF process is a very high speed forming technology for metallic parts. Although, the process is developed in the late 1960's, there is only a recent increase in the industrial interest for its application for manufacturing. This recent interest in understanding the EMF process has been stimulated by the desire of using more aluminium in the automobiles and aircrafts industries. The reduction in the weight of the components and body is commonly reached by using lightweight materials and manufacturing processes which allows the application of thin-walled structures. EMF process is a well known subject, with significant research publications on its experimental and numerical aspects. To summarize the review of the scientific literature, it is observed that EMF process has very high potential for its industrialisation. Peculiar advantages (in forming, joining, assembling, etc.) were observed. These include improved formability, improved strain distribution, reduction in wrinkling, active control of springback, and its application to light metallic alloys such as aluminium.

Experimental studies on diverse application of EMF (flat sheetmetal as well as tube) process were mainly aimed to identify the advantages of EMF. These include study on the formability, elimination of springback, reduction in wrinkling. Furthermore, a vast scientific literature is dedicated to the identification of the process parameters. Influence of various process parameters are also subjected to existing research on EMF process. Optimisation of these characteristics would improve the efficiency of the experimental system. The experimental aspects of the electromagnetic forming process are rather well documented.

From the review of the existing literature, a large number of possibilities of numerically modelling the EMF process are investigated. The numerical modelling can provide the understanding of the process and predict the parameters necessary for accomplishing it as well as to improve its effectiveness. However the process involves a complex study of electromagnetic and mechanical phenomena. The non-coupled, loosely coupled or the fully coupled models have then been developed. Simpler methods proposed with weak or loose coupling provided satisfactory results with good agreement between the numerical predictions and experimental results. These methods as proposed in the literature are found to be very efficient. A fully coupled electromagnetic and mechanical modelling of the process would be the most accurate way to model it. But these methods are complex and for instance analogous to the loosely coupled methods.

Keeping in view the simplicity and efficiency of the loosely coupled approach, we decided to employ this method for the numerical study of EMF process. In this approach, the electromagnetic and mechanical aspects of the forming process are treated as two separate independent problems [53]. The electromagnetic problem is solved using the Maxwell's equation in an independent environment. The results obtained from the electromagnetic problem, such as magnetic field density, electromagnetic force and pressure are then imported in to the mechanical problem. In the mechanical problem at each new time step, the deformation of the workpiece is accounted for the calculation of the new electromagnetic fields.

Reference

[1] Belyy I.V., Fertik S.M., and Khimenko L.T., Electromagnetic Metal forming Handbook, translated by Altynova M.M., Material Science and engineering department, The Ohio State University.

[2] Unger J.A, Modeling and simulation of coupled electromagnetic field problems with application to model identification and metal forming, Doctor Ingénieurs Thesis, University of Dortmund, 2007.

[3] Brahim Bendjima, Contribution à la modélisation par éléments finis des phénomènes électromagnétiques relatifs au magnétoformage, thèse de doctorat, Université de Nantes, 1997.

[4] Mallein V., Magnétoformage de pièces en aluminium pour automobile, Étude expérimentale et développement numérique associe. Thèse de Génie des Procèdes. Grenoble : INPG 2003.

[5] Manish Kamal, A uniform pressure electromagnetic actuator for forming flat sheets, Doctorate thesis, The Ohio State University, 2005.

[6] Mala Seth Dehra, High velocity formability and factors affecting it, Doctorate thesis, The Ohio State University, 2006.

[7] Golovashchenko S.F., Material formability and coil design in electromagnetic forming, *Journal of Materials Engineering and Performance*, DOI: 10.1007/s11665-007-9058-7.

[8] Balanethiram V. S., Hyperplasticity: enhanced formability of sheetmetals at high velocity". Doctorate thesis, The Ohio State University, 1996.

[9] John T. Conway, Exact solutions for the magnetic fields of axisymmetric solenoids and current distributions, *IEEE Transactions* (2001), Vol. 37, no. 4, pp. 2977-2988.

[10] Resnick R., Halliday D., Electricité et magnétisme, Traduit par Lebel A., Thériault C., Physique 2, John Wiley & Sons, INC 1960.

[11] Grover F.W., Inductance calculations; Working formulae and tables, DOVER Publication Inc, New York 1946.

[12] Travail des métaux en feuilles, Formage electromagnétique, Techniques de l’ingenieur, Traité Génie mécanique, B 7 582, pp 1-20.

[13] Kore S.D., Date P.P., Kulkarni S.V., Effects of process parameters on electromagnetic impact welding of aluminum sheets, *International Journal of Impact Engineering* 34, 2007, pp. 1327-1341.

[14] Zhang X., Wang Z.R., Song F.M., Yu L.Z., Lu X., Finite element simulation of the electromagnetic piercing of sheetmetal, *Journal of Materials Processing Technology*(2004)*,* vol. 151,pp. 350-354.

[15] Young-Bae Park, Hoen-Young Kim, Soo-Ik Oh, Design of axial torque joint made by electromagnetic forming, *Thin-Walled Structures 43* (2005); pp. 826-844.

[16] Yu H.P. and Li C.F., Dynamic compaction of pure copper powder using magnetic force, *Acta Metallurgica Sinica(English letters)* 2007; vol. 20, No.4, pp. 277-283.

[17] Vincent J. Vohnout, A hybrid quasi-static/dynamic process for forming large sheet metal parts from aluminum alloys, Doctorate thesis, The Ohio State University, 1998.

[18] Padmanabhan M., Wrinkling and Spring Back in electromagnetic sheetmetal forming and Electromagnetic ring compression. Master of Science Thesis: The Ohio State University, 1997.

[19] Teodora-Emilia MOTOASCA, Electrodynamics in deformable solids for electromagnetic forming, Universitatea “Transilvania”, Brasov, Roumania,2003.

[20] Jozef Bednarczyk, Distribution of forces in the inductors used in metal processing in the pulse magnetic field, *Journal of Materials Processing Technology* (2003), vol. 133,pp. 340-247.

[21] Mamalis A.G., Manolakos, D.E., Kladas, A.G., Koumoutsos, A.K., Electromagnetic forming and powder processing: Trends and developments, *Applied Mechanics Review* 2004, 57; pp. 299-324.

[22] Song F.M., Zhang X., WANG Z.R., Yu L.Z., A study of tube electromagnetic forming, *Journal of Materials Processing Technology*(2004), vol.151; pp. 372-375.

[23] Zhang H., and Murata M., Suzuki H., Effects of various working conditions on tube bulging by Electromagnetic forming, *Journal of Materials Processing Technology* (1995); 48, pp. 113–121.

[24] Yu Hai-ping and Li Chun-feng, Effects of coil length on tube compression in electromagnetic forming, *Transactions of Nonferrous Metals Society of China 17*(2007), pp. 1270–1275.

[25] Al-Hassani S.T.S, Magnetic pressure distribution in the sheetmetal forming, Electrical Methods of Machining, Forming and Coating, *Institute of Electrical Engineering Conference*, publication no 1975, pp. 1-10.

[26] Takatsu N., Kato M., Sato K., Tobe T., High speed forming of metal sheets by electromagnetic forces, *International Journal of Japanese Society for Mechanical Engineering* 1980; 60; pp. 142-148.

[27] Imbert Boyd J.M.S. Increased Formability and the Effects of the Tool/Sheet Interaction in Electromagnetic Forming of Aluminium Alloy Sheet Thesis. Master of Science. Waterloo : University of Waterloo. 2005.

[28] Mala Seth, Vincent J. Vohnout, Glenn S. Daehn, Formability of steel sheet in high velocity impact, *Journal of Materials Processing Technology* (2005), vol. 168, pp. 390-400.

[29] Oliviera D.A., Worswick M.J., Finn M., Newman D., Electromagnetic forming of aluminum alloy sheet: Free-form and cavity fill experiments and model, *Journal of Materials Processing Technology* (2005), vol.170; pp. 350-362.

[30] http://www.matsceng.ohio-state.edu/~daehn/hyperplasticity.html (April 2009).

[31] Anter El-Azab, Mark Garnich, Ashish Kapoor, Modeling of the electromagnetic forming of sheet metals: state-of-the-art and future needs, *Journal of Materials Processing Technology* (2003), vol.142, pp. 744-754.

[32] Jablonski J. and Wrinkler R., Analysis of the electromagnetic forming process, *International Journal of Mechanical Sciences* 20 (1978); pp.315-325.

[33] William H. Gourdin, Analysis and assessment of electromagnetic ring expansion as a high strain-rate test, *Journal of Applied Physics;65* (1989), pp. 411–422.

[34] Imbert J.M., Winkler S.L., Worskick M.J., Oliveira D.A., Golovaschenko S., The effect of tool-sheet interaction on damage evolution in electromagnetic forming of aluminum alloy sheet, *Journal of Engineering Materials and Technology* ,vol. 127 January (2005); pp.145-153.

[35] Hallquist J. “LS-DYNA Theoretical Manual,” Livermore software technology corporation.

[36] Gurson A.L., Continuum theory of ductile rupture by void nucleation and growth: Part-I, yield criteria and flow rules for porous ductile media, *Journal of Engineering Materials Technology,* (1977), vol. 99, pp. 2-15.

[37] Tvergaard V., Influence of voids on shear band instabilities under plane strain conditions, *International Journal of Fracture* (1981), vol. 37(4), pp.389-407.

[38] Tvergaard V., and Needleman A., Analysis of the cup-one fracture in a round tensile bar, *Acta Metallurgica* (1984), vol. 32, pp.157.

[39] Kliener M. and Brosius A., Determination of flow curves at high strain rates using the electromagnetic forming process and an iterative finite element simulation scheme, *Annals of the CIRP* (2006), vol. 55(1).

[40] MSC Software ™, Marc ® 2005, http://www/mscsoftware.com/. (April 2009).

[41] Risch D., Beerwald C., Brosius A., Kleiner M., On the significance of the die design for electromagnetic sheet metal forming, *1st International Conference on High Speed Forming* (2004), pp.191-200.

[42] Foster-Miller Inc., FEMM, Open source FEA software Ver. 3.3 by Meeker D. (2003), http:// femm.foster-miller.net (April 2009).

[43] ANSYS ®, Version 8.0, USA, 2006 (April 2009).

[44] Bendjima B., Feliachi M. Finite element analysis of transient phenomena in electromagnetic forming system. Laboratoire de Recherche en Techniques Inductive, France 1996.

[45] Gregg K. Fenton, Glenn S.Daehn, Modeling of electromagnetically formed sheet metal, *Journal of Materials Processing Technology* (1998), vol. 75, pp. 6-16.

[46] PAM-STAMP ®, User's manual, ESI Group 2005.

[47] Conraux Ph., Pignol M., Robin V., Bergheau J.M., 3D finite element modeling of electromagnetic forming processes, 2nd conference on high speed forming 2006, Dortmund, pp. 73-82.

[48] SYSWELD ®, SYSMAGNA, User's manual, ESI Group, 2005.

[49] Pierre L'Eplattenier, Grant Cook, Cleve Ashcraft, Mike Burger, Art Shapiro, Glenn S. Daehn, Mala Seth, Introduction of an electromagnetic module in LS-DYNA for coupled mechanical-thermal-electromagnetic simulations, *9th International LS-DYNA Users Conference*, Metal forming (2), pp. 17-1 to 17-8.

[50] Institut für Umformtechnik und Leichtbau, Dortmund, Germany, University of Dortmund, http://www.iul.tu-dortmund.de/de/index.php (April 2009).

[51] Svendsen B., Chanda T., Continuum thermodynamic modeling and simulation of electromagnetic metal forming, *Technishe Mechanik*, vol. 23(2003), pp. 103-112.

[52] Stiemer M., Unger J., Blum H. and Svendsen B., Algorithmic formulation and numerical implementation of coupled multifield models for electromagnetic metal forming simulations, *International Journal of Numerical Methods in Engineering.* **68** (2006), pp. 1301–1328.

[53] J.P.M. Correia, M.A. Siddiqui, S. Ahzi, S. Belouettar and R. Davies, A simple model to simulate electromagnetic sheet free bulging process, *International Journal of Mechanical Sciences 50* (2008), pp.1466–1475.

Chapter II

Finite difference model for resolution of the electromagnetic problem of EMF process

Chapter II: Finite difference model for resolution of the electromagnetic problem of EMF process

II.1. Introduction:

A precise and accurate numerical model allows us to avoid the repetition of experiments and creating of a large number of prototypes. The forming processes are not excluded from this domain. Thus several numerical methods are developed during recent time to simulate these processes. These models can correctly predict the behaviour and characteristics of most forming processes with sufficient accuracy and repeatability. To understand the phenomena occurring during the electromagnetic forming process (called EMF process in the following), a numerical model is considered to be highly necessary. This numerical model is needed to be proficient of resolving the transient electrical circuit, electromagnetic equations and then to be applied to the mechanical and structural problem of the EMF process. This chapter presents the description and assumptions that are applied to develop the comprehensive analytical model of the electromagnetic forming process. This model is applicable to flat sheet and with slight modifications in the boundary conditions, it can also be applied to tube expansion and compression. This analytical approach for the solution of the EMF process is referred to as the electromagnetic problem through out this chapter. The approach proposed herein is developed from the previous work of Takatsu *et al.* [1]. Firstly, we reviewed the physical phenomena occurring in the EMF process. The assumptions are next presented. The electromagnetic equations are presented in the general case and derived for axi-symmetric case. From the set of differential equations, a finite difference scheme has been written. For validation purposes, our model predictions are compared with the experimental results available from the literature and with the FEMM [2] predictions. Finally, the influence of mesh size and of the time increment is studied.

II.2. Electromagnetic phenomena description

In EMF process, the analysis of the circuit involves the study of the electromagnetic fields generated in the coil and their effects in the nearby workpiece. To be able to predict the performance of the electromagnetic forming process, the forming system can be represented as an equivalent *RLC* circuit [3]. The equivalent *RLC* circuit representing the electromagnetic forming process is shown in Fig. II-1.

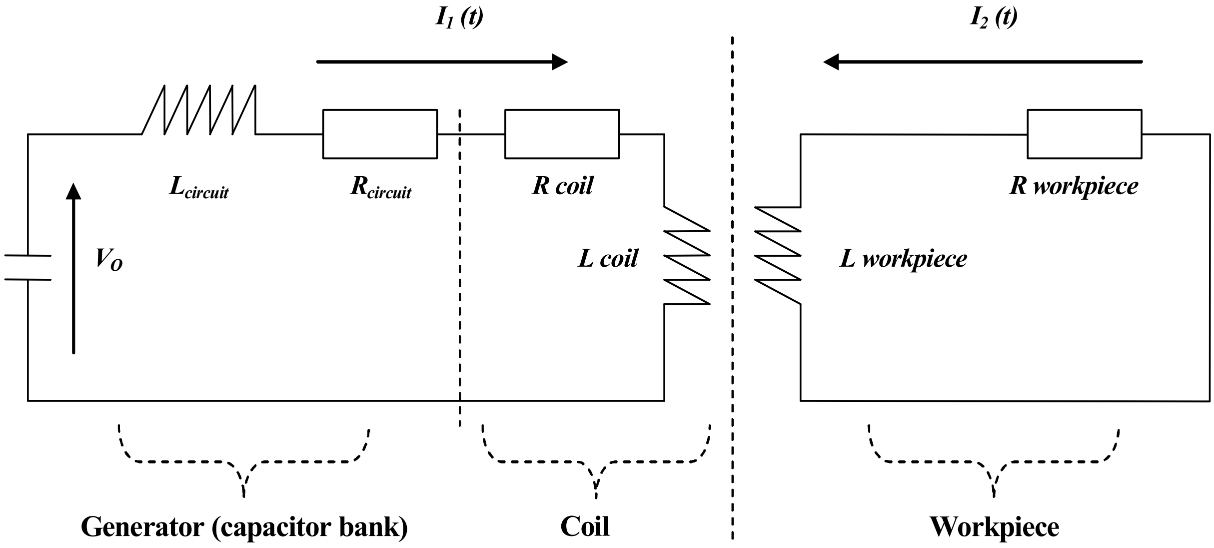

Figure II-1: Equivalent RLC circuit for electromagnetic forming process.

In an electromagnetic forming system, the discharge circuit consists of a capacitor bank *C*, connecting lines with inductance *L* and resistance *R*, as well as the inductance and resistance of the forming coil, which is combined with the workpiece resistance and inductance. When the switch is closed, the discharge of the capacitor bank creates a current pulse $I_1(t)$ in the forming coil. This current generates an electromagnetic field inside the workpiece. This field penetrating the nearby workpiece will further induce an Eddy current $I_2(t)$. The workpiece and the coil are coupled through the magnetic flux developed due to the electromagnetic induction. As a consequence of the interaction between the electromagnetic field and the induced current, electromagnetic body forces are developed, causing the workpiece to deform rapidly, first elastically and finally plastically. These body forces are commonly known as the Lorentz's forces. The currents $I_1(t)$ and $I_2(t)$ are used as primary quantities in the models of electromagnetic forming. Fig. II-2 presents the interaction of the discharge current of the coil with the induced current developed in the workpiece.

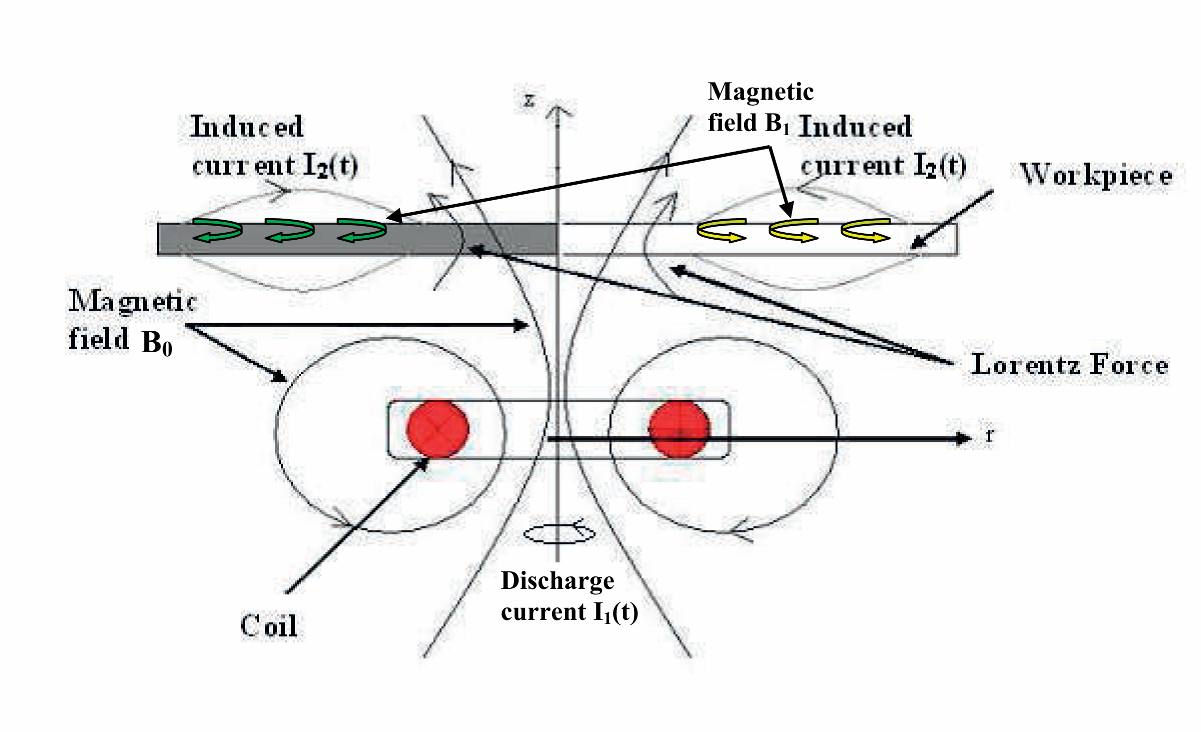

Figure II-2: Electromagnetic forming process, Lorentz force development.

During the actual forming process, the parameters of the circuit (such as discharge current, magnetic field density etc.) are time-dependent. These circuit parameters depend on the geometry of the circuit. This geometry changes when deformation of the workpiece takes place. For the calculation of the equivalent electric circuit elements; the geometry and the material properties of each component of the electromagnetic forming systems are required.

II.3. Assumptions

Use of a numerical method for modelling a process is a complicated job. In most of the cases, certain simplifying assumptions are made to render this mathematical modelling less tedious. However, these approximations and assumption should comply with the actual process. This model is desired to be capable of predicting the process characteristics without compromising the accuracy of the results. For the mathematical modelling of the electromagnetic problem, we supposed a few assumptions. The details of these assumptions are provided below:

1. During the EMF process, the workpiece attains a very high velocity in a few micro seconds, and moves away from the coil. In this case, the electromagnetic field may change due to the varying mutual inductance between the coil and the workpiece. One of the important features of *RLC* circuit is the fact that the efficiency of coupling

between the windings is inversely proportional to the square of the distance between them. Consequently the electromagnetic field should, in principle be calculated using the Maxwell's equations for moving media. This set of equations includes additional velocity terms as compared to those for magnetostatic equations [4]. However, for our model, which is basically a simple approach towards solving the electromagnetic problem for EMF, the interaction between displacing workpiece and magnetic field density is neglected. Manea *et al.* [5] demonstrated that in the EMF process the velocity term comes into significance only if the workpiece velocity is of the order of 10^7 *m/s*. Since the deformation process during the EMF takes place in a few microseconds the velocity is below the values for which the velocity term may affect the magnetic field during the process. Thus propagation of electromagnetic field within a coil-workpiece-air system can be defined by quasi-stationary Maxwell's equations. The velocity of the workpiece attained during the EMF process still remains under the limit of 10^3 *m/s* [6] and the EMF process takes place in an interval of few microseconds, which is far less than the values for which the effects of the motion of the workpiece on the magnetic field are noticeable. Manea *et al.* [5] concluded that for an EMF process the calculations for the electromagnetic field in stationary media may be considered as a good approximation of electromagnetic field acting on the moving workpiece. That is the reason why, in agreement with Manea *et al.* [5], we have assumed that the sheet velocity has no influence on the magnetic field.

2. Furthermore, we assumed that for EMF process that takes place in a very small interval of time, the inductance can be considered to be constant. This results in a constant mutual inductance between the moving workpiece and coil throughout the deformation of the workpiece.
3. The third assumption made for the modelling of the electromagnetic problem is related to the geometry of the tools and workpiece. Due to symmetry of the free bulging and tube electromagnetic process, an axisymmetric configuration for the numerical solution has been used for both workpiece and coil. Consequently, the magnetic field and then the magnetic pressure acting on the sheet do not vary in the circumferential direction. Accordingly, cylindrical coordinate system is introduced for the present problem, the magnetic field, and Eddy current possesses radial and axial components. The $z-axis$ is the axis of symmetry of the configurations. The configurations only depend on the two coordinates (r, z) [7]. Furthermore, the coil is considered to be consisting of N elementary loops. Each loop is carrying the discharge current.

4. In general, the electromagnetic properties of materials strongly depend on the temperature, but in most numerical studies the electromagnetic properties are assumed to be temperature and time invariant and thermal effects are neglected. The aspects typical of EMF processes that make this simplification appropriate: the material velocities are high enough that the changes in the material electrical properties have much less effects on the calculation of the process parameters. However, it must be noted that coil is usually made up of copper alloy. This is due to its high electrical conductivity and adequate mechanical strength. Nevertheless, copper is a diamagnetic material [4, 8], which possesses temperature dependent characteristics as permeability and resistance. From the above assumptions, it follows, that the Eddy current approximation essentially consists of neglecting the relative permeability μ_r of the coil material. Additionally, the temperature dependant resistance coefficient $\rho(t)$ is assumed to be constant, as the temperature rise is very small, its influence on parameters of the configurations may be neglected.

These equations do not exactly model the process; since they do not include workpiece coupling or motion during the discharge, still give a general but accurate idea of discharge current. However, from the estimated discharge current, an approximation of magnetic field, induced current and magnetic pressure on the workpiece can then be made. The intention is to develop a simple but accurate analytical model for both flat sheet forming and compression and expansion of tubes, avoiding the problems related to modelling the end points of the forming coil and the workpiece. The analytical model developed in this work is applicable to both electromagnetic flat sheetmetal and to the tube forming made of conducting materials.

II.4. Electromagnetic equations

Electromagnetic phenomena occurring during EMF process are governed by a set of partial differential equations commonly known as Maxwell’s equations. Maxwell’s equations are used for defining the major electrical and magnetic phenomena taking place during the EMF process. The fundamental equations of the magnetic field within a conducting medium are given as follows:

$$\nabla \times \mathbf{E} = -\partial \mathbf{B} / \partial \mathbf{t} \qquad \text{(II-1)}$$

$$\nabla\times\mathbf{H}=\mathbf{J_f} \tag{II-2}$$

$$\nabla\,\mathbf{J_f}=0 \tag{II-3}$$

$$\nabla\,\mathbf{B}=0 \tag{II-4}$$

$$\mathbf{B}=\mu\mathbf{H} \tag{II-5}$$

$$\mathbf{J_f}=\sigma_{\mathbf{w}}(\mathbf{E}+\mathbf{v}\times\mathbf{B}) \tag{II-6}$$

where **J_f** is the current density, **H** magnetic field intensity, **E** electric field, **B** magnetic flux density, μ permeability, **v** is the velocity of the medium and *t* time for the discharge current. According to our assumption of using quasi-stationary Maxwell's equation, the velocity of the workpiece is neglected. Hence, Eq. II-6 can be rewritten as follows:

$$\mathbf{J_f}=\sigma_{\mathbf{w}}(\mathbf{E}) \tag{II-7}$$

The Maxwell's equations allow us to determine the electromagnetic parameters **E***,* **H***,* $\mathbf{J_f}$ and **B**. The electric field **E** exists due to presence of the electric charge present in the medium; while the magnetic field **H** is the result of the displacement of the charge carriers. The permeability μ is a characteristic of the material. By our assumptions it is given by:

$$\mu=\mu_0 \tag{II-8}$$

where μ_0 is the permeability of free space and its value is given as $\mu_0 = 4\pi$ x 10^{-7} *H/m* The Lorentz force density is defined as follows:

$$\mathbf{F}=\mathbf{J_f}\times\mathbf{B} \tag{II-9}$$

As we have observed, the equations that describe the phenomena of electromagnetic forming are basically a set of partial differential equations. These equations provide the relationship between the magnetic and electric field and time. Combining and rewriting the Maxwell's Eqs. II-1 to II-8, we obtain:

$$-\frac{1}{\mu_0\sigma_{\mathbf{w}}}\nabla^2 B+\frac{\partial B}{\partial t}=\nabla\times\left(\mathbf{v}\times B\right) \tag{II-10}$$

where **v** is the velocity of the disk during the forming process. Since we considered the process to be quasi-stationary, we assume that the velocity term does not affect the magnetic field during the process i.e. $\mathbf{v} = 0$.

To determine the Lorentz force density, it is assumed that the velocity of the workpiece is negligible (or that the sheet remains stationary during the process). Thus the change in the magnetic field, due to the displacement of the workpiece and subsequent changes in its dimension are negligible. A cylindrical coordinate system may be introduced for the definition of electromagnetic problem of circular disc workpiece. Using the Maxwell's equations for the stationary media considering an axisymmetric problem the magnetic field can thus be calculated as its radial and axial components as follows:

$$-\frac{1}{\mu_0 \sigma_{\mathrm{w}}}\left(\frac{\partial^2}{\partial r^2}+\frac{1}{r}\frac{\partial}{\partial r}+\frac{\partial^2}{\partial z^2}-\frac{1}{r^2}\right)B_r+\frac{\partial B_r}{\partial t}=0 \tag{II-11}$$

$$-\frac{1}{\mu_0 \sigma_{\mathrm{w}}}\left(\frac{\partial^2}{\partial r^2}+\frac{1}{r}\frac{\partial}{\partial r}+\frac{\partial^2}{\partial z^2}\right)B_z+\frac{\partial B_z}{\partial t}=0 \tag{II-12}$$

To solve the above differential equations we have to define the boundary conditions for calculating the values of the magnetic fields. The magnetic field in the space between the coil and the work piece is given by the equation:

$$B=B_0+B_1 \tag{II-13}$$

where B_0 is the magnetic field developed by the coil and B_1 is the magnetic field created due to Eddy current in the sheet. The current induced in the sheet is given by:

$$\mathbf{J}_\theta=\frac{1}{\mu_0}\left(\frac{\partial B_r}{\partial z}-\frac{\partial B_z}{\partial r}\right) \tag{II-14}$$

The Lorentz force density is given by its two components in cylindrical coordinate system:

$$f_r= J_\theta\, B_z \tag{II-15}$$

$$f_z=-J_\theta\, B_r \tag{II-16}$$

where f_r is the radial component and f_z is the axial component. The corresponding magnetic pressures are evaluated by integration and are defined by:

$$P_r = \int_{z=0}^{z=h} f_r \, dz \tag{II-17}$$

$$P_z = \int_{z=0}^{z=h} f_z \, dz \tag{II-18}$$

where h is the thickness of the workpiece.

II.5. Finite difference model

Numerical techniques such as finite difference method can be used for the resolution of these equations for simpler geometries. This method is useful for simplifying the partial differential equations to a system of algebraic equations with the help of the initial and boundary conditions. Iterative calculations for the whole domain, already divided into small finite parts, give the solution for the equations under consideration. We decided to apply the finite difference approach for the resolution of the Maxwell's electromagnetic equations for the process of electromagnetic sheetmetal forming. At first, an explicit scheme of time derivative is used for the resolution [9]. Note that the finite difference model is presented for the case where the workpiece is a metal sheet.

II.5.1. Geometry discretization

The finite difference method used to solve these equations is based upon the construction of a grid by discretizing the workpiece into cells of size Δr & Δe to form a uniform grid. Here, Δr is the mesh increment in the radial direction, and the increment through the thickness of the workpiece is Δe. Fig. II-3 presents an example of the discretization of the geometry (in the case of EMF sheet process) for calculating the magnetic fields.

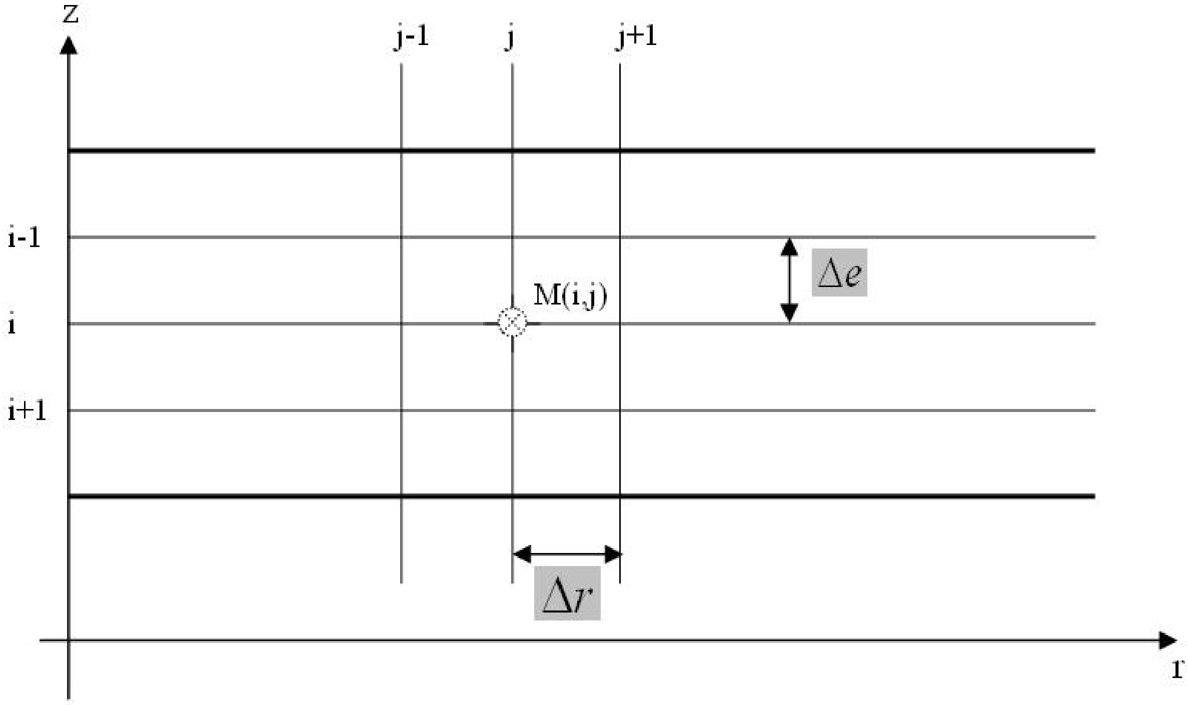

Figure II-3: Workpiece discretization.

The coordinates of a point *M (i,j)*, plotted in Fig. II-3, can be given as:

$$r(M(i,j)) = j\Delta r \tag{II-19}$$

$$z(M(i,j)) = i\Delta z = i\Delta e \tag{II-20}$$

where *i* and *j* are integers defined by

$$0 \le i \le m, 0 \le j \le n \begin{cases} n = R/_{\Delta r} \text{ (radius of the sheet R)} \\ m = e/_{\Delta z} = e/_{\Delta e} \text{ (thickness of the sheet e)} \end{cases} \tag{II-21}$$

II.5.2. Equations discretization

The partial differential expressions in Eq. II-11 and Eq. II-12 are written in the form of finite difference using the central difference with the increments **i (M (i, j))**, and **j (M (i, j))**, as shown in the Fig. II-3. Taking account of the discretization of the problem as shown in Fig. II-3, the partial derivatives with respect to *r* appearing in partial differential equations Eq. II-11 and Eq. II-12 are written as:

$$\frac{\partial^2}{\partial r^2}B_r \approx \frac{B_r\left(M_{i,j+1}\right)\text{-}2B_r\left(M_{i,j}\right)+B_r\left(M_{i,j\text{-}1}\right)}{\Delta r^2} \tag{II-22}$$

$$\text{i.e.}\ \frac{\partial^2}{\partial r^2}B_r \approx \frac{B_r\left(i,j+1\right)\text{-}2B_r\left(i,j\right)+B_r\left(i,j\text{-}1\right)}{\varDelta r^2} \tag{II-23}$$

and

$$\frac{\partial}{\partial r}B_r \approx \frac{B_r\left(i,j+1\right)\text{-}B_r\left(i,j\text{-}1\right)}{2\varDelta r} \tag{II-24}$$

$$\frac{B_r}{r^2} \approx \frac{B_r\left(i,j\right)}{j\left(\varDelta r\right)^2} \tag{II-25}$$

The derivatives with respect to *z*-coordinate are similarly constructed as in Eqs. II-22-and II-25. The partial derivatives with respect to *z* appearing in partial differential equations Eq. II-11 and Eq. II-12 are then written as follows:

$$\frac{\partial^2}{\partial z^2}B_r \approx \frac{B_r\left(M_{i+1,j}\right)\text{-}2B_r\left(M_{i,j}\right)+B_r\left(M_{i\text{-}1,j}\right)}{\varDelta e^2} \tag{II-26}$$

$$\text{i.e.}\ \frac{\partial^2}{\partial z^2}B_r \approx \frac{B_r\left(i+1,j\right)\text{-}2B_r\left(i,j\right)+B_r\left(i\text{-}1,j\right)}{\varDelta e^2} \tag{II-27}$$

and

$$\frac{\partial}{\partial z}B_r \approx \frac{B_r\left(i+1,j\right)\text{-}B_r\left(i\text{-}1,j\right)}{2\varDelta e} \tag{II-28}$$

The above equations describe the partial derivatives with respect to the cylindrical coordinates, while for the time derivative there are several possibilities to express in terms of central difference. In this work, we have decided to use the Euler backward explicit scheme given by:

$$\left(\frac{\partial B_r}{\partial t}\right)^{(k)} \approx \frac{B_r^{k+1}\left(i,j\right)+B_r^{k}\left(i,j\right)}{\Delta t} \tag{II-29}$$

where the exponent k is an increment of time. It has been noted that for the explicit scheme, the solution is not stable. It is necessary to determine the maximum time increment i.e. Δt, conversely the implicit scheme is unconditionally stable but the time for calculation is much longer than the explicit scheme. Nevertheless, we have chosen to use the explicit scheme. With the help of the Eq. II-29, and combining the above equations, we can rewrite Eqs. II-11, II-12 in the form of central difference by replacing the values:

$$\frac{1}{\mu_0\sigma_w}\left[\begin{array}{l} \dfrac{B_r^k(i,j+1)-2B_r^k(i,j)+B_r^k(i,j-1)}{\Delta r^2}+ \\ \dfrac{1}{j\Delta r}\dfrac{B_r^k(i,j+1)-B_r^k(i,j-1)}{2\Delta r}+ \\ \dfrac{B_r^k(i+1,j)-2B_r^k(i,j)+B_r^k(i-1,j)}{\Delta e^2}-\dfrac{B_r^k(i,j)}{j(\Delta r)^2} \end{array}\right]=\frac{B_r^{k+1}(i,j)-B_r^k(i,j)}{\Delta t} \tag{II-30}$$

and

$$\frac{1}{\mu_0\sigma_w}\left[\begin{array}{l} \dfrac{B_z^k(i,j+1)-2B_z^k(i,j)+B_z^k(i,j-1)}{\Delta r^2}+ \\ \dfrac{1}{j\Delta r}\dfrac{B_z^k(i,j+1)-B_z^k(i,j-1)}{2\Delta r}+ \\ \dfrac{B_z^k(i+1,j)-2B_z^k(i,j)+B_z^k(i-1,j)}{\Delta e^2} \end{array}\right]=\frac{B_z^{k+1}(i,j)-B_z^k(i,j)}{\Delta t} \tag{II-31}$$

Rewriting the above equations for *Br* and *Bz*, we can then obtain the two components of the magnetic field in cylindrical coordinate system:

$$\begin{aligned} B_r^{k+1}(i,j)=&\left[1-\frac{\Delta t}{\mu_0\sigma_w}\left(\frac{2}{\Delta r^2}+\frac{2}{\Delta e^2}+\frac{1}{(j\Delta r)^2}\right)\right]B_r^k(i,j)+ \\ &\frac{\Delta t}{\mu_0\sigma_w}\left[\frac{B_r^k(i,j+1)+B_r^k(i,j-1)}{\Delta r^2}\left(\frac{2j+1}{2j}\right)+\frac{B_r^k(i+1,j)+B_r^k(i-1,j)}{\Delta e^2}\right] \end{aligned} \tag{II-32}$$

and

$$B_z^{k+1}(i,j)=\left[1-\frac{\Delta t}{\mu_0\sigma_w}\left(\frac{2}{\Delta r^2}+\frac{2}{\Delta e^2}\right)\right]B_z^k(i,j)+$$
$$\frac{\Delta t}{\mu_0\sigma_w}\left[\frac{B_z^k(i,j+1)+B_z^k(i,j-1)}{\Delta r^2}\left(\frac{2j+1}{2j}\right)+\frac{B_z^k(i+1,j)+B_z^k(i-1,j)}{\Delta e^2}\right] \tag{II-33}$$

As mentioned above, for the explicit scheme of time derivative, it is necessary to find the maximum time increment such that the solution remains stable during the complete analysis. It is found that convergence of the solution is obtained if and only if the following condition is satisfied:

$$\Delta t<\mu_0\sigma_w\left[\left(\frac{2}{\Delta r^2}+\frac{2}{\Delta e^2}+\frac{1}{(j\Delta r)^2}\right)\right]^{-1} \tag{II-34}$$

To assure the convergence of the solution, we can take the maximum value of $j\Delta r$ which means $j\Delta r \simeq R$ the radius of the sheet. In an axi-symmetric model, the induced current has only the azimuthal component given by:

$$J_\theta=\frac{1}{\mu_0}\left(\frac{\partial B_r}{\partial z}-\frac{\partial B_z}{\partial r}\right) \tag{II-35}$$

where we can replace the values from the finite difference in the above equation to have:

$$J^k(i,j)=\frac{1}{\mu_0}\left(\frac{B_r^k(i+1,j)-B_r^k(i-1,j)}{2\Delta e}-\frac{B_z^k(i,j+1)-B_z^k(i,j-1)}{2\Delta r}\right) \tag{II-36}$$

Thus we can calculate the Lorentz force density. The radial component is expressed as:

$$F_r^k(i,j)=J^k(i,j)\ B_z \tag{II-37}$$

and the axial component:

$$F_z^k(i,j)=-\ J^k(i,j)\ B_r \tag{II-38}$$

According to the Eq. II-37 and Eq. II-38 at a constant current flowing through the coil the body force f is proportional to the electromagnetic field density acting at a definite part of the inductor (workpiece). And finally the magnetic pressure acting on the sheet can be estimated by the following equation:

$$
\begin{aligned}
P_r^k(i,j) &= \sum_{i=0}^{n-1}\left[\frac{F_r^k(i,j)+F_r^k(i+1,j)}{2}\Delta h\right] \\
P_z^k(i,j) &= \sum_{i=0}^{n-1}\left[\frac{F_z^k(i,j)+F_z^k(i+1,j)}{2}\Delta h\right]
\end{aligned}
\qquad \text{(II-39)}
$$

II.5.3. Boundary conditions discretization

Boundary conditions for Eq. II-11 and Eq. II-12 are based on the continuity of the magnetic flux density B at the boundaries of the sheet. At the bottom surface of the disk, the magnetic field B is a sum of the coil field B_0 and the magnetic field B_1 which is generated by the Eddy currents flowing through the sheet. At the top surface of the sheet, the magnetic field B is equal to zero. Fig. II-4 presents the details of the boundary conditions applied for the calculation of the magnetic fields:

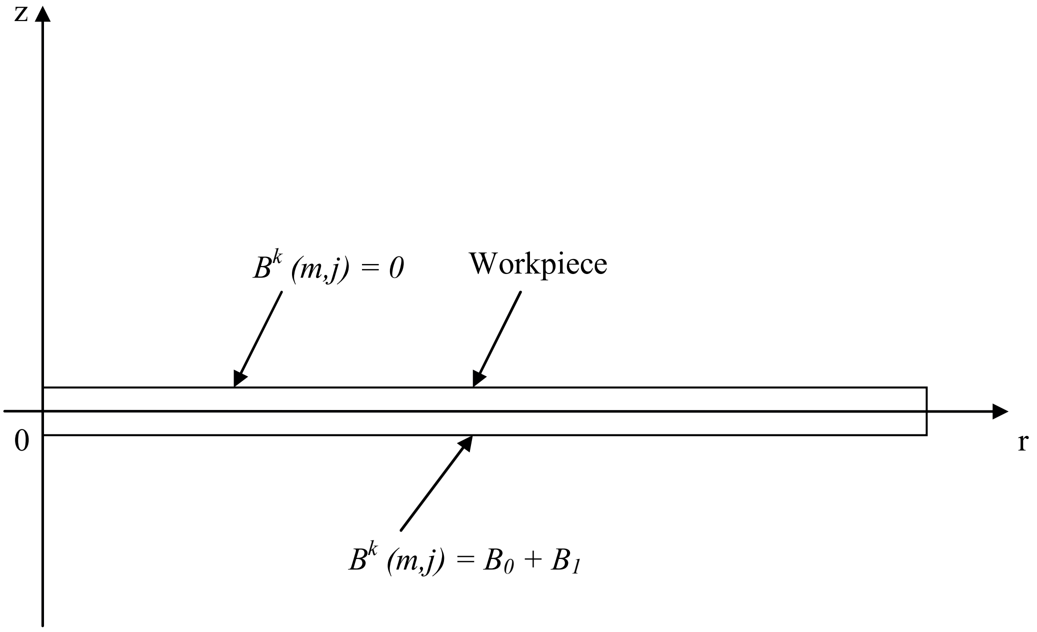

Figure II-4: Details of boundary conditions applied for the calculation of magnetic fields.

The boundary conditions can then be written as follows:

$$\begin{aligned} &B = B_0 + B_1 \text{ at } z = d_g + u_2(t) \\ &B = 0 \text{ at } z = d_g + u_2(t) + e \end{aligned} \tag{II-40}$$

where $u_2(t)$is the vertical deflection of the sheet and d_g the initial gap between the coil and the sheet. To calculate the magnetic fields B_0 and B_1, the workpiece and the coil have been divided in elementary circular loops. If the current $I(t)$ and the Eddy current J_θ are known, the magnetic fields B_0 and B_1 can be determined by summing the contributions of each elementary loop.

In agreement with the boundary conditions defined in Eq. II-40 and for any time step k, the boundary conditions are defined as follows:

$$\begin{cases} B_r^k(0,j) = B_{0r}^k(0,j) + B_{1r}^k(0,j) \\ B_z^k(0,j) = B_{0z}^k(0,j) + B_{1z}^k(0,j) \end{cases} \text{ at } \quad z = d_g + u_2(t) \tag{II-41}$$

and

$$\begin{cases} B_r^k(m,j) = 0 \\ B_z^k(m,j) = 0 \end{cases} \text{ at } \quad z = d_g + u_2(t) + e \tag{II-42}$$

For our case we have considered a few necessary assumptions for the calculation of the magnetic fields at the boundaries and the surfaces of the disc. First we defined that at the top surface of the disc the magnetic field is zero, this is in accordance with the fact that, due to the skin-depth effect, the penetration of the magnetic field is limited to skin thickness inside the disc. The skin-depth is sufficiently small as compared to the total thickness of the disc, such that the field is shielded and does not completely penetrate through the thickness.

Additionally boundary conditions have been applied. At the center and at the maximum radius of the sheet we have assumed that the magnetic fields have negligible effects. The following additional equations can then be written:

$$\begin{cases} B_r^k(i,0) = 0 \\ B_z^k(i,0) = 0 \end{cases} \text{ at } \quad r = 0 \tag{II-43}$$

and

$$\begin{cases} B_r^k(i,n)=0 \\ B_z^k(i,n)=0 \end{cases} \quad \text{at} \quad r=\frac{D}{2} \tag{II-44}$$

Moreover, the initial conditions are taken equal to:

$$\begin{cases} B_r^0(i,j)=0 \\ B_z^0(i,j)=0 \end{cases} \quad \text{at} \quad t=0 \tag{II-45}$$

II.5.4. Determination of magnetic fields B_0 and B_1

II.5.4.1. Determination of magnetic fields B_0

For the solution of the above equations the vector potential A_θ is used. It is assumed that the coil consists of a set of N elementary circular loops each carrying the discharge current flowing through it in a plane representing the coil. The vector potential A_θ developed due the circular loops may be obtained by using the Boit-Savart law. Cylindrical coordinates system has been applied for the definition of the vector potential [10]. It is given in terms of the current density and complete elliptical integrals defined for the coil geometry. The vector potential A_θ is given by:

$$A_\theta(r,z)=\frac{\mu_0}{2\pi}j(r_0,z_0)s_0\sqrt{\frac{r_0}{r}}\left[(2-g)K(g)-\frac{2}{g}E(g)\right] \tag{II-46}$$

where g is the geometrical factor with respect to the source point and target point (for this case the coil and the work piece) given by:

$$g^2=\frac{4r_0 r}{(r_0+r)^2+z^2} \tag{II-47}$$

It is worth mentioning that the product of current density $j(r_0,z_0)$ with the unit surface s_0 in Eq. II-46 is equal to the initial discharge current $I_0(t)$.

$$I(t) = j(r_0, z_0) \times s_0 \tag{II-48}$$

K(g) and *E(g)* are the complete elliptical integrals of the first and second kind respectively, r_0 is the radius of coil, r the point on workpiece where the magnetic potential is required to be calculated and z is the distance between the coil and workpiece. The coordinates of the source point are defined by (r_0, z_0). The coordinates of the target point, where the vector potential is needed to be calculated are defined by (r, z)We assumed that the flat spiral coil is composed of a number of principal concentric loops each with an increasing radial distance [11] from the centre of the coil as shown in Fig. II-5:

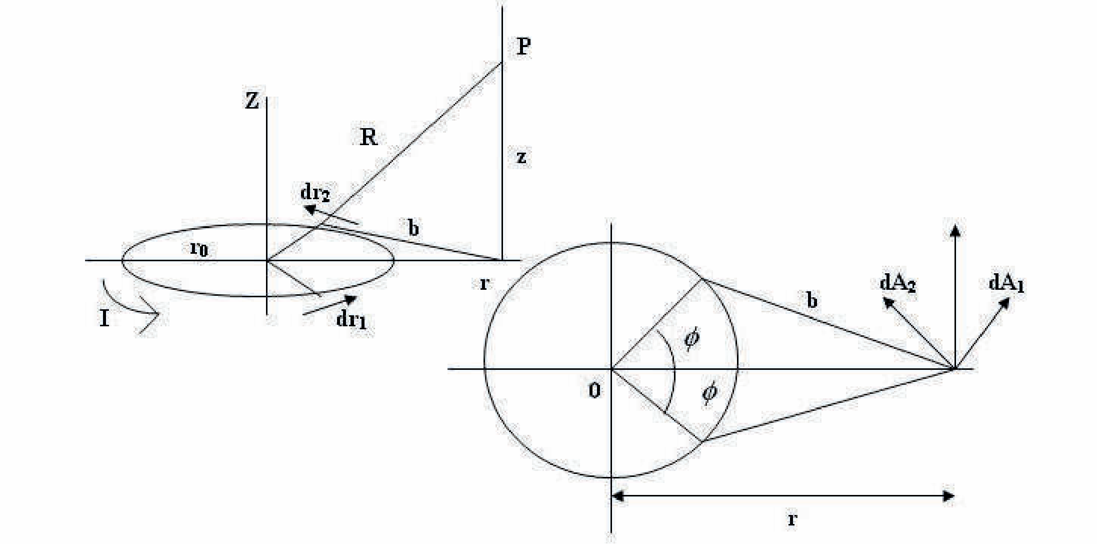

Figure II-5: Detail of the geometrical parameters for a principal loop of the spiral coil.

The magnetic field density B can be calculated using the magnetic vector potential A_θ:

$$\mathbf{B} = \mathbf{curl}(A_\theta) \tag{II-49}$$

In axi-symmetric condition, using the expansion of Eq. II-48 the magnetic field can be decomposed into a radial and an axial component. Using the expansion of the equation [8], the magnetic field can be decomposed into its radial Br and axial Bz components. In terms of the magnetic vector potential these components can be calculated using:

$$B_r = -\frac{\partial A_\theta}{\partial z} \tag{II-50}$$

$$B_z = \frac{A_\theta}{r} + \frac{\partial A_\theta}{\partial r} \tag{II-51}$$

By inserting the expression of magnetic potential A_θ from Eq. II-50 using the cylindrical coordinates *(r,z)* with respect to the elementary coil loop of radius *r* at point *P* at a distance *z* from the coil, the following expression for the radial and axial components of the magnetic field density are obtained using:

$$B_r = \frac{\mu_0}{2\pi} j\left(r_0,z_0\right) s_0 \frac{z}{r} \frac{1}{\left[\left(r_0+r\right)^2+z^2\right]^{\frac{1}{2}}} \left[E\left(g\right)\frac{r_0^{\,2}+r^2+z^2}{\left(r_0-r\right)^2+z^2} - K\left(g\right)\right] \qquad \text{(II-52)}$$

$$B_z = \frac{\mu_0}{2\pi} j\left(r_0,z_0\right) s_0 \frac{1}{\left[\left(r_0+r\right)^2+z^2\right]^{\frac{1}{2}}} \left[E\left(g\right)\frac{r_0^{\,2}-r^2-z^2}{\left(r_0-r\right)^2+z^2} + K\left(g\right)\right] \qquad \text{(II-53)}$$

II.5.4.2. Determination of magnetic fields B_1

As discussed above, it is necessary to calculate the magnetic fields from the coil and the field developed in the sheet due to the Eddy current. Details for the calculation of the magnetic field of the coil can be found above, while the similar method is applied for the calculating the induced magnetic field including modification with respect to the boundary conditions and geometrical requirements as shown in Fig. II-6:

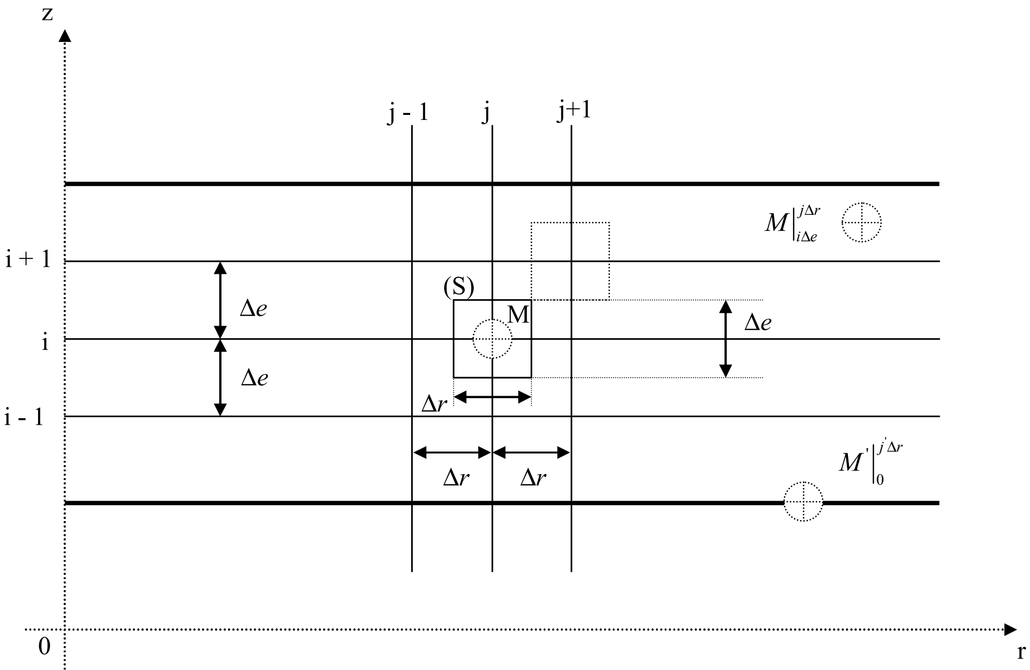

Figure II-6: Domain discretization for calculation of induced magnetic field.

To find the magnetic field developed due to the Eddy current, electromagnetic vector potential A_θ is applied from Eq. II-46. The calculation is similar to the one used for the calculation of the coil magnetic field with added modifications. We considered a differential surface *(S)* within the sheet.

$$S = \Delta e \, \Delta r \tag{II-54}$$

To find the value of the magnetic field for the time step *k*, we have to take the value of $J(i,j)$ for the preceding step *(k-1)*. The magnetic field produced B_1^k at a point $M'\left(j'\Delta r, 0\right)$ due to the induced current $J^{k-1}(i,j)$ which is flowing through the differential surface *(S)* at point $M\left(j\Delta r, i\Delta e\right)$ is given by using the following equations:

$$B_{r_1}^k(i,j) = \frac{\mu_0}{2\pi} J^{k-1}(i,j)\, \Delta e \Delta r \left(\frac{-i\Delta e}{j'\Delta r}\right) \frac{1}{\left[\left(j\Delta r + j'\Delta r\right)^2 + \left(-i\Delta e\right)^2\right]^{1/2}} \left[E(g)\frac{\left(j\Delta r\right)^2 + \left(j'\Delta r\right)^2 + \left(-i\Delta e\right)^2}{\left(j\Delta r - j'\Delta r\right)^2 + \left(-i\Delta e\right)^2} - K(g)\right] \tag{II-55}$$

and

$$B_{z_1}^k(i,j) = \frac{\mu_0}{2\pi} J^{k-1}(i,j)\, \Delta e \Delta r \frac{1}{\left[\left(j\Delta r + j'\Delta r\right)^2 + \left(-i\Delta e\right)^2\right]^{1/2}} \left[E(g)\frac{\left(j\Delta r\right)^2 - \left(j'\Delta r\right)^2 - \left(-i\Delta e\right)^2}{\left(j\Delta r - j'\Delta r\right)^2 + \left(-i\Delta e\right)^2} + K(g)\right] \tag{II-56}$$

For calculating the elliptic integrals *E(g)* and *K(g),* we redefined the geometrical factor *g* given as:

$$g=\left[\frac{4(j\Delta r)(j'\Delta r)}{(j\Delta r+j'\Delta r)^2+(-i\Delta e)^2}\right]^{\frac{1}{2}} \tag{II-57}$$

Then we have to consider all the points *M (i,j)* (for $1 \leq i \leq m$ and $1 \leq j \leq n$). The total magnetic field B_1, is the sum of the all the dB_1 at *M'*.

II.6. Validation of the finite difference model

II.6.1. Comparison with experimental results

We can now focus on the validation of the numerical model of the electromagnetic forming processes. This preliminary test of the numerical model provides a check on the accuracy of the results obtained through the in-house finite difference code. At first, the numerical analysis is employed to model the electromagnetic problem when the workpiece is not considered. Afterwards, we carried out another simple test when the flat workpiece is considered to be fixed at its end i.e. at rest. The geometry of the tests is inspired by the experiments of Takatsu *et al.* [1]. The experimental apparatus is plotted in Fig II-7.

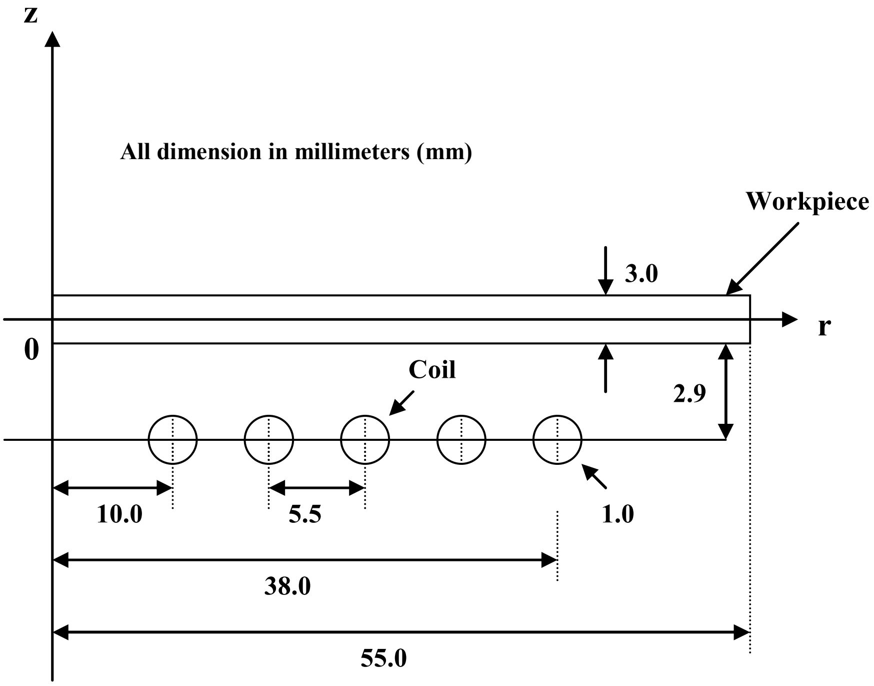

Figure II-7: Model of the free forming process using flat spiral coil.

The experimental setup used by Takatsu *et al.* [1] is summarized in Table II-1. The dimensions of the flat spiral coil, of the workpiece and the physical parameters of materials are also presented in Table II-1. The initial gap d_g between the sheet and the coil has been taken equal to *2.9 mm*. The workpiece is an aluminium alloy of *3 mm* thickness. The diameter of the workpiece used is *110 mm*.

Table [II-1]: Material and geometrical properties of the system

Coil	
No. of windings N	5
Material	Copper
Maximum radius of ring of coil	1 mm
Maximum radius of spiral coil	40 mm
Pitch	5.5 mm
Circuit capacitance C_o	40 µF
Electrical conductivity σ_{Cu}	58 MS/m
Workpiece	
Material	Aluminium alloy Al 1050
Thickness h_o	3 mm
Diameter	110 mm
Electrical conductivity σ_{Al}	36 MS/m
Air	
Electrical conductivity	0 MS/m

Takatsu *et al.* [1] performed their tests with a *5 turn* flat spiral coil connected to a capacitor bank of *40 µF*, with total inductance of *2.86 µH* and total circuit resistance of *28.5 mΩ*. The initial charging voltage of the capacitor bank is equal to *2 kV*. The frequency and the discharge current are calculated using the characteristics of the electric circuit and its parameters. Neglecting the variations of the mutual inductance during the forming operation, the discharged current $I_1(t)$ flowing in the flat spiral coil is approximately described by the following equation:

$$I_1(t)=I_0\, e^{-t/\tau} \sin \omega t \tag{II-58}$$

where I_0 represents the maximum intensity of the discharge current, τ the damping coefficient of the circuit, it characterises the decreasing exponential of the current, ω the angular frequency. The maximum intensity of the discharge current I_0 is given as:

$$I_0 = V_0 \sqrt{\frac{C_0}{L}} \tag{II-59}$$

where V_0 represents the charging input voltage, L the total inductance of the circuit, and C_0 the total capacitance of the circuit. The damping coefficient τ is obtained using:

$$\tau = \frac{2L}{R} \tag{II-60}$$

Depending on the values of the circuit elements and parameters, both currents $I_1(t)$ and $I_2(t)$ may be under-damped, critically damped or over-damped. This is why their shapes and specific time intervals are important for the electromagnetic forming process. Details of the effects of the discharge current frequency are discussed in the next chapter. The electrical energy stored in the capacitor bank for the electromagnetic forming process is given by:

$$E = \frac{1}{2} C_0 V_0{}^2 \tag{II-61}$$

For the initial charging voltage V_0 of 2 kV, the values of circuit parameters have then been calculated: $I_0 = 7.48\ kA$, $\omega = 9.34$ x $10^4\ rad/s$ and $\tau = 2.42$ x $10^{-4}\ s$. Using the parameters mentioned above, the evolution of the intensity of the discharge current, for the initial charging voltage of $2\ kV$, flowing through the coil is presented in Fig. II-8. For the EMF process the primary circuit discharge current is a damped harmonic sinusoidal function. The peak value of the current occurs during the first half cycle. The discharge current reaches its first positive peak, almost $17.5\ \mu s$. The current subsequently is damped to much lower values. This indicates that the effects of the mutual inductance between the workpiece and the coil current last for a very small interval. This strengthens our assumption for the constant inductance, the effects of the mutual inductance may be considered to be of very minute in nature, and the deformation of the workpiece takes place mostly because of the inertial forces and high deformation velocities.

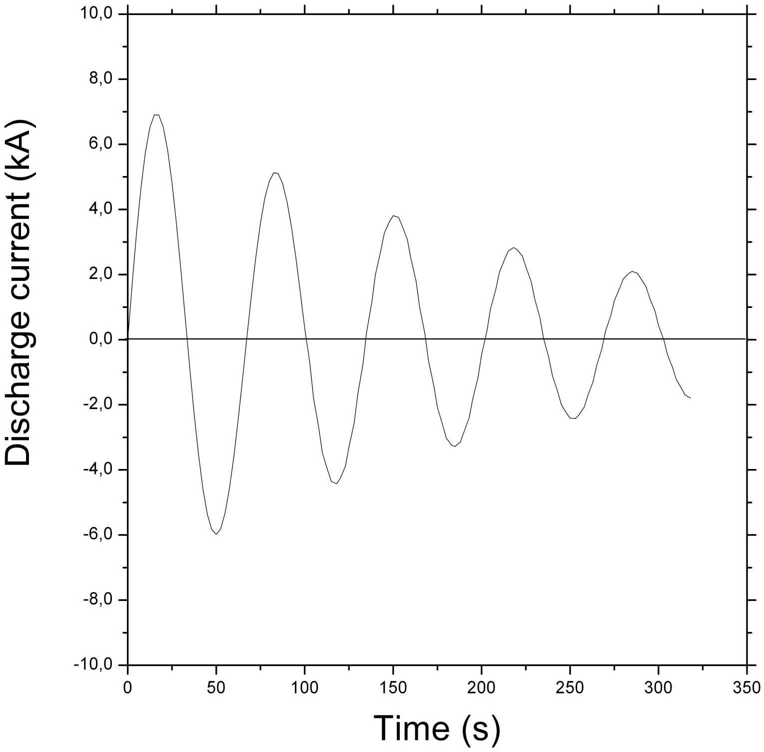

Figure II-8: Evolution of the intensity of the discharge current flowing through the flat spiral coil.

The workpiece is divided in *110* equally spaced intervals along the radius and *20* equally spaced intervals through the thickness. This meshing is applied such that *Δt* gives the stable numerical analysis and the convergence of the solution is obtained. The total time of calculation is *270 μs*. Fig. II-9a presents the distribution of the magnetic field (the axial component B_z and the radial component B_r) in the absence of the workpiece for the first half cycle of the discharge current at *17.5 μs* where the current attains its maximum magnitude. Afterwards the distribution of the magnetic field with a fixed workpiece is plotted in Fig. II-9b for the first half cycle of the discharge current at *17.5 μs* where the current attains its maximum magnitude. In Fig. 9 solid lines are numerical results while the scattered symbols are the experimental results taken from Takatsu *et al.* [1].

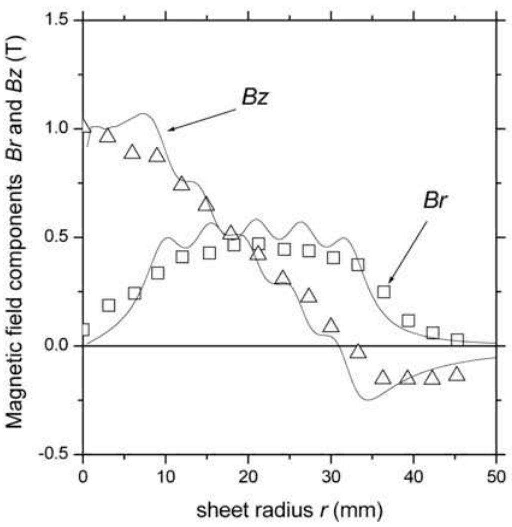

(a)

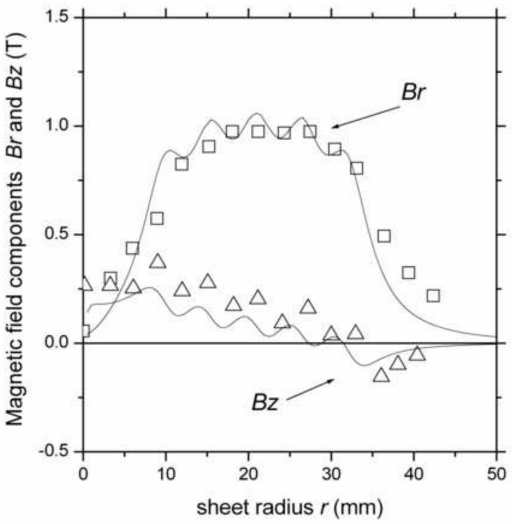

(b)

Figure II-9: Radial distribution of the magnetic field B:
(a) without a workpiece and (b) with a fixed aluminium workpiece.

In Fig. II-9 it can be noted that the magnitude of the radial component of the magnetic field is much larger than the magnitude of the axial component. As computed from Eq. II-15 it is concluded that the axial component of the electromagnetic force density f_z contributes mainly in the deformation of the workpiece. In Fig. II-10 solid lines are numerical results while the scattered symbols are the experimental results taken from Takatsu *et al.* [1]. The numerical predictions obtained with our finite difference code are in a sufficiently good agreement with the available experimental results [1]. The distribution of the axial magnetic force density f_z is presented in Fig. II-10. A slight overestimation of the axial magnetic force density f_z is observed, in Fig. II-10, for a time value equal to *13.2 μs*. However we can conclude that the numerical predictions are in agreement with the results of Takatsu *et al.* [1].

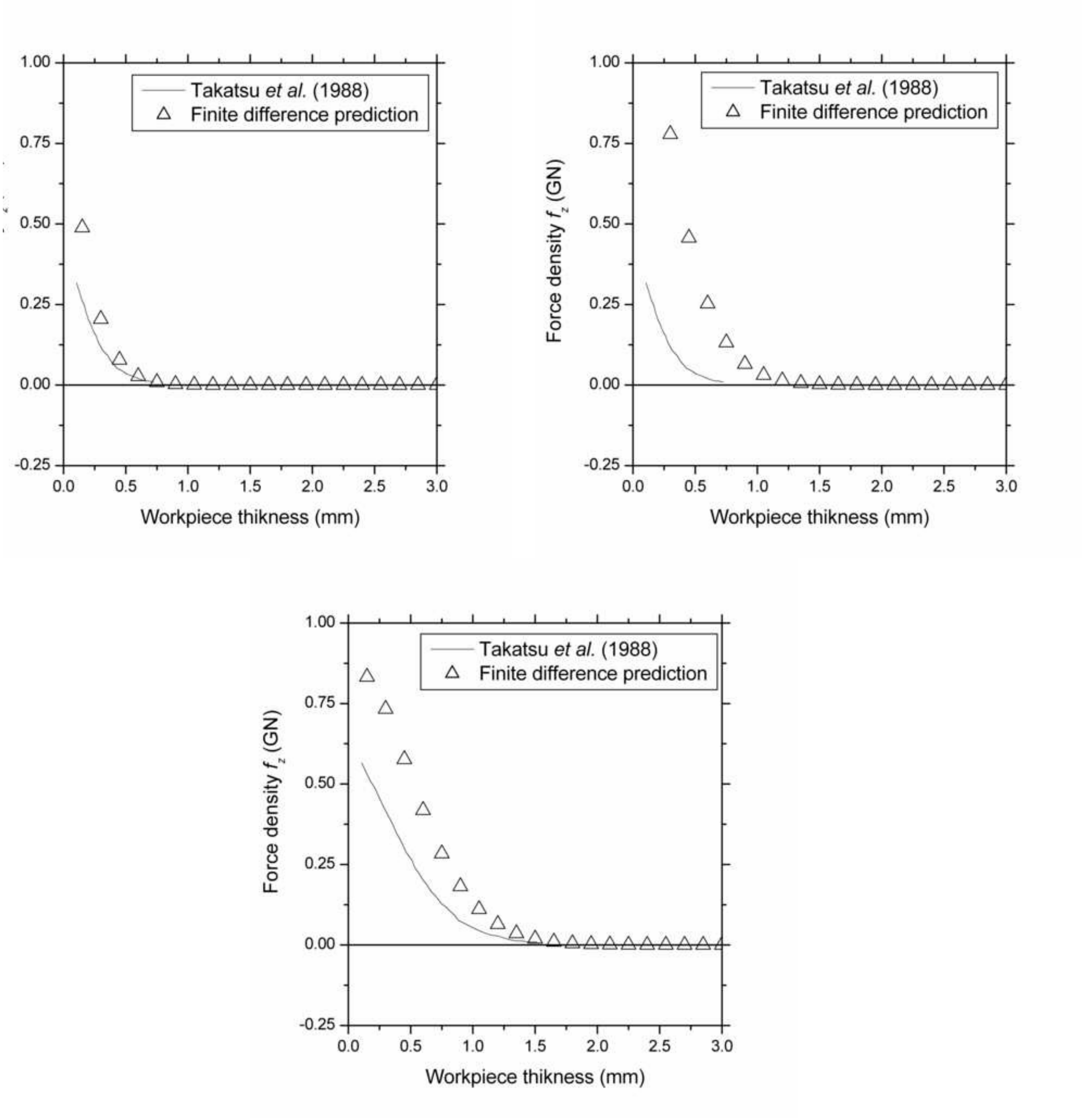

Figure II-10: Magnetic force density fz distribution inside the aluminium workpiece at: (a) 6.8μs, (b) 13.2μs and (c) 19.6μs.

To understand the penetration of the axial force density f_z in the workpiece thickness during the electromagnetic process, we have plotted in Fig. II-11 the spatial distribution (in the plane (r, z)) of the axial force density f_z. It is noticeable that the magnitude of the axial force gradually increases as the current reaches its maximum and then it is diffused through the thickness with decreasing magnitudes. The force achieves its high magnitude near the bottom surface of the disk, and then gradually distributes. Consequently, the skin-depth effect is noticeable through the thickness of the workpiece [11]. After the peak current, the force density decreases near the bottom surface of the disk but still remains constant inside the workpiece during a few microseconds. With the decrease of the current, the force density decreases as the time elapses.

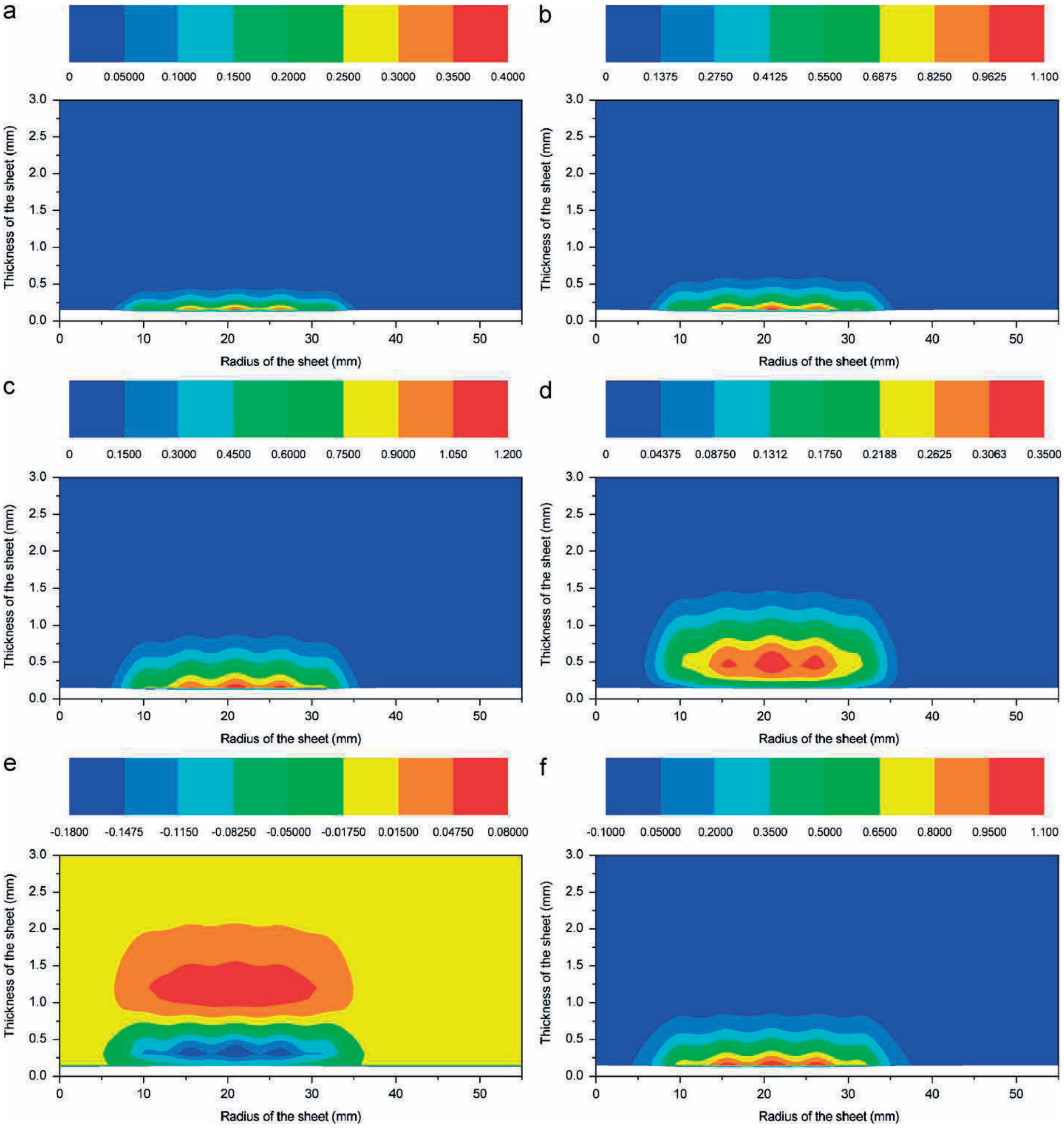

Figure II-11: Diffusion of axial force density (GN) in the plane (r, z) as function of time: (a) at t = 5 µs, (b) at t = 10 µs, (c) at t = 17.5 µs, (d) at t = 25 µs, (e) at t = 35 µs and (f) at t = 50 µs.

Our finite difference code predicted accurately the electromagnetic phenomena occurring during an EMF process. The comparison of experimental results with our numerical predictions has provided satisfactory good agreement.

II.6.2. Comparison with FEMM

For the validation of the results obtained through the finite difference programme, we have used FEMM [2]. The advantage of this software is that it resolves simultaneously the corresponding Maxwell’s equations related to the electromagnetism phenomena and works on a single meshing. FEMM [2] is an open source suite of programmes for solving low frequency electromagnetic problems on two-dimensional planar and axisymmetric domains. It is a simple, accurate, and low computational cost product, popular in science, engineering, and education. The programme currently addresses linear/nonlinear magnetostatic problems, linear/nonlinear time-harmonic magnetic problems, linear electrostatic problems, and steady-state heat flow problems. Magnetostatic problems are problems in which the fields are time-invariant. FEMM [2] addresses some limiting cases of Maxwell’s equations. The magnetic problems addressed are those that can be considered as “low frequency problems,” in which displacement currents can be ignored. FEMM [2] goes about finding a field that satisfies the Maxwell’s equations via a magnetic vector potential approach. The advantage of using the vector potential formulation is that all the conditions needed to be satisfied, have been combined into a single equation. The algorithm applied for the FEMM [2] simulations is presented in the Fig. II-12.

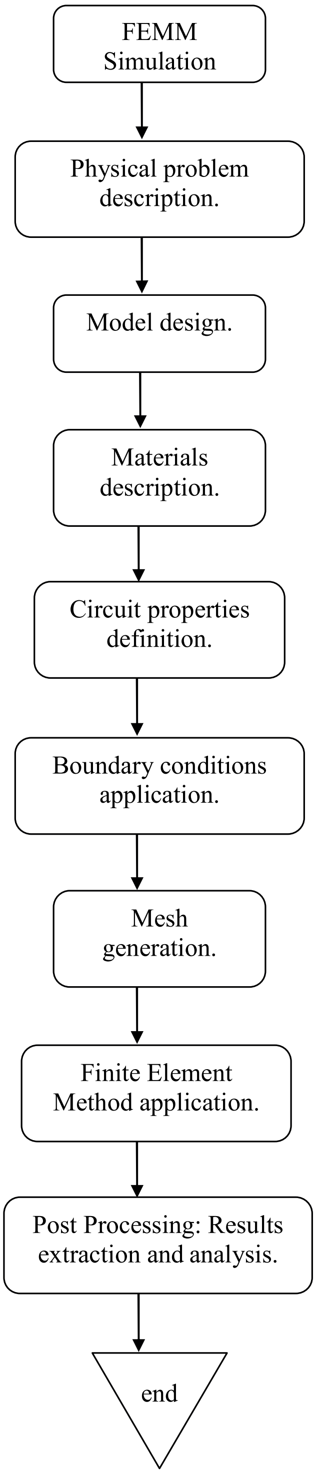

Figure II-12: Flowchart of FEMM modelling.

The simulations were carried out with the experimental conditions presented in Takatsu *et al.* [1]. The experimental setup is composed of a circular aluminium disc *AA-1050* sheet of *110 mm* diameter and *3.0 mm* thickness. The sheet is placed above a flat spiral copper coil of maximum radius *40 mm*. The distance between the disc and the coil is *2.9 mm*. The coil discharge current is measured using analytical parameters same as that used in the finite difference electromagnetic problem. At the maximum peak value of the current presented in Fig. II-8, the current has a frequency of *14.88* x 10^3 *Hz*. According to the symmetry of the coil and the disc, only half of the region is included in the analysis i.e an axi symmetric model with axis of symmetry about the *z-axis*. The region around the disc and coil is considered as air, the radius of the coil rings is assumed to be *1 mm*. The finite element model of the electromagnetic forming process is presented in Fig. II-13a. FE mesh is shown in Fig. II-13b, where the near-field air region is also presented with finer meshing. The near-field air is also meshed with equilateral triangular elements in order to propagate the magnetic field generated by the coil. Fine meshing is used for the region (air) in the vicinity of the coil and disc called as the near-field air region, where a coarse meshing is applied to the region in the far-field air [2]. The work piece and the coil wires are meshed using triangular elements. The FEMM mesh divisions are shown in the Fig. II-13b. There are *1100437* elements and *551504* nodes in total for the whole model used for simulations. Fig. II-13 shows the mesh lines for the different areas of numerical model. The coil and the workpiece region are concentrated with higher density of elements to help to maintain good grid resolution for current density calculations.

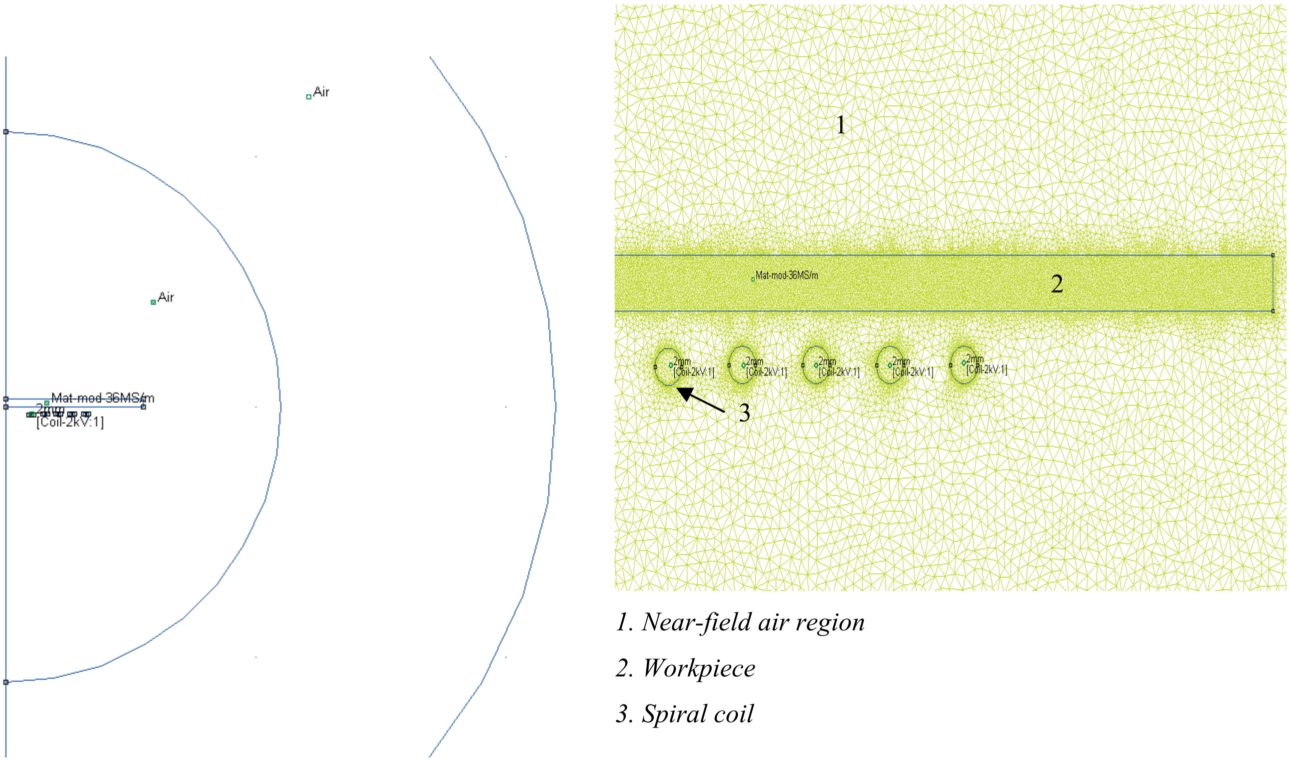

1. Near-field air region

2. Workpiece

3. Spiral coil

(a) *(b)*

Figure II-13: FEMM analyses (a) Model and (b) meshing of the model with flat spiral coil.

Asymptotic boundary conditions, as presented in the FEMM [2] for air, are applied in the near-field and far-field regions. This boundary condition approximates the impedance of an unbounded open space. In this way we can model the field of the coil in an unbounded space while still only modelling a finite region of that space [2]. Because of the axi-symmetric model, the nodes at the axis of symmetry (at $r = 0$) are restricted to zero-potential boundary condition [2]. Fig. II-14 shows distribution of magnetic field obtained from the simulation at time $17.5\ \mu s$, where the current reaches its peak value. The penetration of the electromagnetic field into the workpiece can be observed. Here we observe that the magnetic field has not leaked through the thickness of the workpiece, which justifies the phenomenon of the skin-depth and skin effect during the electromagnetic forming process.

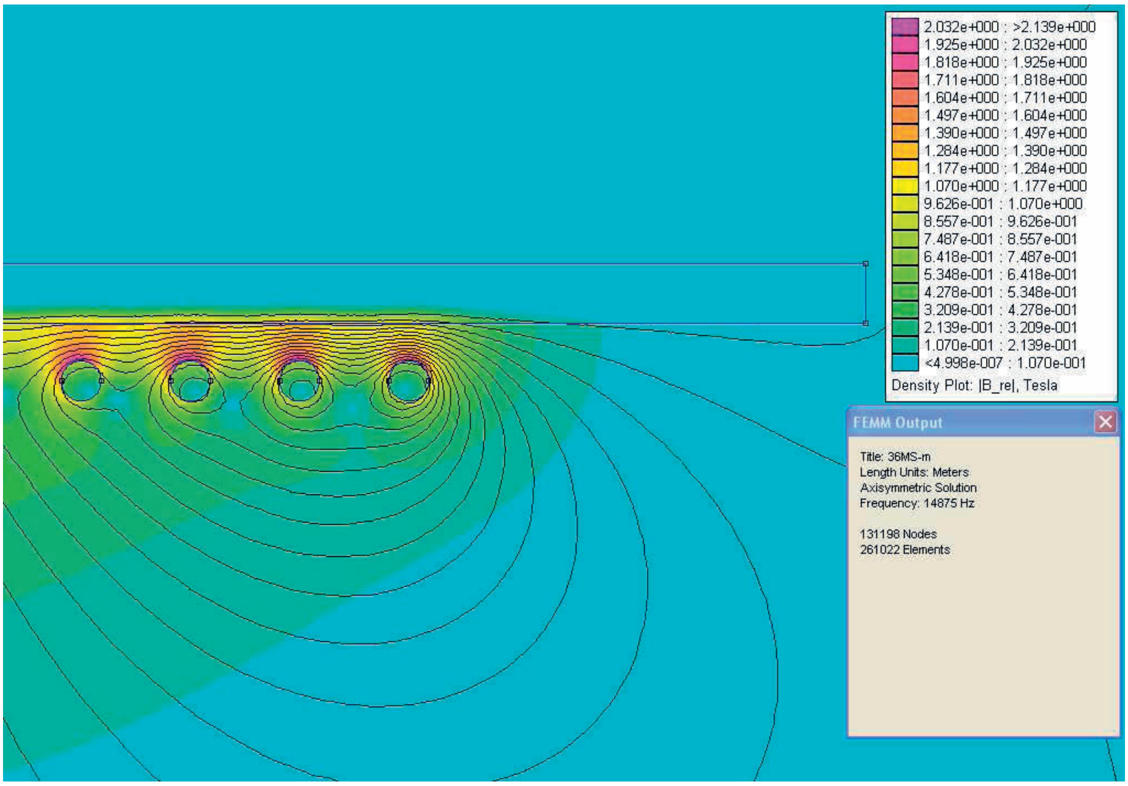

```
Title: 36MS-m
Length Units: Meters
Axisymmetric Solution
Frequency: 14875 Hz

131198 Nodes
261022 Elements
```

Figure II-14: Distribution of magnetic field B at time 17.5 µs.

The FEMM prediction for the radial distribution of the magnetic field B is compared to the experimental results from Takatsu *et al.* [1] and to the in-house code predictions. The radial distribution of the magnetic field components are presented in Fig. II-15.

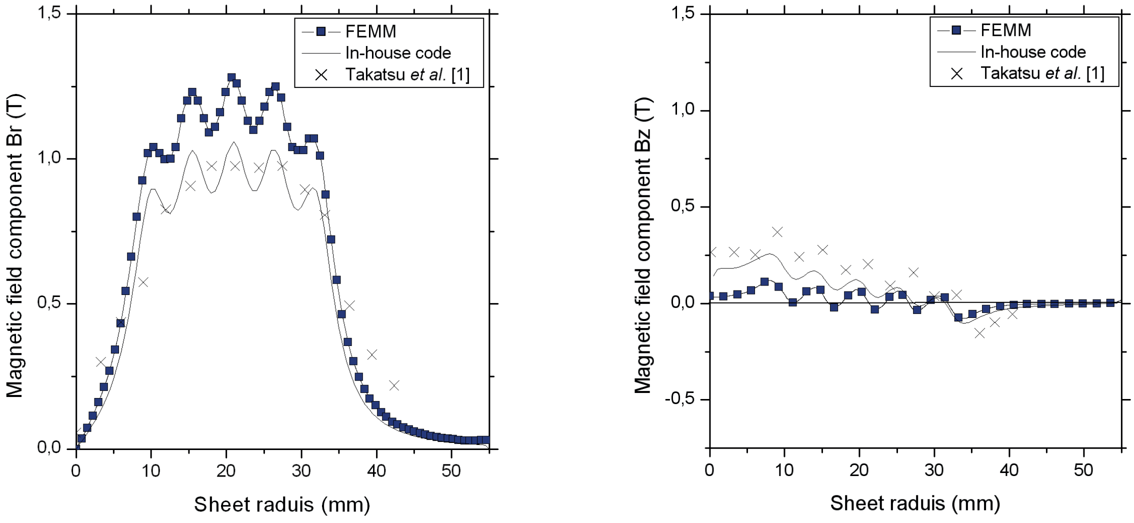

(a) *(b)*

Figure II-15: Comparison between experimental and numerical distribution of electromagnetic field (a) Radial component B_r (b) axial component B_z.

It is observed in the Fig. II-15a that there exists a slight difference between the results from the FEMM and finite difference code. The results obtained from the in-house finite difference code are in better agreement with the experimental results from Takatsu *et al.* [1] than FEMM predictions. The comparison between the experimental results and simulations for the axial component B_z of the electromagnetic field is presented in the Fig. II-15b. It is observed that the magnitude of the axial component of B is much weaker than the radial component. The radial component of magnetic field density governs the forming process, resulting in axial electromagnetic force acting on the workpiece. The results obtained from the in-house finite difference code are in fairly good agreement both from the point of view of experimental comparison and their validation with FEMM simulations.

II.7. Influence of numerical parameters

Finite difference methods for solving differential equations are principally based on the numerical parameters and the techniques generally applied [12]. We mentioned earlier in this chapter that the explicit integration scheme, used for the resolution of Maxwell's equation is stable if the time increment verifies Eq. II-34. Therefore, we carried out a parametric study of the effects of the numerical parameters on the predictions of the finite difference code. In this parametric analysis, we studied the influence of mesh size as well as the effect of time increment.

II.7.1. Influence of mesh size

The influence of the workpiece dicretization is studied with a number of different combinations of radial increments *n* and through thickness increments *m*. In the axiymmetric model, the thickness of the workpiece used for the preliminary calculation is *3.0 mm*, while the radius is *55 mm*. In Table II-2, different combinations of workpiece meshing applied for the finite difference calculations are presented. The values of the maximum stable time increment Eq. II-34 are also presented.

Table [II-2]: Combination of workpiece meshing in finite difference code

Through thickness increment ***m***, Radial increment ***n*** ***m*** x ***n***	$\Delta r = R/n$	$\Delta e = e/m$	$\mu_0\sigma_w\left[\left(\frac{2}{\Delta r^2}+\frac{2}{\Delta e^2}+\frac{1}{(j\Delta r)^2}\right)\right]^{-1}$
4 x 110	5.00 E-04	7.50E-04	3.9148E-06
6 x 110	5.00 E-04	5.00E-04	2.82737E-06
10 x 110	5.00 E-04	3.00E-04	1.49686E-06
20 x 110	5.00 E-04	1.50E-04	4.66914E-07
6 x 220	2.50 E-04	5.00E-04	1.13096E-06
10 x 220	2.50 E-04	3.00E-04	8.3432E-07
20 x 220	2.50 E-04	1.50E-04	3.74218E-07

The value of the maximum stable time increment (Eq. II-34), is greater than *1* x *-7 s*, thus for investigating the effects of the workpiece meshing, we use a time increment $\Delta t = 1 \times 10^{-7}\ s$.

Fig. II-16, shows the comparison between different combinations of workpiece meshing applied during the finite difference calculations. The comparison is based on a constant number of elements through the thickness of the workpiece, while the number of elements is increased for the radial length. We observed that, as the explicit integration scheme remains stable during the various combinations applied for the analyses, the distribution of the electromagnetic field densities are not influenced by mesh sizes.

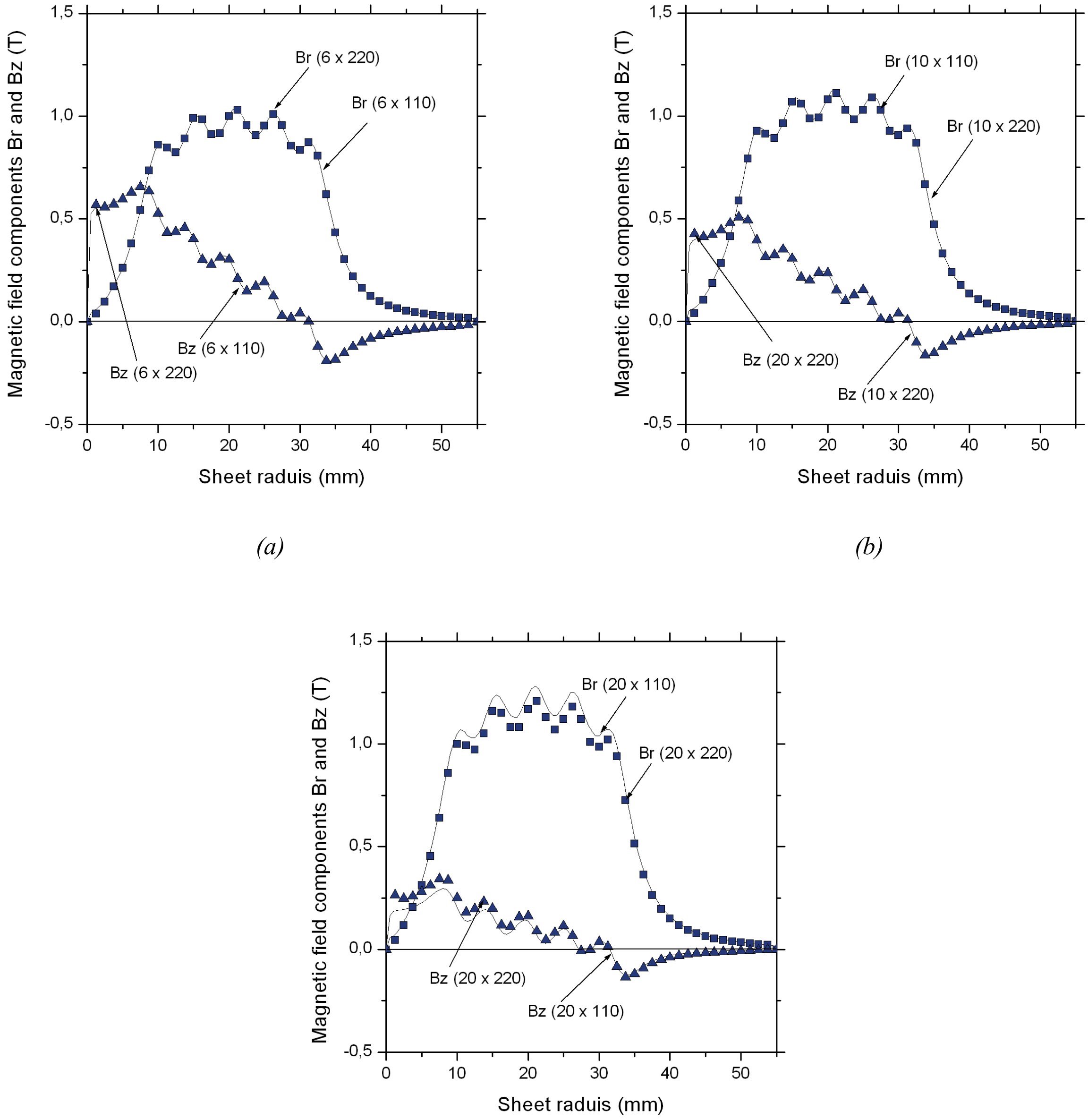

(a) *(b)*

(c)

Figure II-16: Comparison for radial distribution of magnetic field for different combination of workpiece. meshing used in finite difference code (a) 6 x *110 & 6* x *220 (b) 10* x *110 &10* x *220 (c) 20* x *110 & 20* x *220.*

The comparison of the radial component of the magnetic field density B_r is shown in Fig. II-17. The number of elements applied for the radial length of the workpiece is kept constant, while the meshing is altered through thickness. We compared the distribution of radial component of the magnetic field. The numerical predictions for the workpiece meshing are compared with the experimental results obtained from Takatsu *et al.* [1].

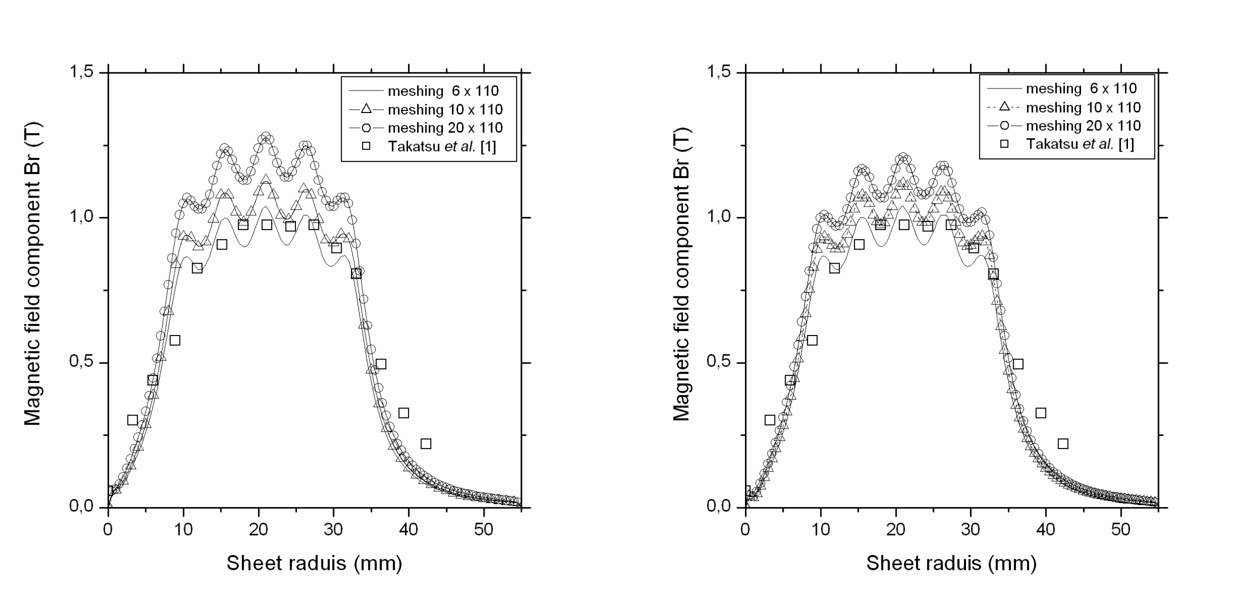

(a) *(b)*

Figure II-17: Comparison between experimental and numerical distribution of electromagnetic field for effects of workpiece meshing (radial meshing) (a) 110 elements, (b) 220 elements.

In Fig. II-17, the predictions of the magnetic field density are in agreement with the experimental results [1]. However the increase of mesh density in thickness direction induces a slight increase of the radial component of magnetic field density. We plotted the distribution of radial force component for the different meshing. The penetration of the radial force density at a position of *20 mm* (position on workpiece where the maximum magnetic pressure has been observed) from the centre of the workpiece is presented in Fig. II-18.

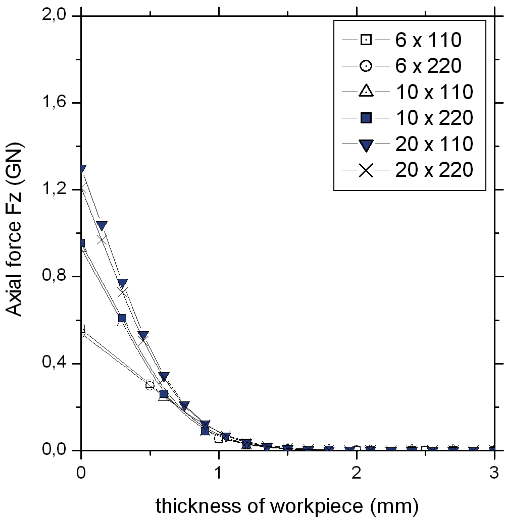

Figure II-18: Axial force density Fz distribution through thickness for different workpiece meshing.

Regardless of the very small difference of the distribution of the magnetic field density, there exists a difference between the penetrations of the axial force through thickness for the different combination of meshing applied. We observed from Fig. II-15 to Fig. II-18 that the magnitude of the magnetic field density is altered due to the increase in the number of element through the thickness of the workpiece. Optimization of the mesh used for the numerical calculations seems very important in order to correctly and accurately predict the experimental trends. A coarse mesh (*4* or *6* elements through the sheet thickness) seems to be sufficient to correctly predict the radial component of the magnetic flux and then the axial component of the Lorentz force density.

II.7.2. Effects of time increment Δt

Time increment is considered to be very important for the numerical resolution of finite difference problems in the explicit time integration scheme. The stability and the convergence depend mainly on the time increment applied for the analysis. If the time increment condition is not satisfied (Eq. II-34), the numerical solution may not converge and will not be stable. Two different time increments were applied to study the influence of the time step on the finite difference explicit integration scheme used for the electromagnetic problem i.e. $dt = 1 \times 10^{-7}\ s$ and $dt = 1 \times 10^{-9}\ s$. We compared the results obtained for the different combinations of the workpiece meshing with the two time increments. The results are presented in Fig. II-19:

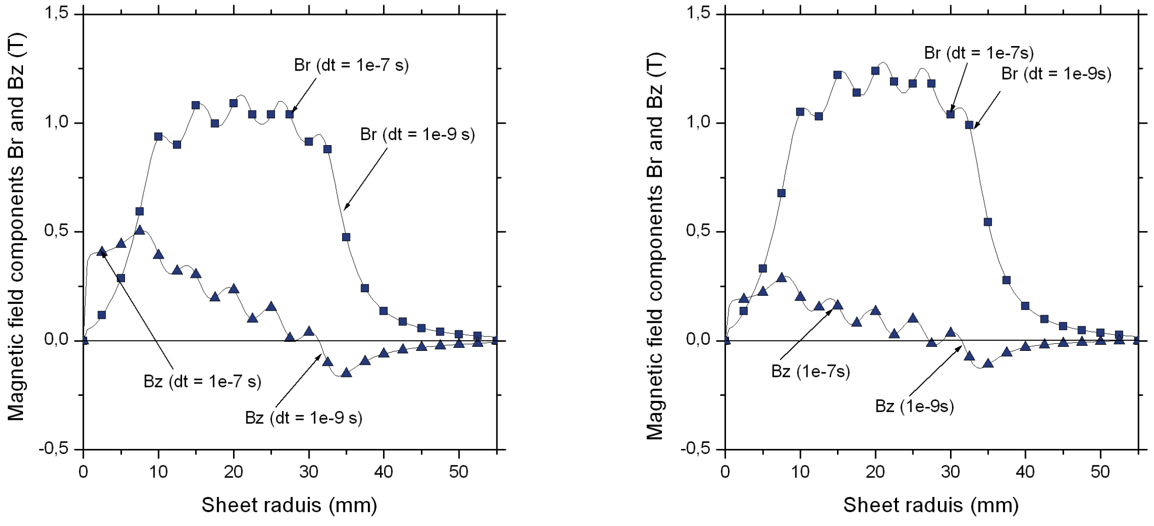

(a)

(b)

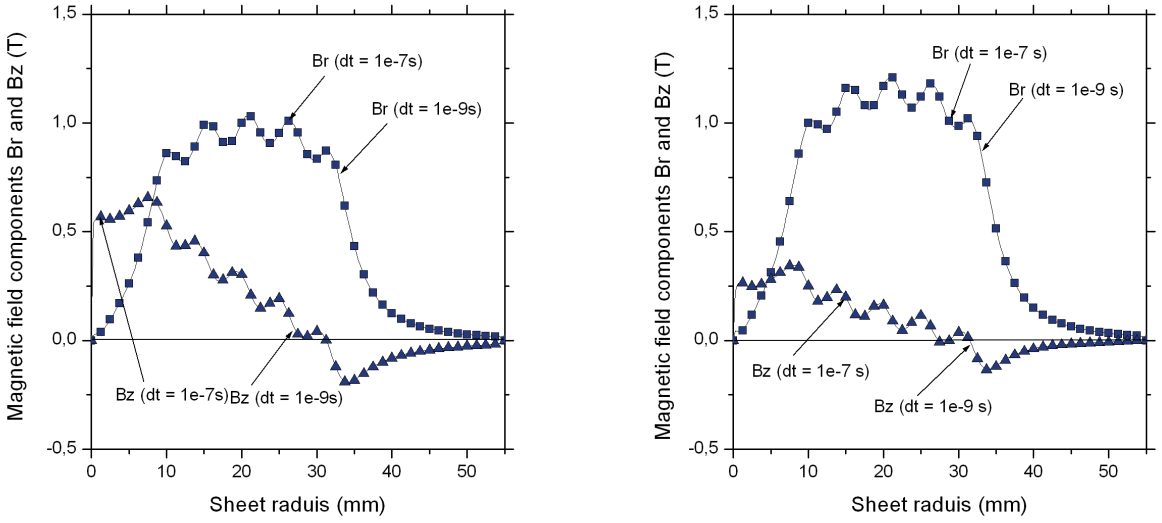

(c) *(d)*

Figure II-19: Comparison for radial distribution of magnetic field for different time increments used in finite difference code (a) 10 x *110 (b) 20* x *110 (c) 6* x *220 (d) 20* x *220.*

As shown in Fig. II-19, the effects of the time increments are found to be very small, for each combination of the workpiece meshing. The comparison of the penetration of the axial force calculated for the two increments and for different meshes is presented in Fig. II-20. The predicted radial component of the magnetic flux seems not to be affected by the value of time increment. Consequently the penetration of the axial force does not vary to a great extent with different time steps applied for the calculations. Finally, the time increment *Δt* has a weak influence on the finite difference predictions.

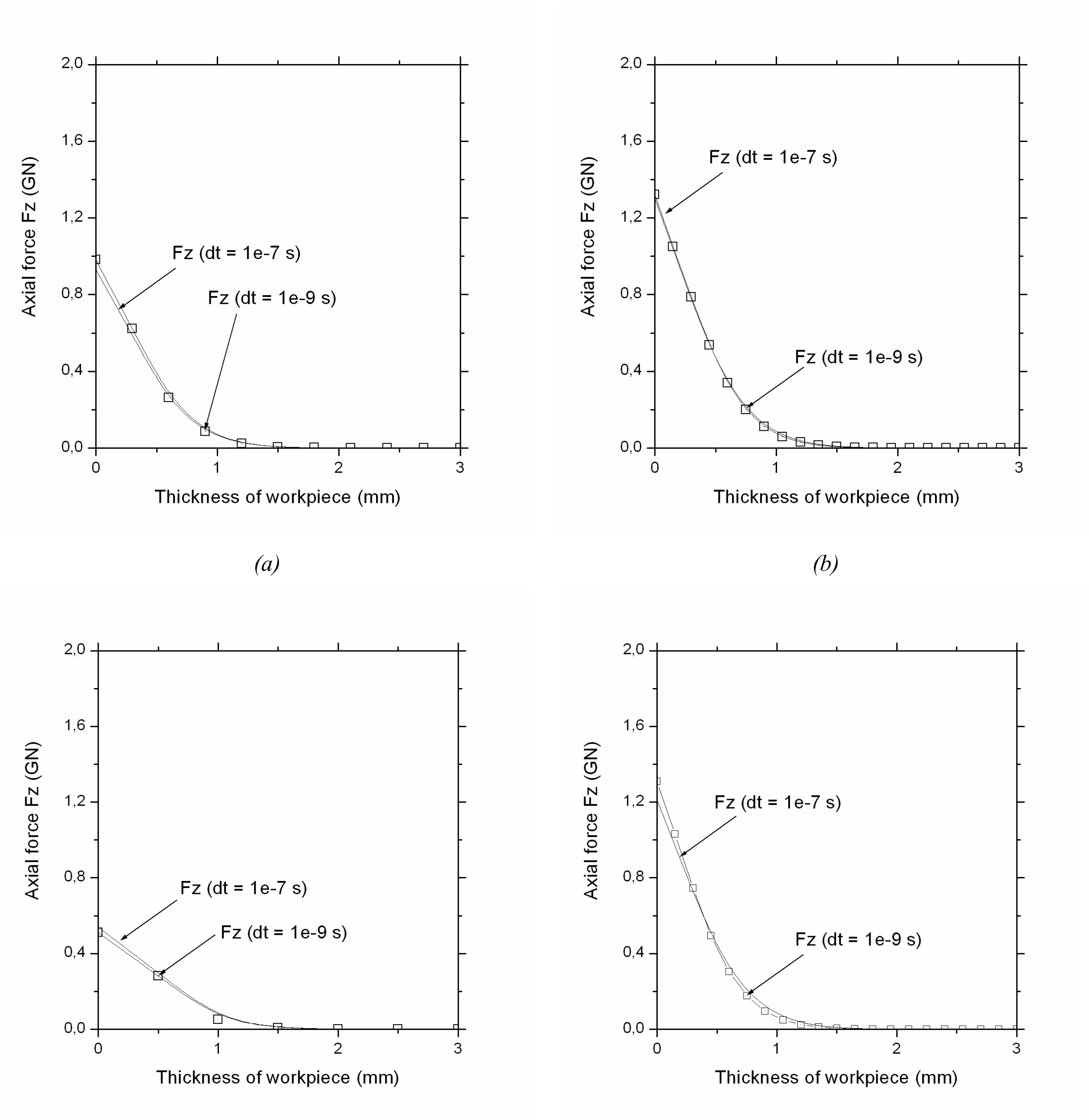

(a) *(b)*

(c) *(d)*

Figure II-20: Comparison of axial force density Fz distribution through thickness different (a) 10 x *110 (b) 20* x *110 (c) 6* x *220 (d) 10* x *220.*

Here, hollow square symbols represent $dt = 1 \times 10^{-9}\ s$, while corresponding lines are for $dt = 1 \times 10^{-7}\ s$. Little variation is observed from the point of view of changing time increments.

Conclusion

In this chapter we have developed an analytical and a numerical tool which can accurately calculate the basic parameters such as electromagnetic field density, electromagnetic force distribution and coil discharge current which are necessary for the understanding of the electromagnetic forming process. The developed in-house code is based on hypotheses that the magnetostatic Maxwell's equations can be applied to the electromagnetic problem for electromagnetic forming process. An explicit finite difference scheme has been used to solve the set of partial differential equations derived from the Maxwell's equation. The in-house code has been used to simulate the experiments proposed by Takatsu *et al.* [1]. Propagation of magnetic field through the workpiece and the diffusion of the magnetic forces into the sheet are presented. The predicted results are in agreement with the experimental ones available in the literature (Takatsu *et al.* [1]). The numerical results also showed that, in both cases, the electromagnetic force density decays rapidly in time and space. The results have demonstrated that the electromagnetic volume force is concentrated near the lower interface, thus near the surface closest to the forming coil. Finite element simulations of the experiments proposed by Takatsu *et al*. [1] have also been performed with the free software FEMM [2]. The finite difference predictions are in agreement with FEMM predictions. Efficiency of the calculation code based on finite difference method is demonstrated with sufficient coherence between the FEMM predictions and the experimental results found in literature [1].

A parametric study to investigate the effects of mesh size and the influence of time increment is also carried out. These analyses provide an insight on the influence of workpiece discretization on the stability of the finite difference programme. The distribution of the electromagnetic field distribution was also examined with different workpiece meshings. It is found that the workpiece meshing has a weak influence on the distribution of magnetic field, if the condition of convergence and stability for time increment are satisfied. Furthermore, the effects of the time increment on the finite difference predictions have been studied and lead to a conclusion that the value of time increment does not affect the numerical predictions. After the validation and verification of our in-house code, developed for the resolution of the electromagnetic problem, we can now proceed to its applications: electromagnetic sheet and tube forming.

References

[1] Takatsu N., Kato M., Sato K., Tobe T., High speed forming of metal sheets by electromagnetic forces, *International Journal of Japanese Society for Mechanical Engineering* 1980*; 60*; pp. 142-148.

[2] FEMM4.0, http://femm.foster-miller.net/wiki/HomePage (April 2009).

[3] Jablonski J. and Wrinkler R., Analysis of the electromagnetic forming process, *International Journal of mechanical sciences 20* (1978); pp.315-325.

[4] Resnick R., Halliday D., Electricité et magnétisme, Traduit par Lebel A., Thériault C., Physique 2, John Wiley & Sons, INC 1960.

[5] Manea T.E., Verweij, M.D., Blok, H., The importance of velocity term in the electromagnetic forming process, *Proceedings of 27th General Assembly of the International Union of Radio Science*, URSI 2002, Maastricht; pp. 112-115.

[6] Haiping Y.U., Chunfeng L.I., Effects of current frequency on electromagnetic tube compression, *Journal of Material Processing Technology 209* (2009). pp. 1053-1059.

[7] Al-Hassani S.T.S, Magnetic pressure distribution in the sheet metal forming, *Electrical Methods of Machining, Forming and Coating*, Institute of Electrical Engineering Conference, publication no 1975, pp. 1-10.

[8] Mamalis A.G., Manolakos, D.E., Kladas, A.G., Koumoutsos, A.K., Electromagnetic forming and powder processing: Trends and developments, *Applied Mechanics Review* 2004, 57; pp. 299-32

[9] J.P.M. Correia, M.A. Siddiqui, S. Ahzi, S. Belouettar and R. Davies, A simple model to simulate electromagnetic sheet free bulging process, *International Journal of Mechanical Sciences 50* (2008), pp.1466–1475.

[10] Craik, D., Magnetism: Principles and Applications, NY: Wiley, **1995**.

[11] BENDJIMA B., FELIACHI M. *Finite element analysis of transient phenomena in electromagnetic forming system.* Laboratoire de Recherche en Techniques Inductive, France, 1996.

[12] Euvrard D., Résolution numérique des équations aux dérivées partielles, Edition Marson, 1994.

Chapter III

Finite element implementation and application of the EMF Numerical model

Chapter III: Finite element implementation and application of the EMF Numerical model

III.1. Introduction

As discussed earlier, EMF is a complex process involving plastic deformation of a workpiece resulting from the electromagnetic field interactions. Numerical simulations offer better understanding of physics and behaviour of EMF process. It then allows optimising and predicting the parameters necessary for forming a part (sheet or tube) and thus improving the efficiency of the process. Our aim is to develop a simple but accurate numerical model that can simulate a sheet or a tube EMF process. The electromagnetic problem of EMF process has been solved in the previous chapter; subsequently, we can now proceed to model the mechanical problem. We have chosen to develop a finite element (called in the following FE) model to solve the mechanical problem occurring during an EMF process. The FE has been performed with the commercial FE code ABAQUS/Explicit [1]. The FE model developed herein is coupled with the in-house finite difference. In this chapter the implementation of the in-house finite difference code (developed in the earlier chapter) into a FE model is first presented for two geometries: a disc sheet and a tube. Then the application of the FE model for flat sheet forming is presented. Afterwards the FE model for tube forming is presented. Numerical study on both compression and expansion of radial tubes is carried out. The numerical results obtained are compared with the experimental and numerical ones available in literature [2, 3, 4].

III.2. Implementation of in-house finite difference code in ABAQUS

In this study we consider the electromagnetic and the mechanical aspect of an EMF process as two independent problems. The finite difference method has been employed to solve the electromagnetic equations. The pressure acting on the sheet due to the Lorentz forces is estimated, while neglecting the influence of the sheet velocity on the magnetic field. Then it has been treated as a load in the mechanical problem. In order to simulate the mechanical problem occurring during an EMF process, we have decided to use the commercial FE code ABAQUS/Explicit [1]. The magnetic problem is solved with the in-house finite difference code presented in the previous chapter. The in-house finite difference programme is then rewritten in the form of a user-defined subroutine VDLAOD. In ABAQUS, the user-defined subroutine VDLOAD is used to describe the variation of the magnitude of the distributed load and pressure as a function of position, time, velocity, etc. for a group of points, each of which appears in an element-based or surface-based non-uniform load definition. The in-house finite difference programme is hence modified to incorporate these changes to conform to the VDLAOD requirements that includes the definition of the variables (for calculating electromagnetic pressure), the number of elements (mesh definition), the step time (value of time since the step began), the current coordinates of each point for which the load (electromagnetic pressure) is to be calculated. At the beginning of a time step of the workpiece deformation, the deformed geometry is recorded in the in-house finite difference code. Next the discharged current flowing through the coil $I_1(t)$ is calculated; and the magnetic field density within the workpiece is computed Eq. II-11 and Eq. II-12. Then the Eddy current, the body forces and the magnetic pressures are calculated Eq. II-17 to II-18. Finally, the pressure calculated is applied as a distributed mechanical load on the lower surface of the workpiece to calculate the new workpiece deformation. The schematic flow chart of the implemented algorithm is illustrated in the Fig. III-1

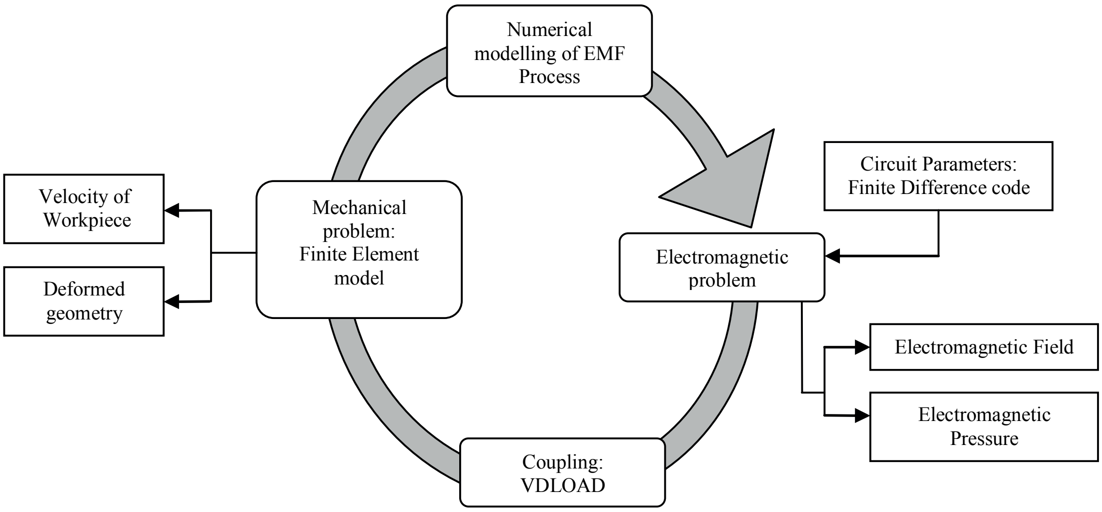

Figure III-1: Schematic representation of the integration of the in-house finite difference in the commercial FE code ABAQUS/Explicit.

III.3. EMF applications and results

III.3.1. Electromagnetic circular flat sheet forming process

III.3.1.1. FE Model

Experiments carried out by Takatsu *et al*. [2] were used as a reference for validation purposes of the proposed model. Takatsu *et al.* [2] have proposed an electromagnetic free bulging sheet test. The experimental setup used in [2] is presented in Fig. III-2.

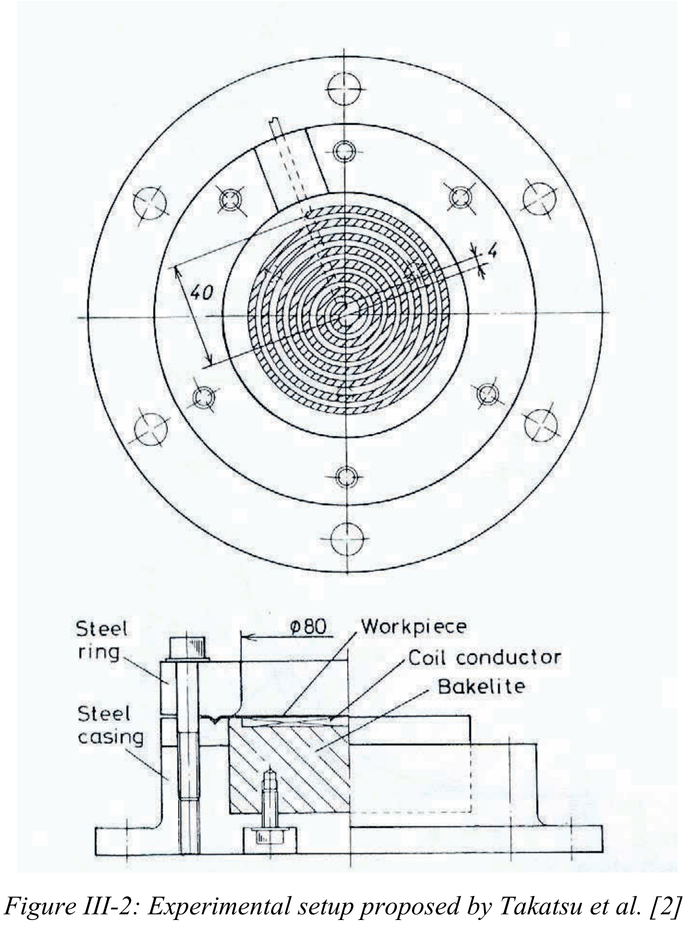

Figure III-2: Experimental setup proposed by Takatsu et al. [2].

Takatsu *et al.* [2] used a circular flat sheet of annealed aluminium alloy *JIS A1050* of *110 mm* diameter with *0.5 mm* thickness. The blank holder has an internal diameter of *80 mm*. The coil employed is a pancake single layer copper coil, with *5* turns having an effective diameter of *80 mm* with a *5.5 mm* pitch. Takatsu *et al.* [2] performed their tests with flat spiral coil connected to a capacitor bank of *40 μF*, with total inductance of *2.86 μH* and total circuit resistance of *28.5 mΩ.* For the experiments, the initial charging voltage of the capacitor bank is now equal to *6 kV*. The initial gap *dg* between the sheet and the coil has been taken equal *1.6 mm*. The evolution of the discharge current Eq. II-57 is presented in Fig. III-3.

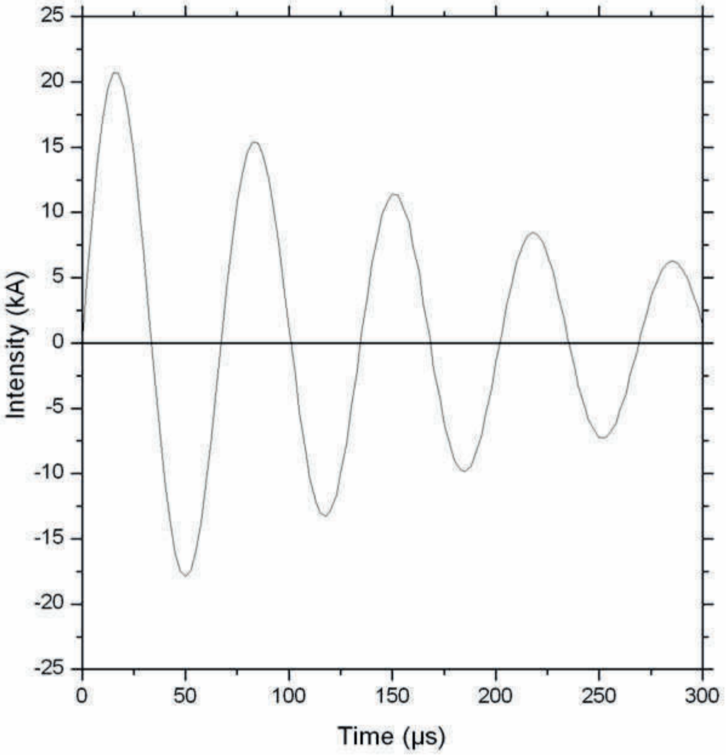

Figure III-3: Evolution of the intensity of the discharge current at 6 kV flowing through the flat spiral coil.

Due to the symmetry of the process, the finite element simulations were conducted with an axisymmetric assumption with *z-axis* as the axis of symmetry. This simplification is used because of the symmetrical distribution of forces and reduces the computing cost without affecting the results, yet providing very accurate and efficient numerical predictions. The geometry of the FE model is presented in Fig. III-4.

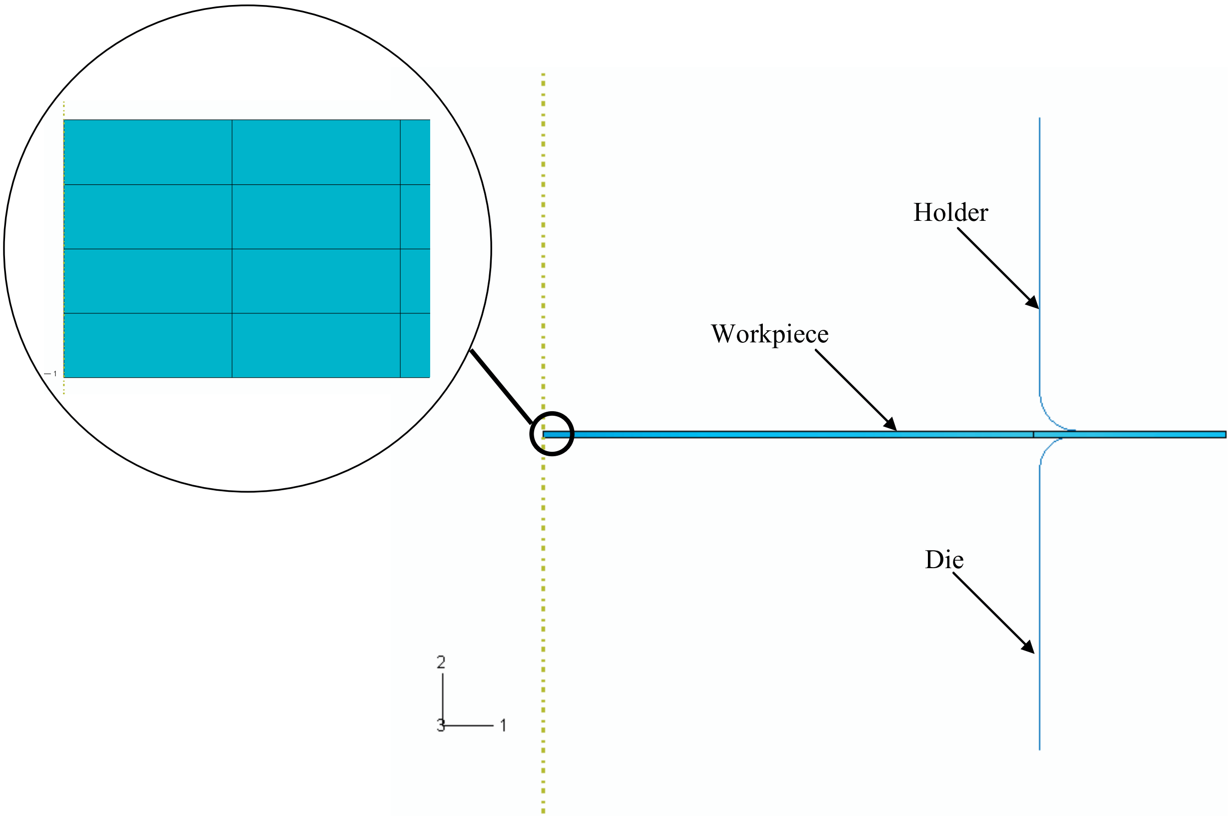

Figure III-4: Geometry of the FE model in ABAQUS for electromagnetic free bulging sheet test.

In the present FE model, the sheet is considered as a deformable axisymmetric planar part while the die and holder are modelled using analytical rigid elements (*R3D4* in ABAQUS Reference manuals [1]). The sheet was meshed with *CAX4R* elements [1] which is a four node bilinear axisymmetric quadrilateral element with reduced integration. The thickness of the workpiece is equal to *0.5 mm*, therefore, we used four elements through the sheet thickness. Along the radial length of the sheet we created a partition in order to correctly apply the magnetic pressure generated by the discharging coil. Since the coil maximum effective diameter is *80 mm*, the partition on the deformable workpiece is created at *40 mm* from the centre. A total *170* elements are applied along the radial length of the workpiece in the FE model. A dynamic explicit time integration scheme (ABAQUS/Explicit) is employed. The simulation process time is fixed to $270\,\mu s$ in agreement with the experiments [2]. In the simulations, contact conditions are needed to be considered between the die and the sheet as well as between the sheet and the holder. Coulomb friction law has been used with a friction coefficient of *0.25*. The geometrical parameters used for FE simulations are summarized in Table III-1.

Table [III-1]: Material and geometrical properties of electromagnetic free bulging sheet test.

Coil	
No. of windings N	5
Material	Copper
Maximum radius of ring of coil	1 mm
Maximum radius of spiral coil	40 mm
Pitch	5.5 mm
Circuit capacitance C_o	40 µF
Electrical conductivity σ_{Cu}	58 MS/m
Workpiece	
Material	Aluminium alloy Al 1050
Thickness h_o	0.5 mm
Diameter	110 mm
Electrical conductivity σ_{Al}	36.0 MS/m
Density	2.75 10^3 kg/m^3
Young’s Modulus	80.7 GPa
Poisson’s ratio	0.33
Material constant σ_0	118 MPa
Hardening exponent n	0.27
Holder	
Diameter (internal)	80 mm

The magnetic pressure, computed from the finite difference code is implemented as a mechanical pressure via the user-defined subroutine VDLOAD in the commercial FE code ABAQUS/Explicit. The magnetic pressure acts on the lower surface of the sheet in the upwards direction, for the free bulging of the sheet. The action of the magnetic pressure is adapted at each time increment to the new position of the workpiece structure and its currents node locations. We also incorporated the effect of downwards gravitational acceleration to conform to the real forming process. The upper and lower blank holders are considered to be fixed during the forming process. We considered a gap of *1 µm* between the upper blank holder and the workpiece.

It is well known that the fundamental constitutive behaviour (stress, strain, strain-rate relations) for most metals changes qualitatively at high strain rates. Above these strain rates, the apparent strain rate sensitivity of the material increases markedly. To better understand the high speed forming process and to account for the rate dependent dynamic phenomenon; different material model were employed. In order to compare the sheet behaviour during the EMF process, a quasi-static hardening model of Hollomon type power law was used into ABAQUS/Explicit calculations. The classical Hollomon's law is expressed as:

$$\sigma = \sigma_0 \left(\varepsilon^p\right)^n \tag{III-1}$$

where σ is the effective stress, ε^p the effective plastic strain, σ_0 and n are material constants. The hardening exponent n is taken equal to *0.27* and the material constant σ_0 equal to *118 MPa*. The values of the hardening exponent n and of the material constant σ_0 have been taken equal to those used by Takatsu *et al.* [2]. With this set of values, the rate-dependant hardening power law reproduces appreciatively the behaviour of the hardening law used by Takatsu *et al.* [2]. Fig. III-5 presents the comparison between the logarithmic law used by Takatsu *et al.* [2] and the classical Hollomon hardening law.

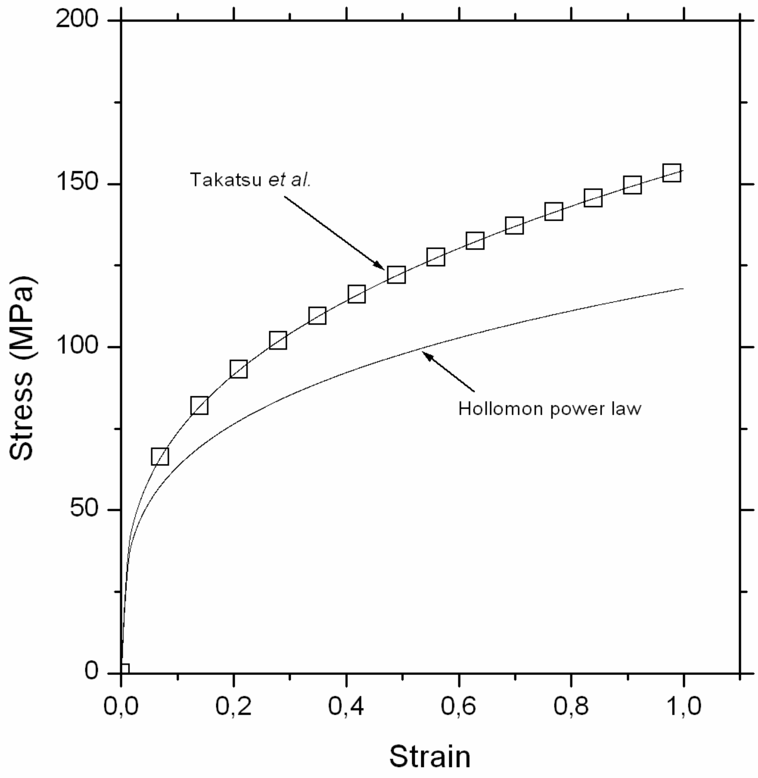

Figure III-5: Comparison between logarithmic law used by Takatsu et al. [2] and the Hollomon power law for hardening.

III.3.1.2. Results

For all of the processes, the velocity of the sheet has been first analysed in order to ascertain the assumption accounted for the calculation of the magnetic forces based on the work of Manea *et al.* [5]. The maximum velocity attained during the forming process is of the order of *100-150 m/s* as shown in Fig. III-6, which is in agreement with the experimental observations of Manea *et al.* [5]. The numerically predicted velocity of the workpiece can be rendered as a high velocity as compared to the velocity reached during quasi-static conventional forming processes. But still found to be small enough to fulfil the assumption that the sheet velocity does not affect the magnitude of the electromagnetic field density during the forming process (in agreement with Manea *et al.* [5] sheet velocity $v < 10^7$ *m/s*).

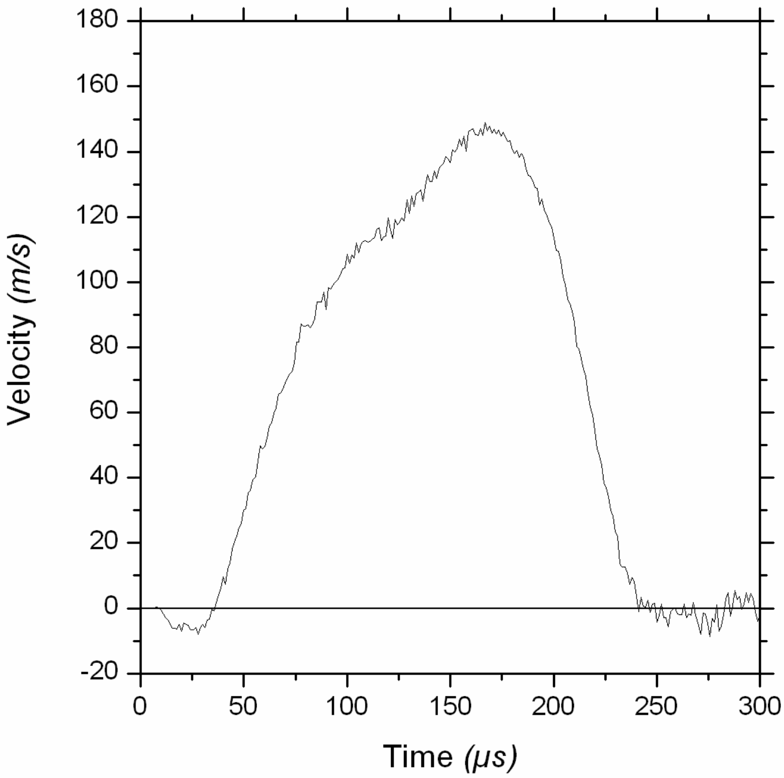

Figure III-6: FE predictions of vertical velocity of the centre of the workpiece as a function of time.

The principal assumption is verified. We can now proceed to the comparison with the experimental results [2]. Fig. III-7 presents the deformed mesh (for a *180°* revolution of the axisymmetric model) of the workpiece at different time values and for the rate independent hardening law Eq. III-1. The deformed meshes computed with ABAQUS/Explicit reproduce qualitatively the high speed photographs of the deformed sheet realized by Takatsu *et al.* [2]. The predictions obtained are consistent with experimental results of the deformation of the workpiece during the forming process.

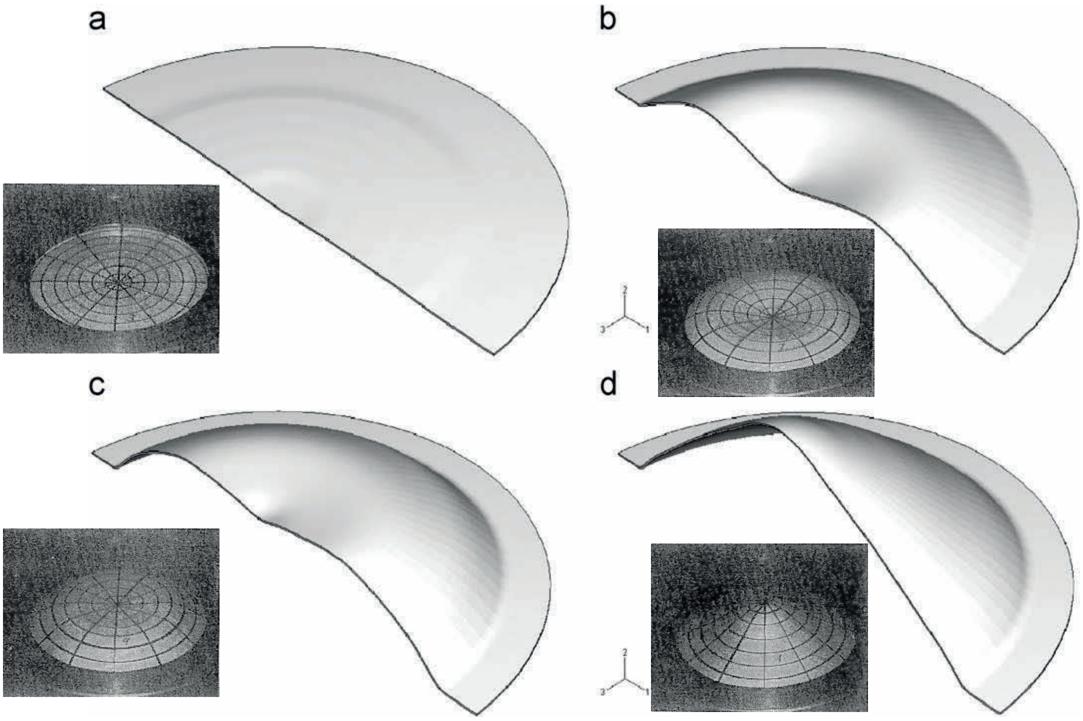

Figure III-7: FE predictions and experimental geometry of deformed sheet at different time values: (a) at t = 19 μs, (b) at t = 95 μs, (c) at t = 135 μs and (d) at t = 240 μs.

Fig. III-8a presents the vertical displacement the pole of the sheet (centre point of the sheet, *r = 0 mm*) as a function of time. Fig. III-8b presents the vertical displacement of a point on the sheet at a distance of *20 mm* from the pole, where the influence of the magnetic pressure is maximum. In Fig. III-8 solid lines are numerical results while squares are experimental results taken from Takatsu *et al.* [2]. It is observed that, at the beginning of the deformation process during the simulations, the centre of the sheetmetal does not move while the rest of the sheet starts deflecting. In fact the magnetic pressure is equal to zero creating a dead spot for the distribution of magnetic pressure at the centre of the sheet and it has the maximum value near the sheet region where the radius is equal to *20 mm*. The centre of the sheet is mainly moved by the inertial effects. As attempted and in agreement with Takatsu *et al.* [2], the predictions obtained with Hollomon type power law Eq. III-1 are coherent with experimental results for the vertical deflection of the sheet at the end of the process. We can conclude that the predicted results are globally in agreement with the experimental results [2].

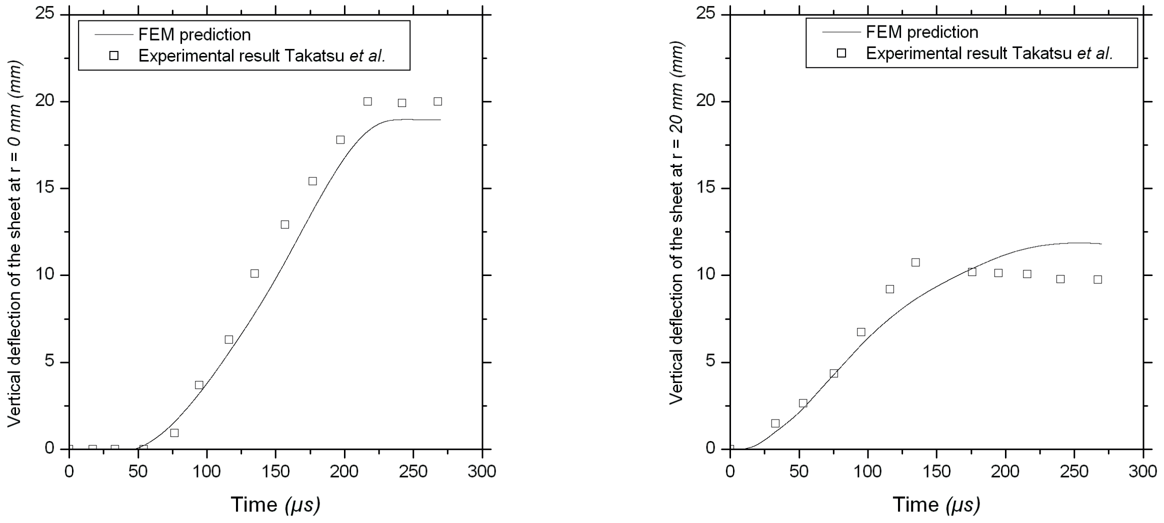

(a) *(b)*

Figure III-8: Vertical deflection of the sheet
(a) for a sheet radius equal to 0 mm.(b) for a sheet radius equal to 20 mm.

The FE results achieved with ABAQUS/ Explicit were then employed for the counter verification of our in-house finite difference code. The updated geometrical coordinates of the deformed workpiece at different time steps, was used for calculating the distribution of magnetic field density and magnetic pressure from our in-house finite difference code. Fig. III-9 shows the deformed geometry of the workpiece predicted with ABAQUS/Explicit at difference time steps.

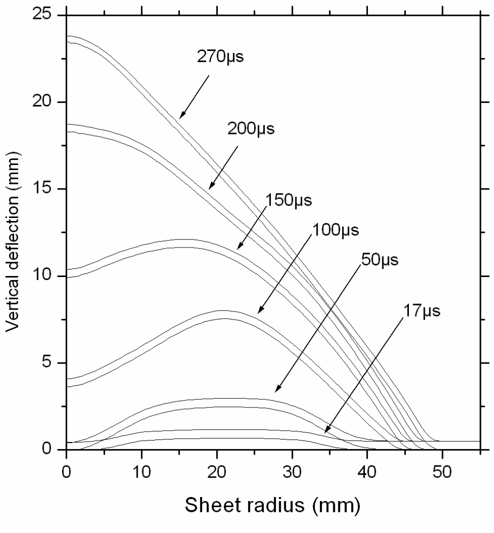

Figure III-9: FE predictions of deformed geometry of the workpiece at different time values.

At each of these step times, a FE simulation was carried out with the free FE code FEMM. The results obtained from the in-house finite difference code for the deformed geometry and the FEMM predictions were compared in order to validate our finite difference model. This comparison for different time steps is presented in Fig. III-10.

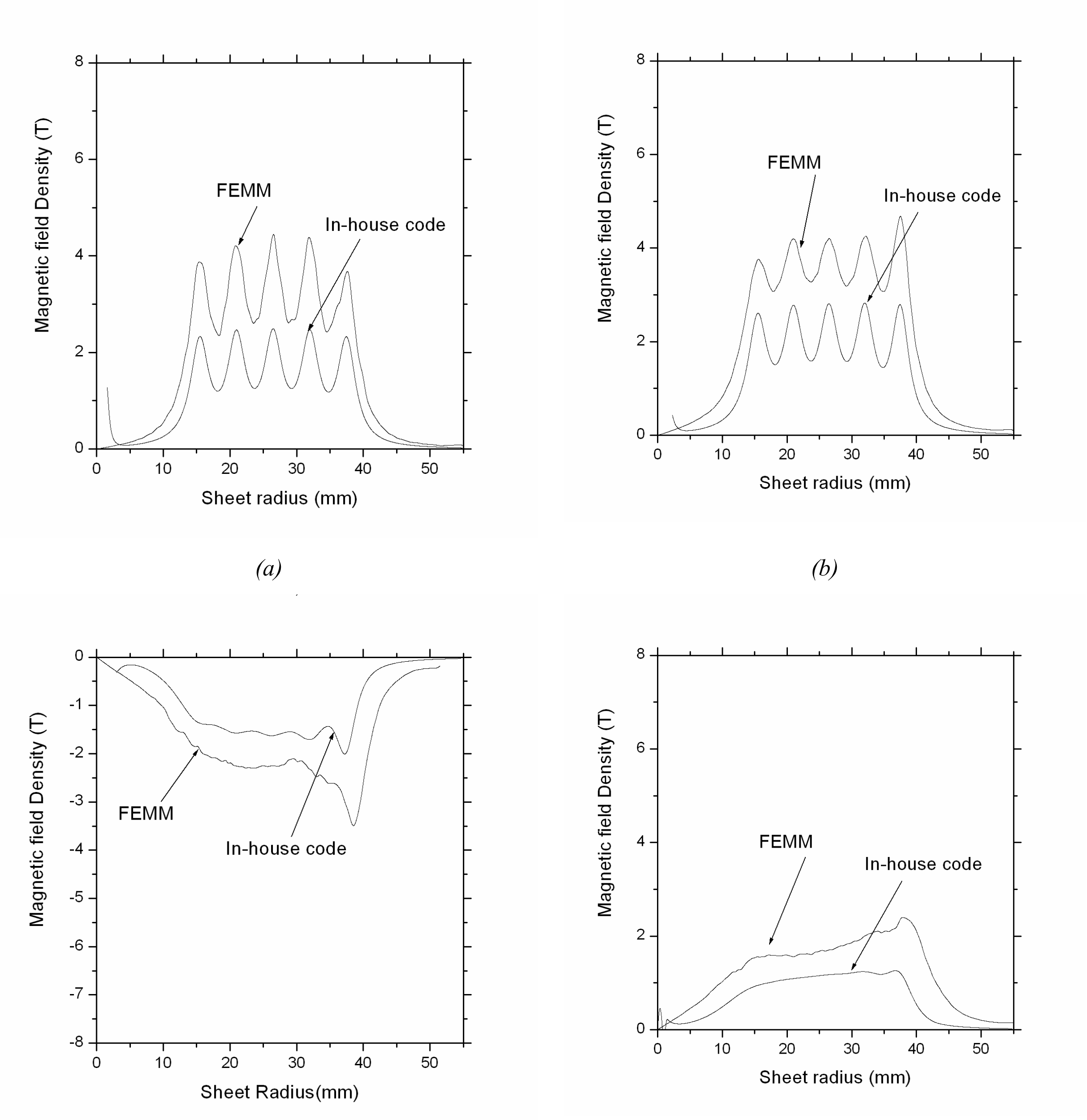

(a) *(b)*

(c) *(d)*

Figure III-10: Comparison of the radial distribution of magnetic field density at different time values: (a) at t = 10 μs, (b) at t = 17 μs, (c) at t = 50 μs and (d) at t = 85 μs.

The magnetic field density at *50 μs* is negative while the discharge current is at its first negative peak value. The results obtained with the in-house code and with the FEMM are in agreement, for each time step related to new deformed geometry of the workpiece Fig. III-10. As the geometry of the workpiece changes, the gap distance between the discharging coil and the sheet increases. This results in a lower mutual inductance between the coil and the workpiece. Thus, the magnitude of the magnetic field density decreases as the workpiece moves away from the coil. Consequently the magnetic pressure developed due to this magnetic induction decreases at each new time step, while the deformation of the workpiece continues. A very important conclusion can be drawn from Fig. III-10: the deformation of the workpiece is principally driven by the first impact of the magnetic pressure, while the continuation of the deformation is rendered basically due to the inertial effects of high velocity impact.

III.3.2. Electromagnetic tube forming process

III.3.1.1. Case of tube expansion

III.3.1.1.1. FE Model

A tube expansion experiment is proposed in Zhang *et al.* [3]. The coil is coaxial, concentric with the tube and placed inside it for the bulging process. A schematic view of the forming process is presented in Fig. III-11.

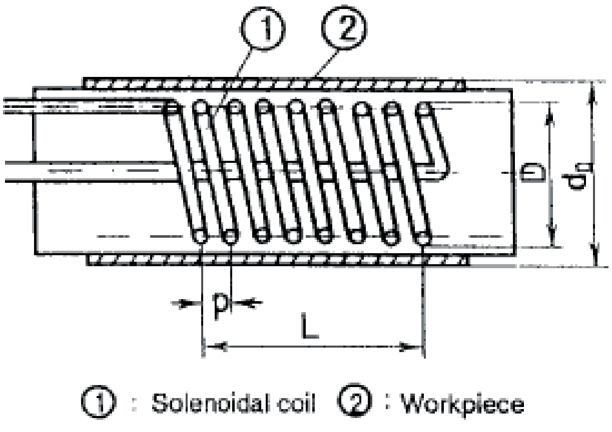

Figure III-11: Schematic view of the tube bulging process (Zhang et al. [3]).

The dimensions and working conditions for the tube bulging process are reported in the Table III-2.

Table [III-2]: System and material parameters for the case of tube expansion

Coil	
Number of turns *N*	35
Internal radius	18.5 mm
Groove pitch	3 mm
Coil length	100 mm
Circuit parameters	
Charging energy	1.0 kJ
Circuit inductance	5 µH
Circuit resistance	60 mΩ
Workpiece (tube)	
Internal radius	20 mm
Thickness	1 mm
Density	$2.75 \mathrm{x} 10^3$ kg/m^3
Young's modulus	80.7 GPa
Poisson's ratio	0.3
Conductivity	36 MS/m

Zhang *et al*. [3] performed their experiments for different working conditions, using a set of capacitors banks of total capacitance ranging from *20 µF* to *1600 µF*. Similarly to study the effect of coil length three different coil lengths were considered i.e. *200,100* and *80 mm*. In the present study, our attention is only focused on the effects of the capacitance of the capacitor bank. The coil length is arbitrarily fixed to *100 mm*. The discharge current is calculated with Eq. II-57 defined in the second chapter. Fig. III-12 shows the temporal variation of the discharge current for the difference capacitor banks as function of capacitance. We can notice that as the capacity increases, the frequency of the current increases but the amplitude/ magnitude decreases.

The first positive peak of the discharge for each capacitance is located at different time interval. The maximum values of discharge currents calculated for coil length of *100 mm*, and the corresponding experimental values are presented in Fig. III-13. These calculated values are in agreement with the experimental ones from Zhang *et al*. [3] as shown in Fig. III-13.

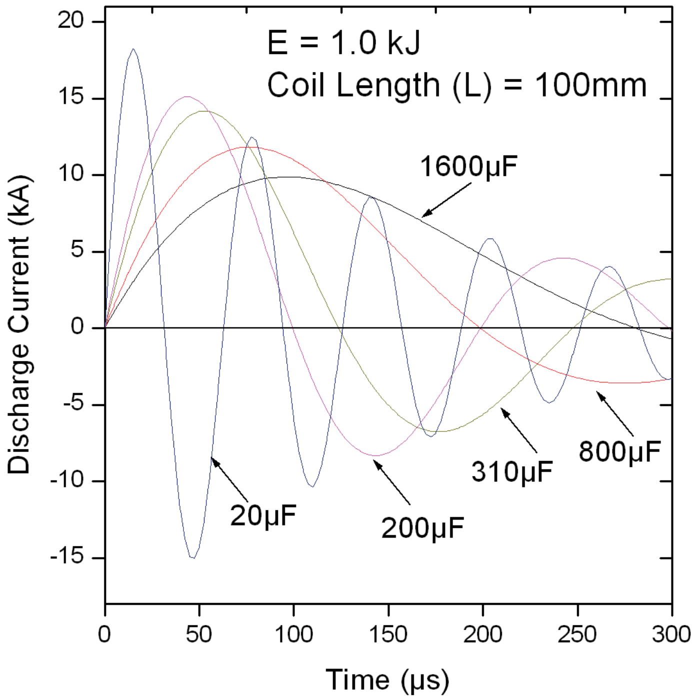

Figure III-12: Evolution of the discharge current for different values of capacitances.

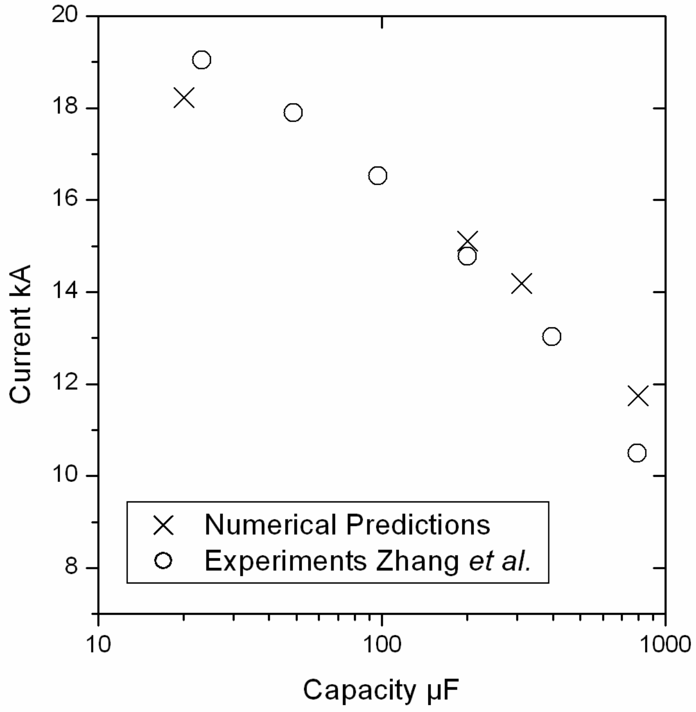

Figure III-13: Variation of maximum current with capacitance.

A grid of *6* elements through thickness and *140* elements for height of the tube has been used for the calculations of magnetic pressure in the in-house finite difference code. Fig. III-14 presents the results obtained from the in-house finite difference code for the radial and axial components of the magnetic flux densities at respective first positive peak of discharge current, for the different capacitances used for the calculation of magnetic pressure.

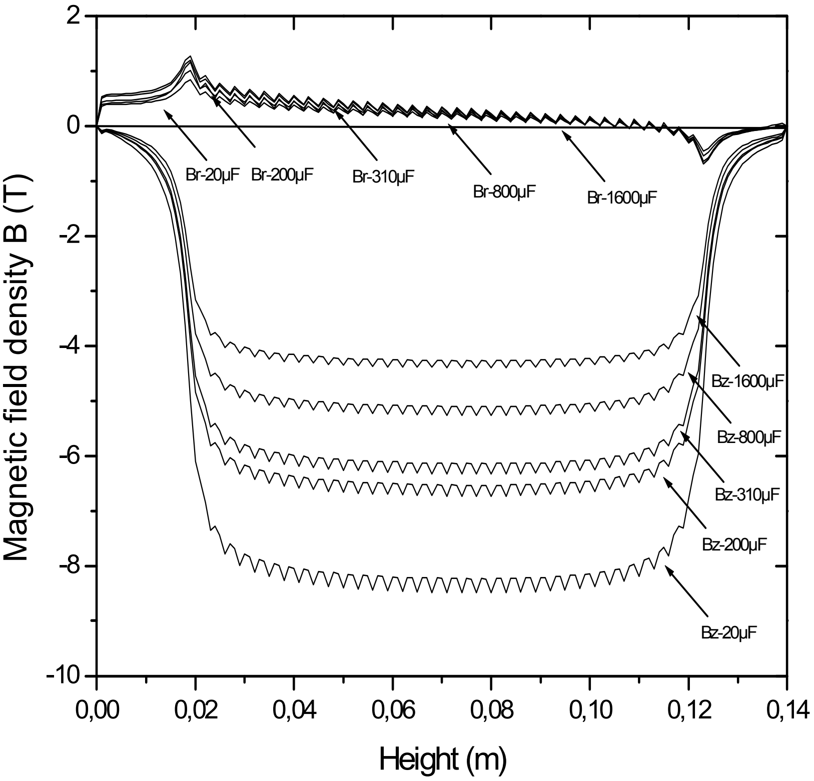

Figure III-14: Evolution of magnetic field densities for different capacitances used for simulations.

It is observed that when the capacitance is low, the magnitude of current is the large, so as the frequency of the wave form. Therefore, the magnitude of the magnetic field density decreases with the increment of capacity, which results in lower magnetic pressure. It is also noticeable that the magnitude of the axial magnetic field density is much higher as compared to its radial component that results in a larger radial magnetic pressure exerted on the tube. Afterwards we verified the results obtained from the in-house finite difference code with the predictions obtained from the FE simulations carried out for an axisymmetric electromagnetic FE model developed with the freeware code FEMM [6]. For the respective capacitances used, the results obtained are given in Fig. III-15. The results shown in Fig. III-15 are calculated for the maximum discharge current for the respective value of capacitance.

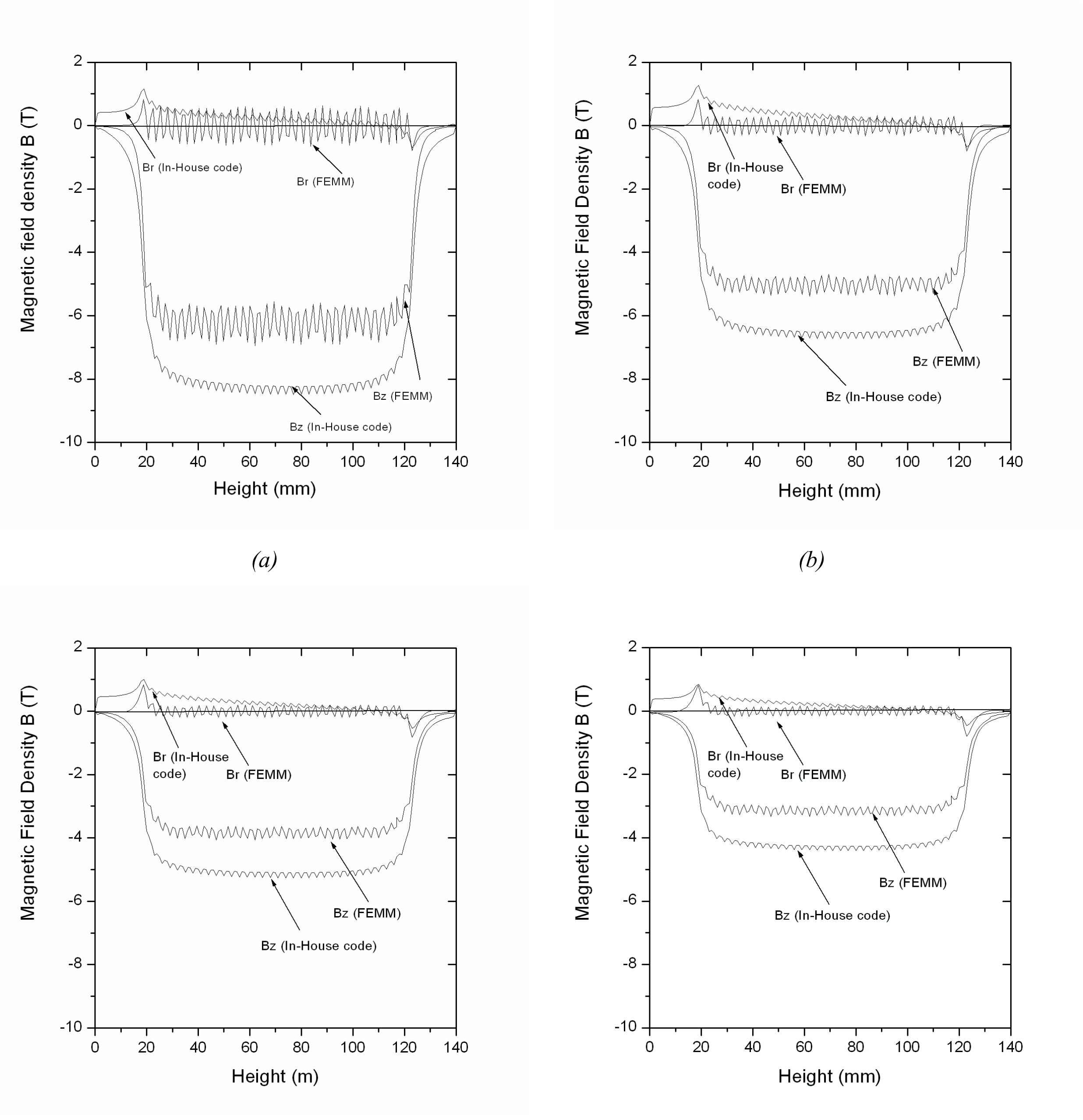

(a) *(b)*

(c) *(d)*

Figure III-15: Comparison of magnetic field predictions from in-house code and FEMM results (a) 20 μF, (b) 200 μF, (c) 800 μF, (d) 1600 μF.

As shown in Fig. III-15, there exists a small variation between the results obtained from the in-house code and those from the FEMM. In fact, the finite difference code slightly underestimates the values of the axial component of the magnetic field, B_z. This may be attributed to the unavailability of the process parameters from the work of Zhang *et al.* [3].

The distribution of the magnetic pressure calculated for the different capacitances is shown in Fig. III-16. The pressure is calculated for the peak discharge current for each capacitance applied. We can observe that the magnitude of the radial pressure decreases as the capacity increases.

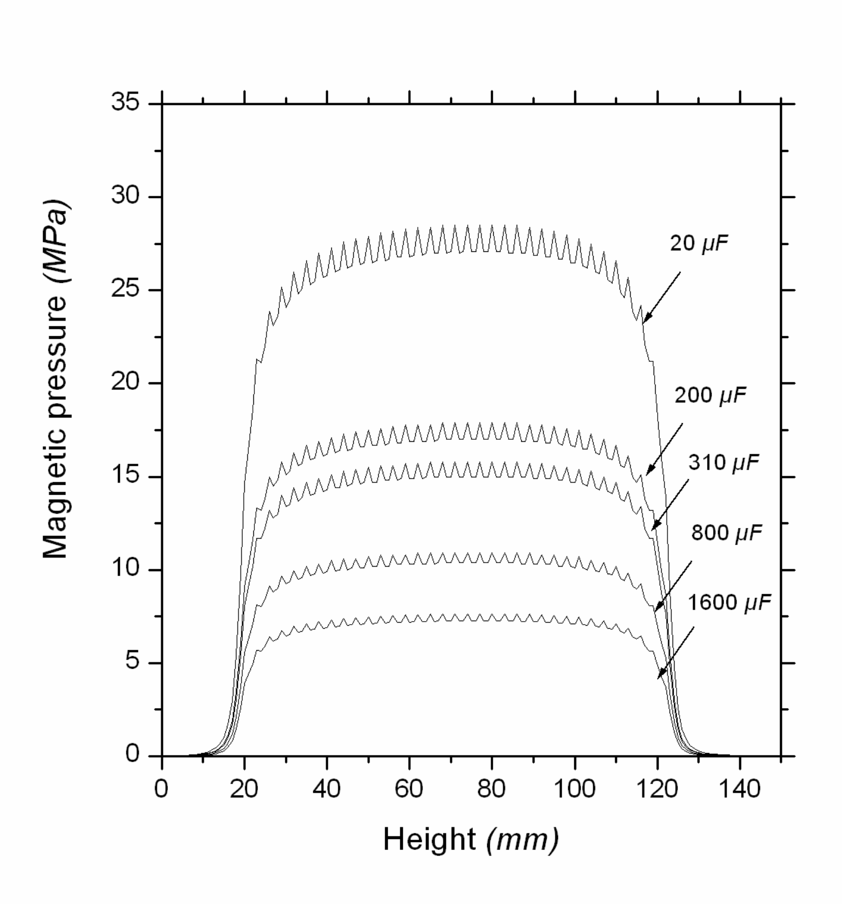

Figure III-16: Distribution of radial magnetic pressure.

After the preliminary verifications of the in-house finite difference code with FEMM, the FE simulations for tube expansion were carried out with the commercial FE code ABAQUS/Explicit [1]. An axisymmetric model is applied, with the same gridding (*6* elements through thickness and *140* elements for height of the tube) as used for the calculations of magnetic pressure in the in-house finite difference code. The application of *140* elements through the height of the workpiece is one of the limitations of the VDLOAD user-defined subroutine, as the maximum number of elements in array in VDLOAD should not surpass *140* elements. The magnetic pressure calculated from the in-house finite difference code is included via the user subroutine VDLOAD as a mechanical pressure applied at the inner wall of the tube. The tube was meshed with *CAX4R* elements [1] which is a four node bilinear axisymmetric quadrilateral element with reduced integration. The tools are modelled using analytical rigid elements (R3D4 in ABAQUS Reference manuals [1]). During the simulation the tools are considered to be fixed. The simulations are performed for several values of capacitance. Therefore the simulation process times are taken equal to the first positive periods of the discharge current. The simulation process time are fixed to *300 μs*. In the simulations contact conditions are needed to be considered between the die and the sheet as well as between the sheet and the holder. Coulomb friction law has been used with a friction coefficient of *0.25*. The geometry and the mesh are presented in Fig. III-17.

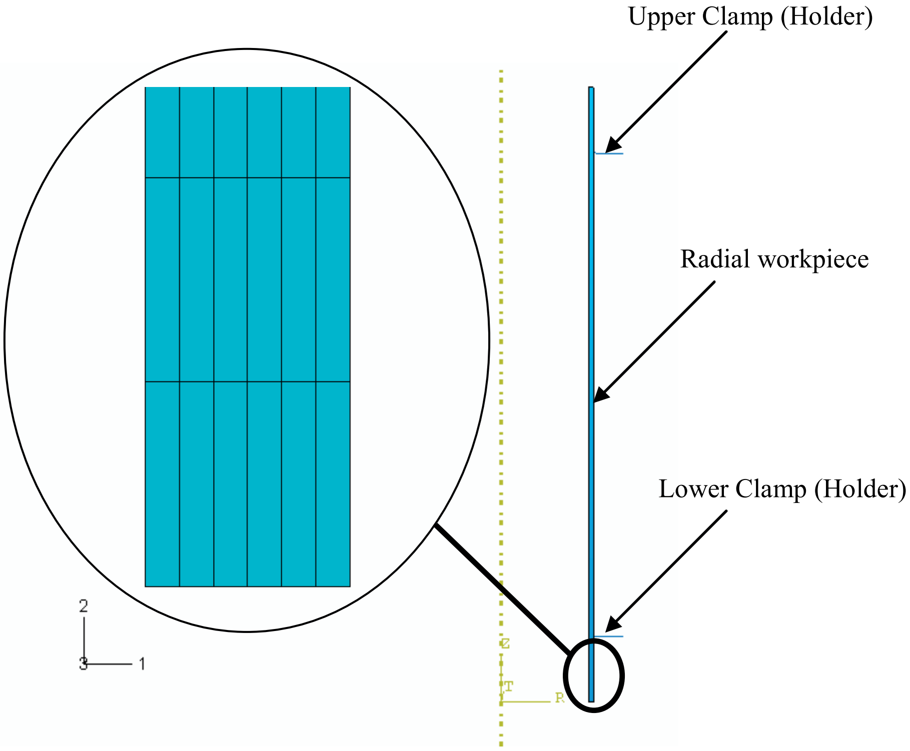

Figure III-17: Geometry of the electromagnetic tube expansion process used in ABAQUS/CAE.

The material parameters used in the finite element simulation are approximated to model an aluminium alloy. We used the same material constitutive behaviour as applied for the sheetmetal free bulging forming process. A rate dependant power is applied, which approximates the aluminium alloy used in the experiments of Zhang *et al.* [3].

III.3.1.1.2. Results

For all the values of capacitance, the velocity of the tube has been first analysed in order to verify the assumption accounted for the calculation of the magnetic forces based on the work of Manea *et al.* [5]. The maximum velocity attained during the forming process is of the order of *100-150 m/s* for all the capacitance values. It is small enough to fulfil the assumption that the sheet velocity does not affect the magnitude of the electromagnetic field density during the forming process (in agreement with Manea *et al.* [5] sheet velocity < $10^7 m/s$). Fig. III-18 depicts the evolution of the velocity of the centre of the tube during the expansion. For each case, the velocity of the tube is measured until the first positive half-cycle of the discharge current.

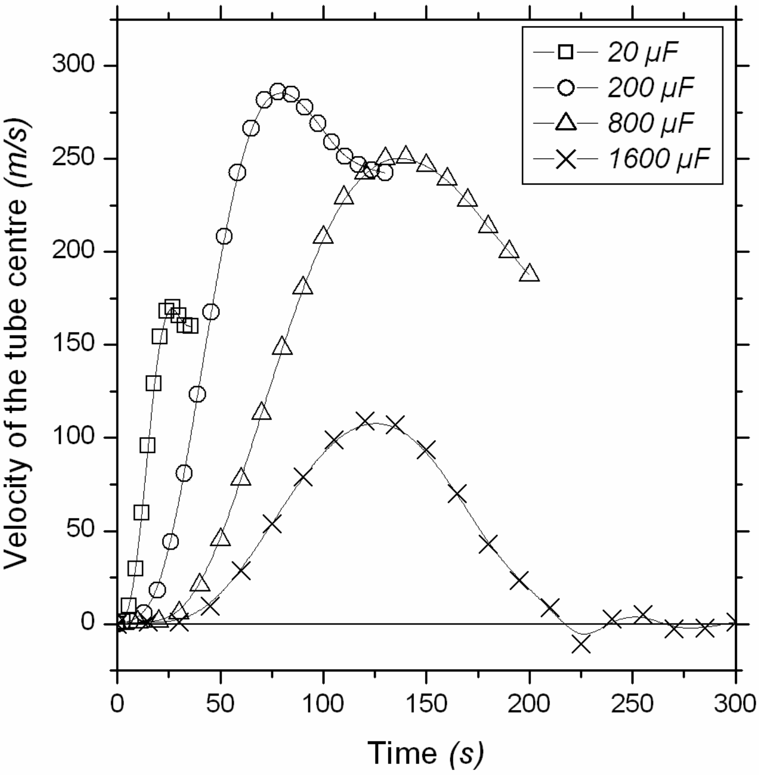

Figure III-18: FE predictions of vertical velocity of the centre of the tube as a function of time.

In Fig. III-19 the deformed profiles of the tube for the simulation are presented for the step time at peak discharge current for each capacity. It is observed that the deformation of the tube is more pronounced at the centre of the tube than at the corners. This is due to the maximum magnetic pressure exerting at almost ½ height of the tube and the surroundings moved later because of the lower pressure which is in accordance with the experiments [3]. The FE predictions are in good agreement with the experimental profiles [3].

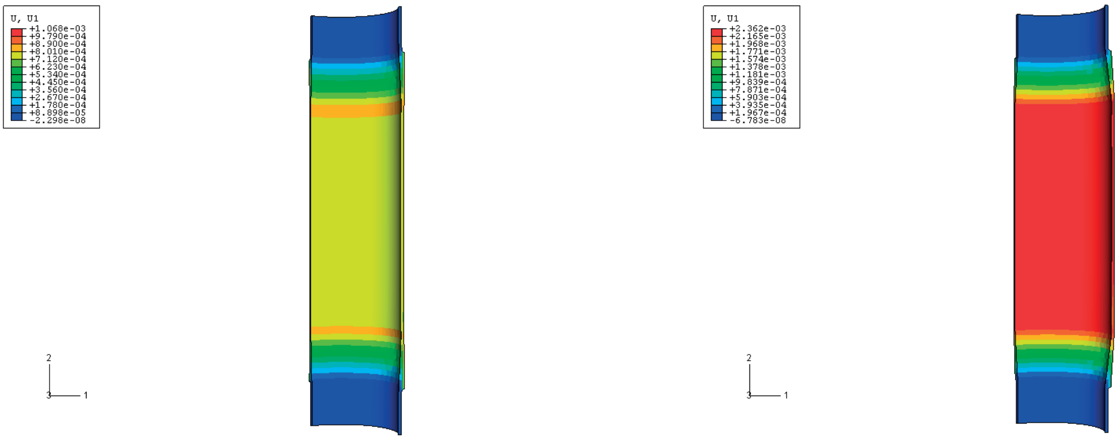

20 µF at 15 µs

200 µF at 45 µs

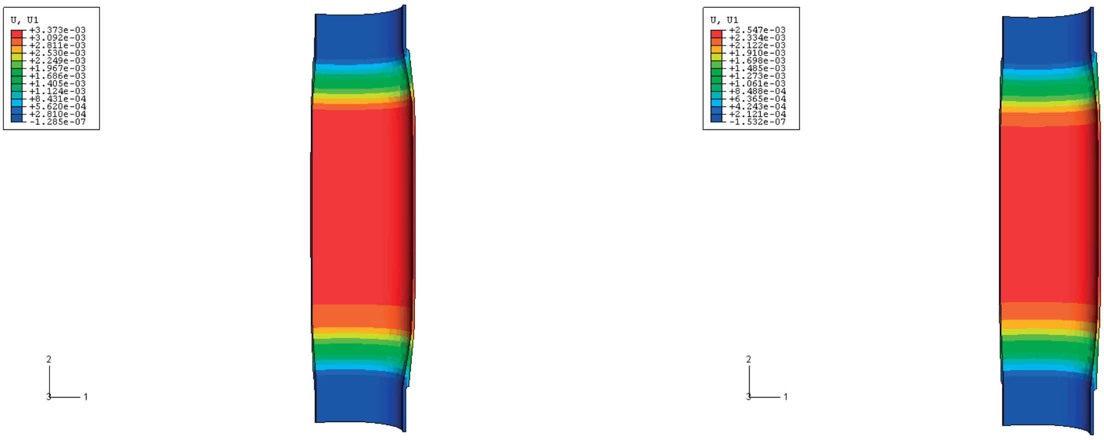

800 µF at 75 µs

1600 µF at 97.5 µs

Figure III-19: FE predictions of tube profiles in the case of tube expansion.

In Fig. III-20, the experimental values [3] of fractional change in the radius of the tube, $\Delta r/r$, are compared with the predictions at a constant coil length of *100 mm* and charging energy of *1 kJ*. In Fig. III-20 the numerical predictions reproduced the experimental trend observed by Zhang *et al.* [3]. However, a slight variation between the numerical results and the experimental ones [3] is noticed in Fig. III-20. Further explanations can be presented. This deviation may have occurred due to unavailability of the material properties from the experimental point of view from Zhang *et al.* [3]; since we used a simple and approximate material constitutive plasticity model in our simulations. This variation in the predicted results may also be accounted for the lack of available circuit parameters: for instance total inductance of the forming system, resistance and gap distance. Moreover, it is noticeable that we assumed a constant inductance while the effects of the velocity term were neglected.

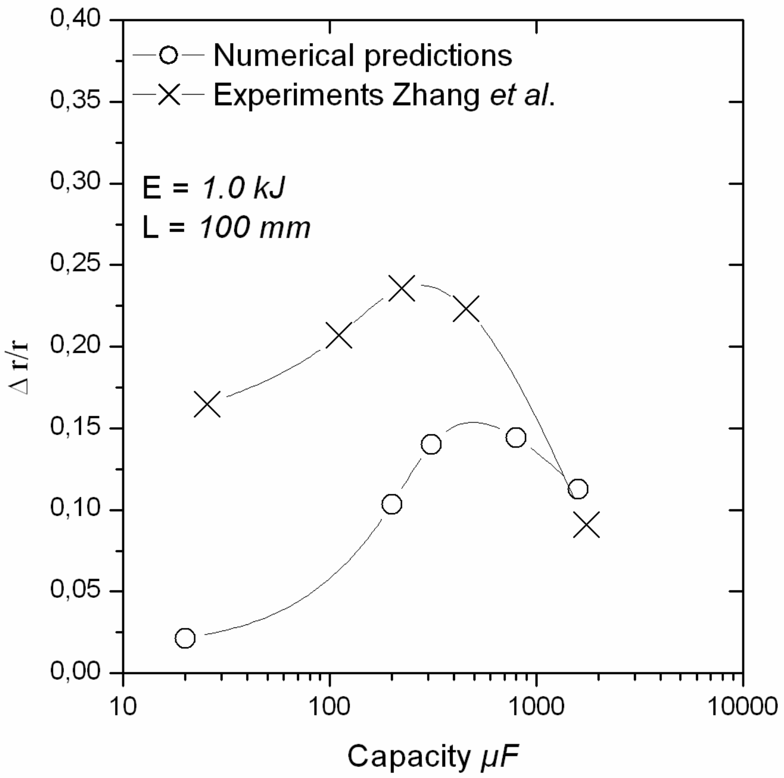

Figure III-20: Fractional radial deformation of the tube as function of capacity.

The numerical results predict the experimental trends. A variation in the results obtained from the simulation can be accounted for the approximation and assumption applied to the finite element model.

III.3.1.2. Case of tube compression

III.3.1.2.1. FE Model

Tube compression is one of the most common operation performed using the electromagnetic forming process. It is applied for reduction of tube diameter, joining of rings and making bends at certain position on a pipe. In tube compression process, a coaxial, concentric coil is placed around the tube to be formed, Fig. III-21. In order to simulate the tube compression operation for electromagnetic forming process, experimental and numerical data from Karch *et al.* [4] have been used.

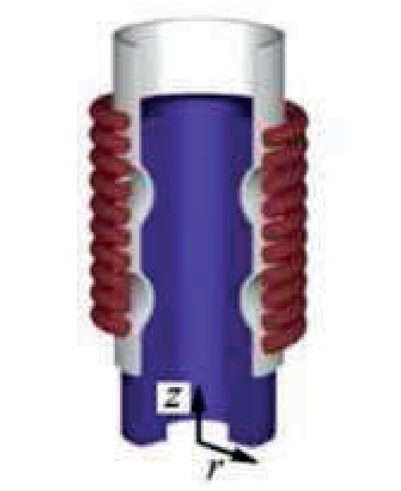

Figure III-21: A schematic view of electromagnetic tube compression process.

Karch *et al.* [4] used in their experiments aluminium tubes of *AA 6060* alloy with an external diameter of *40 mm*, a length of *75 mm* and with a wall thickness of *2 mm*. A *14* turn copper coil of *27 mm* length with a cross sectional area of *3.8775 mm²* is used for the discharge current. We carried out the tube compression simulations using the data complying with the simulation presented in Karch *et al.* [4]. The circuit parameters employed in the experiments are summarized in Table III-3.

Table III-3. System and material parameters in case of tube compression experiments [4].

Coil	
No. of windings N	14
Internal radius of ring of coil	22 mm
Coil length	27 mm
Circuit parameters	
Charging energy	1.3 kJ
Circuit inductance	1.5 μH
Circuit resistance	63 $m\Omega$
Workpiece	
Material	Aluminium alloy Al 6060
Electrical conductivity σ_{Al}	36 MS/m
Internal radius	20 mm
Thickness	2 mm
Length	75mm

Here, we would like to mention that due to lack of availability of data related to the EMF circuit, parameters of the forming system such as total inductance, resistance and charging energy were assumed in order to reproduce the approximate discharge current as presented in the experimental work of Karch *et al.* [4]. Only the information related to the machine parameters is provided and no in-depth details of the experimental setup were found. The discharge current is calculated with Eq. II-57 defined in the second chapter. Fig. III-22 shows the evolution of the discharge current applied for the tube compression process.

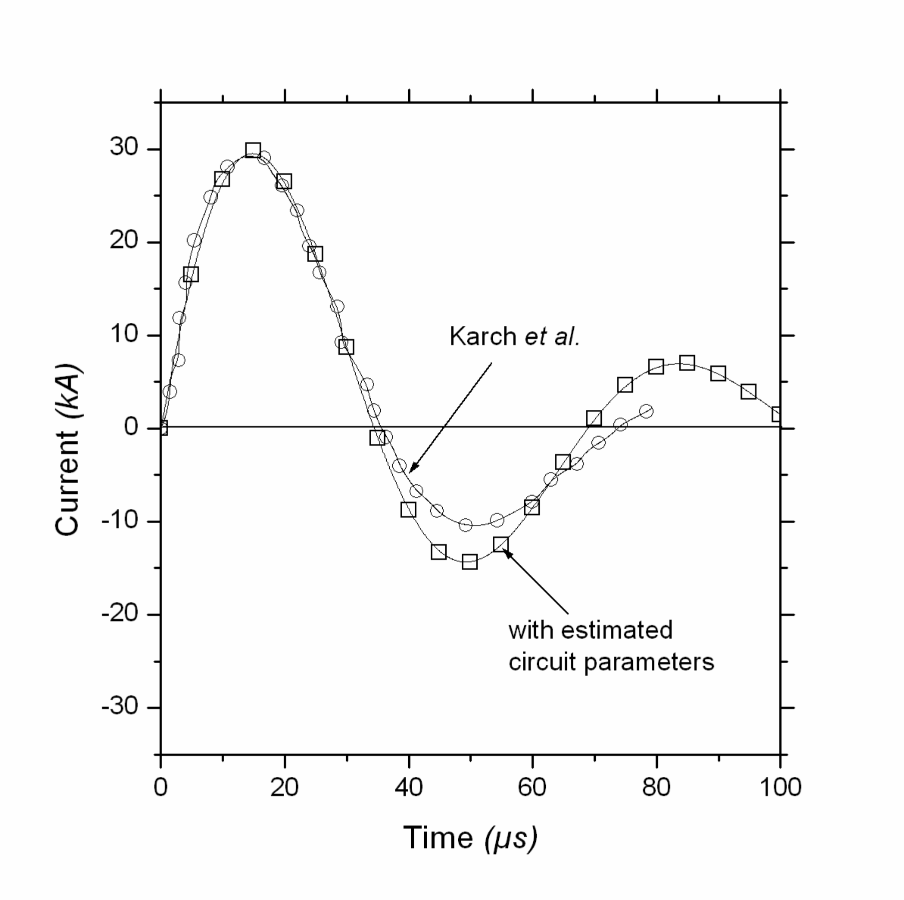

Figure III-22: Temporal evolution of discharge current with the conditions defined in [4].

A grid of *6* elements through thickness and *75* elements for tube height have been used for the calculations of magnetic pressure in the in-house finite difference code. In Fig. III-23, the axial distribution of the two components of the magnetic field density is shown. The comparison between our in-house finite difference predictions and FEMM simulation results provide a good correlation for the axial component of the magnetic field density, B_z.

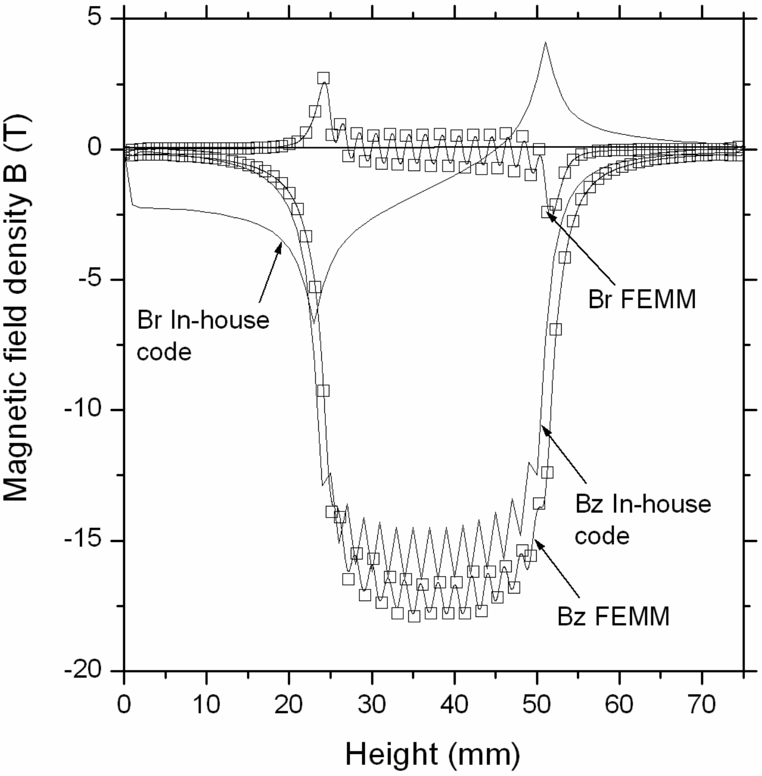

Figure III-23: Distribution of magnetic field density for tube compression.

The FE simulations of the tube compression process proposed by Karch *et al.* [4] have been performed with the commercial FE code ABAQUS/Explicit [1]. The process is defined as an axisymmetric model. The FE model for tube compression process is presented in Fig. III-24. As in the finite difference simulations, we used *6* elements through the thickness while *75* elements were applied for the length of the tube. The tube was meshed with *CAX4R* elements [1] which is a four node bilinear axisymmetric quadrilateral element with reduced integration. The tools are modelled using analytical rigid elements (*R3D4* in ABAQUS Reference manuals [1]).

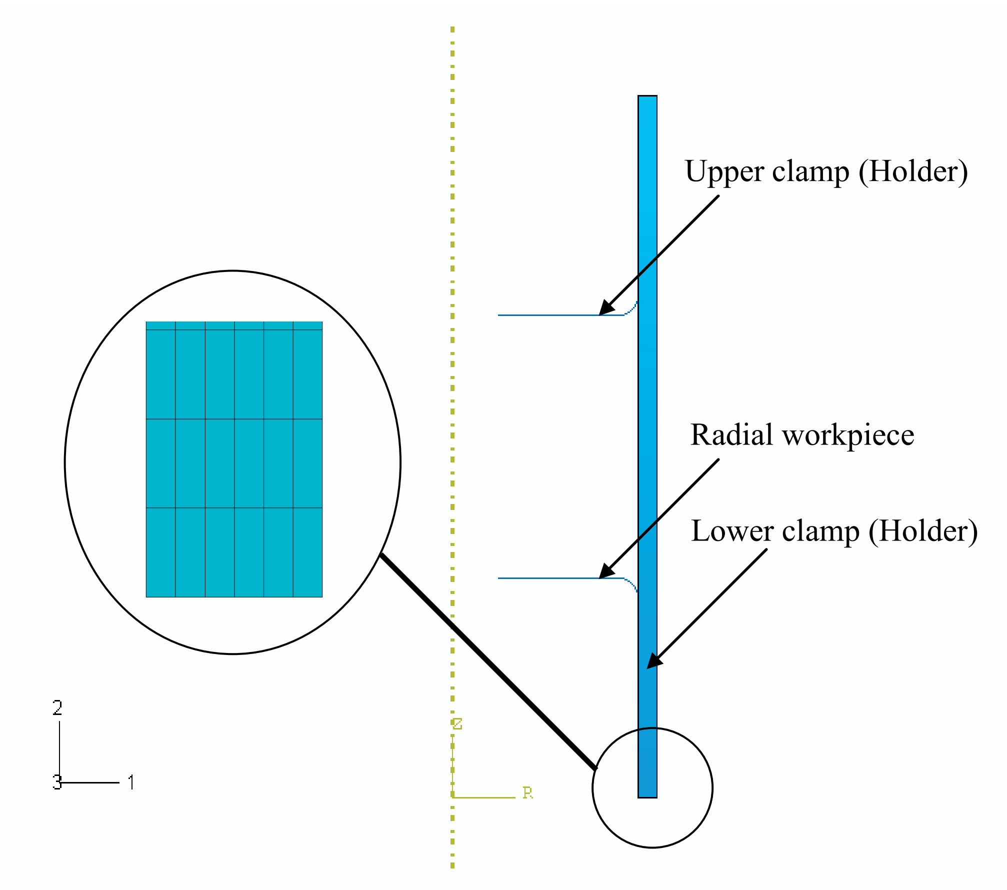

Figure III-24: FE model for electromagnetic tube compression process.

During the simulation the tools are considered to be fixed. In agreement with Karch *et al.* [4], the total simulation time was taken to be equal to *150 µs*. The magnetic pressure calculated from the in-house finite difference code is included via the user subroutine VDLOAD as a mechanical pressure applied at the outer wall of the tube. Conforming to the numerical simulations of Karch *et al.* [4], we modelled the hardening behaviour of the tubes with a homogenous linear isotropic modified Johnson-Cook [7] model given by:

$$\sigma = \left(A + B\varepsilon^{n}\right)\left(1 + \alpha \dot{\varepsilon}^{\beta}\right)\left[1 - \left(\frac{T - T_{r}}{T_{m} - T_{r}}\right)^{m}\right] \qquad \text{(III-2)}$$

The material constants for the Johnson-Cook law are presented below in Table III-4.

Table III-4. System and material parameters of the calculation.

A	111 MPa
B	415 MPa
N	0.512
α	0.02758
β	0.36167
M	1.1
T_m	611 C
T_r	25 C

Fig. III-25 presents the variation of the Johnson-Cook hardening law with respect to different strain rates. This material presents weak rate strain sensitivity.

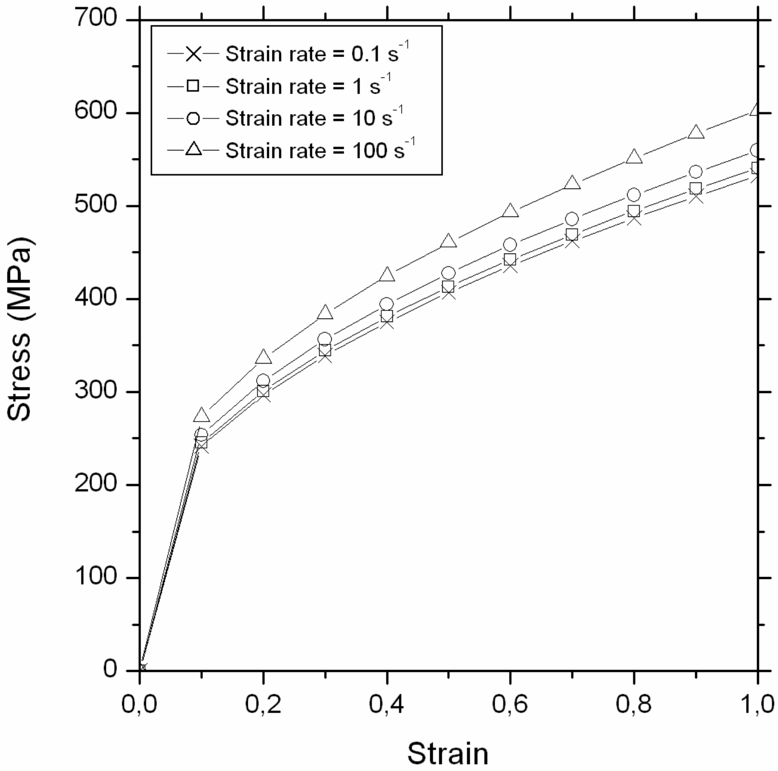

Figure III-25: Johnson-Cook hardening law for different strain rates.

III.3.1.2.2. Results

The velocity of the tube has been first analysed in order to verify the assumption accounted for the calculation of the magnetic forces based on the work of Manea *et al.* [5]. Fig. III-26 presents the comparison between the calculated radial velocity of the tube centre as a time function and the experimental and numerical results of Karch *et al.* [4]. Solid lines are results from the literature while squares are our FE predictions. Regardless of the very short period for the tube deformation during the forming process (about *100 μs*), the forming velocity is found to be quite large (maximum velocity obtained is about *200 m/s*). The numerical results during the simulation of tube compression are found to be in agreement with both experimental and numerical results of Karch *et al.* [4].

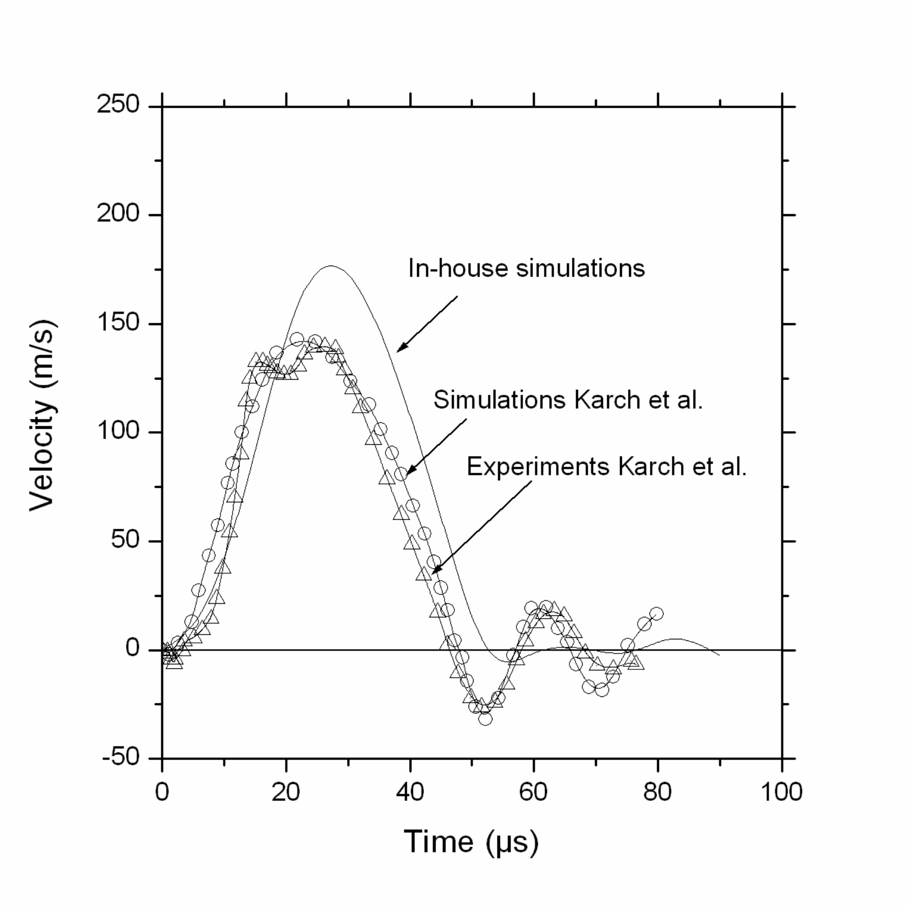

Figure III-26: Velocity of the centre of the tube as function of time in case of electromagnetic tube compression process.

The deformed shaped obtained after the completion of the simulation for tube compression is plotted in Fig. III-27.

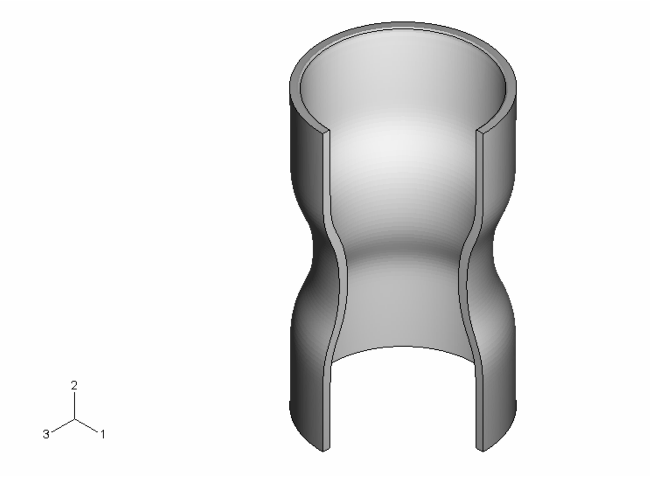

Figure III-27: An example of tube deformation obtained with ABAQUS/Explicit.

The deformation of the tube centre is plotted as a function of time in Fig. III-28. As depicted in Fig. III-28, the deformation of the tube centre is achieved at approximately *50 µs*, during the first half-cycle of the discharge current. The prediction of the deformation of the tube centre from our simulations is compared with, both experimental results and simulations performed by Karch *et al.* [4].

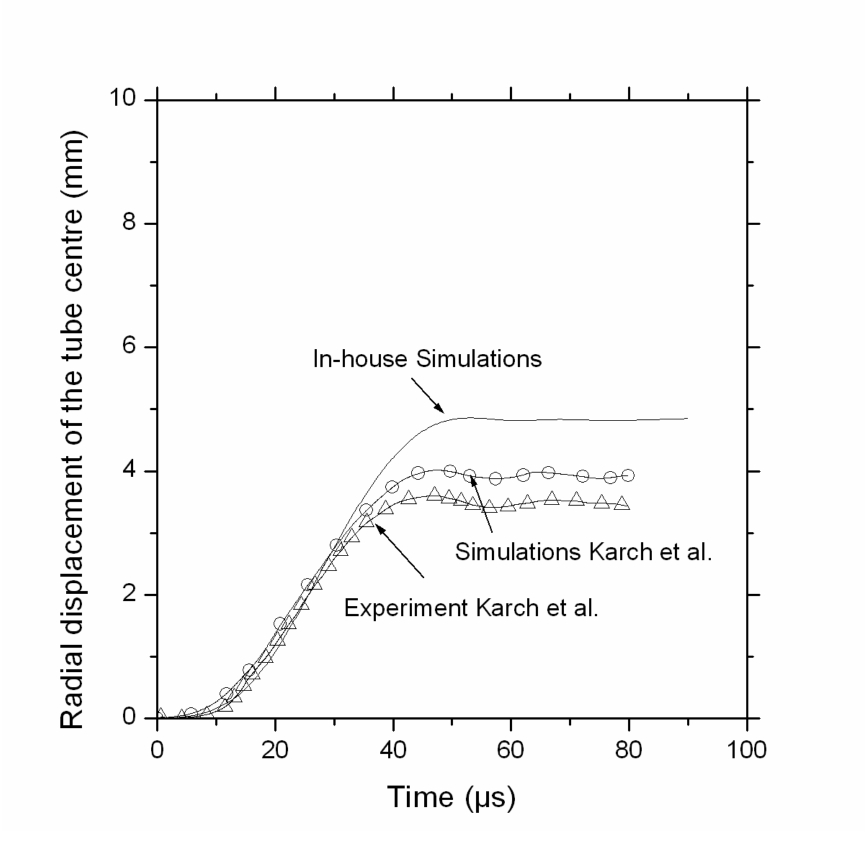

Figure III-28: Comparison of Tube deformation as function of time.

The estimated displacement from our simulations slightly overestimates experimental and simulation data obtained from the work of Karch *et al.* [4]. Simialry, this overestimation is due to the unavailability of pertinent information regarding the system parameters such as the inductance, resistance and material properties. These parameters were assumed such that the discharge current has the same waveform as mentioned in the experiments of Karch *et al.* [4]. In contrary to our simulations, in the FE simulations of Karch *et al*. [4] the thermal effects due to joule heating by Eddy currents and plastic work has been taken into account.

Conclusion

A sequentially coupled numerical model for EMF process has been developed. This model includes the resolution of electromagnetic problem, on one hand, and analyses the deformation process on the other. In this chapter the finite difference code has then been introduced in the commercial FE code ABAQUS/Explicit [1] via a user-defined subroutine VDLOAD. FE simulations of axi-symmetric electromagnetic forming processes have been performed. Three EMF processes have been studied: an electromagnetic free bulging test [2], a tube expansion test [3] and a tube compression test [4]. The preliminary FE results demonstrate that the hypotheses of the magneto-stationary Maxwell's equations are verified. In the case of the sheet forming, the maximal velocity has been found equal to *100–120 m/s*. In the case of the tube, the maximal velocity was found equal to *100–200m/s*. The FE predictions are globally in agreement with the experimental results [2, 3, 4].

References

[1] ABAQUS/Explicit, Version 6.5 Manuals, Hibbitt, Karlsson and Sorensen Inc., Pawtucket, USA, 2005.

[2] Takatsu N., Kato M., Sato K., Tobe T., High speed forming of metal sheets by electromagnetic forces, *International Journal of Japanese Society for Mechanical Engineering* 1988 ; 60, pp. 142-148.

[3] Zhang H., and Murata M., Suzuki H., Effects of various working conditions on tube bulging by Electromagnetic forming, *Journal of Materials Processing Technology;* 48 (1995), pp. 113–121.

[4] Karch C. and Roll K., Transient simulation of electromagnetic forming of aluminium tubes, *Advanced Materials Research,* vol. 6-8 (May 2005), pp. 639-646.

[5] Manea, T.E., Veweij, M.D., Blok, H., The importance of velocity term in the electromagnetic forming process, *Proceedings of 27th General Assembly of the International Union of Radio Science*, URSI 2002, Maastricht, pp. 112-115. *Science*, URSI 2002, Maastricht, pp. 112-115.

[6] FEMM4.0, http://femm.foster-miller.net/wiki/HomePage (April 2009).

[7] Johnson G.R., Cook W.H., Fracture characteristics of three metals subjected to various strains, strain rates, temperatures and pressures, *Engineering Fracture Mechanics*, vol. 21, no.1 (1985), pp. 31-48.

Chapter IV

Parametric study of EMF process and prediction of springback

Chapter IV: Parametric study of EMF process and FE predictions of springback

IV.1 Introduction

In order to ensure the quality of a product as well as the efficiency of a process, it is necessary to understand the effects of the process parameters. FE simulations are very useful to optimize a process because they can reduce time and cost needed for industrialization of process. In EMF process, various process parameters affect the performance of the system [1]. In general, the distribution of the magnetic field in the region between the coil and the workpiece is influenced by the circuit characteristics. The circuit parameters are principally defined by stored energy and the geometrical parameters of the forming system such as workpiece and coil geometry [2]. With the aim of investigating the influence of these parameters on the deformed workpiece geometry, FE simulations (with ABAQUS/Explicit [3]) based on the experiments proposed by Takatsu *et al.* [4] are used in this chapter. Thereafter, we proceed to compare a conventional deep drawing process with an EMF operation of a metal sheet. A similar deformed final geometry of the workpiece is obtained in the two forming processes. The numerical predictions for the springback from the conventional forming and EMF process are compared.

IV.2 Influence of process parameters

This chapter examines the effects of process parameters on the distribution of the magnetic field density and on the deformation of the workpiece during an EMF process. In order to understand and optimize the effects of the process parameters, we studied different cases: at first the influence of the electrical conductivity of the workpiece is accounted for, then the effects of sheet thickness at a constant electrical conductivity is studied, after which the effects of the gap distance are investigated. These parameters are the ones related to the workpiece parameters and geometry. Thereafter, the effects of frequency of discharge current and the charging voltage are investigated as the circuit parameters. The numerical calculations were performed using an in-house finite difference code developed for the electromagnetic problem [5]. Furthermore, the results of the in-house code were compared with the free FE code FEMM [6]. Subsequently, the influence of the different process parameters onto the workpiece deformation is also investigated.

IV.2.1 Effects of workpiece conductivity σ_w

In order to study the effects of the material conductivity, three values of electrical conductivity, σ_w, are used: *5*, *36* and *60 MS/m*. As in chapter 2, the sheet thickness is considered as *3 mm*, which corresponds with the experiments of free bulging of Takatsu *et al* [4]. The metal sheet is considered to be fixed. The discretization of the workpiece was assumed to be *20* x *110*, which means *20* elements in the thickness direction while *110* elements along the radius of the workpiece are applied. For the three values of electrical conductivity, calculations with our in-house finite difference code [5] and with the free FE code FEMM [6] have been performed. Predictions obtained with our in-house finite difference code [5] and with the free FE code FEMM [6] are presented in Fig. IV-1. The magnetic field densities plotted in Fig. IV-1 corresponds to the first peak of the discharged current. It is noticed in Fig. IV-1 that the magnitude of the magnetic field density computed with FEMM [6] and with our in-house finite difference code [5] does not change to a greater extent with the different values of electrical conductivity.

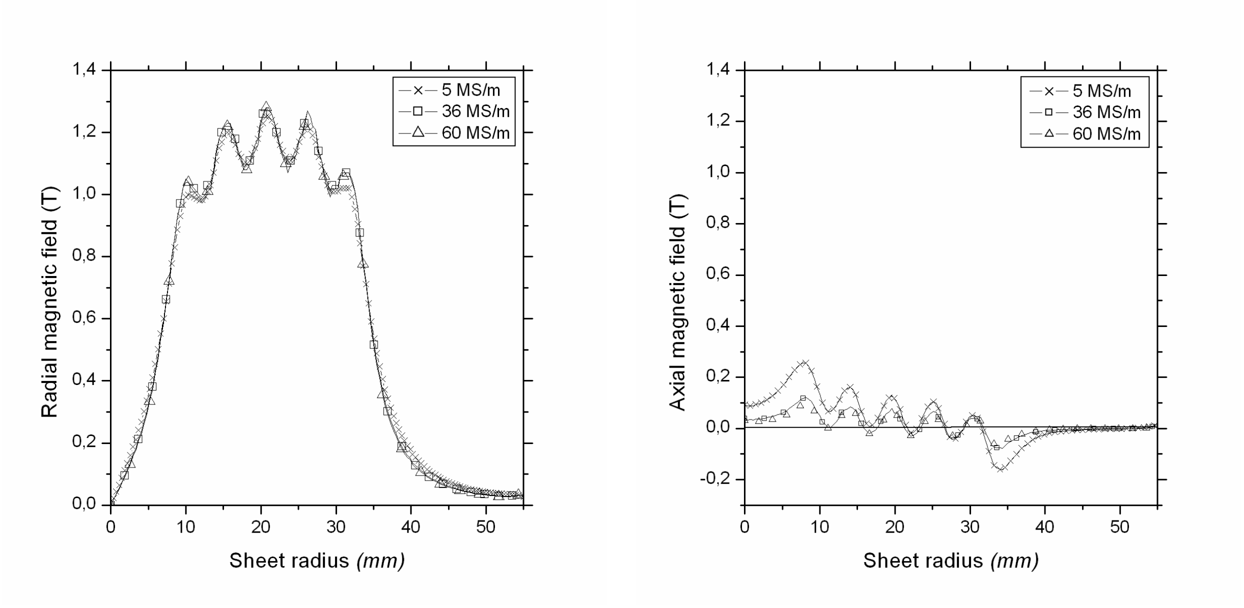

(a)

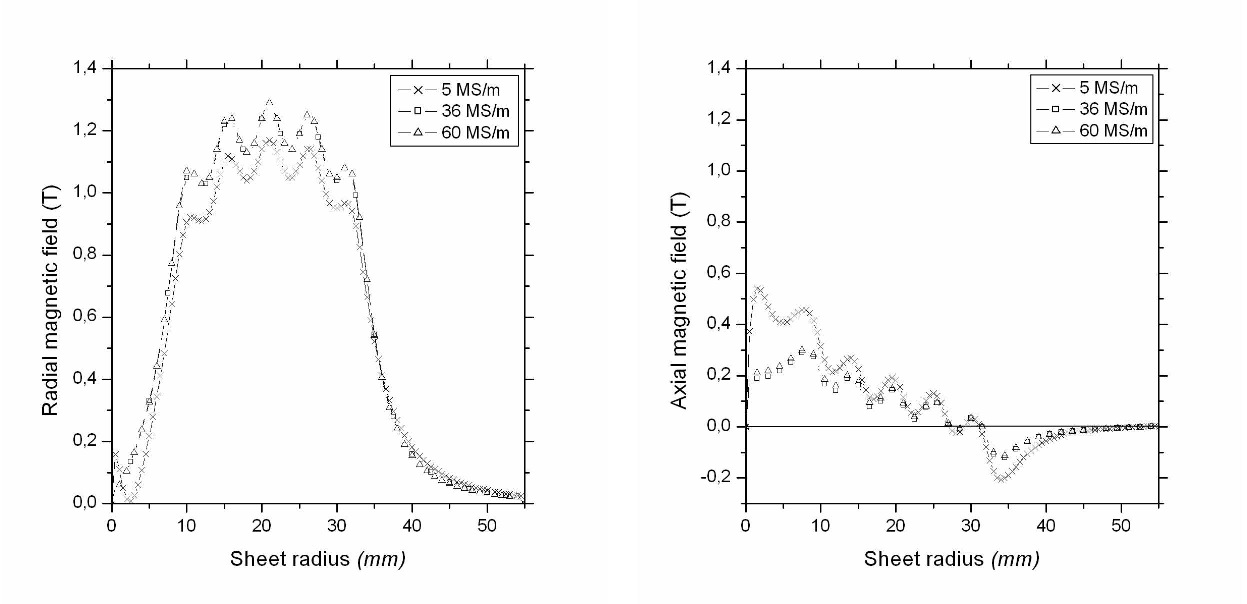

(b)

Figure IV-1: Influence of workpiece conductivity σ_w on magnetic field:
(a) FEMM results and (b) in-house Finite difference code.

The influence of electrical conductivity on the axial component of the Lorentz force density is also investigated, Fig. IV-2.

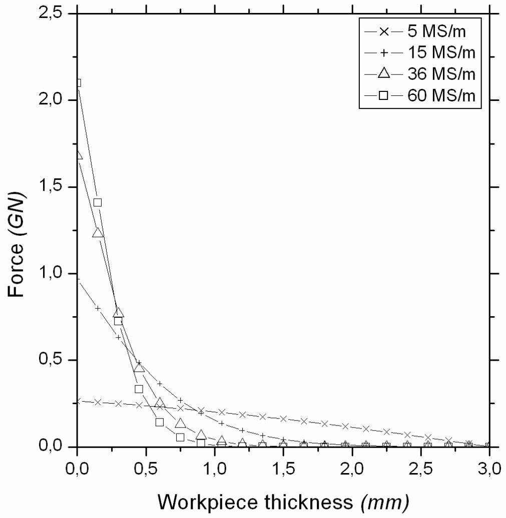

Figure IV-2: Influence of electrical conductivity on axial force distribution through thickness.

The maximum values of the Lorentz force are achieved at the first positive peak of discharge current and for a sheet radius roughly equal to *22 mm*. In Fig. IV-2, the penetration of the axial force through workpiece thickness is presented at the first positive peak for the different values of electrical conductivity. At the bottom surface of the workpiece, near the coil, the magnitude of the axial component of Lorentz force is high for the higher electrical conductivity. For all the values of electrical conductivity, the Lorentz force decreases largely through the sheet thickness. However, the decrease is more pronounced for higher values of electrical conductivity. Consequently, the phenomenon of the magnetic force shielding within the skin-depth is observed. Higher workpiece conductivity results in better shielding of the magnetic field; this limits the magnetic field diffusion through the sheet thickness.

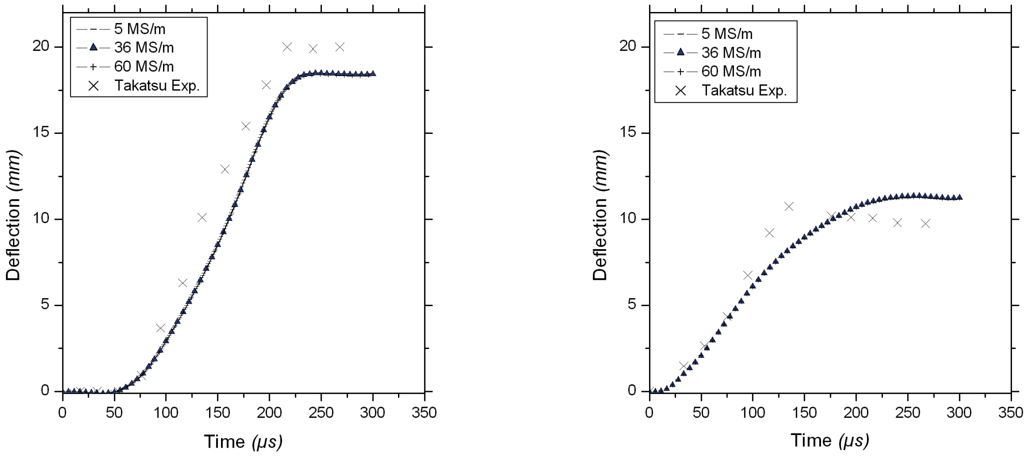

(a) *(b)*

Figure IV-3: Vertical deflection of the disc obtained with ABAQUS/Explicit [3] for different electrical conductivities: (a) for a sheet radius equal to 0 mm (b) for a sheet radius equal to 20 mm.

After these preliminary calculations, numerical simulations of the free bulging EMF process are carried out with the commercial FE code ABAQUS/Explicit [3]. For memory, the test geometry and the FE model are described in details in chapter 3. The thickness of the workpiece is now taken equal to *0.5 mm* (in accordance with Takatsu *et al.* [4]). Consequently the meshing was also adapted to this thickness (*4* x *170* elements; *4* elements through the thickness and *170* elements along the sheet radius). The vertical deflection of the workpiece centre and of a point *20 mm* away from the centre is depicted in Fig. IV-3. We noticed that the electrical conductivity has minor effects on the workpiece deformation. This is attributed to two reasons. First, the magnitude of the magnetic field density barely varies with the change of electrical conductivities. Second, the sheet is very thin and then the Lorentz force does not penetrate through the sheet thickness. The pressure acting on the sheet remains constant, even if the electrical conductivity changes. Finally, the electrical conductivity has a minor influence on the magnetic flux density, the Lorentz force and then on the maximum height achieved by the metal sheet in free bulging EMF test.

IV.2.2. Influence of wall thickness e

Another parameter that affects the efficiency of the EMF process is the workpiece thickness, *e*. The electrical conductivity of the workpiece is fixed to *36 MS/m* in accordance with the experiments of Takatsu *et al.* [4]. Firstly the metal sheet is assumed to be fixed. Three different sheet thicknesses are considered: *0.5*, *1* and *1.5 mm*. For each thickness, the finite difference grid employed in our in-house code is adapted. The respective sheet mesh discretizations which are used are presented below in the Table IV-1.

Table IV-1. Workpiece thicknesses and the corresponding meshes

Wall thickness	**Workpiece discretisation Δe x Δr**
1.0 mm	*20* x *110*
0.75 mm	*10* x *110*
0.5 mm	*10* x *110*

For the three values of sheet thickness, calculations with our in-house finite difference code [5] have been performed. The axial components of the Lorentz forces predicted at the first current peak and for a sheet radius around of *22 mm* are presented in Fig. IV-4. As attempted, the magnitude of the axial component of the Lorentz force increases as the sheet thickness decreases.

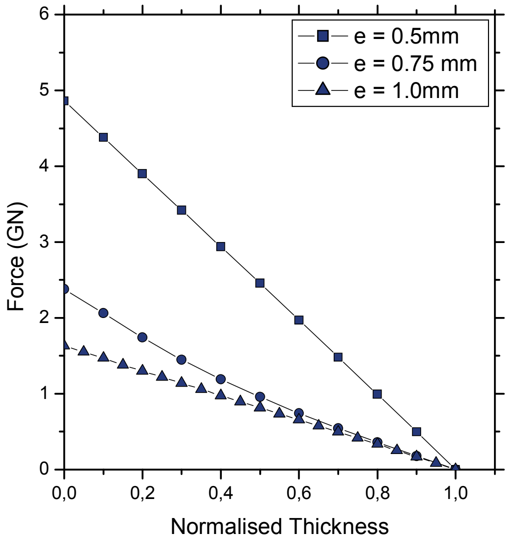

Figure IV-4: Axial force distribution through thickness at peak value of discharge current for different values of sheet thicknesses.

After these preliminary calculations, numerical simulations of the free bulging EMF process are carried out with the commercial FE code ABAQUS/Explicit [3]. As the sheet thickness changes, the number of elements through the thickness of the workpiece is increased. The FE mesh must then be adapted to each thickness such that the aspect ratio *Δe/Δr* remains constant.

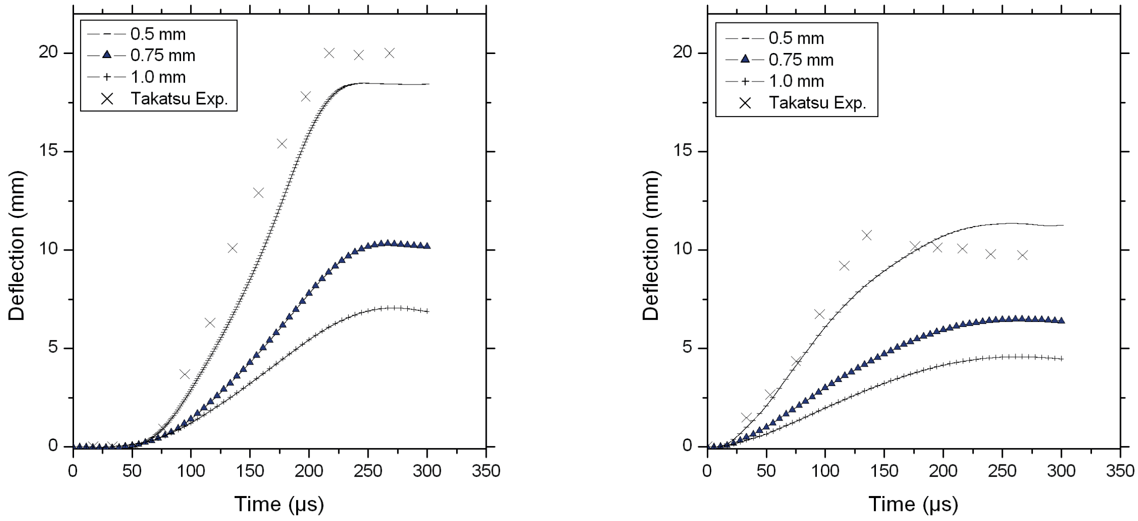

(a) *(b)*

Figure IV-5: Predicted vertical deflections of the sheet for various sheet thicknesses: (a) for a sheet radius equal to 0 mm (b) for a sheet radius equal to 20 mm.

The vertical deflections of two points of the workpiece are presented in Fig. IV-5. The first point corresponds to the sheet centre (Fig. IV-5a) and the second one to a point *20 mm* away from the centre (Fig. IV-5b). The FE predictions plotted in Fig. IV-5 show that the higher the sheet thickness, lower is the workpiece deflection during the process. The sheet thickness has a significant influence on the magnetic flux density, the Lorentz force and then on the maximum height achieved by the metal sheet in free bulging EMF test.

IV.2.3. Effect of Gap distance dg

In this section, the influence of gap distance is studied. In accordance with the experiments of Takatsu *et al*. [4], the electrical conductivity of the workpiece is kept constant at *36 MS/m* and the sheet thickness is taken equal to *3 mm*. Firstly, the metal sheet is assumed to be fixed.

Three different values of gap distance were considered: *1.5*, *3* and *4.5 mm*. The discretization of the workpiece is defined to be *20* x *110*, which means *20* elements in the thickness direction while *110* elements along the radius of the workpiece are applied. For the three values of gap distance, calculations with our in-house finite difference code [5] have been performed. Predictions obtained with our in-house finite difference code [5] are presented in Fig. IV-6 and Fig. IV-7. The distribution of the radial component of the magnetic field density predicted for three gap distance values is presented in Fig. IV-6.

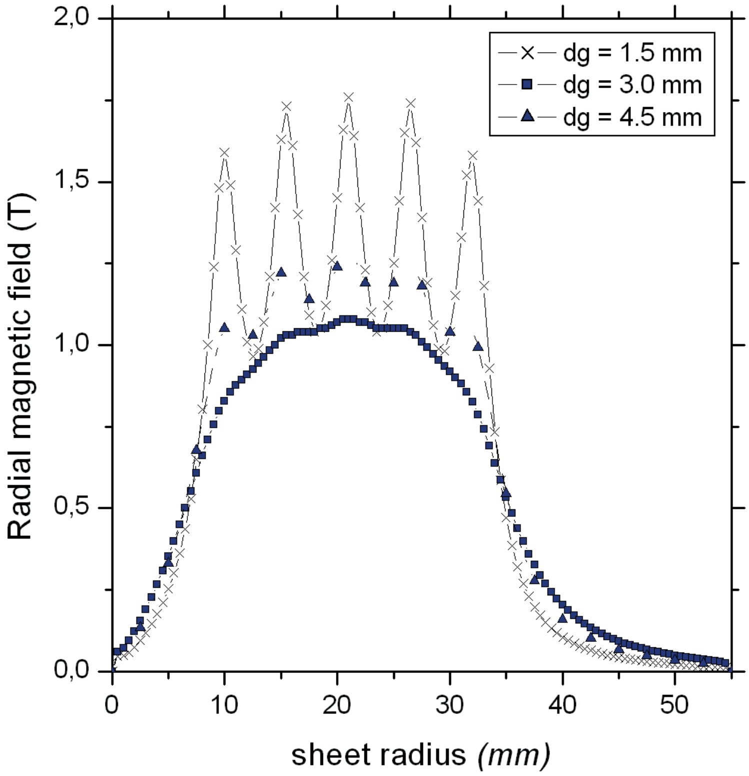

Figure IV-6: Radial distribution of the radial component of magnetic field Br for three values of gap distance.

In changing the relative gap distance between the coil and the workpiece, the distribution of the magnetic field intensity in the space will be affected. From Fig. IV-6, the smaller the gap between the workpiece and coil is, the lesser is the mutual inductance hence higher magnetic field. From Fig. IV-6, the distance between the workpiece and the coil seems to play a major role in the distribution of the magnetic field. The diffusion of the axial force through the thickness at a radial position (equal to *22 mm*) and the different gap distance values are presented in the Fig. IV-7. As indicated above, the magnetic force density increases through the thickness of the workpiece with the low gap distance. The distance between the coil and workpiece slightly influences magnetic force and therefore, decreases in the magnetic field density.

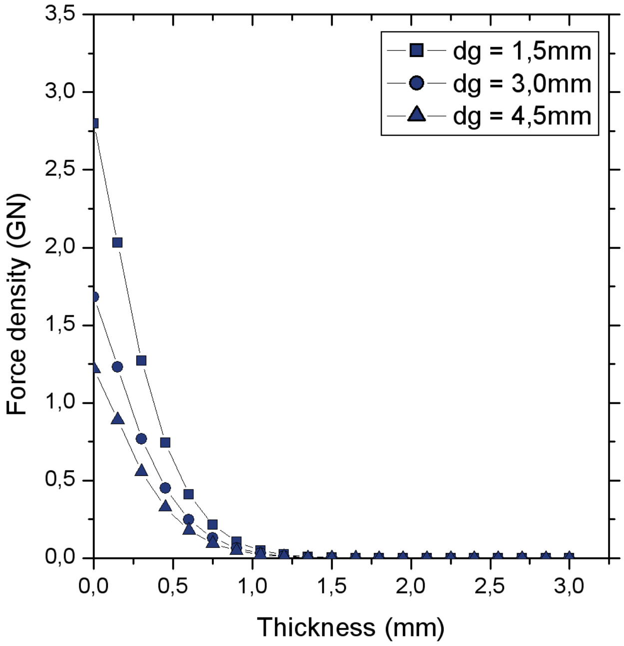

Figure IV-7: Axial force Fz distribution through thickness at peak value for different values of gap distance.

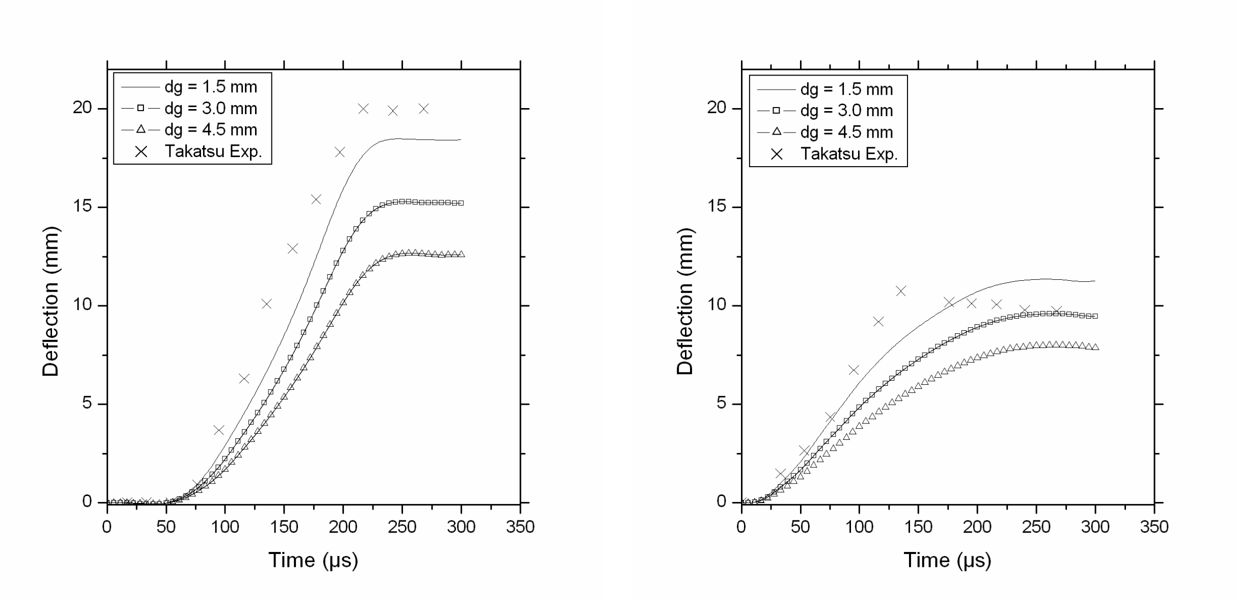

(a) *(b)*

Figure IV-8: Vertical deflection of the sheet predicted for different gap distance values:
(a) for a sheet radius equal to 0 mm, (b) for a sheet radius equal to 20 mm.

After these preliminary calculations, numerical simulations of the free bulging EMF process are carried out with the commercial FE code ABAQUS/Explicit [3]. The electrical conductivity of the workpiece is kept constant at *36 MS/m.* The thickness of the workpiece is now taken equal to *0.5 mm* (in accordance with Takatsu *et al.*[4]). Consequently the meshing was also adapted to this thickness (*4* x *170* elements; *4* elements through the thickness and *170* elements along the sheet radius). The vertical deflection of the workpiece centre and of a point *20 mm* away from the centre is depicted in Fig. IV-8. The deflection of workpiece centre is significantly affected by the change of gap distance. Therefore the distance between the workpiece and the coil plays a major role in the free bulging EMF of a metal sheet.

IV.2.4. Influence of discharge current frequency ω

The discharge current frequency is one the most significant parameters that is required to be investigated and optimized for the analysis of EMF process. The effects of the current frequency are very complicated as it depends on several other circuit parameters. In a given discharge circuit for EMF process, the discharge current frequency is mainly determined by the total capacitance of the capacitor bank or by the total inductance (mainly by changing the geometry of the coil). The frequency of the discharge current depends upon the circuit parameters as follows:

$$\omega = \frac{1}{\sqrt{LC}} \qquad \text{(IV-1)}$$

where C is the capacitance of the capacitor bank and L the inductance of the circuit. In this section, the changes in the frequency have been obtained by modifying the total inductance of the circuit. The discharge energy is then held constant while the inductance of the circuit is changed. Different values of current frequency have been employed: *46.75*, *62.30*, *74.80*, *93.50*, *116.78*, *140.25* and *187.50* MHz. From Eq. II-57 defined in the second chapter, the temporal evolutions of the discharge current are calculated and plotted in Fig. IV-9.

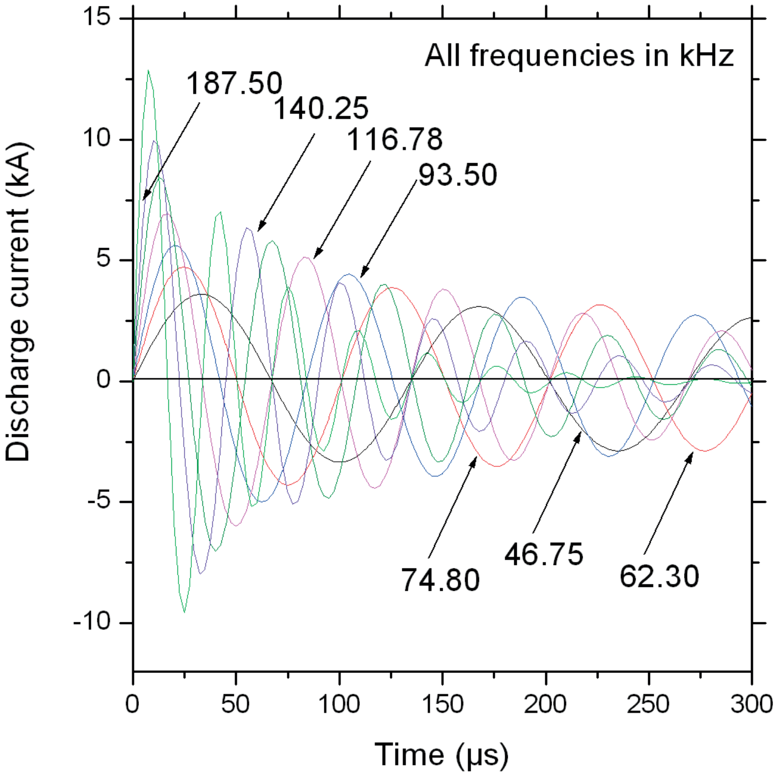

Figure IV-9: Evolution of the discharge current intensity flowing through the flat spiral coil for different values of discharge frequency.

For each frequency plotted in Fig. IV-9, the first positive maximum peak of the discharge current is obtained at a different time step. Simulations with our finite difference code are carried out for the different values of time for which the first positive maximum peak of the discharge current is obtained. As defined in the other sections, the electrical conductivity of the workpiece is kept constant at *36 MS/m* and the sheet thickness is taken equal to *3 mm*. The metal sheet is assumed to be fixed. The gap distance between the coil and the workpiece is taken equal to *1.5 mm*. The discretization of the workpiece was defined to be *20* x *110*, which means *20* elements in the thickness direction while *110* elements along the radius of the workpiece are used. The distribution of the radial magnetic field density, B_r is presented in Fig. IV-10, for each discharge current frequency. The B_r values obtained correspond to each first positive peak of the discharge currents respectively.

The damping of the discharge current is slower if the frequency is low, Fig. IV-10. Moreover, the magnitude of the current is also low, when the frequency is small. We can conclude that when the frequency is low, the magnitude of the current is lower with larger decaying time.

Thus, the magnitude of magnetic field density decreases when discharge current frequency decreases, Fig. IV-10. Our predictions are in agreement with the results presented in Haiping and Chunfeng [7].

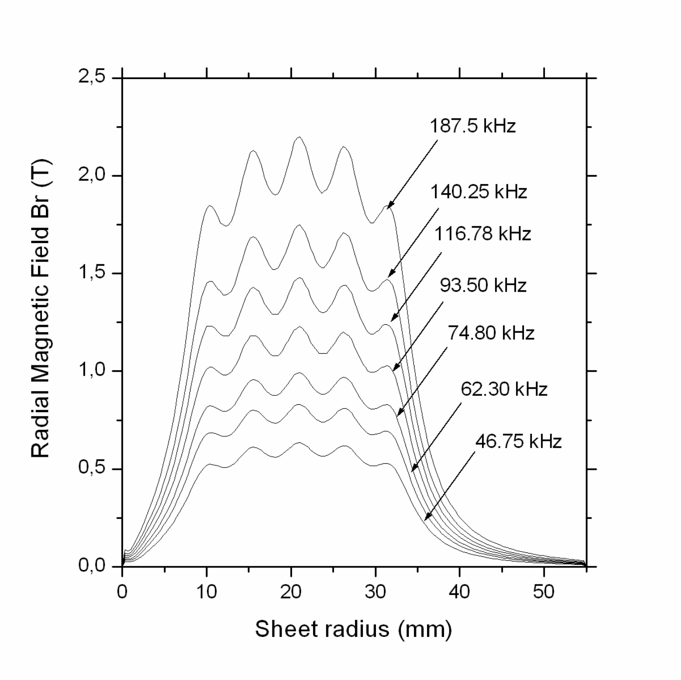

Figure IV-10: Distribution of the radial component of magnetic field Br as function of discharge current frequency

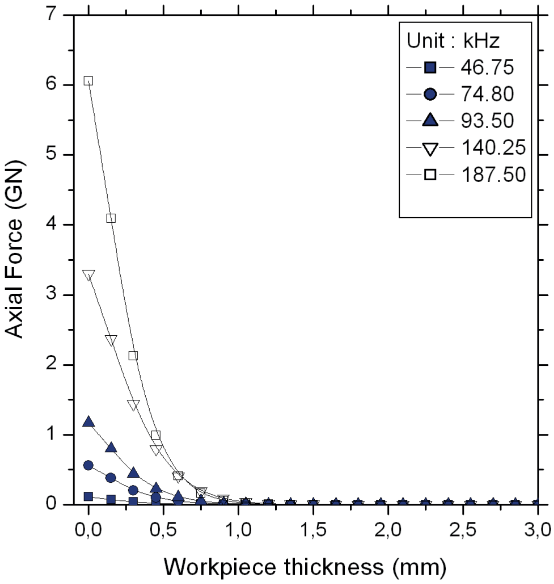

Figure IV-11: Distribution through thickness of the axial component of the Lorentz force Fz for different discharge current frequency values.

In Fig. IV-10, the maximum value of the magnetic flux density is obtained for a radius roughly equal to *22 mm*. At this sheet radius value and at each maximum positive magnitude of the discharge current, the penetration of the Lorentz force is plotted in Fig. IV-11. In order to evaluate the effect of the frequency, the penetration of the force at the maximum positive magnitude of the discharge current is compared. As attempted, the maximum values of the axial component of the Lorentz force is obtained at the sheet surface close to the coil. From Fig. IV-11, the magnitude of axial component of the Lorentz force increases as discharge current frequency increases since the first peak current magnitude increases as discharge current frequency increases.

Table IV-2. Current frequency and corresponding maximum magnetic field and maximum magnetic pressure

Current Frequency	**Peak Time**	**Br_{max}**	**Pz_{max}**
kHz	μs	T	MPa
187.50	7.5	2.15	1.85
140.25	10.0	1.71	1.18
116.125	12.5	1.44	0.842
93.50	17.5	1.13	0.552
74.875	22.5	0.916	0.377
62.30	27.5	0.767	0.263
46.75	32.5	0.586	0.153

As mentioned in paragraph 2, the axial pressure acting on the sheet can be calculated by integrating the axial component of the Lorentz force through the sheet thickness. Due to the uniform distribution of the magnetic pressure, the maximum magnetic field density and maximum pressure are experienced roughly at the middle of the disc (*22.5 mm* from the centre). The maximum values of the axial magnetic pressure and of radial magnetic field density are reported in Table IV-2. We observed that the pressure increases when current frequency increases. Higher frequencies have larger magnitude with short peak time period, however, for the lower frequency the pulse has longer period with slower decay. Thus the deformation of the workpiece may be quicker for higher frequencies as compared to the lower ones. As mentioned above, higher discharge current frequency results in quick damping of the current, while the increase in the current magnitude is obtained. Thus we can conclude that higher frequency may balance a low conductivity and a large wall thickness, resulting in high magnetic pressure.

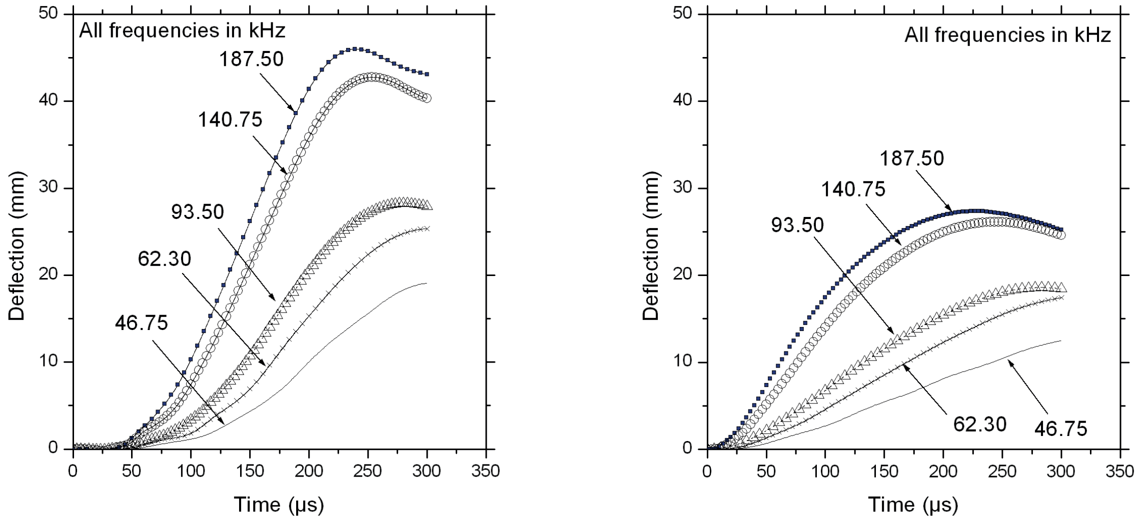

(a) *(b)*

Figure IV-12: Vertical deflection of the sheet for different discharge frequency values: (a) for a sheet radius equal to 0 mm (b) for a sheet radius equal to 20 mm.

Numerical simulations of the free bulging EMF process are next carried out with the commercial FE code ABAQUS/Explicit [3]. All the simulations are carried out for constant energy of *80 J*. The electrical conductivity of the workpiece is kept constant at *36 MS/m*. The initial gap distance between the coil and the workpiece is taken equal to *1.5 mm*. The thickness of the workpiece is now taken equal to *0.5 mm* (in accordance with Takatsu *et al.* [4]). Consequently the meshing is also adapted to this thickness (*4* x *170* elements; *4* elements through the thickness and *170* elements along the sheet radius). The displacement of the two particular points (at the centre and at a radius of *20 mm*) predicted by ABAQUS/Explicit [3]are presented in Fig. IV-12. The predicted displacement is higher when the discharge current frequency is higher. It is noticed that the displacement of sheet centre begins roughly at *50 μs*, which means after the first positive peak of each discharge current. The displacement of the sheet center is driven by the kinetic forces of the process but it is independent of discharge current frequency.

IV.2.5. Intensity of the charging voltage V_0

In this section, the influence of charging voltage V_0 is studied. In accordance with the experiments of Takatsu *et al.* [4], the electrical conductivity of the workpiece is kept constant at *36 MS/m* and the sheet thickness is taken equal to *3 mm*. The metal sheet is assumed to be fixed. Three values of the charging voltage have been used: a low value (*3 kV*), a medium value (*6 kV* corresponds to the experiments of Takatsu *et al.* [4]) and high value (*9 kV*). The discretization of the workpiece is defined to be *20* x *110*, which means *20* elements in the thickness direction while *110* elements along the radius of the workpiece are applied. For the three values of charging voltage, calculations with our in-house finite difference code [5] have been performed. Predictions obtained with our in-house finite difference code [5] are presented in Fig. IV-13. The distribution of the radial component of the magnetic field density predicted for three charging voltage values is presented in Fig. IV-13.

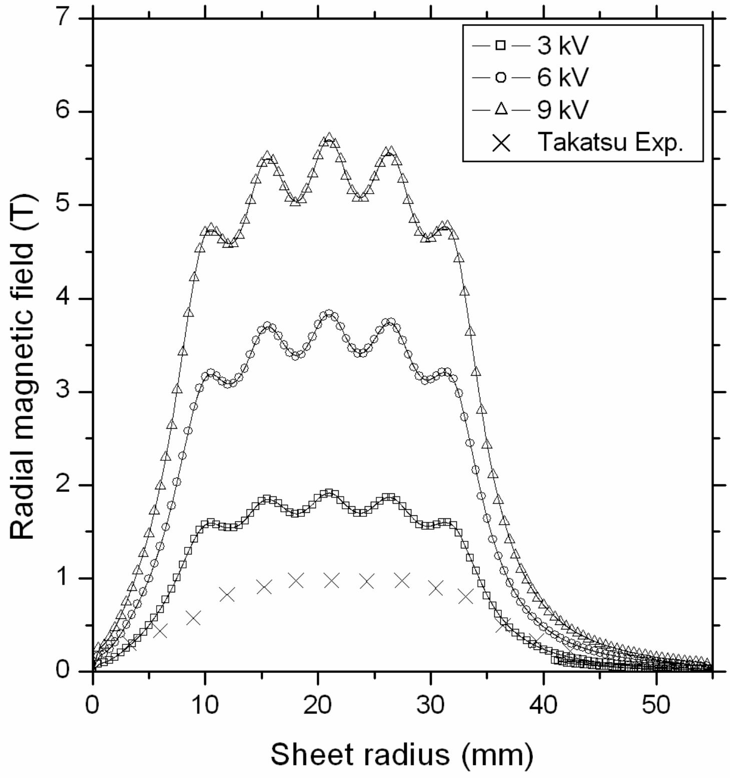

Figure IV-13: Radial distribution of radial component of magnetic field Br for different charging voltage values.

In Fig. IV-13, we observe that the higher the charging voltage is, the higher is the magnitude of the magnetic field. The large magnetic field develops due to high charging voltages, results in a higher Lorentz force acting through the thickness of the workpiece. This is illustrated in Fig. IV-14.

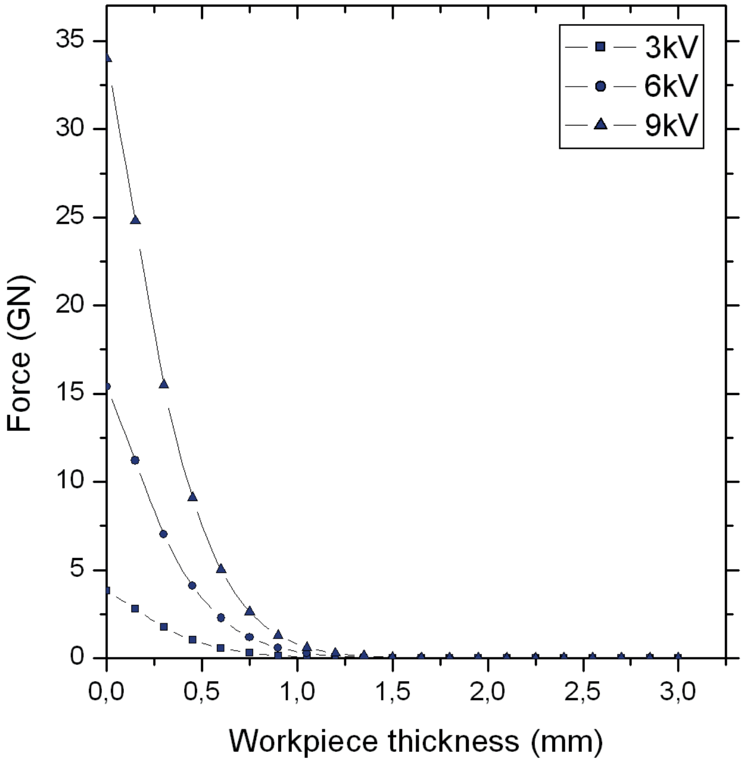

Figure IV-14: Distribution through thickness of axial Lorentz Fz for different values of charging voltages.

On the contrary, in Fig. IV-14, the axial component of Lorentz force vanishes at different distance values from the sheet surface close to the coil. In Fig. IV-14, the axial component of Lorentz force vanishes at a distance of *1 mm* from the sheet surface close to the coil. This critical distance is independent of charging voltage values. The penetration of the Lorentz force through sheet thickness is then independent of charging energy value.

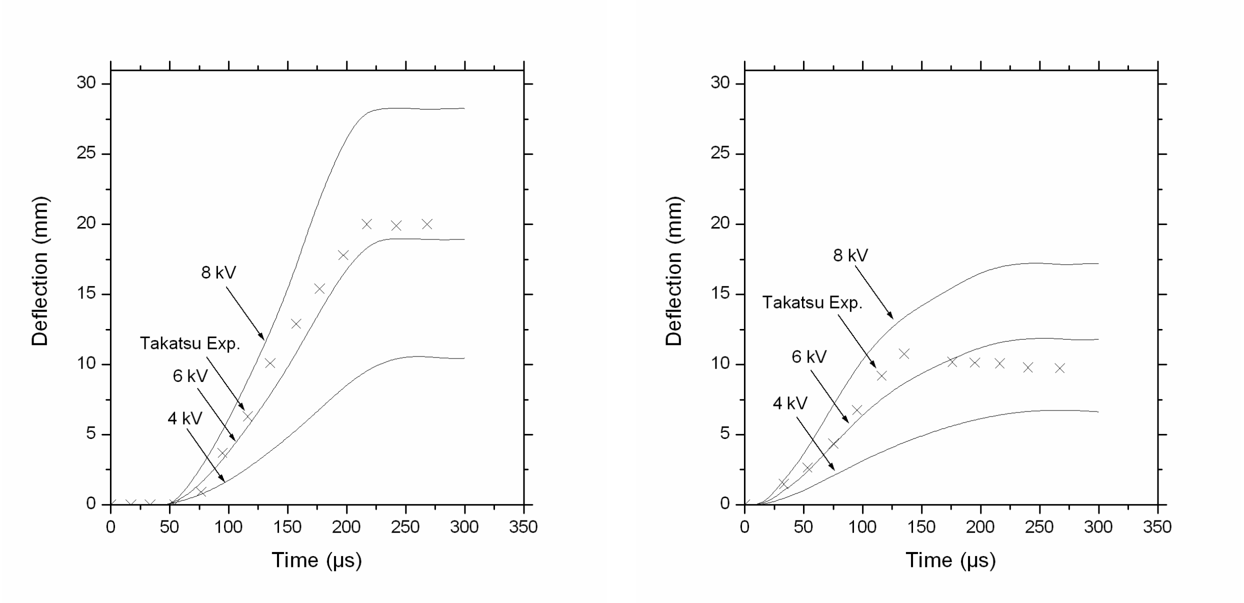

(a) *(b)*

Figure IV-15: Vertical deflection of the sheet at different charging voltage V_0 :
(a) for a sheet radius equal to 0 mm (b) for a sheet radius equal to 20 mm.

FE simulations of the free bulging EMF process are next carried out. The test geometry and the FE model are described in details in chapter III. The electrical conductivity of the workpiece is kept constant at *36 MS/m*. The initial gap distance between the coil and the workpiece is taken equal to *1.5 mm*. The thickness of the workpiece is now taken equal to *0.5 mm* (in accordance with Takatsu *et al.* [4]). Consequently, the meshing is also adapted to this thickness (*4* x *170* elements; *4* elements through the thickness and *170* elements along the sheet radius). The FE simulations have been performed for the three different values of charging voltage. The predicted displacements of the pole (centre point of the workpiece*, r = 0 mm*) and of a point at a radial distance of *20 mm* from the centre are presented in Fig. IV-15. For all the cases, the centre of the workpiece lags in deformation. This is due to the dead spot in the pressure distribution associated at the centre of the spiral coils. The pole deforms upwards due to inertial effects, producing the final shape. As accounted, the sheet deformation depends on the initial charging voltage in the capacitor bank. The deformation of the sheet increases as the charging voltage increases.

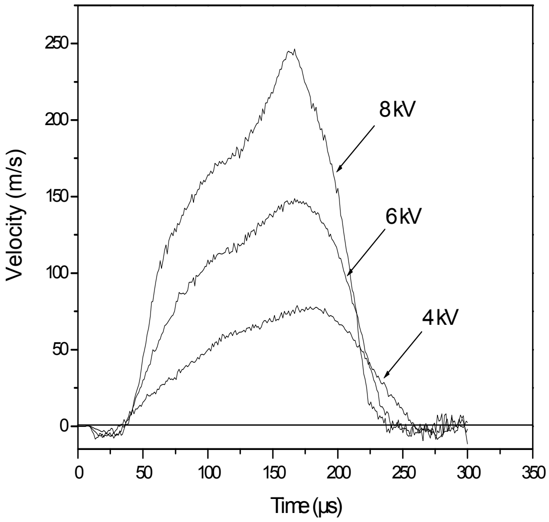

Figure IV-16: Axial velocity of the workpiece for different charging voltages V_0.

For each charging voltage, the axial velocity at the centre of the sheet is plotted, Fig. IV-16. Only the magnitude of the axial velocity is affected by the charging energy. The maximum value of the velocity recorded in our FE simulations is around of *250 m/s*. This value has been obtained for the higher charging voltage (i.e. *9 kV*). The predicted velocities are small enough to fulfil the assumption that the sheet velocity does not affect the magnitude of the electromagnetic field density during the forming process (in agreement with [8], sheet velocity < 10^7 *m/s*). For all the charging voltages studied, the peak velocity is observed at around *150 µs* for each case. After this the velocity decreases. We noticed the presence of negative velocity values by the end of the simulations. This is due to the decaying of the energy diffusion from plastic deformation and inertial effects in the FE simulations.

IV.3. Springback predictions

When a sheetmetal is bent, it strains both plastically and elastically. Since all the materials have a finite elastic modulus, normally plastic deformation is followed by some elastic recovery when the load and tooling are removed. During the unloading process, elastic strain is released and the residual stresses are redistributed through the workpiece, resulting springback [9]. Springback (very commonly known as elastic recovery) is related to the change in shape between fully loaded and unloaded configurations of the material, encountered during a bending/ forming process. A common example of the dimensional discrepancies due to springback after tooling removal is shown in Fig. IV-17.

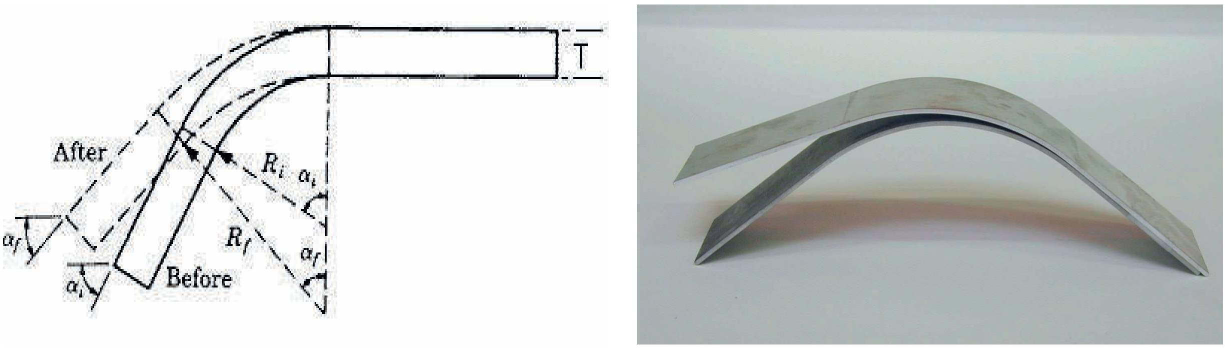

(a) *(b)*

Figure IV-17: Springback in sheetmetal forming process [9, 10].

Sheetmetal forming processes require a detailed and precise prediction of springback to avoid assembly problems. In the past, the prediction of the final workpiece geometry after bending, were dependent upon the designer's experience. The final shape predictions normally involved trials and errors to achieve the desired results. With the development of numerical tools, these trials and errors can radically be eliminated, while the final geometry can accurately be foreseen using appropriate methods. For almost all commercial FE codes available at the market, and for most of the numerical studies carried out in the literature, a static implicit analysis with the one-step unloading scheme has been used to predict springback. In the one-step unloading scheme, artificial boundary conditions must be added to prevent rigid body motion and avoid convergence problems since tooling is suppressed. In this study, the springback predictions are performed with the commercial FE code ABAQUS/Standard [11] (static implicit solver) using the one-step unloading scheme. In order to obtain a better understanding on how EMF can reduce springback, we have decided to simulate and to compare three different forming processes: an electromagnetic free bulging process, an electromagnetic die forming process and a conventional deep drawing process.

IV.3.1. Springback in free bulging EMF process

As presented in chapter III, the FE simulations of the deformation process are carried out using the commercial FE code ABAQUS/Explicit [3]. Three different energy levels, with changing charging voltages, are used to account for changing deformation levels during the free bulging: *4 kV*, *6 kV* and *8 kV*. For the FE predictions of springback, the commercial FE code ABAQUS/Standard [11] is employed. ABAQUS/Standard [11] is a static implicit (time scheme integration) solver. The results from the forming simulation in ABAQUS/Explicit [3] are imported into ABAQUS/Standard [11], and a static analysis calculates the springback. During the springback simulation, an artificial stress state that equilibrates the imported stress state is applied automatically by ABAQUS/Standard [11] and gradually removed during the simulation. The displacement obtained at the end of the simulation is the springback and the stresses give the residual stress state. In the FE simulations of the springback, the mesh of the metal sheet used with ABAQUS/Explicit [3] is conserved in ABAQUS/Standard [11]. Furthermore, the upper and lower holders are removed in the springback simulation. New boundary conditions are applied to the metal sheet, such that the centre of the workpiece is restrained in *x* and *z* direction and the rotation around the *y* axis is also constrained. The final shapes of the sheets obtained for the three charging voltages are presented in Fig. IV-18.

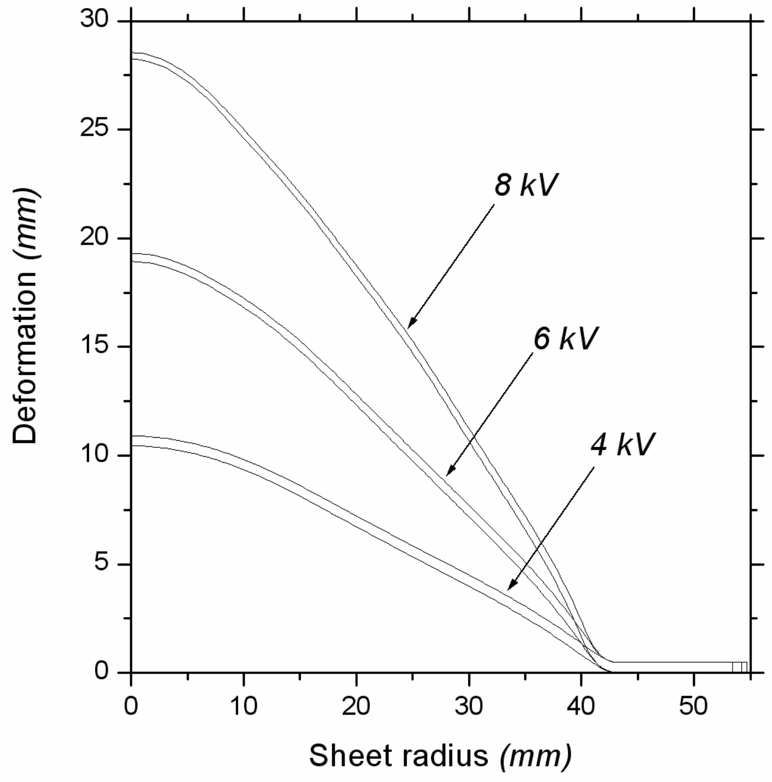

Figure IV-18: Deformed geometry predicted with ABAQUS/Explicit in the case of free bulging EMF process.

With the increase in the charging voltage, the metal sheet undergoes a larger deformation, Fig. IV-18. The radial distribution of effective plastic strain achieved at the final time (*300 μs*) is measured at mid thickness of the sheet and is plotted in Fig. IV-19.

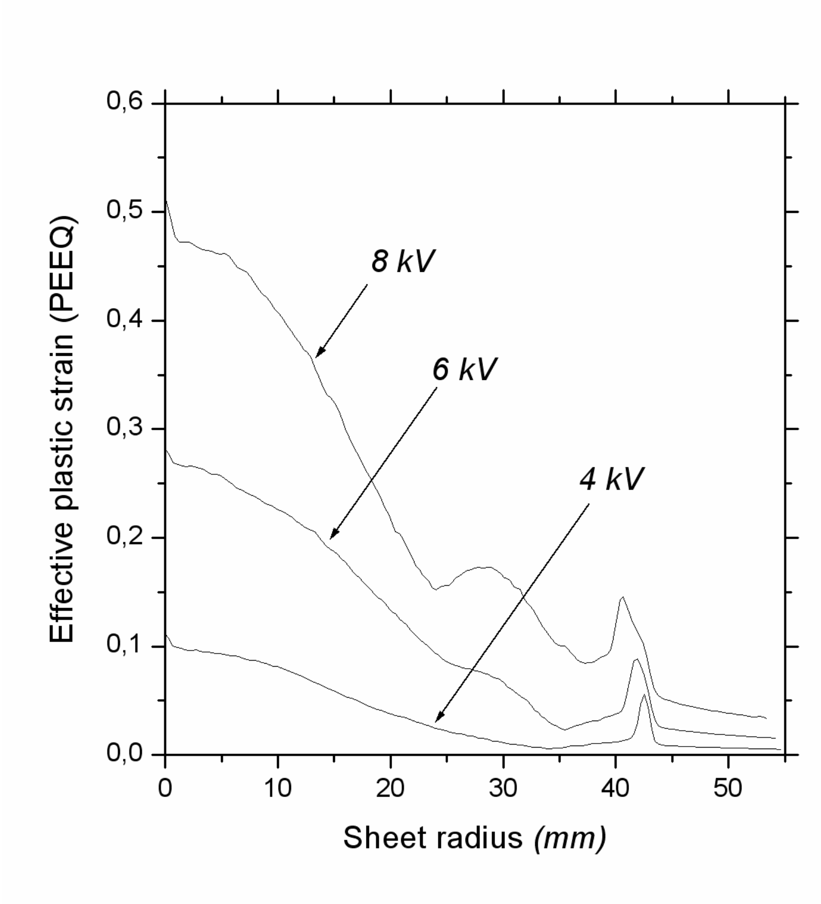

Figure IV-19: Radial distribution of effective plastic strain at final time step of forming simulation.

As attempted, in Fig. IV-19, higher voltage results in higher effective plastic strain values and then in a higher sheet deformation during the free bulging EMF process. The centre of the workpiece undergoes large plastic deformation, while the edges contain very low levels of plastic strain. As it is well-known, higher the plastic deformation during a forming process is, the lower would be the elastic recovery after unloading. For comparison purposes, in Fig. IV-20, the deformed geometry and the geometry after unloading are then superimposed for each case of charging voltage.

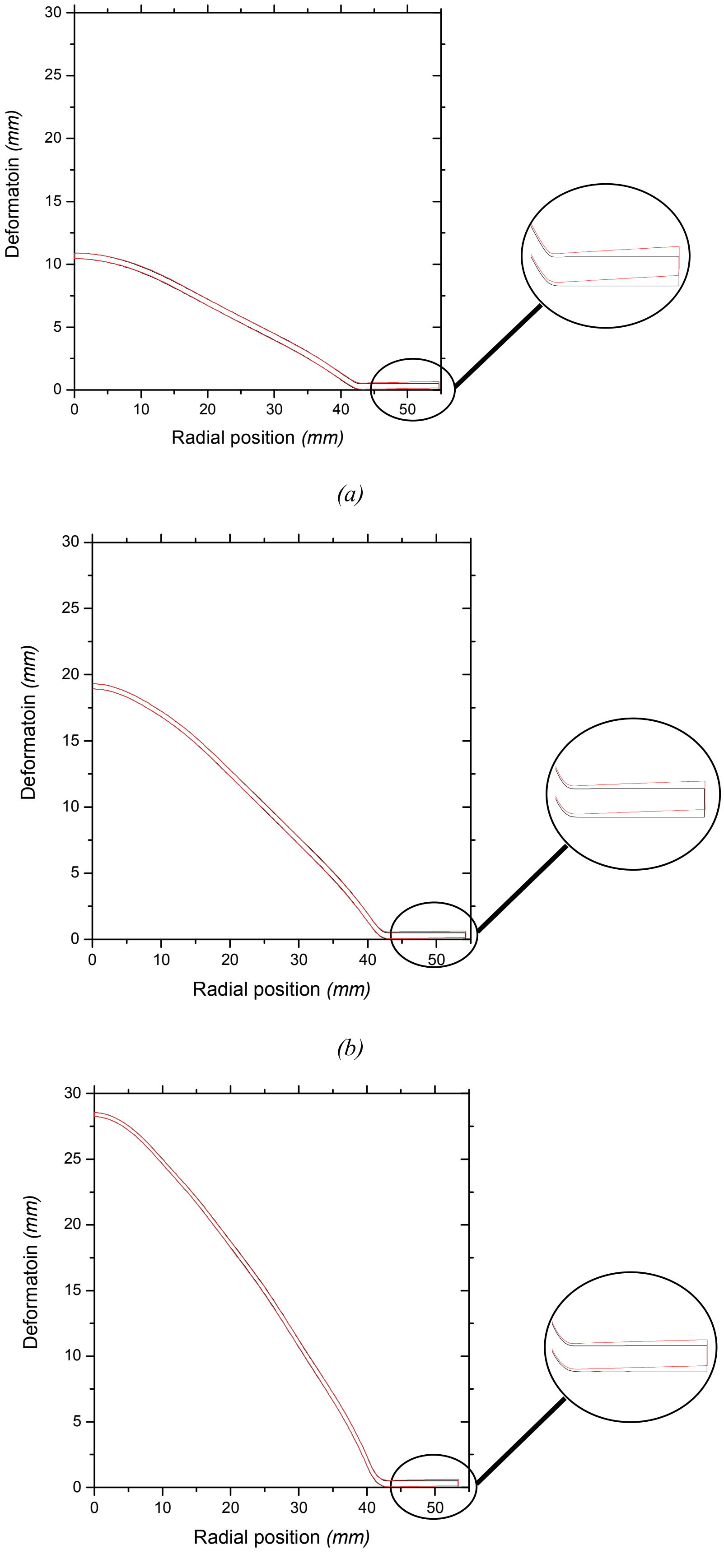

(a)

(b)

(c)

Figure IV-20: Comparison of deformed geometry with the geometry obtained after elastic recovery (springback) for free bulging simulations (a) 4 kV (b) 6kV (c) 8 kV.

For all the charging voltages studied, the springback is only concentrated in the sheet region in contact with the holders, Fig. IV-20. The amount to which the geometry has changed during the free bulging EMF process can be considered as very low. The weak values of elastic recovery observed in Fig. IV-20 can perhaps be attributed to very high deformation velocities and to high effective plastic strain levels achieved in EMF.

IV.3.2. Springback in die EMF process

In the second series of simulations, we used a conical die placed on top of the workpiece. The height of the forming die was fixed at approximately *16 mm*, which is consistent with the deformed height achieved for a free bulging test at *6 kV* charging voltage. During the forming process, a blank holder force is applied to restrict the vertical movement of the die due to the impact/contact of metal sheet. Two different values of blank holder force are employed: *5 kN* and *10 kN*. The final deformed geometry of the sheet does not change when the blank holder force changes. In the present study, we present only the predictions obtained with a blank holder force equal to *10 kN*. Final deformed geometry for three different charging voltage values is presented in Fig. IV-21.

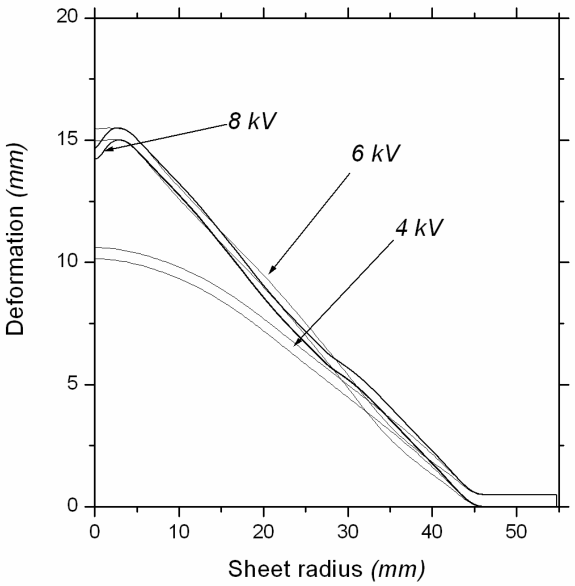

Figure IV-21: Deformed geometry predicted with ABAQUS/Explicit for EMF process with a die.

As the height of the forming die is fixed at approximately *16 mm*, the workpiece had not come into contact with the die for a *4 kV* charging voltage, Fig. IV-21. However for the other two charging volatge values, the deformation of the workpiece attained the contact. A rebound phenomenon of the workpiece after the contact with the die is observed for *8 kV* charging voltage, Fig. IV-21. This is attributed to the very high workpiece acceleration during the discharge of the current at higher voltage, resulting in very high magnetic pressure developed during the first positive half cycle [12]. The metal sheet stored a high level of kinetic energy during the EMF process. This high value of kinetic energy must be transferred from the workpiece to the die [13]. But for the charging voltage of *8 kV*, the kinetic energy can not dissipate completely, thus the rebound phenomenon occurs, Fig. IV-21.

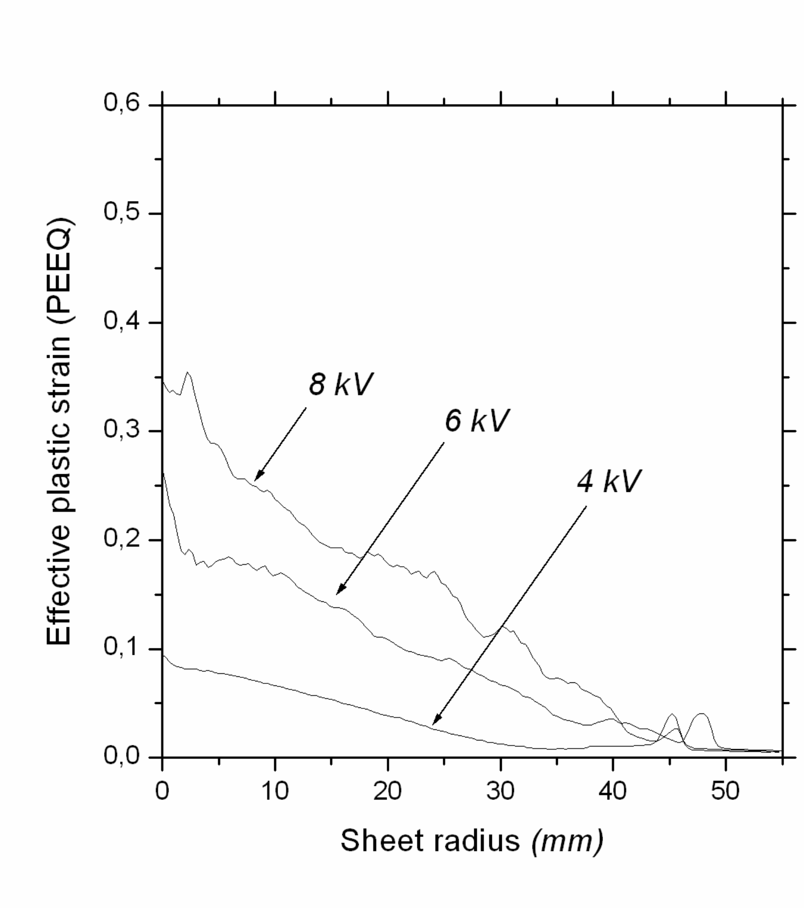

Figure IV-22: Radial distribution of effective plastic strain at final time step of forming simulation (case of EMF process with a conical die).

The effective plastic strain developed during the forming process with a conical die is studied. The comparison between the different radial distributions of plastic strain achieved for the three charging voltages is presented in Fig. IV-22. For the charging voltages of *4 kV* and *6 kV*, the plastic strain magnitudes achieved are comparable to the ones obtained during the free bulging EMF simulations. Similar trends for the levels of plastic strains for the three voltages is achieved, such that, for higher voltage the strain is higher, while for low voltage this value is slightly inferior. However, for the charging voltage of *8 kV*, the plastic strain distribution changes drastically. The magnitude of the effective plastic is lower when a conical die is used than in the case of free bulging (maximum value of *0.35* with a die and *0.5* with out a die). For all charging voltages, the geometries obtained after forming and after unloading have been compared. The metal sheet deformation comparisons are presented in Fig. IV-23.

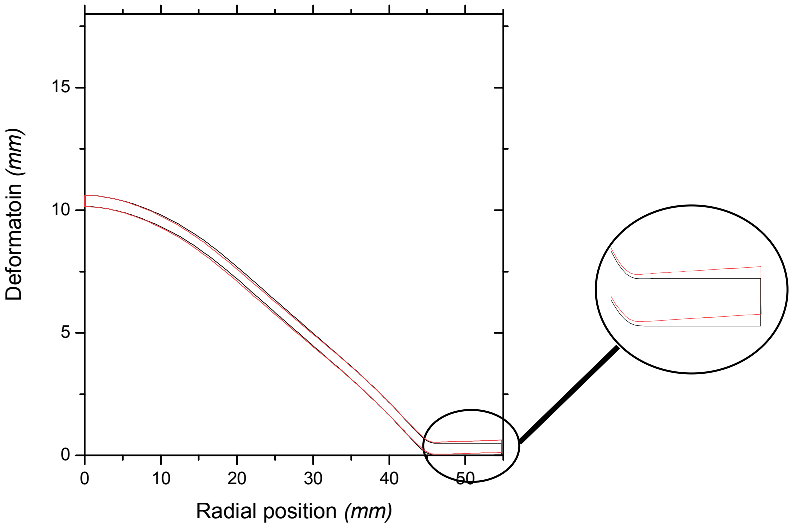

(a)

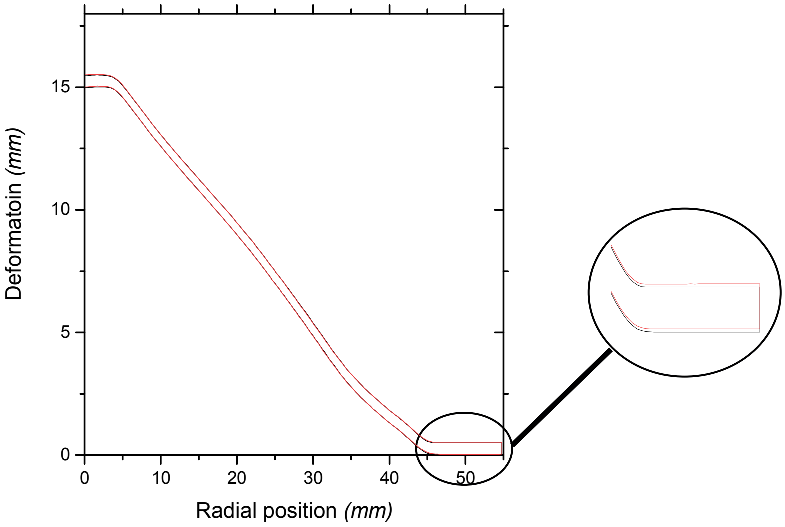

(b)

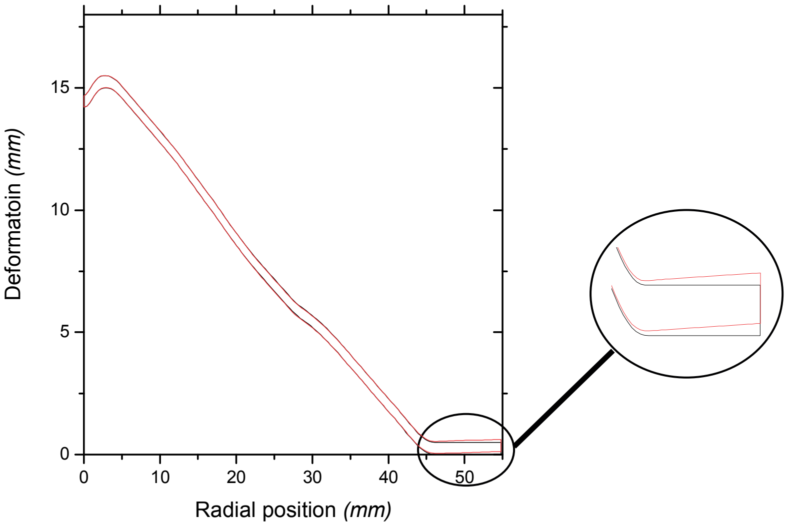

(c)

Figure IV-23: Comparison of deformed geometry with the geometry obtained after elastic recovery (springback) for FE simulations with a conical die (a) 4 kV (b) 6kV (c) 8 kV.

In the case of EMF with a conical die, the springback is only concentrated in the sheet region in contact with the holders, Fig. IV-23. The same result has been obtained in the case of free bulging EMF process. We noticed that the elastic springback observed after the EMF die forming process is of very low magnitude for all the three cases of the charging voltage. It is noticed that the springback is quasi non-existent for a charging voltage of *6 kV*, Fig. IV-23b. the springback increases when charging voltage is too high or too low, Fig. IV-23 case (a) and (c).

IV.3.3. Springback in a conventional deep drawing process

Conventional forming processes are normally considered as quasi-static deformation processes. In contrast to the high velocity forming processes, the deformation of the workpiece takes place at a considerably low speed. In order to compare the numerical prediction obtained from the two EMF process, we considered a deep drawing process. The workpiece material parameters were kept as same as the ones used for EMF forming processes. An axisymmetric approach is used. A punch is employed to obtain the deformation of the workpiece. An upwards velocity amplitude is used to defined the motion of the punch. This time varying amplitude of velocity corresponds to the total deformation attained after the free bulging process at *6 kV* discharge voltage, such that the deformation obtained after the punch displacement is the same as the one obtained after the EMF free forming process. The FE model developed for the simulations of the deep drawing process is presented in Fig. IV-24.

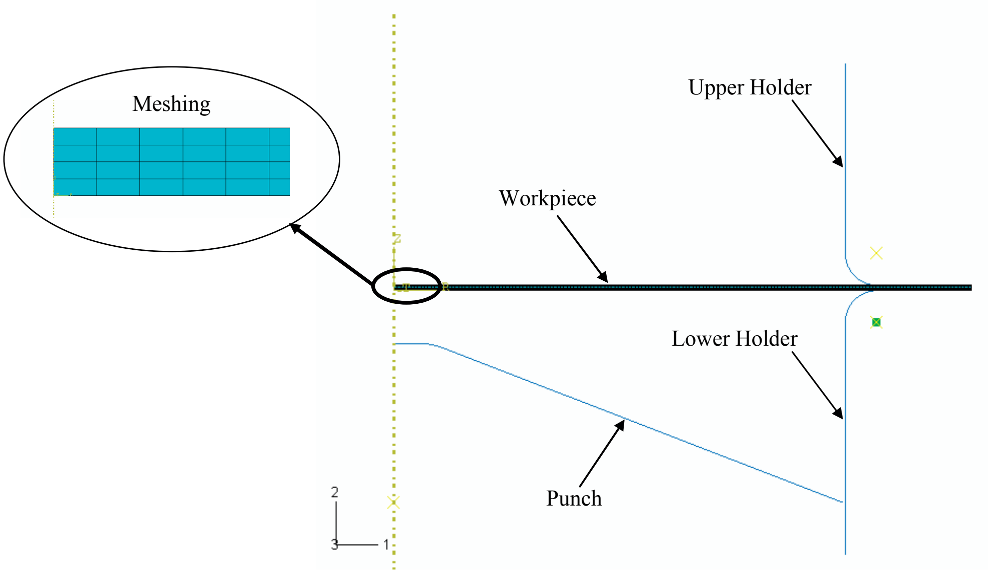

Figure IV-24: FE model for the simulation of deep drawing process.

The workpiece is meshed with *4* elements along the thickness, while *170* elements are applied in the radial direction which is consistent to the mesh used for the EMF free bulging process. The total time for the workpiece deformation during the simulation is fixed to *44 ms*.

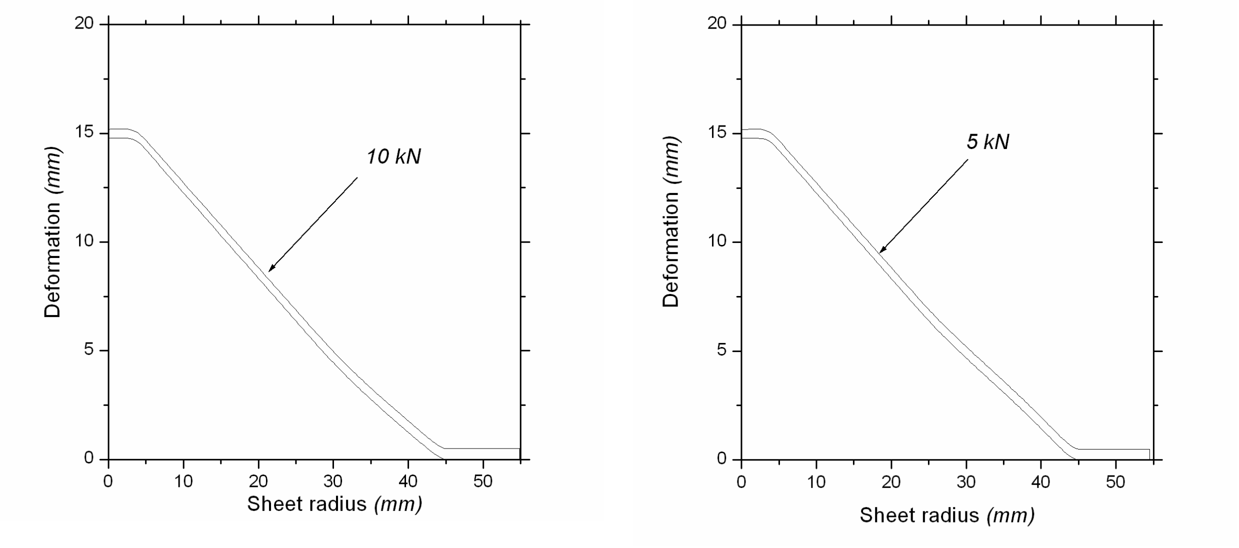

(a) *(b)*

Figure IV-25: Predicted deformed geometry in the case of a conventional deep drawing process: holder force of 5 kN (a) and of 10 kN (b).

Two different values of holder force (*5 kN* and *10 kN*) have been used to study the effects of clamping on workpiece deformation during the deep drawing process. The final deformed geometry of the workpieces is presented in Fig. IV-25.

The predicted deformed geometries are identical. The radial distributions of effective plastic strain obtained after the completion of the workpiece deformation are presented in Fig. IV-26. The plastic strain magnitude obtained with a holder force of *10 kN* is slightly higher than the one with a holder force of *5 kN*.

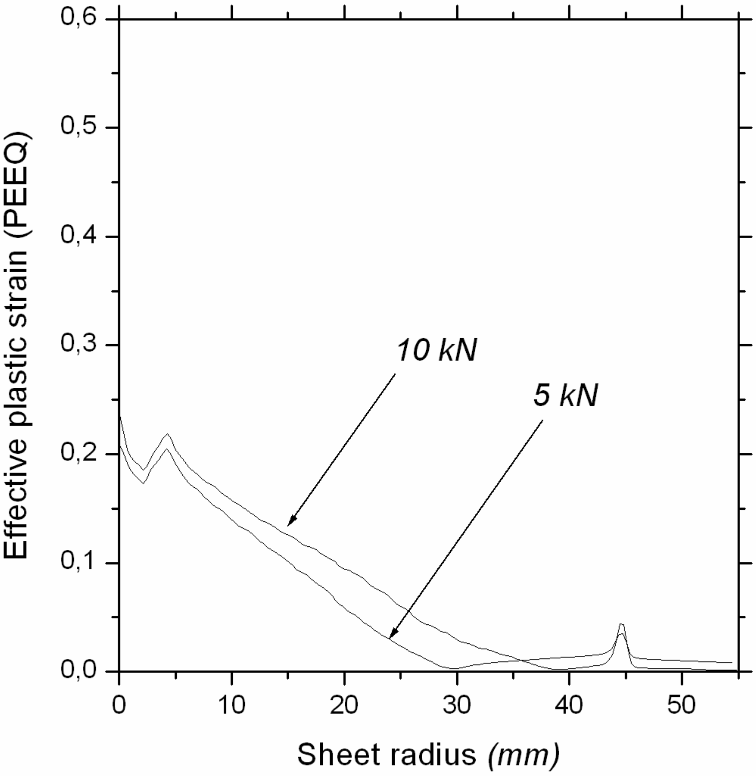

Figure IV-26: Radial distribution of effective plastic strain at final time step of deformation in the case of deep drawing process.

The springback predictions have been carried out in the same framework presented in section IV-3.1. Thus, the tooling is removed after the forming step. Additional boundary conditions have been added to avoid rigid body motions. ABAQUS/Standard [11] has been used to perform the FE predictions of springback. The comparison between the geometry achieved after the forming step and the geometry achieved after springback is shown in Fig. IV-27.

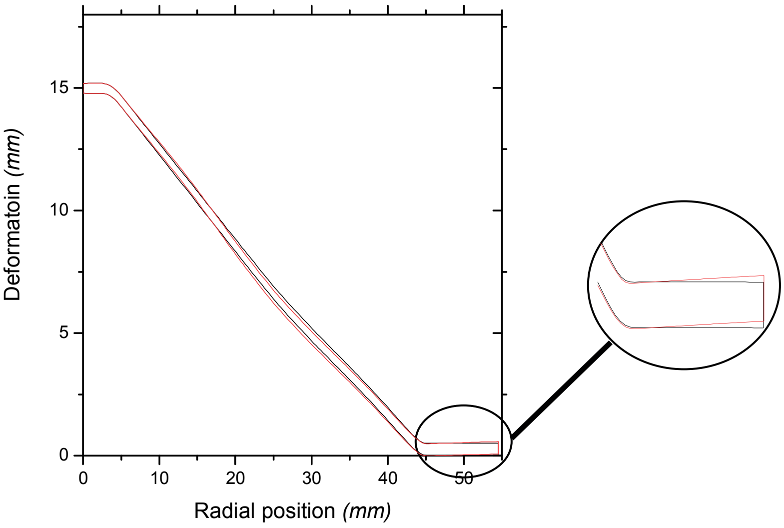

(a)

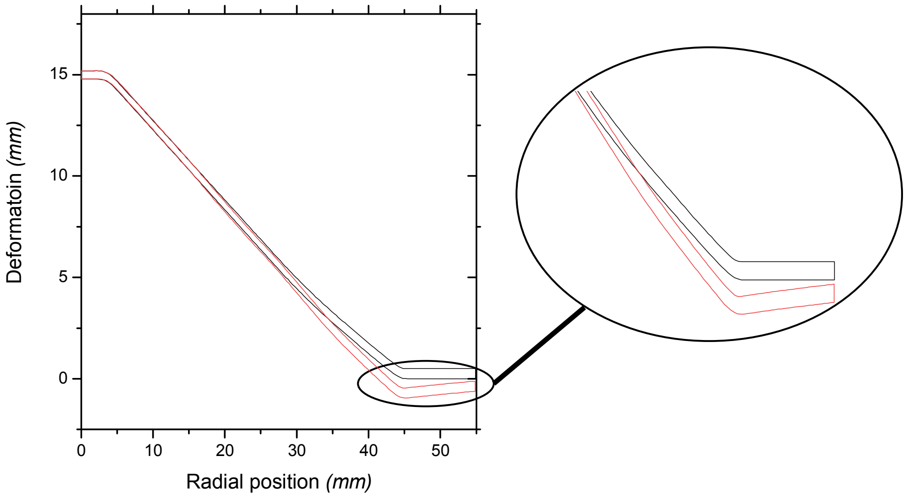

(b)

Figure IV-27: Comparison between the deformed geometry after the forming step with the geometry obtained after tooling removal (springback) for deep drawing simulations: holder force of 5 kN (a) and of 10 kN (b).

It is noticed that the springback is quasi non-existent for a blank holder force equal to *5 kN*, Fig. IV-27a. The springback increases significantly when the blank holder force increases, Fig. IV-27b. In order to compare the different forming processes, we have decided to compare the radial distribution of the effective plastic strain at the end of the forming step. The comparison of numerical predictions for the different forming processes is presented in Fig. IV-28.

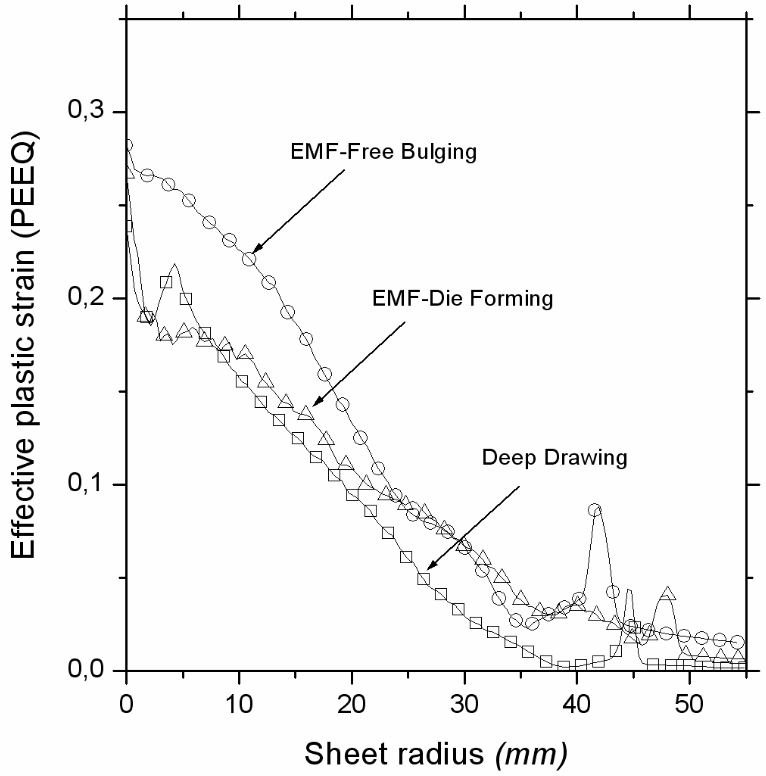

Figure IV-28: Comparison between the different forming processes: effective plastic strain.

For all the processes, the levels of the effective plastic strain are approximately similar at the centre of the workpiece, Fig. IV-28. However, for the conventional deep drawing simulation, the effective plastic strain decreases abruptly as we go away from the centre towards the edges. The radial distribution of effective plastic strain is uniform in the case of EMF. To show the advantage of EMF on the springback reduction, the final geometries (i.e. after the springback) predicted in the classical deep drawing and in the EMF with a conical die have been plotted in Fig. IV-29. The results in Fig. IV-29 have been obtained with a blank holder force of *10 kN*.

In Fig. IV-29, the springback is much more pronounced in the deep drawing simulation as compared to the final geometry obtained after the unloading in the case of EMF with a conical die. This reduced springback can be attributed to comparably higher plastic deformation achieved during the EMF process. Another reason which can explain the springback reduction is the very high speed of deformation during the EMF process. The high strain rates obtained during the EMF process provide inertial effects that plastically deform the material in a few microseconds. The springback reduction predicted by FE simulations is in agreement with the experimental results available in the literature [10].

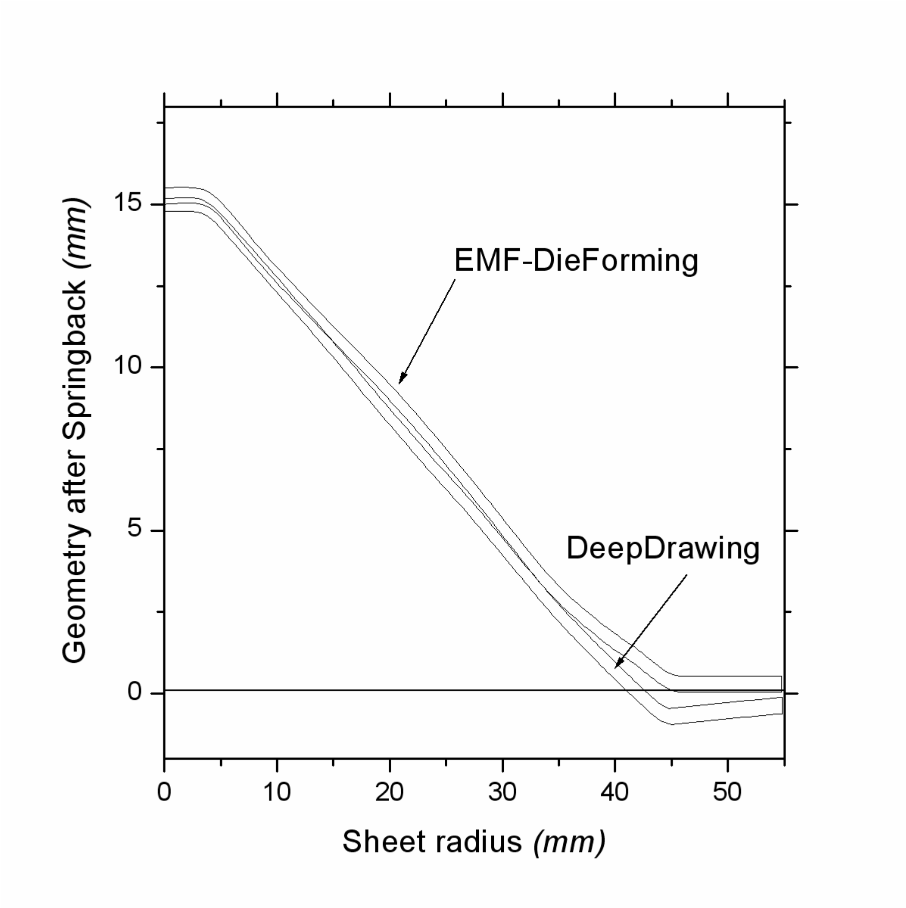

Figure IV-29: Springback predictions for deep drawing and EMF with a conical die.

Conclusion

In industrial processes, the sufficient knowledge of the influence of the process and geometrical parameters is inevitable. Determination of the optimum characteristics of the discharging circuit for the specific range of technology can provide major contribution towards the industrialization of the EMF process. In this chapter, the analysis of the process parameters within EMF of a sheetmetal is carried out. From the study, the following conclusions can be drawn:

1. Higher electrical conductivity of the workpiece results in higher magnetic field density. The shielding of the magnetic field is better with the depth of the workpiece. The shielding of the Lorentz force is improved. However, the deflection of the workpiece does not vary for the different electrical conductivities applied for the simulations.

2. The workpiece thickness influences the flow of the magnetic field during the process. The diffusion of the magnetic field is slower when the thickness is higher. The total deformation of the workpiece is smaller for larger sheet thickness. However, very low sheet thickness may contribute to the permeation of the magnetic field through the skin-depth, thus resulting in loss of Lorentz body forces. A combination of optimum frequency and sheet thickness will result in an efficient forming process.

3. The gap between the workpiece and the forming coil play a major role in the deformation process. The mutual inductance within the circuit component changes as the gap between the sheet and coil is increased. Smaller gap results in a lower inductance, and the penetration of the magnetic force is improved. This, results in higher magnetic pressure developed between the coil and the sheet.

4. It is difficult to investigate the effect of coil current frequency on the workpiece deformation, since it depends on several other factors. A higher frequency may account for a material of a low electrical conductivity, as the wave form of the current is very short with a very high positive peak. For the case of lower frequency, the pressure impulse has a smaller magnitude but is longer in time period, in comparison

to the duration of the workpiece deformation. Optimization of the current frequency by altering the capacitance of the bank, or changing the total inductance of the circuit would provide maximum deformation of the workpiece.

5. Another important parameter is the charging voltage. It governs the energy stored in the forming system. In this study, we observe that the higher the charging voltage is; higher are the magnetic field densities. The direct relation is also observed between the penetration of magnetic force and charging voltage. The final deflection of the workpiece is higher for high energy levels. The Lorentz body force exerted on the workpiece is proportional to energy discharge through the coil in the space between the coil and the workpiece.

In this chapter, numerical tools are also used for the prediction of the effects of several process parameters on the EMF process. The results obtained are satisfactory from the point of view of comparison with experiments [4], and can be used for design purposes. Further investigation on some other inter-related process parameters may open new doors for the implementation of the EMF process in the industry. Furthermore, a comparative study has been led so as to understand why the springback is reduced in EMF. Three different processes have been compared: EMF free forming, EMF with a conical die and conventional deep drawing. FE predictions allow us to compare the radial distribution of effective plastic strain in the different forming operations. In EMF, the radial distribution of effective plastic strain is more uniform than in a conventional deep drawing process. Moreover, the levels of the effective plastic strain are globally higher in EMF than in deep drawing. The springback predictions have next been performed. The FE results of the springback show that EMF reduces springback. This result is in agreement with the experimental results available in the literature [10]. The springback reduction seems to be due to the high plastic strain levels reached and to high strain rates experienced by the metal sheet.

References

[1] Kliener M., Beerwald C., Homberg W., Analysis of process parameters and forming mechanisms within the electromagnetic forming process, *Annals of the CIRP 54/01/2005*; pp. 225-228.

[2] Zhang H., and Murata M., Suzuki H., Effects of various working conditions on tube bulging by Electromagnetic forming, *Journal of Materials Processing Technology;* 48 *(1995),* pp. 113–121.

[3] ABAQUS/Explicit, Version 6.5 Manuals, Hibbitt, Karlsson and Sorensen Inc., Pawtucket, USA, 2005.

[4] Takatsu N., Kato M., Sato K., Tobe T., High speed forming of metal sheets by electromagnetic forces, *International Journal of Japanese Society for Mechanical Engineering* 1988 ; 60, pp. 142-148.

[5] Correia J.P.M., Siddiqui M.A.,. Ahzi S, Belouettar S. and Davies R., A simple model to simulate electromagnetic sheet free bulging process, *International Journal of Mechanical Sciences 50 (2008)*, pp.1466–1475.

[6] FEMM4.0, http://femm.foster-miller.net/wiki/HomePage

[7] Haiping Y.U., Chunfeng L.I., Effects of current frequency on electromagnetic tube compression, *Journal of Material Processing Technology 209 (2009).* pp. 1053-1059.

[8] Manea T.E., Verweij, M.D., Blok, H., The importance of velocity term in the electromagnetic forming process, *Proceedings of 27th General Assembly of the International Union of Radio Science*, URSI 2002, Maastricht; pp. 112-115.

[9] Crisbon Delfina Joseph, Experimental measurement and finite element simulation of springback in stamping aluminum alloy sheets for auto-body panel application, Master Thesis, Mississippi State University 2003.

[10] Padmanabhan M., Wrinkling and Spring Back in electromagnetic sheet metal forming and Electromagnetic ring compression. Master of Science Thesis: The Ohio State University, 1997.

[11] ABAQUS/Standard, Version 6.5 Manuals, Hibbitt, Karlsson and Sorensen Inc., Pawtucket, USA, 2005.

[12] IMBERT BOYD J.M.S. Increased Formability and the Effects of the Tool/Sheet Interaction in Electromagnetic Forming of Aluminium Alloy Sheet Thesis. Master of Science. Waterloo : University of Waterloo. 2005.

[13] Risch D., Beerwald C., Brosius A., Kleiner M., On the significance of the die design for electromagnetic sheet metal forming, *1st International Conference on High Speed Forming* (2004), pp.191-200.

CONCLUSION AND PERSPECTIVES

Conclusion

The overall goal of this research work is to develop a numerical model for the EMF process. Experimental studies can be very expensive, whereas numerical analyses are comparatively economical and allow wider range of parameters to be investigated in a short period of time. Using the latest techniques in the computational domain, a simpler, still robust and efficient numerical tool is developed during our research study. The aim was to provide a method that not only accurately predicts the final properties of the deformed workpiece, but also provide the control over the calculation of the basic circuit and process parameters. In order to achieve the proposed goal, the evolution of all the quantities that characterizes the EMF system is needed to be investigated during the deformation process. The number of these parameters is rather large and besides there is a very strong interaction between them, most of these have been accounted for in our research work. The whole design procedure has been presented to provide an optimal numerical setup for EMF process. Details of the basic theory of EMF process are included for enhancing the knowledge about this high speed forming technique.

For the modelling of the EMF process, we have considered an iterative step-by-step approach. The multiphysics phenomena related to the EMF process are dealt with two sub-problems: an *electromagnetic problem* describing the dynamics of electromagnetic fields and calculation of electromagnetic pressure; and a *mechanical problem* related to the mechanics of deforming workpiece and moving material. These sub-problems are mutually coupled to completely define the EMF system under consideration. Some initial assumptions have been made in order to develop an accurate numerical model that can easily compute the properties related to the EMF process. The numerical predictions are compared with experimental ones and satisfactory agreement has been obtained. The general trends of the experiments have been suitably captured by the simulations.

The electromagnetic problem is approached using a finite difference method for the resolution of pertinent Maxwell's equations with explicit time integration scheme. On the other hand, the mechanical problem is resolved using the commercial finite element code *ABAQUS*. The two problems are coupled together with the help of a user-defined sub-routine *VDLOAD*. The electromagnetic pressure calculated from the electromagnetic problem is used as a transient load in the mechanical problem. At each new time step, with the changing workpiece geometry, the new value for this magnetic pressure is calculated and applied to the bottom surface of the deformed geometry. The validation and verification of the results obtained is carried out using the free open-source finite element software *FEMM*. The proposed model can be used to solve many troublesome issues in this high speed metal forming process. Simulations and validations can also be applied with relative accuracy to industrial applications which would lead to reduction of cost and time. Furthermore, the numerical model developed through this research work is applicable to both sheetmetal as well as tubular EMF processes including expansion and compression.

Another aspect related to the higher formability and the reduced elastic springback is addressed using our in-house model. Comparisons between a conventional forming process (deep drawing) and EMF die forming are carried out. The quantitative analyses of the elastic springback and plastic deformation attained are conducted. It was found that the elastic springback in EMF process is lesser than the one obtained for conventional forming process. Consequently, the equivalent plastic deformation is higher in the case of EMF process. The new insight from the present study details the deformation mechanism of the workpiece.

Globally, a very broad database has been developed through this study, which will provide the basis for future works. This work has opened new doors for research in the domain of innovative non-conventional high speed forming technologies.

Future Work

In future, certain improvements in the modelling may be conducted. First of all, it is worth mentioning that although our numerical model reproduced effectively the experimental trends, certain physical phenomena which were neglected in our simulations (for instance effect of mutual inductance) might provide better results. Moreover; we observe that our model can further be extended to three dimensional applications. It would be interesting to develop a similar three dimensional model for industrial applications. Many forming processes are often non-axisymmetric and are best handled in a three dimensional environment. Solid mesh elements that can capture through thickness and shear stress can be included in this 3D model. Different complex geometries may be tested to validate the capabilities of the in-house code for industrial applications.

Another possible idea for future research related to the EMF process may be the development of a complex theoretical model that takes into account the changes in the electrical parameters with the deforming workpiece. Such a model may be capable of dealing with the changes in the mechanical properties of the workpiece as well as all the components of the electromagnetic system. Rigorous effort may be required to develop such a theoretical model, since the interactions between the phenomena are very complicated. Most of the process parameters are interdependent, thus high computational efforts will be needed to put forward for this future work. The model developed herein; still needs further refinement and exercise to increase the predictive ability. Further improvement in the calculations of the basic process parameters which are unavailable from the existing literature for certain simulations may render the model more accurate. Certain simplifying assumptions may be removed, to accurately capture the experimental trends.

Other areas which need improvement are material constitutive modelling. More appropriate model which accounts for large strain, higher strain rates and temperature will be best suited to model the high velocity forming process. Effects of several other geometrical and process parameters can be accounted for in the future studies. This may include influence of temperature, mutual inductance, coil material, workpiece material, permeability etc. Furthermore, in the same continuity, application of our in-house code to paramagnetic material such as low carbon steel may also be investigated. A similar study could be carried out for on-hand validation of the in-house numerical model in conjunction with experiments to make the numerical design of EMF process more efficient.

The numerical investigation carried out provided very in-depth insight into the EMF process. Further research into EMF should be continued to gain profound knowledge of the deformation dynamics. This study marks the way for further detailed studies in future about various aspects of the EMF process. New domains of the research are open for exploration.

Bibliography

[ABA, 09] ABAQUS/Explicit, Version 6.5 Manuals, Hibbitt, Karlsson and Sorensen Inc.,Pawtucket, USA, 2005.

[AEA, 03] Anter El-Azab, Mark Garnich, Ashish Kapoor, Modeling of the electromagnetic forming of sheet metals: state-of-the-art and future needs, *Journal of Materials Processing Technology* (2003), vol.142, pp. 744-754.

[AHS, 75] Al-Hassani S.T.S, Magnetic pressure distribution in the sheet metal forming, Electrical Methods of Machining, Forming and Coating, *Institute of Electrical Engineering Conference*, publication no 1975, pp. 1-10.

[ANS, 09] ANSYS ®, Version 8.0, USA, 2006 (April 2009).

[BAL, 96] Balanethiram V. S., Hyperplasticity: enhanced formability of sheet metals at high velocity". *Doctorate Thesis*, The Ohio State University, 1996.

[BEL, 96] Belyy I.V., Fertik S.M., and Khimenko L.T., Electromagnetic Metal forming Handbook, translated by Altynova M.M., Material Science and engineering department, The Ohio State University.

[BEN, 96] Bendjima B., Feliachi M. Finite element analysis of transient phenomena in electromagnetic forming system. Laboratoire de Recherche en Techniques Inductive, France 1996.

[BRA, 97] Brahim Bendjima, Contribution à la modélisation par éléments finis des phénomènes électromagnétiques relatifs au magnétoformage*, Thèse de Doctorat*, Université de Nantes, 1997.

[CON, 06] Conraux Ph., Pignol M., Robin V., Bergheau J.M., 3D finite element modeling of electromagnetic forming processes, *2nd Conference on High Speed Forming* 2006, Dortmund, pp. 73-82.

[CRI, 03] Crisbon Delfina Joseph, Experimental measurement and finite element simulation of springback in stamping aluminum alloy sheets for auto-body panel application, *Master Thesis*, Mississippi State University 2003.

[EUV, 94] Euvrard D., Résolution numérique des équations aux dérivées partielles, Edition Marson, 1994.

[FEM, 09] Foster-Miller Inc., FEMM, Open source FEA software Ver. 3.3 by Meeker D. (2003), http:// femm.foster-miller.net (April 2009).

[GOL, 05] Golovashchenko S.F., Material formability and coil design in electromagnetic forming, Journal of Materials Engineering and Performance, *DOI: 10.1007/s11665-007-9058-7.*

[GRE, 98] Gregg K. Fenton, Glenn S.Daehn, Modeling of electromagnetically formed sheet metal, *Journal of Materials Processing Technology* (1998), vol. 75, pp. 6-16.

[GRO, 46] Grover F.W., Inductance calculations; Working formulas and tables, DOVER Publication Inc, New York 1946.

[GUR, 77] Gurson A.L., Continuum theory of ductile rupture by void nucleation and growth: Part-I, yield criteria and flow rules for porous ductile media, *Journal of Engineering Materials Technology*, (1977), vol. 99, pp. 2-15.

[HAI, 09] Haiping Y.U., Chunfeng L.I., Effects of current frequency on electromagnetic tube compression, *Journal of Material Processing Technology* 209 (2009). pp. 1053-1059.

[HAL, 09] Hallquist J. "LS-DYNA Theoretical Manual," Livermore software technology corporation.

[IBS, 05] IMBERT BOYD J.M.S. Increased Formability and the Effects of the Tool/Sheet Interaction in Electromagnetic Forming of Aluminium Alloy Sheet

Thesis. Master of Science. Waterloo : University of Waterloo. 2005.

[IJM, 05] Imbert J.M., Winkler S.L., Worskick M.J., Oliveira D.A., Golovaschenko S., The effect of tool-sheet interaction on damage evolution in electromagnetic forming of aluminum alloy sheet, *Journal of Engineering Materials and Technology* ,vol. 127 January (2005); pp.145-153.

[IMB, 05] Imbert Boyd J.M.S. Increased Formability and the Effects of the Tool/Sheet Interaction in Electromagnetic Forming of Aluminium Alloy Sheet *Thesis. Master of Science.* Waterloo : University of Waterloo. 2005.

[IUL, 09] Institut für Umformtechnik und Leichtbau, Dortmund, Germany, University of Dortmund, http://www.iul.tu-dortmund.de/de/index.php (April 2009).

[JAB, 78] Jablonski J. and Wrinkler R., Analysis of the electromagnetic forming process, *International Journal of Mechanical Sciences* 20 (1978); pp.315-325.

[JCW, 85] Johnson G.R., Cook W.H., Fracture characteristics of three metals subjected to various strains, strain rates, temperatures and pressures, *Engineering Fracture Mechanics*, vol. 21, no.1 (1985), pp. 31-48.

[JOZ, 03] Jozef Bednarczyk, Distribution of forces in the inductors used in metal processing in the pulse magnetic field, *Journal of Materials Processing Technology* (2003), vol. 133,pp. 340-247.

[JPM, 08] J.P.M. Correia, M.A. Siddiqui, S. Ahzi, S. Belouettar and R. Davies, A simple model to simulate electromagnetic sheet free bulging process, *International Journal of Mechanical Sciences* 50 (2008), pp.1466–1475.

[JTC, 01] John T. Conway, Exact solutions for the magnetic fields of axisymmetric solenoids and current distributions, *IEEE Transactions* (2001), Vol. 37, no. 4, pp. 2977-2988.

[KAR, 05] Karch C. and Roll K., Transient simulation of electromagnetic forming of

aluminium tubes, *Advanced Materials Research*, vol. 6-8 (May 2005), pp. 639-646.

[KBH, 05] Kliener M., Beerwald C., Homberg W., Analysis of process parameters and forming mechanisms within the electromagnetic forming process, *Annals of the CIRP 54/01/2005*; pp. 225-228.

[KLB, 06] Kliener M. and Brosius A., Determination of flow curves at high strain rates using the electromagnetic forming process and an iterative finite element simulation scheme, *Annals of the CIRP* (2006), vol. 55(1).

[KOR, 07] Kore S.D., Date P.P., Kulkarni S.V., Effects of process parameters on electromagnetic impact welding of aluminum sheets, *International Journal of Impact Engineering* 34, 2007, pp. 1327-1341.

[MAL, 03] Mallein V., Magnétoformage de pièces en aluminium pour automobile, Étude expérimentale et développement numérique associe. *Thèse de Doctorat Génie des Procèdes*. Grenoble : INPG 2003.

[MAM, 04] Mamalis A.G., Manolakos, D.E., Kladas, A.G., Koumoutsos, A.K., Electromagnetic forming and powder processing: Trends and developments, *Applied Mechanics Review* 2004, 57; pp. 299-324.

[MAN, 05] Manish Kamal, A uniform pressure electromagnetic actuator folr forming flat sheets, *Doctorate thesis*, The Ohio State University, 2005.

[MAR, 09] MSC Software ™, Marc ® 2005, http://www/mscsoftware.com/. (April 2009).

[MAV, 05] Mala Seth, Vincent J. Vohnout, Glenn S. Daehn, Formability of steel sheet in high velocity impact, *Journal of Materials Processing Technology* (2005), vol. 168, pp. 390-400.

[MSD, 06] Mala Seth Dehra, High velocity formability and factors affecting it, *Doctorate thesis*, The Ohio State University, 2006.

[MVB, 02] Manea T.E., Verweij, M.D., Blok, H., The importance of velocity term in the electromagnetic forming process, *Proceedings of 27th General Assembly of the International Union of Radio Science*, URSI 2002, Maastricht; pp. 112-115.

[OLI, 05] Oliviera D.A., Worswick M.J., Finn M., Newman D., Electromagnetic forming of aluminum alloy sheet: Free-form and cavity fill experiments and model, *Journal of Materials Processing Technology* (2005), vol.170; pp. 350-362.

[OSU, 09] http://www.matsceng.ohio-state.edu/~daehn/hyperplasticity.html (April 2009).

[PAD, 97] Padmanabhan M., Wrinkling and Spring Back in electromagnetic sheet metal forming and Electromagnetic ring compression. *Master of Science Thesis*: The Ohio State University, 1997.

[PAM, 09] PAM-STAMP ®, User's manual, ESI Group 2005.

[PLE, 08] Pierre L'Eplattenier, Grant Cook, Cleve Ashcraft, Mike Burger, Art Shapiro, GlennDaehn, Mala Seth, Introduction of an electromagnetic module in LS-DYNA for coupled mechanical-thermal-electromagnetic simulations, *9th International LS-DYNA Users Conference, Metal forming* (2), pp. 17-1 to 17-8.

[RES, 60] Resnick R., Halliday D., Electricité et magnétisme, Traduit par Lebel A., Thériault C., Physique 2, John Wiley & Sons, INC 1960.

[RIS, 04] Risch D., Beerwald C., Brosius A., Kleiner M., On the significance of the die design for electromagnetic sheet metal forming, *1st International Conference on High Speed Forming* (2004), pp.191-200.

[SON, 04] Song F.M., Zhang X., WANG Z.R., Yu L.Z., A study of tube electromagnetic forming, *Journal of Materials Processing Technology*(2004), vol.151; pp.

372-375.

[STI, 06] Stiemer M., Unger J., Blum H. and Svendsen B., Algorithmic formulation and numerical implementation of coupled multifield models for electromagnetic metal forming simulations, *International Journal of Numerical Methods in Engineering.* **68** (2006), pp. 1301–1328.

[SUN, 94] Sung Ho Lee and Dong Nyung Lee, A finite element analysis of electromagnetic forming for tube expansion, Transaction of ASME, *Journal of Engineering Materials and Technology,* vol.116 1994; pp. 250-254.

[SVE, 03] Svendsen B., Chanda T., Continuum thermodynamic modeling and simulation of electromagnetic metal forming, *Technishe Mechanik*, vol. 23(2003), pp. 103-112.

[SYS, 09] SYSWELD ®, SYSMAGNA, User's manual, ESI Group, 2005.

[TAK, 80] Takatsu N., Kato M., Sato K., Tobe T., High speed forming of metal sheets by electromagnetic forces, *International Journal of Japanese Society for Mechanical Engineering* 1980; 60; pp. 142-148.

[TDI, --] Travail des métaux en feuilles, Formage electromagnétique, Techniques de l'ingenieur, Traité Génie mécanique, B 7 582, pp 1-20.

[TEM, 03] Teodora-Emilia MOTOASCA, Electrodynamics in deformable solids for electromagnetic forming, *Doctorate Thesis*, Universitatea "Transilvania", Brasov, Roumania,2003.

[TNM, 84] Tvergaard V., and Needleman A., Analysis of the cup-one fracture in a round tensile bar, *Acta Metallurgica* (1984), vol. 32, pp.157.

[TVE, 81] Tvergaard V., Influence of voids on shear band instabilities under plane strain conditions, *International Journal of Fracture* (1981), vol. 37(4), pp.389-407.

[UNG, 07] Unger J.A, Modeling and simulation of coupled electromagnetic field

problems with application to model identification and metal forming, *Doctor Ingénieurs Thesis*, University of Dortmund, 2007.

[VIN, 98] Vincent J. Vohnout, A hybrid quasi-static/dynamic process for forming large sheet metal parts from aluminum alloys, *Doctorate thesis*, The Ohio State University, 1998.

[WHG, 89] William H. Gourdin, Analysis and assessment of electromagnetic ring expansion as a high strain-rate test, *Journal of Applied Physics*;65 (1989), pp. 411–422.

[YOU, 05] Young-Bae Park, Hoen-Young Kim, Soo-Ik Oh, Design of axial torque joint made by electromagnetic forming, *Thin-Walled Structures* 43 (2005); pp. 826-844.

[YUH, 07] Yu H.P. and Li C.F., Dynamic compaction of pure copper powder using magnetic force, *Acta Metallurgica Sinica*(English letters) 2007; vol. 20, No.4, pp. 277-283.

[YUP, 07] Yu Hai-ping and Li Chun-feng, Effects of coil length on tube compression in electromagnetic forming, *Transactions of Nonferrous Metals Society of China 17*,(2007), pp. 1270–1275.

[ZHA, 04] Zhang X., Wang Z.R., Song F.M., Yu L.Z., Lu X., Finite element simulation of the electromagnetic piercing of sheet metal, *Journal of Materials Processing Technology*(2004)*,* vol. 151,pp. 350-354.

[ZMS, 95] Zhang H., and Murata M., Suzuki H., Effects of various working conditions on tube bulging by Electromagnetic forming, *Journal of Materials Processing Technology* (1995); 48, pp. 113–121.

Appendix I

List of International Publications in Journals and communications

List of International Publications in Journals and communications

Articles dans des revues Internationales

1. Correia J.P.M, **Siddiqui M.A.**, Ahzi S., Belouettar S.,.Davies R., A simple model to simulate electromagnetic sheet free bulging process, *International Journal of Mechanical Sciences, 50(2008,) pp.1466–1475.*

2. **Siddiqui M.A.**, Correia J.P.M., Ahzi S. and Belouettar S., A numerical model to simulate electromagnetic sheet metal forming process, *International Journal of Material Forming, Volume 1, Supplement 1, 2008, pp.1387-1390 (DOI 10.1007/s12289-008-0123-z).*

Congrès Internationaux avec actes

3. Correia J.P.M., **Siddiqui M.A**., Ahzi S., and Khaleel M.A., Numerical study of wrinkling and springback in electromagnetic sheet metal forming, *IDDRG 2006 International Deep Drawing and Research Group Conference Porto, Portugal, 19-21 Juin 2006.*

4. **Siddiqui M.A.**, Correia J.P.M., Ahzi S.and Belouettar S., A numerical model to simulate electromagnetic sheet metal forming process, *11th ESAFORM'2008 conference on material forming, Lyon, France 23-25 Avril 2008.*

5. **Siddiqui M.A.**, Correia J.P.M., Ahzi S. and Belouettar S., Electromagnetic forming process: estimation of magnetic pressure in tube expansion and numerical simulation, *12th ESAFORM'2009 conference on material forming, Twente, The Netherlands, 27 -30 Avril 2009.*

Reporters’ Notes and remarks